UNIVERSITY OF SOUTHAMPTON

Physics of Hollow Cathode Breakdown and Steady-State Operation with Several Inert Gas Propellants

Ismat M. Ahmed Rudwan

Thesis submitted for Doctor of Philosophy

Astronautics Research Group
School of Engineering Sciences
September 2003

UNIVERSITY OF SOUTHAMPTON

ABSTRACT

FACULTY OF ENGINEERING AND APPLIED SCIENCES
AERONAUTICS AND ASTRONAUTICS

Doctor of Philosophy

PHYSICS OF HOLLOW CATHODE BREAKDOWN AND STEADY STATE OPERATION WITH SEVERAL INERT GAS PROPELLANTS

by Ismat M. Ahmed Rudwan

Electron bombardment ion thrusters currently form the cutting-edge of spacecraft propulsion technology. Offering substantial mass savings in comparison to chemical thrusters and being an enabling technology for some high energy missions, these devices have passed, in recent years, from a high state of development to actual application in space. This was primarily due to the efforts of such agencies as NASA with its highly successful technology demonstrator Deep Space 1, along with their commercial application in NSSK of communication satellites.

Alternative propellants for xenon might be necessary for high specific impulse missions and as cheaper alternatives for reduction of operating costs. Prior to this, operation with these gases has to be demonstrated and any adverse effects on thruster performance incurred by their use have to be identified. In particular, characterisation of these gases has to be carried out in the ion thruster's primary electron production region, the hollow cathode. The hollow cathode, in spite of its importance to the thruster's operation, was poorly understood. This is due to the difficulty of conducting non-intrusive investigations on the small scale required in the hollow cathode cavity.

Experiments have been performed on the T6 hollow cathode to characterise four propellants: xenon, krypton, argon and a krypton/xenon mix in the natural occurring ratio. An extensive study was conducted on the hollow cathode internal plasma dealing with two aspects of hollow cathode operation: the transient (starting) phase and the steady state phase. Discharge initiation characteristics were investigated for these selfsame propellants for a wide range of mass flow rates and cathode tip temperatures. Discharge initiation was found to be repeatable and occurred at low values of keeper potential. A novel set of experiments was carried out on the breakdown plasma optical emission using photomultiplier tubes. The steady state work involved characterisation of the hollow cathode discharges for all the propellants in diode configuration. This was then followed by a spectroscopic investigation of the hollow cathode internal plasma under different discharge conditions. The spectroscopic techniques enabled a non-intrusive comparison and study of the discharge for the different propellant species.

Simple models and theories were developed to describe HC behaviour. Penning ionisation was found to be active during the breakdown phase, leading to anomalous breakdown behaviour. A new theory is proposed that relates the plume and spot modes and transition between them to the current collection mechanism at the anode.

Like one that stands upon a promontory,
And spies a far-off shore where he would tread,
Wishing his foot were equal with his eye;
And chides the sea that sunders him from thence,
Saying, he'll lade it dry to have his way.

Richard,
Henry the Sixth

Acknowledgements

"I can no other answer make but thanks,
And thanks, and ever thanks; too oft good turns
Are shuffl'd off with such uncurrent pay"

First I would like to thank **Dr. S. B. Gabriel**, who, apart from his instigation of this project, supervision and technical assistance throughout, has been a huge support when things went wrong. Most importantly, he had faith in the author when he himself had none. He provided extended financial support, and a great working environment. To him the author is eternally indebted, and indeed 'thanks' can be too little a word.

Thanks are due to **Dave Fearn** at DERA/QinetiQ, for his encouragement, support and for securing the loan of the T6 hollow cathode.

The technical assistance and know-how of **Simon Klitz**, **Rob Stansbridge** and **Ed Rayner** was called upon throughout this project, which they have made possible. I must also thank **Frank Crawford** for his simulations, which have supported the theoretical part of this work.

I have been blest with an amazing group of friends who made this journey memorable

I would like to thank **George Michalareas** for being by my side on this road, his help, advice, diversions etc. are unforgettable. My brother in arms, "*we few, we happy few, we band of brothers*". **Sarah Jane**, for being who she is; her help, support and encouragement were a blessing, thank you. **Mohammed** 'the M.O.E.' **Shehata**, who has been there for me ever since I can remember, to you a special thanks. From Abu Dhabi I wish to thank **Ayman Al-Ameen** and **Nazar Awad** my friends since childhood for their love and support, and **Yousif Ameen** 'from a tribe called J' for those long drives on the sea front and for teaching me to appreciate the finer things in life. Special thanks are also due to **Adil** 'Abu al3awadil' **Babiker** and **Majd Zoroob**, who are respectively, the mayor and deputy mayor of Southampton, and **Dr. Robert** 'I AM a Dr.' **George**. I wish to also thank the Jordanian queens **Noor** 'wife' **Dajani** and **Muna Zawaydeh**, and my 'little sis' **Shanu Gupta**, **Ibn Auf** , **Biggie** and **Phil** for being like a family to me.

Many thanks to the office gang who made the research enjoyable: **Neil**, **Duncan**, **Sabrina**, **Gavin**, **Balaji**, **Christoph**. Particular regards to **Paolo Gessini** for his proof reading of this thesis and the numerous interesting conversations we've had over the years that usually went on till daybreak. My housemates **Kossi**, **Sam**, **Mourad** and our honorary members **Isaac, Yassin, Gihanjili** and **Tarik**, thank you, for turning a house into a home.

Finally, to my family; **Rashida**, **Farouk,** my angels **Abeer** and **Afraa,** and little **Mohammed,** thank for everything. Mom this is dedicated to you.

CONTENTS

Chapter 1 INTRODUCTION 1

1.1 The benefits of ion propulsion 1

1.2 Ion thruster development 3

1.3 Objectives of the current study 6

1.4 Thesis structure 8

Chapter 2 BACKGROUND AND LITERATURE REVIEW 10

2.1 Principles of Kaufman-type ion thruster operation 10

2.2 The hollow cathode discharge 13

2.2.1 Hollow cathode construction 14

2.2.2 Hollow cathode emission theory 15

2.2.3 Hollow cathode operating modes 19

2.2.4 HC internal plasma diagnostics 21

2.2.4.1 Measurements in HCs operating on mercury 21

2.2.4.2 Measurements in HCs operating on xenon 26

2.2.5 Hollow cathode discharge initiation (Starting) 28

2.2.5.1 Experience with mercury 28

2.2.5.1.1 Proposed HC initiation theory based on the mercury results 36

2.2.5.2 Experience with xenon 38

Chapter 3 THEORETICAL BACKGROUND 42

3.1 Plasma spectroscopy 42

3.1.1 Plasma radiation 43

3.1.2 Plasma models and types of equilibrium 45

3.1.2.1 LTE model 47

3.1.2.2 Corona model 48

3.1.2.3 Validity Criteria 50

Validity of the assumption of Maxwellian electron population in a HC plasma 50

Range of validity of the LTE and corona plasma models 51

HC plasma optical depth 54

3.1.2.4 Collisional- Radiative (C-R) model 58

3.1.3 Spectroscopic methods for plasma parameter evaluation 63

3.1.3.1 Ratio of line intensities 63

Ratio of lines of the same species 64

Ratio of lines of the same element at different stages of ionisation 66

3.1.3.2 Continuum methods 67

Relative continuum intensities 68

3.2 Electrical breakdown in gases 69

3.3 Hollow cathode discharge modelling 72

3.3.1 The Siegfried-Wilbur model 74

3.3.2 The Salhi-Turchi model 78

Chapter 4 EXPERIMENTAL APPARATUS **82**

4.1 Mechanical system 83

4.1.1 Vacuum chamber 83

4.2 Experimental subsystems 84

4.2.1 Hollow cathode in diode configuration 84

4.2.2 Propellant feed system 87

4.3 Electrical supply system 89

4.4 Diagnostics 90

4.4.1 Optical diagnostics 90

4.4.1.1 Spectrometer and CCD array 90

4.4.1.2 Photomultiplier tube 93

4.4.1.3 Monochromator 94

4.4.1.4 Optical fibre and optical fibre shield 95

4.4.2 Hollow cathode tip temperature measurement 98

Chapter 5 EXPERIMENTAL PROCEDURES **99**

5.1 General experimental procedure 99

5.1.1 Vacuum system 99

5.1.2 Propellant flow rate calibration 100

5.2 Discharge initiation experiments 102

5.2.1 Range of experiments 102

5.2.2 Breakdown voltage dependence on propellant flow rate and tip temperature 103

5.2.3 Discharge initiation optical emission studies 105

5.2.3.1 Broadband discharge initiation optical emission study 105

5.2.3.2 Spectroscopic discharge initiation optical emission study 106

5.3 Steady state spectroscopy 107

5.3.1 Range of experiments 108

5.3.1.1 Range of Propellant flow rates 108

5.3.1.2 Range of discharge currents 108

5.3.2 Experimental set-up 109

5.3.3 Hollow cathode start-up and thermal equilibrium 109

5.3.4 Discharge characterisation 110

5.3.5 Spectroscopic investigation 113

5.3.5.1 Spectral calibration 113

5.3.5.2 Full optical emission spectra experiments 114

5.3.5.3 Variation of emission line intensity with propellant flow rate and discharge current 115

Chapter 6 RESULTS **117**

6.1 Introduction to the results 117

6.2 Starting results 117

6.2.1 V_{bk} dependence on propellant flow rate and tip temperature 118

6.2.1.1 V_{bk} dependence on mass flow rate 118

6.2.1.2 V_{bk} dependence on tip temperature 121

6.2.1.3 Comparison of the results for different gases 124

6.2.2 Hollow cathode breakdown plasma broadband optical study 126

6.2.2.1 Breakdown broadband emission dependence on $\dot{m}$ and T 126

6.2.2.1.1 Optical emission dependence on mass flow rate 127

6.2.2.1.2 Optical emission dependence on tip temperature 130

6.3 Steady-state results 132

6.3.1 Discharge characterisation 132

6.3.1.1 Discharge voltage-current characteristics 133

6.3.1.2 Discharge voltage dependence on $\dot{m}$ 137

6.3.2 Full optical emission spectra experiments 139

6.3.2.1 Xenon results 140

6.3.2.2 Krypton results 144

6.3.2.3 Argon results 147

6.3.3 Dependence of emission line intensity on propellant flow rate and discharge current 150

6.3.3.1 Dependence of gas species emission line intensity on discharge current 150

6.3.3.2 Dependence of gas species emission line intensity on propellant flow rate 153

6.4 Anode deposit 156

Chapter 7 DISCUSSION 159

7.1 Hollow cathode breakdown 159

7.1.1 Anomalous HC breakdown & Penning ionisation 159

7.1.1.1 Estimation of metastable population in the propellant gases 165

7.1.1.2 Presence of barium in inert gas 167

7.1.2 The role of the cathode orifice and breakdown statistics 171

7.2 Spectroscopic results 182

7.2.1 Discussion of the analysis methods employed 182

7.2.2 Calculation of electron temperature and density 185

7.3 Prediction of cathode operating parameters using a modified Siegfried-Wilbur model 194

7.4 Theory of plume to spot transition 199

7.4.1 Review of previous discharge characterisation studies 199

7.4.1.1 Siegfried and Wilbur 199

7.4.1.2 Fearn and Patterson 203

7.4.2 Results of the discharge characterisation work in the present study 210

Dependence on $\dot{m}$ 210

Dependence on I_a 216

7.4.3 Existing theories for plume to spot transition 221

7.4.4 Proposed plume to spot transition theory 223

7.4.4.1 Effect of propellant flow rate 233

7.4.4.2 Effect of discharge current 238

7.4.4.3 Geometrical factors influencing discharge behaviour 251

7.4.5 Full thruster configuration 255

7.4.6 Implications of the theory 256

Chapter 8 CONCLUSIONS 259

8.1 The HC breakdown characteristics 259

8.2 Characterisation of the steady-state HC discharge 262

8.3 The HC discharge plasma parameter estimation, modelling and theory of operation in the plume and spot modes 262

8.4 Novelty and applicability of the work 265

8.5 Recommendations for future work 267

Appendix A The Instrumented T6 Hollow cathode **269**

A.1 The modified T6 hollow cathode 270

A.2 Development of the sapphire fibre optic probe 272

A.3 Experimental arrangements 278

A.4 Conclusion 282

Appendix B Computational modelling of HC neutral flow **284**

Appendix C Spectral line widths and profiles **288**

C.1 Natural broadening 289

C.2 Doppler broadening 290

C.3 Stark broadening 291

References **293**

LIST OF FIGURES

Figure 2.1: A modern Kaufman-type ion thruster [112] 11

Figure 2.2: Schematic of a typical orificed ion thruster hollow cathode 14

Figure 2.3: Voltage-current characteristics of a hollow cathode discharge showing plume to spot transitions at different values of mass flow rate [33] 20

Figure 2.4: Variation of electron temperature with mass flow rate in the UK-10 hollow cathode internal plasma [46] 22

Figure 2.5: Plasma electron number density as a function of flow rate in the UK-10 hollow cathode internal plasma [46] 23

Figure 2.6: Variation of cathode plasma potential and electron temperature profiles with distance from the orifice plate at 0.31mg/s, for several values of discharge current [146] 24

Figure 2.7: Variation in electron density with distance from the orifice at 0.31mg/s, for several values of discharge current [146] 25

Figure 2.8: Experimental set-up for the spectroscopic investigations in the UK-25 hollow cathode operating on Xe [101] 27

Figure 2.9: Detailed schematic of the diode system employed in the mercury starting experiments [48] 29

Figure 2.10: Discharge initiation data for a cathode containing tubular insert at $\dot{m}$ ~0.12mg/s [48] 30

Figure 2.11: Envelopes of discharge initiation data as a function of mass flow rate for T =1300 ^{o}C [48] 31

Figure 2.12: The discharge initiation behaviour cathode containing rolled foil insert, superimposed are the results for a tubular insert cathode [48] 32

Figure 2.13: Discharge initiation behaviour of curved orifice cathodes [48] 33

Figure 2.14: Insert configuration used in the non-bariated cathode tests [48] 34

Figure 2.15: Discharge ignition behaviour with and without barium [48] 34

Figure 2.16: Variation in discharge ignition behaviour with change in orifice size [48] 35

Figure 2.17: V_{bk} as a function of cathode tip temperature for different values of $\dot{m}$ [124] 39

Figure 2.18: V_{bk} as a function of $\dot{m}$ for different values of T [124] 39

Figure 3.1: Energy level diagram for a hydrogenic species of charge Z 44

Figure 3.2: Validity limits of LTE and corona models for ***(a)*** *xenon,* ***(b)*** *krypton, and* ***(c)*** *argon plasma* 53

Figure 3.3: Ratio of number densities from theoretical model for $n_e=10^{14}$ cm^{-3} 63

Figure 3.4: Breakdown voltage as a function of $(P \times d)$ for several gases [162] 71

Figure 3.5: Illustration of cylindrical slices of the arc adjacent to HC surface used in the Kennedy model: (a) current balance at steady state, (b) power balance [81] 73

Figure 3.6: Schematic of the ion production region in a hollow cathode operating on Hg, whose boundaries are defined by L_e, the emission length. [145] 75

Figure 4.1: The Vacuum chamber with accompanying hardware 82

Figure 4.2: Vacuum system schematic [33] 84

Figure 4.3: T6 hollow cathode dimensions (dimensions in mm) 85

Figure 4.4: Schematic of the hollow cathode arrangement in diode configuration (dimensions in mm) 86

Figure 4.5: Photograph of the hollow cathode in diode configuration 87

Figure 4.6: The propellant feed system [33] 88

Figure 4.7: Electrical power supply arrangement in diode configuration 89

Figure 4.8: The Oriel MS127i spectrograph's optical design [157] 91

Figure 4.9: Grating efficiency plot for 300l/mm grating 92

Figure 4.10: Grating efficiency plot for 2400l/mm grating 92

Figure 4.11: Quantum efficiency plot of Instaspec IV CCD array 93

Figure 4.12: H6780 photosensor module frequency response curve 94

Figure 4.13: Grating efficiency plot for monochromator 1200l/mm grating 95

Figure 4.14: Transmission properties of the FC-UV200-1 optical fibre 96

Figure 4.15: Transmission properties of the Oriel 77678 Multi-track optical fibre bundle 97

Figure 4.16: Transmission properties of the quartz shield 97

Figure 4.17: Optical pyrometer calibration 98

Figure 5.1: Comparison between calibration data for Edwards [33] Milligan [112] and the current set-up 101

Figure 5.2: Experimental set-up for investigation of breakdown voltage dependence on flow rate and tip temperature 103

Figure 5.3: Experimental set-up for breakdown broadband optical emission studies 105

Figure 5.4: Experimental set-up for discharge initiation spectroscopy 107

Figure 5.5: Experimental set-up for steady state discharge investigations 109

Figure 5.6: Illustration of the system used to compare propellant flow rate for different gases 112

Figure 5.7: Line output of Hg(Ar) spectral calibration lamp 113

Figure 6.1: Discharge initiation voltage as a function of propellant flow rate (Xe) 119

Figure 6.2: Discharge initiation voltage as a function of propellant flow rate (Kr) 119

Figure 6.3: Discharge initiation voltage as a function of propellant flow rate (Ar) 120

Figure 6.4: Discharge initiation voltage as a function of propellant flow rate (Kr/Xe) 120

Figure 6.5: Discharge initiation voltage as a function of cathode tip temperature (Xe) 122

Figure 6.6: Discharge initiation voltage as a function of cathode tip temperature (Kr) 122

Figure 6.7: Discharge initiation voltage as a function of cathode tip temperature (Ar) 123

Figure 6.8: Discharge initiation voltage as a function of cathode tip temperature (Kr/Xe) 123

Figure 6.9: Comparison of V_{bk} as a function of $\dot{m}$ for Xe, Kr, Ar and Kr/Xe (at 1299°C tip temperature) 124

Figure 6.10: Comparison of V_{bk} as a function of $\dot{m}$ for Xe, Kr, Ar and Kr/Xe (at 929°C tip temperature) 125

Figure 6.11: Comparison of V_{bk} as a function of T for Xe, Kr, Ar and Kr/Xe (at 1mg/s propellant flow rate) 125

Figure 6.12: Comparison of V_{bk} as a function of T for Xe, Kr, Ar and Kr/Xe (at 0.2mg/s propellant flow rate) 126

Figure 6.13: Plot of a typical result from PMT investigation of breakdown in argon (Art289, $\dot{m}$ =1mg/s and T=1299°C) 127

Figure 6.14: Plot of the dependence of V_k temporal behaviour on mass flow rate during breakdown (1299°C) 128

Figure 6.15: PMT output voltage during breakdown, dependence on mass flow rate (1299°C) 128

Figure 6.16: Plot of the dependence of V_k temporal behaviour on tip temperature during breakdown (1mg/s) 130

Figure 6.17: PMT output voltage during breakdown, dependence on tip temperature (1mg/s) 131

*Figure 6.18: Discharge voltage dependence on I_a for xenon discharge at **(a)** 1mg/s (plume mode) and **(b)** 3.29mg/s (spot mode)* 133

Figure 6.19: Anode V-I characteristics for the T6 operating on xenon 134

Figure 6.20: Anode V-I characteristics for the T6 operating on krypton 135

Figure 6.21: Anode V-I characteristics for the T6 operating on argon 135

Figure 6.22: Anode V-I characteristics for the T6 operating on Kr/Xe 136

Figure 6.23: Comparison of anode V-I characteristics for all gases in the spot mode 136

Figure 6.24: Keeper V-I characteristics for the T6 operating on xenon 137

Figure 6.25: Discharge voltage dependence on $\dot{m}$ for xenon discharge at 5A anode current 138

Figure 6.26: Comparison of V_a as a function of $\dot{m}$ for all gases 139

Figure 6.27: Optical emission spectrum from the hollow cathode internal plasma with xenon at 1mg/s and 5A discharge current (300l/mm grating) 141

Figure 6.28: Optical emission spectrum from the hollow cathode internal plasma with xenon at 1mg/s and 5A discharge current (2400l/mm grating) 142

Figure 6.29: Optical emission spectrum from the hollow cathode internal plasma with krypton at 1mg/s and 5A discharge current (2400l/mm grating) 145

Figure 6.30: Optical emission spectrum from the hollow cathode internal plasma with argon at 1mg/s and 5A discharge current (2400l/mm grating) 148

Figure 6.31: Time trace of KrII line intensity as a function of discharge current in spot mode (2.415Aequiv) 151

Figure 6.32: Normalised intensity of KrII lines as a function of I_a in spot mode, $\dot{m}$ = 2.415Aequiv 152

Figure 6.33: Comparison of Ar, Kr & Xe normalised first ionisation emission line intensity as a function of discharge power in spot mode 152

Figure 6.34: Comparison of KrII and KrI normalised line intensity as a function of P_D in spot mode 153

Figure 6.35: Time trace of the line intensity of three KrII emission lines as a function of $\dot{m}$ (I_a=5A) 154

Figure 6.36: Comparison of XeII and XeI line intensity as a function of $\dot{m}$ in the spot mode where the electrical set up is kept approximately constant 155

Figure 6.37: Photograph of anode with area of deposit indicated 156

Figure 6.38: SEM of deposited material 157

Figure 6.39: Illustration of ED-XRF [192] 157

Figure 6.40: ED-XRF spectrum of deposit 158

Figure 7.1: Ionisation coefficient η as a function of E/P_o for several Ne-Ar mixtures where $100 \times a$= argon percentage (thus $a=0$ is pure Ne, and $a=1$ is pure Ar) [88] 161

Figure 7.2: (a) *Breakdown voltage dependence on $P_o \times d$ for several gases and Ne-Ar mixtures [32], formation of a double minimum due to Penning ionisation better illustrated in figure* (b) *[125]* 163

Figure 7.3: Total cross-sections for the metastable excitation in Ar, Kr and Xe [108] 166

Figure 7.4: Barium evaporation rate as function of temperature for a 'new' 4:1:1 dispenser cathode [27] 168

Figure 7.5: Comparison of V_{bk} as a function of $\dot{m}$ for Xe (on the T6) and Hg (on the T4) [48] 171

Figure 7.6: 1*V contours of electric potential for:* (a) *a flat 0.3mm dia. tip (similar to the T4 Hg case [48]).* (b) *a flat 1.4mm dia. tip.* (c) *a bevelled 1.4mm dia. tip (similar to the T6 case), for several keeper potentials* 173

Figure 7.7: Probability of an uninterrupted sequence of electron avalanches initiated by a single electron as a function of overvoltage [109] 177

Figure 7.8: Discharge initiation characteristics using an internal electrode [48] 180

Figure 7.9: Log I vs λ for continuum in a xenon discharge, $\dot{m}$ =1mg/s, I_a=5A 183

Figure 7.10: Intensity ratio of the XeII 433.052nm and XeI 450.100nm lines as a function of electron temperature for several n_e values 184

Figure 7.11: n_e as a function of T_e predicted by both LTE model and equation (3.47) for the C-R model in xenon and argon discharge, $\dot{m}$ = 1mg/s and I_a = 5A in both gases 184

Figure 7.12: C-R Boltzmann plot of ArII lines from T6 cathode argon discharges in both spot and plume modes at several values of $\dot{m}$, I_a=5A, correlation coefficient > 0.92 186

Figure 7.13: Electron temperature and density in the T6 HC operating on argon as a function of $\dot{m}$ at I_a=5A 186

Figure 7.14: C-R Boltzmann plot of KrII lines from T6 cathode krypton discharges in both spot and plume modes at several values of $\dot{m}$, I_a=5A, correlation coefficient > 0.89 187

Figure 7.15: Electron temperature and density in the T6 HC operating on krypton as a function of $\dot{m}$ at I_a=5A 187

Figure 7.16: C-R Boltzmann plot of XeII lines from T6 cathode xenon discharges in both spot and plume modes at several values of $\dot{m}$, I_a=5A, correlation coefficient > 0.93 188

Figure 7.17: Electron temperature and density in the T6 HC operating on xenon as a function of $\dot{m}$ at I_a=5A 188

Figure 7.18: Effect of discharge current on plasma density, comparison between modelling results on Xe and experimental results from Siegfried [145] on Hg 197

Figure 7.19: T_s as a function of discharge current, comparison between modelling and experimental results from a T6 cathode operating on Xe [44] 197

Figure 7.20: Electron temperature and plasma potential profiles in the plume mode [146] 200

Figure 7.21: Electron density profiles in the plume mode [146] 200

Figure 7.22: Electron temperature and plasma potential profiles in the spot mode [146] 201

Figure 7.23: Electron density profiles in the spot mode [146] 201

Figure 7.24: Illustration of the experimental apparatus used by Patterson and Fearn [40] 203

Figure 7.25: Discharge characteristics and discharge modes as a function of the main discharge parameters, for d_o=1.3mm, d_k=1.5mm and I_k=1A [45] 204

Figure 7.26: Anode and keeper noise as a function of I_a at several values of $\dot{m}$ [40] 205

Figure 7.27: Cathode pressure as a function of $\dot{m}$ [121] 206

Figure 7.28: Anode voltage current characteristics using: **(a)** *laboratory power supply* **(b)** *battery [40]* 207

Figure 7.29: Cathode temperature as a function of $\dot{m}$ and d_o at I_a=15A [45] 208

Figure 7.30: Influence of orifice diameter on the boundaries of the discharge regions [44] 208

Figure 7.31: Effect of d_k on the boundaries of the discharge regions [44] 209

Figure 7.32: Effect of $\dot{m}$ on the visual and electric characteristics of the discharge in both plume and spot modes for xenon at I_a=5A and I_k=1A 212

Figure 7.33: Visual observations and anode and keeper voltage dependence on $\dot{m}$ for an argon discharge at I_a = 5A and I_k = 1A 213

Figure 7.34: Visual observations and anode and keeper voltage dependence on $\dot{m}$ for aa krypton discharge at I_a = 5A and I_k = 1A 213

Figure 7.35: Visual observations and anode and keeper voltage dependence on $\dot{m}$ for a Kr/Xe mix discharge at I_a = 5A and I_k = 1A 214

Figure 7.36: Comparison of the emission spectrum of argon discharge at 1mg (with luminous cloud upstream of keeper), 1.5mg/s, 2mg/s (both with luminous cloud downstream of keeper) and 3.4mg/s (spot mode), at I_a = 5A and I_k = 1A 215

Figure 7.37: Anode and keeper voltage dependence on I_a for argon discharge, I_k = 1A 217

Figure 7.38: Anode and keeper voltage dependence on I_a for krypton discharge, I_k = 1A 217

Figure 7.39: Anode and keeper voltage dependence on I_a for Kr/Xe mix discharge, I_k = 1A 218

Figure 7.40: Anode and keeper voltage dependence on I_a for xenon discharge, $I_k = 1A$ 218

Figure 7.41: Visual characteristics of the discharge operating modes 219

Figure 7.42: Correspondence between keeper noise and anode low frequency high amplitude noise when cloud is in keeper vicinity, xenon discharge $\dot{m} = 0.7mg/s$, $I_k = 1A$ 220

Figure 7.43: Illustration of a variety of double layer axial potential profiles corresponding to identical potential differences applied to the system boundaries. The structures are known as double layers due to the presence of at least two parallel charge sheets [61]. 226

Figure 7.44: **(a)** *Visual characteristics of a virtual anode in a discharge with uniform plasma properties and pressure profile.* **(b)** *Expansion of operating gas and plasma downstream of a HC.* **(c)** *Illustration of the effect of the downstream expansion of plasma and propellant on the visual characteristic of a "virtual" anode in a HC discharge* 227

Figure 7.45: Axial potential profile of a "potential hill" detected by Williams and Wilbur [172] downstream of a HC in plasma contactor, shown to correspond to the visual structure of the type (c) double layer in the plume mode virtual anode 230

Figure 7.46: Ion current to HC with luminous cloud inside the cathode-keeper space 234

Figure 7.47: Effect of increasing $\dot{m}$ at constant I_a on the visual characteristics of the discharge 237

Figure 7.48: Figure 7.48: Functional dependence of the electron density at the anode location due to the expansion of the HC plasma ($n_{e,A}$), and ($(n_e)_{A,p}$) the required density at the anode location for passive current collection on I_a. 239

Figure 7.49: **(a)** *Functional dependence of the electron density upstream of double layer ($n_{e,u}$) on I_D from the modified Siegfried-Wilbur model, along with linear increase of $(n_e)_{r,o}$ the electron density required to keep virtual anode at same position O (figure 7.50) with I_D.* **(b)** *Comparison of rate of change of $(n_e)_{r,o}$ and $n_{e,u}$ with I_D* 242

Figure 7.50: The three possible scenarios for dependence of the virtual anode size on discharge current: a) at low I_D, the rate of increase of upstream electron density with current demand is less than that required to maintain the virtual anode at position O and the virtual anode expands. b) both rates are equal and the virtual anode remains the same c) rate of electron production at cathode is greater than that required at O and virtual anode contracts 242

Figure 7.51: Reproduction of the discharge characteristics and discharge mode map of Patterson and Fearn [45], with lines of constant $\dot{m}$ inserted 244

Figure 7.52: Time resolved plots of plasma potential in front of a current collecting disc at low pressure during **(a)** *formation of double layer and* **(b)** *destruction of double layer [148]* 249

Figure 7.53: Illustration of double layer formed at boundaries of a discharge tube with variable cross-section [26] 254

Figure 7.54: **(a)** *Schematic of HC with "fireball" indicated* **(b)** *Measured axial plasma potential and electron temperature profiles with "fireball" present [69]* 254

Figure A.1 Schematic of T6 hollow cathode for probe access [196] 271

Figure A.2: Manufacturer's transmission plot for VIS-IR grade sapphire optical fibre 273

Figure A.3: Schematic of the sapphire fibre optic probe 274

Figure A.4: Photograph of sapphire optical fibre probe 275

Figure A.5: Manufactured jigging assembly for laser welding of optical probe metal sheath 277

Figure A.6: Proposed experimental arrangement for spatially resolved discharge initiation experiments 279

Figure A.7: Proposed experimental arrangement for spatially resolved spectroscopic measurements of the HC plasma in steady state 280

Figure A.8: Photograph of the completed modified T6 hollow cathode (Photo courtesy of QinetiQ) 283

Figure B.1: Reference cathode geometry [25] 285

Figure B.2: Centreline axial neutral density profile, xenon 1mg/s, insert 1473K 285

Figure B.3: Centreline axial pressure profile, xenon 1mg/s, insert 1473K 285

Figure B.4: Centreline axial velocity profile, xenon 1mg/s, insert 1473K 285

Figure B.5: Radial density drop at an axial location 1mm downstream of the anode facing side of the keeper 285

*Figure B.6: Pressure (**a**) and neutral density (**b**) as a function of mass flow rate at various locations (indicated in Figure B.1) on the cathode centreline* 286

LIST OF TABLES

Table 3.1: Optical depth of xenon, krypton & argon first ionisation and neutral excitation lines assuming Doppler line broadening 57

Table 3.2: Atomic properties of the propellant gas atoms and ions 61

Table 4.1: Manufacturer's specifications for the H6780 photosensor module 93

Table 6.1: Identified emission lines for xenon discharge (2400l/mm grating) 143

Table 6.2: Identified emission lines for krypton discharge (2400l/mm grating) 146

Table 6.3: Identified emission lines for argon discharge (2400l/mm grating) 149

Table 6.4: Relative abundance of elements 158

Table 7.1: Metastable energy levels and Ionisation potentials of the rare gases [105] 164

Table 7.2: The plasma parameters (n_e, T_e) as a function $\dot{m}$ correlated to the visual appearance of the discharge 191

Table 7.3: HC operating parameters predicted by a modified Siegfried-Wilbur model for a hollow cathode operating on xenon at $\dot{m}$ = 3.29mg/s and I_a = 5A 195

Table A.1: Technical specifications for the sapphire optical fibre 275

Table C.1: Calculated Stark ($\Delta\lambda_{1/2}^{S}$) and Doppler ($\Delta\lambda_{1/2}^{D}$) half-widths (in Å) for two prominent lines at typical values of T_e and n_e [65] 288

LIST OF ACRONYMS

AES	Atomic-Emission-Spectroscopy
AIAA	American Institute of Aeronautics and Astronautics
CCD	Charge-Coupled Device
C-R	Collisional-Radiative equilibrium model
DERA	Defence Evaluation and Research Agency
DS1	Deep Space 1
DSMC	Direct Simulation Monte Carlo
ED-XRF	Energy Dispersive X-ray Fluorescence spectrometry
EMI	Electromagnetic Interference
ESA	European Space Agency
FWHM	Emission line full width at half maximum
GEO	Geostationary Earth Orbit
GTO	Geostationary Transfer Orbit
HC	Hollow cathode
HWHM	Emission line half width at half maximum
IPP	Ion Propulsion Package
IPR	Ion Production Region
IR	Infra Red
LEO	Low Earth Orbit
LTE	Local Thermodynamic Equilibrium
NA	Numerical Aperture
NASA	National Aeronautics and Space Administration
NSSK	North South Station Keeping
NSTAR	NASA Solar Electric Propulsion Technology Application and Readiness
OGE	Optogalvanic Effect spectroscopy
PMT	Photomultiplier Tube
QE	Quantum Efficiency
RIT	Radio frequency Ionisation Thruster

SEM	Scanning Electron Microscope
SERT	Space Electric Rocket Test
SI	Specific Impulse
UV	Ultra Violet
VIS	Visible

LIST OF SYMBOLS

A	Surface Area
A_c	Area of the end faces of the IPR
A_{dl}	Surface area of virtual anode
A_e	Surface area of electron emitting region of the insert
A_{or}	Hollow cathode the orifice area
A_s.	Total surface area of the IPR
A_t.	Exposed surface area of cathode tip
$A(p,q)$	Atomic transition probability between levels p and q
c	Speed of light in vacuum
$\overline{c}_e$	Mean electron velocity
$\overline{c}_o$	Mean thermal velocity of the atoms
C_A	Cross-sectional area of tantalum tube
D	Distance
d	Hollow cathode orifice diameter
d	Electrode separation
d_k	Cathode-keeper separation
d_o	Hollow cathode orifice diameter
E	Electric field
E_{Ba}	Barium evaporation rate
E_s	Electric field at surface
$E(\infty)$	Ionisation energy
$E_{\infty Z}(p)$	Ionisation energy from the atomic p level.
$E(p)$ or $E_Z(p)$	Energy at atomic level p
e	Electronic charge
$f(p,q)$	Oscillator strength
g_o	Sea level gravitational acceleration
$g_Z(p)$	The statistical weight of the p level of species of charge Z

h	Planck's constant
I	Current, Intensity
I_D	Discharge current
I_a	Anode (discharge) current
I_c	Critical discharge current for plume to spot transition
I_e	Electron emission current
I_k	Keeper current
I_i	Ion current to surface
I_{eq}	Ion current through cathode orifice
I_{pr}	Rate of electron liberation from surface
I_{pc}	Volume ion production rate at the cathode
I_s	Drift current
I_{sp}	Specific Impulse
$I(p,q)$	emission line intensity arising from a transition between levels p and q
$J(v,x)$	Emission coefficient of frequency v in the x direction
j_o	Primary electron current density leaving cathode surface
j_a	Electron current density reaching anode surface
j_{ft}	Field enhanced-thermionic emission current density
j_i	Bohm current density
j_{th}	Thermionic emission current density
k	Boltzmann's constant
k_c	Tantalum thermal conductivity
L_e	Length of electron emitting region in a hollow cathode insert
$L(\omega)$	Emission line shape factor
$ln\,\Lambda$	The Coulomb logarithm
M_o	Mass of spacecraft at start of manoeuvre
M_f	Spacecraft mass at end of manoeuvre
m *or* m_i	Atomic (or ionic) mass
m_e	Electronic mass
m_i	Ionic mass
m_o	Atomic mass
$\dot{m}$	Propellant flow rate (in Aequiv or mg/s units)
N	Gas number density

n_e	Electron density
$(n_e)_{A,p}$	The required electron density at the anode location for passive current collection
$n_{e,A}$	The electron density at the anode location due to expansion of the HC plasma
n_{ep}	Primary electron density
$(n_e)_{r,o}$	Required upstream electron density for virtual anode to remain at position O
$n_{e,u}$	Electron density upstream of double layer
n_i	Ion density
n_o	Neutral number density
$n_Z(p)$	Number densities of the p level of species of charge Z
P	Pressure
P_D	Discharge power
P_r	Probability of a successful avalanche at a given excess voltage
$P(x)$	Power deposited into volume element x
p	Atomic energy level ($p = g$ for an atom in the ground state)
p_s	Thermal level
p_{cs}	Net power deposited by cathode emitted electrons per unit area
p_{loss}	Power lost by electron collisions per unit area
p_j	Joule heating term
$\dot{Q}_{th}$	Power loss from HC due to conductive and radiative processes
R	Gas constant
R, r_c	Hollow cathode radius
S_Z	An atom or ion of charge $+Ze$
$S_{Z,g\to\infty}$	Collisional ionisation coefficient for a species of charge Z from the ground level to the continuum
$S(v,x)$	Source function
r_p	Probe radius
r_o	Classical electron radius
T	Temperature, Cathode tip temperature
T_e	Maxewillian electron temperature
T_i	Ion temperature

T_o	Ambient temperature
T_s	Insert surface Temperature
t	Time
t_{cont}	Particle containment time
t_{ee}	Electron-electron relaxation time
t_f	Formative time lag
t_{rad}	Energy decay time for continuum radiation
t_s	Statistical time lag
t_{tot}	Total time lag for spark breakdown
$\mathcal{T}$	Thrust
u	Particle velocity
V	Voltage, Volume
V_a	Anode (discharge) potential
V_{ad}	Anode potential fall
V_{bk}	Breakdown voltage
V_c	Potential drop across cathode sheath
V_{dl}	Potential drop across double layer
V_i	Ionisation potential
V_k	Keeper voltage
V_m	Energy of metastable atom
V_p	HC plasma potential, potential drop across the cathode sheath
V_s	Static or steady-state sparking potential
Δv_r	Spacecraft velocity increment
v_e	Effective exhaust velocity
v_p	Primary electron velocity
$X_{g\rightarrow p}$	Collisional excitation coefficient from the ground level to level p
Z	Ion charge
α	First Townsend coefficient
$\alpha_{1/2}$	Theoretical half-width of reduced Stark profile
$\alpha^{RR}_{z+1,g}$	Radiative recombination coefficient

$\alpha^3_{Z+1,g}$	Three-body recombination coefficient
β	Ionisation fraction
γ	Townsend secondary breakdown coefficient
γ_d	Oscillator damping constant
ε	Emissivity of material
ε_o	Permittivity of free space
ζ_Z	Number of electrons in the outermost occupied shell (n^*) of species Z
η	Rate of destruction of species of charge Z in quantum level p
η	Breakdown efficiency function
θ	Ratio of the partition functions of the ion and neutral
κ	Rate of production of species in a quantum level p
λ	Wavelength
λ_e	Electron mean free-path
λ_{ee}	Electron-electron mean-free path
λ_{ei}	Electron-ion mean-free path
λ_{ii}	Ion -ion mean-free path
λ_o	Central wavelength of an emission line
λ_{pr}	Primary electron energy exchange mean free path
$\Delta\lambda_D$	The Doppler width of an emission line
$\Delta\lambda_N$	Emission line full width at half maximum
$\Delta\lambda^{\ S}_{1/2}$	Emission line half-width due to Stark broadening
$\Delta\lambda^{\ D}_{1/2}$	Emission line half-width due to Doppler broadening
μ	Atomic weight
ν_{pq}	Emitted or absorbed frequency in a p-q transition
ξ_{Z+1}	Number of vacancies in the last shell of species Z
σ	Plasma conductivity
σ_d	Cross-section for de-excitation metastables by collisions with neutral atoms
σ_i	Ionisation cross-section
σ_{iP}	Cross-section for ionisation by metastable impact
σ_m	Cross-section for excitation into metastable from ground state

σ_{SB}	Stefan-Boltzmann constant
τ	Optical depth
ϕ_s	Work function
ϕ_e	Effective work function
$\chi(v,x)$	Absorption coefficient of frequency v in the x direction
φ_e	Electron flux into virtual anode
φ_i	Ion flux out of virtual anode
ω_{pq}	Emission line frequency
ω_o	Frequency of the emission line centre
ω_N	Emission line half width at half maximum
Ω	Activation energy for barium evaporation

Chapter 1

INTRODUCTION

1.1 The benefits of ion propulsion

Satellites, after leaving their launch vehicle, require some means of on-board propulsion. This is necessary for a variety of purposes, which can be divided into primary and in-orbit secondary propulsive roles. For satellites in geostationary orbit (GEO), there is a requirement for secondary propulsion during the length of the satellite lifetime for orbit maintenance and attitude control, to counteract the gravitational effects of the sun, the moon and the earth's oblateness which tend to perturb the spacecraft orbit. Low earth orbit (LEO) satellites, existing in a rarefied atmosphere, require on-board secondary propulsion to conduct correction manoeuvres for the effects of atmospheric drag and for attitude control. The primary propulsive role involves tasks such as propelling interplanetary probes to their final destination and conducting orbit transfer manoeuvres from a temporary orbit to the final operational orbit (for example a satellite delivered to a geostationary transfer orbit (GTO) requires on-board propulsion to transfer it to GEO).

These operational requirements were traditionally fulfilled by a chemical propulsion system, which entails the expansion of a gas through a divergent nozzle. The expanding gas can either be 'cold' (simply a pressurised gas expanding from a storage vessel) or the gas can be heated by a reaction of the fuel/oxidiser type. Energy is added to the gas by the combustion reaction and thus the achievable exhaust velocities are fundamentally limited by the energy released in the chemical reaction. The maximum exhaust velocity that can be obtained with such a system is around 4.7 km/s [41].

The significance of the exhaust velocity to the efficiency of a space propulsion system

is best illustrated by the simple rocket equation:

$$\Delta v_r = v_e \, ln\left(\frac{M_o}{M_f}\right) \tag{1.1}$$

Here Δv_r is the required velocity change to conduct a manoeuvre, v_e is the propellant effective exhaust velocity, M_o and M_f are the masses of the spacecraft at the start and end of the manoeuvre. Inspection of equation (1.1) reveals the importance of achieving as high an exhaust velocity as possible. A high exhaust velocity reduces the fuel required for a given manoeuvre; consequently, this reduction in fuel allows a higher final mass (or payload) fraction to be achieved. Because a rocket's mass ratio decreases exponentially with increasing exhaust velocity, even a small improvement in exhaust velocity can lead to an appreciable increase in useful payload size for a given vehicle.

Another often used figure of merit for a propulsion system is the engine's Specific Impulse (SI) (I_{sp}). This is defined as the ratio of the thrust ($\mathcal{T} = \dot{m} v_e$), to the total mass rate of flow of propellant, $\dot{m}$, in terms of sea level weight:

$$I_{sp} = \frac{\mathcal{T}}{\dot{m} g_o} = \frac{v_e}{g_o} \tag{1.2}$$

where g_o is the sea level gravitational acceleration.

In order to overcome the chemical propulsion limits on the maximum achievable exhaust velocities some propulsion systems, such as ion thrusters, decouple the expellant and the energy input source. Ion thrusters make up a branch of what is collectively known as 'Electric Propulsion Systems". An electric propulsion system is defined as a system that causes: "*The acceleration of gases for propulsion by electrical heating and/or by electric and magnetic body forces*" [70]. In the ion thruster class, electrostatic body forces are used to accelerate positively charged particles. The attainable exhaust velocities are only limited by the capabilities of the available power supplies and, ultimately, by the speed of light [41].

To quantify the potential benefits of employing an ion thruster system: Chemical propulsion systems have a maximum expected SI of around 480s. These values imply that, to achieve a desired final velocity, a significant amount of propellant is required, which can, in some cases, exceed the dry mass of the spacecraft. By contrast, ion thrusters using xenon propellant can easily achieve exhaust velocities of 30-60km/s, corresponding to a specific impulse of 3100-6100s [47]. This is an order of magnitude higher than chemical systems, with a reduction by the same factor expected (for small Δv_r) in the propellant mass.

The reduction in propellant mass requirement can be used to increase the useful payload. Alternatively, it can be used to decrease the total vehicle mass, and hence launch costs, or the operator can opt for extending the mission lifetime. The high specific impulse of ion engines makes them an enabling technology for some high energy missions which have been, until their advent, impossible. Having said that, the use of an ion propulsion system does incur some penalties. These include a need for substantial electric power, with the associated penalties of increased thruster complexity and dry mass when compared to an equivalent chemical system. This mass penalty is, however, more than offset by the overall mass saving in numerous cases.

1.2 Ion thruster development

The first description or "definition of the concept" of ion propulsion is usually attributed to R.H. Goddard [156], who informally indicated as far back as 1906 (when very little was yet known about electrons and ions) the possibility of using charged particles as exhaust for rocket engines. Twenty three years later, Professor Herman Oberth dedicated a chapter to electric propulsion in his classic treatise on rocketry and space propulsion [120]. In the intervening years prior to the beginning of the war, ion propulsion in general does not seem to have received much attention. In the post-war period, the advances in rocketry and the development of promising practical space electric power sources such as nuclear reactors caused a renewed interest in the field, with notable contributions by Shepherd & Cleaver [143], Forbes [52], Lawden [93],

Spitzer [151] and Romick [137]. Stuhlinger [152, 153, 154, 155, 156] published a series of papers in which the feasibility of the ion propulsion system was studied and some problem areas were identified and addressed.

By the late 1950's, several experimental studies were underway on various ion propulsion concepts. Harold R. Kaufman in 1959 began working at NASA Lewis on improving the efficiency of the ion generation and acceleration processes. His work culminated a year later in the operation of the world's first broad-beam electron-bombardment ion thruster [75, 76]. In recognition of his pioneering work, all ion thrusters sharing Kaufman's design still bear his name.

Benefiting from the strong political will that existed during the space race era, the subsequent development of ion propulsion systems proceeded at a phenomenal pace. By 1970 the maturity of the propulsion system was demonstrated by two flight tests under NASA's SERT (Space Electric Rocket Test) program. SERT I, launched in July 1964, was the first successful space test of an electrical propulsion system, in which a Kaufman-type thruster was operated for 31 minutes over a sub-orbital ballistic flight [70]. The SERT II test, which followed in 1970, was actually an on Earth-orbit, long duration test-bed of ion thruster technology. It investigated such issues as the radio frequency noise generated by the thruster and it demonstrated successful charge neutralisation of the ion beam. It is interesting to note that the SERT II test achieved 11.5 years of successful operation. Subsequent development activities continued through parallel programs in both the US and UK on the application of Kaufmann thrusters to satellite North South Station Keeping (NSSK). Work has also been directed towards alternative ion production schemes, which has resulted in the development of the multi-pole electron bombardment devices in the USA [98], and devices employing radio-frequency ionisation sources in Germany [84].

In early thrusters, mercury was usually used as propellant, because of its low ionisation potential, large atomic mass and its relative ease of storage. However, the lack of available power on spacecraft and concerns, from the usually conservative spacecraft operators, with mercury contamination of spacecraft surfaces and the near space environment, led to a temporary decrease in interest in ion propulsion, in spite of its high state of development and the significant benefits from its use. Fortunately,

in the mid 1980's, when more power became available on spacecraft, a shift occurred towards using xenon as a propellant. Xenon, being an inert gas, eliminated the risk of contamination. It also greatly simplified thruster design by removing the need for flow vaporisers and isolator heaters which were required to keep mercury in vapour form, but it also greatly complicated the required feed systems.

Presently, ion propulsion is slowly gaining a place as a prominent, reliable and, most importantly, flight qualified technology. This is mostly due to the efforts of organisations involved in its development, through programs such as NASA's NSTAR program (NASA Solar Electric Propulsion Technology Application and Readiness) and Hughes (now Boeing) offering the technology as standard on the their communication satellites. The NSTAR program resulted in the XIPS-30 electron bombardment ion thruster, which was the primary propulsion for NASA's Deep Space 1 (DS1) mission. Launched in October 1998, DS1 was intended as a technology demonstrator for 12 advanced technologies, which included its propulsion system. It successfully completed its primary mission to asteroid 1992KD in September 1999 and the mission was extended to fly by Comet Borrelly, which was achieved in September 2001. The operation of the ion thruster throughout the mission's long duration was flawless. DS1 was retired in December 18, 2001.

Closer to earth, space operation of ion propulsion systems has been demonstrated in the NSSK role by the Hughes telecom satellites and more recently with ESA's ARTEMIS telecommunication satellite. The efficiency, versatility and (perhaps) elegance of the ion propulsion concept is nowhere better illustrated than in the ARTEMIS mission. Launched in July 2001, ARTEMIS has an Ion Propulsion Package (IPP) for NSSK, consisting of two RIT-10 radio-frequency ion thrusters and a pair of UK-10 Kaufman-type electron bombardment ion thrusters [183]. A malfunction in the launcher's upper stage resulted in an orbit apogee of 17,500km, far short of the targeted GTO with an apogee of 35,850km. A daring recovery mission was then started. The reserves of chemical fuel were expended in raising the satellite to a circular orbit of 31,000km. New steering strategies, involving significant reprogramming of the original control software, were then used to conduct an orbit-raising manoeuvre using the satellite's on-board ion propulsion engines. The long salvage operation, which lasted 18 months, was successfully concluded with

ARTEMIS achieving its designated GEO orbit in January 2003. The ion propulsion system, operating outside its predetermined role, was able to change this mission from a total loss to "arrival on station", with almost seven years of normal use predicted [183].

1.3 Objectives of the current study

The main focus of this thesis is the hollow cathode (HC) discharge, which is the electron production region in the Kaufman thruster and its sole means of neutralising the space charge of the ion beam. The hollow cathode is not unique to the Kaufman thruster and fulfils the same roles in both the ring-cusp design [98] and the Hall-effect thrusters [203]. In electrostatic thrusters using the radio-frequency (RF) ionisation process, it is used for neutralisation only. HC's are also employed as a plasma-bridge neutraliser to control spacecraft charge [172]. In this light, the findings of this work will have wide ranging applicability.

Hollow cathode performance has a decisive impact on overall thruster stability, efficiency and lifetime. Some of the major issues of concern in modern HC's are here listed:

1. The production of noise and oscillatory disturbances in HC discharges, which can have a negative impact on overall thruster stability. This affects both the efficiency and the levels of electromagnetic interference (EMI) produced by the thruster.

2. The severe sputter erosion, attributed to high energy ions and observed on structures downstream of high current HC's, which can limit thruster lifetime.

3. Cathode lifetime and performance degradation, which is primarily caused by depletion of the low work function material in the dispenser, and ion bombardment sputter erosion of cathode surfaces.

There exists a lack of understanding of the basic processes occurring in the HC cavity. And hence, all of the above concerns are avoided or mitigated rather than understood.

Operators usually embark on comprehensive characterisation and life-testing to identify conditions leading to excessive decrease in lifetime (high cathode temperature) or conditions leading to the generation of noise and oscillation. These conditions are then avoided and an operational envelope is defined. This is a relatively costly process. Introducing a new design, or even using a new propellant with an old proven design, requires a repetition of the extensive characterisation exercise.

There are two main, and complementary, objectives to this investigation. The first is operational and economic. Xenon is currently the propellant of choice for gridded ion thrusters, but, as has been suggested by Fearn [42], in order to enable high Δv_r missions, the use of propellants with a lower atomic mass, such as argon, might be necessary. The feasibility of operating the HC using these alternative propellants has to be demonstrated. Moreover, there is an interest in decreasing the propellant cost in missions, and during the development and ground testing phases (especially life-tests). A Kr/Xe mixture in the naturally-occurring ratio (1:12, Xe:Kr volumetric ratio), for example, could offer a 15 fold cost saving when compared to pure xenon, and 2-3 fold cost saving when compared to pure krypton. It was thus proposed to carry out a characterisation of a T6 HC discharge using the four gas propellants argon, krypton, xenon and a krypton/xenon mix in the naturally occurring ratio. The characterisation was to be carried out over as wide a range of cathode operating conditions as possible, with a view to identify operating conditions that cause the onset of instability and noise, and to assess any performance penalties of operating with the alternative gases.

The second, and more fundamental, aim is to further the current (poor) state of understanding of HC physics. This entails conducting empirical investigations of the two stages of cathode operation: discharge initiation (starting) and steady state. The physical processes occurring in the HC interior plasma are not very well understood. This is mainly due to lack of measurements of the plasma parameters. Furthermore, the starting phase of the HC discharge has not been the subject of extensive investigation.

To study the steady-state behaviour, it was proposed to carry out a spectroscopic investigation of the HC internal plasma simultaneously with the characterisation of the various propellants. That would enable the measurement of HC plasma properties

and their dependence on cathode operating parameters, which would give some insight into the physical processes taking place and facilitate the construction of a model of the HC discharge. In the same vein, the processes leading to the establishment of the discharge and the setting up of a plasma in the HC suffer from the same shortage of experimental investigation and its attendant effect of a lack of understanding. It was also proposed that the same empirical process of comprehensive characterisation and monitoring of the plasma formation using the selfsame gases would shed some light into the transient, initiation phase of the HC discharge.

It has to be mentioned here that, at the beginning of this investigation, the objectives of this work were to conduct a spatially-resolved spectroscopic study of the cathode internal plasma in steady state and to conduct a temporally and spatially-resolved spectroscopic study of the breakdown phase of the HC discharge. To this end, a special hollow cathode was designed which facilitated probe access, and some novel, high temperature optical fibre sensors were designed and constructed. This activity, along with the design and procurement of the experimental apparatus, occupied the first two and a half years of this PhD, but regretfully work on the instrumented hollow cathode did not pass the design stage for a long period of time. The manufacturer's delays made continuation of the project very difficult, and the emphasis of the research had to be changed. The work on the instrumented hollow cathode is the subject of Appendix A, to which the reader is referred for more details.

1.4 Thesis structure

The following chapter, chapter 2, aims to present a review of the available literature and the current state of knowledge of HC behaviour. It starts by an introduction to the basics of Kaufman-type ion thruster operation and a brief description of each of the plasma regions contained in the thruster (the HC internal plasma, the coupling plasma, the main discharge plasma and the beam plasma). It then moves on to describe the HC discharge, in which this work is more concerned, in more detail. The HC construction and the various proposed electron emission mechanisms from its surface are discussed. The chapter then details the present state of knowledge and the previous

work carried out in the HC internal plasma. It ends with a similar description of the work carried out to date on HC starting. Areas of uncertainty are highlighted and discussed.

Chapter 3 gives a description of the various models of the plasma state and demonstrates that the HC discharge, with all the inert gases used here, is best described by the Collisional-Radiative (C-R) model. Following the establishment of the plasma model, the various techniques that can be used to interpret the spectroscopic data are reviewed. Then a brief presentation of the general gaseous breakdown theory is made, which is of relevance to the breakdown part of this investigation. The chapter ends with a review of some of the models developed by investigators for the HC discharge.

Chapter 4 contains a discussion of the experimental equipment used in this work, including the vacuum chamber and associated systems, the T6 enclosed-keeper HC in diode test configuration and the electrical set up. Finally, a description of the diagnostic equipment employed is also given.

Chapter 5 is concerned with the experimental set-ups and procedures used in the various test programs. It describes the range of experiments performed and illustrates the procedures and precautions taken to ensure repeatable and accurate results.

Chapter 6 gives a comprehensive report of the experimental results of this study. The chapter begins with a presentation of the results from the discharge initiation investigations, which is then followed by those for the steady-state phase. The trends in the results are highlighted and comparison is made between the various propellants. The analysis and discussion of the results is left to chapter 7, in which simple models and theories are developed to describe HC behaviour.

Chapter 8 contains a synopsis of the main conclusions of this study, with recommendations for future work.

Chapter 2

BACKGROUND AND LITERATURE REVIEW

Introduction

This chapter introduces some of the basic background concepts of relevance to the present study. The chapter commences with an overview of the principles of operation of a Kaufman ion thruster, and a brief description of the several distinct plasma regions within it. These are, namely, the hollow cathode internal plasma, the coupling plasma, the main discharge plasma and the beam plasma. This is followed by a review of the current state of knowledge of the hollow cathode plasma conditions, the main subject of this thesis. The ignition and steady-state operation of the hollow cathode, in spite of being critical to the performance of the thruster system, are poorly understood. The chapter presents the experimental observations and theoretical work to date on these two aspects of hollow cathode operation.

2.1 Principles of Kaufman-type ion thruster operation

The Kaufman-type thruster's method for ion production is by electron bombardment of the neutral propellant. As previously mentioned, mercury was used in the early thrusters. In the mid 1980s a shift occurred towards using xenon, which is currently the propellant of choice. The concept behind any ion thruster system is essentially straightforward. It functions by achieving four tasks: 1) Production of electrons, 2) Acceleration of the electrons to ionise a neutral gas, 3) Acceleration of the resulting ions to high velocities to produce thrust and, finally, 4) Neutralisation of the ion beam space charge. The methods the Kaufman type engine employs to fulfil these tasks lead to the formation of four distinct plasma regions in the thruster. These regions,

illustrated in figure 2.1, are: the hollow cathode plasma, the coupling plasma, the main discharge plasma and the beam plasma.

The cathodes used in the early thrusters were simply lengths of refractory metal wire, which emitted electrons thermionically when a current was passed through them. These were, however, particularly susceptible to sputter erosion, which severely limited their expected lifetime. This durability issue led to the introduction of hollow cathodes. The hollow cathode is basically a refractory metal tube, terminated at one end by an orificed plate. A dispenser containing a low work function material is included inside the cathode to enhance its electron emission.

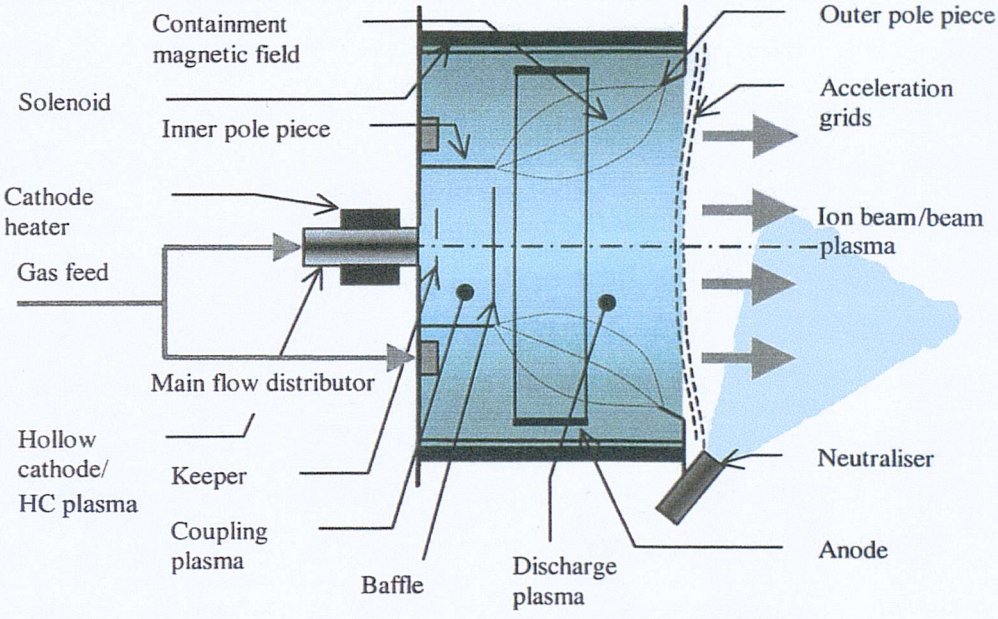

Figure 2.1: A modern Kaufman-type ion thruster [112]

Initiation of the main discharge proceeds as follows: The discharge to the HC is first initiated by flowing propellant through it, heating it to thermionic emission temperatures and then applying a positive potential of a few hundred volts to an electrode situated a few millimetres from the tip, known as the '*keeper*'. Following breakdown, the discharge is then transferred to the main discharge chamber by applying a few tens of volts to a cylindrical anode. The keeper's function does not end with discharge initiation and it continues to draw current from the discharge during steady-state operation. This is done to guard against the cathode electron emission being extinguished by an interruption in the main current to the anode or ion beam.

The presence of the keeper thus ensures the continuity of the HC discharge in the event of an interruption and also simplifies the process of re-establishing the main discharge, hence the name "keeper" electrode.

The ionised gas emerges from the hollow cathode into the coupling plasma. This region of space is separated from the main discharge plasma by the inner pole piece and a non-magnetic baffle disc. The design of the baffle disc/pole piece assembly introduces a potential difference between the coupling plasma and the main discharge. The electrons accelerated through this potential difference form the primary electron population in the discharge chamber, with typical energies in the 20-30eV range.

Partially-ionised propellant and primary electrons stream from the coupling plasma into the discharge chamber. There, they are joined by more neutral propellant introduced directly into the discharge chamber through a hollow ring on the thruster backplate. The ionisation efficiency in the discharge chamber is greatly enhanced by an applied, azimuthally symmetric, divergent magnetic field. This field is usually generated by solenoids or permanent magnets equispaced around the discharge chamber circumference. Inside the discharge chamber, the field links the cylindrical inner and outer pole pieces. As the primary electrons emerge from the baffle annulus, they are confined by this magnetic field, which forces them to spiral around the field lines and prevents them from streaming directly to the anode. This effectively increases the probability of them achieving ionising collisions. These electron-neutral collisions cause a primary electron to lose its energy and lead to the formation of an ion and a secondary electron. The primary and secondary electrons continue to spiral around the field lines and may participate in further collisions before ultimately diffusing across the magnetic field lines to be collected by the anode.

The downstream limit of the main discharge plasma is defined by the thruster's extraction electrodes. The ions produced in the main discharge drift in all directions, and are unaffected by the magnetic field because of their large Larmour radius. Those ions that drift towards the exhaust plane of the thruster are accelerated by the extraction electrodes into a linear, high-velocity (30 to 50km/s) ion beam. The ion extraction system is usually comprised of two to three closely spaced, perforated electrodes. These typically contain several thousands apertures to facilitate the ion

flux through them. The first grid, known as the screen grid, is maintained at the cathode potential and acts as a virtual ion source for the extraction system. The second grid or the accelerator grid is maintained at a high negative potential of 1 to 3 kilovolts relative to the screen grid and is thus responsible for the ion accelerating electric field. A third decelerator grid is included to mitigate sputtering damage of the accelerator grid surface produced by charge-exchange ions, which is one of the life-limiting processes in the thruster.

To prevent the build up of space charge, it is necessary to neutralise the positive space charge of the emerging ion beam. This is accomplished by electrons emitted from a hollow cathode, identical to the one used in the discharge chamber, located just downstream of the exit plane. A plasma is formed in this neutraliser by a discharge between the cathode and a keeper electrode, electrons are extracted from this plasma according to requirement. The neutraliser consumes small amounts of propellant, operating at xenon flow rates typically a few percent of those in the thruster.

2.2 The hollow cathode discharge

In electron-bombardment ion engines, hollow cathodes serve the dual purpose of providing primary electrons to ionise the propellant gas, and for neutralisation of the ion beam space charge. The HC is, paradoxically, one of the most important subsystems of the ion thruster and, at the same time, amongst the least understood. Considerable effort has been directed at optimising its performance and extending its lifetime. However, the basic physics of operation of the HC is not understood, and, for expediency, the development work has been based on empirical experience. This lack of understanding stems mainly from the considerable difficulty of conducting plasma measurements in the severely limited space (~ 1-2mm dia.) of the hollow cathode cavity.

This section attempts to compile the current state of knowledge of HC phenomena in both the steady-state and the transient (discharge initiation) phases of operation. It first describes HC construction and details the various proposed emission and

operating mechanisms. It then goes on to review the steady-state plasma measurements carried out in the HC cavity, followed by a review of experimental studies on the discharge initiation dependence on cathode parameters. Based on some of the measurements reported here, a number of investigators have proposed models for the physical processes occurring in the HC discharge. This is the subject of a later discussion in chapter 3.

2.2.1 Hollow cathode construction

A schematic of a typical hollow cathode is shown in figure 2.2.

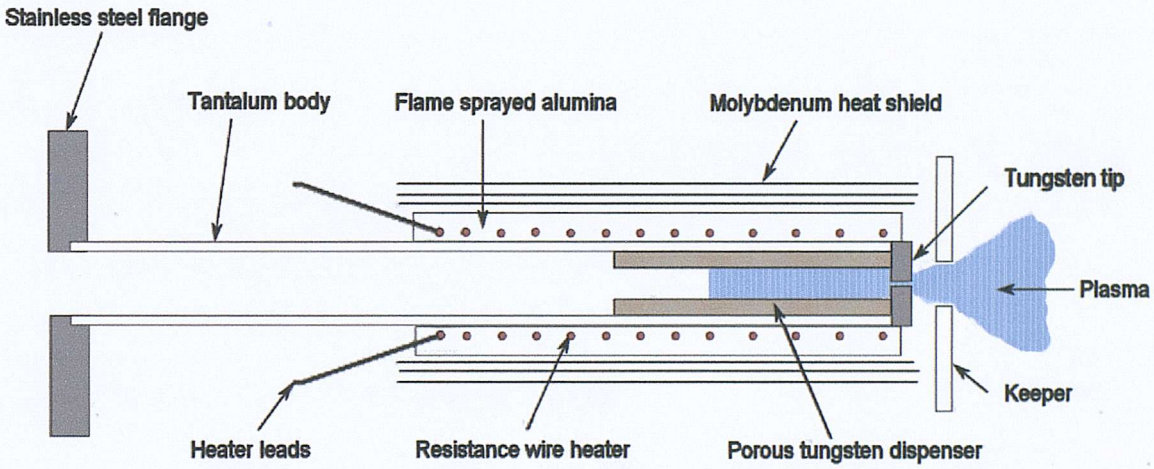

Figure 2.2: Schematic of a typical orificed ion thruster hollow cathode.

The hollow cathode main body is essentially a tantalum tube (of less than 1cm diameter) with a tungsten tip, containing a small orifice (~1mm diameter), electron beam welded to the downstream end. In newer designs, specifically the T6 hollow cathode [40], the cathode is machined from solid, such that the tip and the tube are made of the same material. This is done so as to minimise the risk of tip weld failure. The cathode is surrounded by resistance heater wire, which is wound around the cathode body. The heater wire was usually embedded in flame sprayed alumina. Recently, however, machineable ceramics have been preferred for ease and consistency of manufacture. The heater is used to raise the temperature of the cathode to thermionic emission temperatures (about 1000°C for a standard cathode) prior to

starting the discharge. After discharge initiation has ensued, it can be switched off, as ion bombardment of the insert surface can maintain the energy input required for electron emission. A multi-turn molybdenum heat shield surrounds the assembly in order to minimise radiative losses and therefore reduce the power requirement for heating. Neutral gas is fed from the other end of the cathode via a flange.

Lowering the work function of the hollow cathode surface would enhance the thermionic emission current dramatically. Thus, hollow cathodes usually contain a source of low work function barium (or in some cases LaB_6). Initial hollow cathode designs had the interior surfaces simply coated with a triple oxide mixture containing the substance. These designs suffered from rapid depletion of the internal coating, probably due to evaporation and/or ion sputtering. They were later modified to utilise rolled foil inserts coated with the same emissive mix, which provided a greater surface coverage of barium, but coating depletion persisted to be a problem. Porous tungsten dispensers were later developed. These are essentially hollow porous tungsten cylinders impregnated with a 4:1:1 mixture of BaO, CaO and Al_2O_3 (refer to figure 2.2), which provide long operational lifetimes (order of 10,000s of hours) and robustness (which is a requirement due to the severe launch environment).

2.2.2 Hollow cathode emission theory

The hollow cathode is simply an efficient source of electrons for the discharge. The fundamental question of what mechanism (or mechanisms) is responsible for electron emission from the insert surface has not yet been conclusively answered. Several mechanisms have been put forward in an attempt to explain the high emission currents observed.

Heating a metallic object gives energy to electrons in the conduction band, enabling them to break free and escape the surface. The process, known as thermionic emission, is dependent on the work function and temperature of the emitting surface. The electron current density from a thermionically emitting surface is described by the Richardson-Dushman equation [22]:

$$j_{th} = \frac{4\pi m_e e k^2 T_s^2}{h^3} exp\left(\frac{-e\phi_s}{kT_s}\right) \quad (2.1)$$

where T_s is the surface temperature, m_e is the mass of an electron, k is the Boltzman constant, h is the Planck constant, e is the electronic charge and ϕ_s is the work function of the material.

Inspection of equation (2.1) reveals the importance of the low work function material in reducing the required power input to maintain a given cathode emission current density. For hollow cathodes employing a heater and an impregnated insert, it seems that thermionic emission is necessary to facilitate discharge initiation at low values of breakdown voltage (<1KV) and moderate values of tip temperature, but the site of this emission has not been established. Work done using internal electrodes at DERA [48] has demonstrated that thermionic emission is by no means a fundamental requirement for starting.

Once the discharge has been initiated using the keeper electrode and the current has been drawn to the anode, the high current densities involved preclude thermionic emission as the only mechanism of current production. The presence of a very dense plasma inside the cathode, as confirmed by Langmuir probe and spectroscopic measurements [101, 115, 146], suggests that high electric fields might be produced by space charge sheath effects. Field enhancement of the thermionic emission occurs due to the reduction in the surface potential barrier brought about by a positive space charge sheath. This is known as the Schottky [22] effect, which effectively lowers the work function of the emitting surface by an amount proportional to the square root of the electric field:

$$\phi_e = \phi_s - \left(\frac{eE_s}{4\pi\varepsilon_o}\right)^{\frac{1}{2}} \quad (2.2)$$

Where ϕ_e is the effective work function due to field enhancement, ε_o is the permitivity of free space and E_s is the electric field adjacent to the surface.

The Schottky equation gives the current density due to field enhancement (j_{ft}) in

terms of the thermionic current density without field enhancement (j_{th}) and the electric field at the surface (E_s) [46] :

$$\log j_{ft} = \log j_{th} + \frac{e^{\frac{3}{2}}}{2kT}\left(\frac{E_s}{\pi \varepsilon_o}\right)^{\frac{1}{2}} \qquad (2.3)$$

It was suggested in [130, 46] that, in steady state operation of hollow cathodes, electron emission takes place at constant current density, i.e., the emitting area increases as more current is demanded from the cathode. Furthermore, emission is thought to occur at the outer edge of the orifice and then, as more current is demanded, the emitting area increases to include the entire orifice wall. If an even further increase is required (and the area required exceeds that of the orifice walls), the current must be drawn from the inner face of the tip and the inner wall of the cathode dispenser. It has been hypothesised that this process is linked to cathode transition from plume to spot mode, refer to sections 2.2.3 and 7.5.3. Experiments carried out in [130] on several orifice diameters seem to support this model and indicate that the current density is in the range of 2×10^5 to 5×10^5 A/m^2. This has been further confirmed by ion bombardment markings on cathodes run for long periods at constant discharge current and by experiments done using stepped and curved orifice cathodes [46]. Several mechanisms have been put forward capable of enhancing the electric field at the surface and therefore the field emission mechanism. Fearn and Philip [46] suggested that the value of E_s might be considerably increased locally due to charge distribution effects in the positive space charge sheath. Sajben [184] described a further mechanism, involving the adsorption of alkali metal atoms (e.g. barium) from a seeded plasma onto a metal surface. These atoms leave the metal surface as atoms or ions, which might considerably increase the ion density close to the cathode wall, subsequently leading to a large enhancement of E_s and increasing the Schottky effect.

Alternative mechanisms to the Schottky effect have also been proposed involving secondary electron emission from the insert surface due to ion or metastable impact or the photoelectric effect. The photo-emission process was first proposed by Krishnan [86], as a result of studies into large diameter hollow cathodes. Calculations by Malik [100] on the expected photo-electric yield from a typical xenon discharge adjoining a

tungsten oxide surface, however, seem to indicate an almost negligible contribution to the total current, with the estimated electron current densities falling far short of those required for the discharge. Malik [100] further suggested an alternative emission mechanism whereby VUV photons interact with Al_2O_3 from the insert surface to create intermittent electroformed metallic filaments. However, as reference [33] states, the lack of free surface Al_2O_3 suggest that this mechanism is unlikely in HC's.

The release of electrons from the surface by the impact of metastable atoms was first discussed by von Engel and Robson [163] and invoked by Fearn and Philip [46, 130] to explain the HC high current emission. High yields are expected when the excitation energy is close to the work function of the insert surface. Philip calculated that a random flux of mercury metastables impacting on tantalum is sufficient to give an emission current as high as $9\times10^5 A/m^2$, which is capable of maintaining the required current density. Nevertheless, contrary to expectation, experiments by the same author on non-bariated cathodes have resulted in considerably higher voltages and cathode temperatures for a given discharge current. Since this mechanism is not dependent on the presence of a low work function material, its removal was not expected to hamper cathode operation. This indicates that other significant mechanisms are at work and the probable overestimation of metastable flux to the surface and/or yields per impacting excited atom. It is possible that this mechanism is also applicable to inert gas operation but further investigation is required to confirm this and to estimate the electron yields to be expected.

Singly ionised Xe ions of low energy, falling through a sheath potential of the order of 10V, are expected to yield roughly 0.02 electrons per ion impacting a clean tungsten surface (refer to page 782 of reference [96]). Under typical cathode conditions, the ion current to the surface accounts for ~30% of the total discharge current [145], which implies that secondary electron emission is 2 percent of that, i.e. less than 1% of the total current will be due to secondary electron emission by ion impact. Siegfried [145], also estimates that the combined contribution of secondary emission due to mercury ions and excited atoms is less than 5% of total current. Nevertheless, emission coefficients from complex, low work function surfaces, such as the insert, can be higher than the above analysis. Measurements on surfaces of similar

composition are, regretfully, unavailable.

There is, nowadays, what could be termed a general (but by no means universal) consensus that field-enhanced thermionic emission is the dominant emission process in this type of HC under normal operating conditions [33, 140, 145, 146, 112, 115]. This, however, is far removed from implying that field-enhanced thermionic emission is the sole emission process. The secondary emission processes might for example become more prominent at very low discharge current or flow rate conditions, where the plasma density and hence the field enhancement is expected to be small. As suggested in [146], the intense radiation and high ionisation observed at the orifice would support the idea that within the orifice itself photoemission from the orifice surface can be important. Furthermore, volume ionisation can be a significant contributor to the total emission [146]. The latter point is highlighted because this work, as will become later apparent, proposes the existence of auxiliary ionisation mechanisms in the propellant gas involving impurity species, which are expected to lead to a substantial increase in ionisation efficiency.

2.2.3 Hollow cathode operating modes

The description of the steady state hollow cathode discharge is complicated by the presence of two distinct operating modes that are critically dependent on the discharge current and propellant flow rate: the spot mode and the plume mode. The observation of these two modes is particularly associated with hollow cathode tests in diode configuration. In these tests the cathode-keeper assembly is mounted in vacuum a few centimetres from a disc anode (see figure 2.8). This configuration, although markedly different from that in full thruster geometry, has been used by numerous authors (see for example [28, 40, 115, 146]) to investigate the characteristics of the HC discharge.

The plume mode is observed at low discharge currents and low mass flow rates. It constitutes a noisy discharge with high operating voltages. Its visual signature is a large plume of plasma downstream of the cathode tip. The spot mode, on the other hand, occurs at high mass flow rates and discharge currents, and possesses a quiescent, low voltage discharge characteristic. Visually, the observation of an intense

luminous spot at the cathode orifice is associated with this operating mode. Transition between the two modes can occur suddenly if either mass flow rate or discharge current is varied. The transition exhibits a hysteresis effect (figure 2.3) dependent on whether the discharge current (or flow rate) is being increased or decreased.

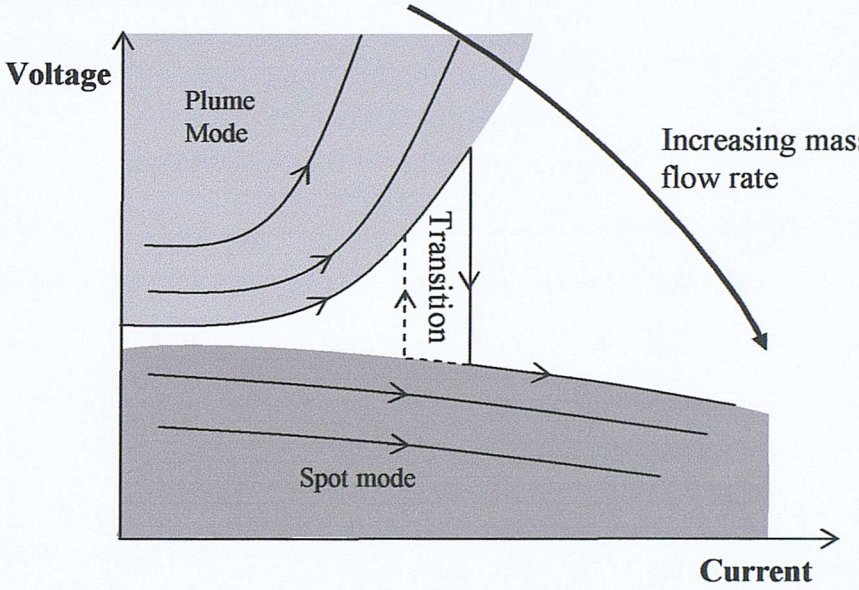

Figure 2.3: Voltage-current characteristics of a hollow cathode discharge showing plume to spot transitions at different values of mass flow rate [33].

There is considerable evidence that this dual mode behaviour is suppressed with operation in full thruster geometry, where the cathode seems to exhibit the more favourable spot mode. It is suggested that this is probably due to the higher pressure within the discharge chamber and the presence of the magnetic field [40, 33, 112]. Several explanations have been given in the literature for the existence, and transition between, the two modes. The mode transition has been associated with either: movement of the cathode sheath boundary [28], the expansion of the current emission area from the cathode orifice into the main cathode body [130], or the keeper's current collection mechanism [102]. Although each of these theories have supporting experimental evidence, they can only explain some, but not all, of the observed characteristics of the spot and plume modes.

A more comprehensive description of this feature of the HC discharge is presented in section 7.5, where, in light of the findings of this work, a new theory of plume to spot transition is proposed, which will be shown to explain virtually all of the associated characteristics.

2.2.4 HC internal plasma diagnostics

The cathode orifice maintains a high neutral density inside the cathode by restricting the propellant flow. This enhances the ionisation probability of the neutral propellant atoms by energetic electrons emitted from the hollow cathode insert surface and leads to the formation of a dense internal plasma, which in turn sustains its required energy input by ion bombardment of the emitting surface.

In order to determine the properties of the internal plasma (which will dictate the performance of the hollow cathode and consequently that of the thruster) and to identify which of the proposed processes occur in the HC discharge, a number of experimental investigations have been conducted. Historically, these measurements have closely followed the development of the Kaufman thruster, with the earlier work conducted on mercury propellant in the 1970s, and the subsequent fundamental research being carried out with xenon gas. The measurement of internal plasma properties has not proved to be an easy task, hampered by the small physical dimensions of the hollow cathode cavity and the high plasma density. Regardless of the method of choice, whether Langmuir probe or remote spectroscopic measurements, this has imposed limitations on the reliability, range and usefulness of the resulting data.

2.2.4.1 Measurements in hollow cathodes operating on mercury

Langmuir probe measurements of the internal plasma were conducted by Fearn and Philip [46] using a UK-10 cathode, and by Siegfried and Wilbur [146] who used a SERT II cathode.

Fearn and Philip [46] conducted their investigation of the internal hollow cathode plasma in diode configuration, using small cylindrical Langmuir probes placed at 1-2mm from the upstream face of the tip. The experiments were conducted, at constant tip temperature (1250°C) and constant discharge current (1.5 A), using mercury as propellant. Mass flow rate was varied between 0.03 - 0.25 mg/s. Electron temperature

and electron number density results for a fixed location were obtained as a function of flow rate.

The results for the electron temperature (figure 2.4) showed a trend of decreasing electron temperature with increasing mass flow rate, from a value of 7000K (0.6eV) at 0.03mg/s to 770K (0.066eV) at 0.25mg/s. This is an expected result, as an increase in mass flow rate will lead to an increase in neutral density, which decreases the electron mean free path and energy gain between collisions. The ionisation at the lower values of T_e probably proceeds via stepwise ionisation or collisions involving the high energy electrons existing at the tail of the Maxwellian distribution.

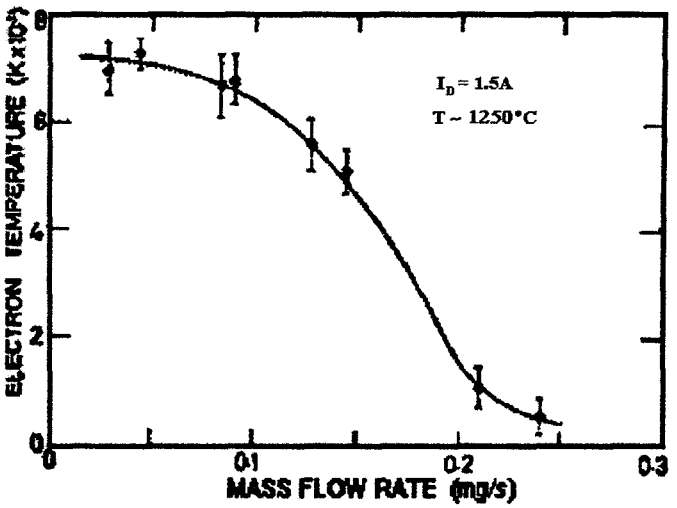

Figure 2.4: Variation of electron temperature with mass flow rate in the UK-10 hollow cathode internal plasma [46].

The results for the electron number density were less intuitive. Even at low flow rates the value did not exceed $5\times10^{17}m^{-3}$, which was an order of magnitude lower than the densities measured downstream of the orifice plate. Fearn and Philip ascribed this to probe perturbation of the plasma depressing the plasma population in the probe's vicinity. A rapid decrease in electron density was also observed with increasing flow rate (see figure 2.5). One probable explanation [46] involves the assumption that the plasma extends only a short distance into the cathode (which is indeed a widely accepted assumption in the current hollow cathode models (section 3.3)). Then, if the probe is situated at the diffusion edge of the plasma, as the mass flow rate increases, the ambipolar diffusion coefficient (which is inversely proportional to the neutral

density) decreases and the boundary of the internal plasma becomes steeper. Thus, the probe would sample a volume of falling degree of ionisation with increasing cathode flow rate.

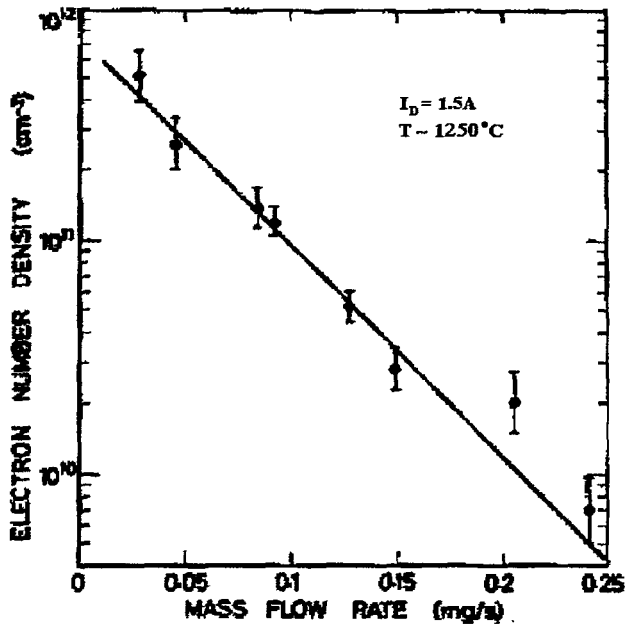

Figure 2.5: Plasma electron number density as a function of flow rate in the UK-10 hollow cathode internal plasma [46].

Siegfried and Wilbur [146] also conducted tests on the internal cathode plasma using cylindrical Langmuir probes. Their SERT II cathode was in diode configuration and used mercury propellant. Two Langmuir probes were used to measure plasma properties, one located upstream and the other downstream of the orifice plate. Each was capable of axial motion along the hollow cathode axis, which allowed estimation of the spatial variation of plasma parameters. Measurements were taken with the internal Langmuir probe from 5-15mm upstream of the orifice plate for 0.2 and 0.31mg/s flow rates and discharge currents ranging from 0.5 to 9A. This allowed, incidentally, empirical measurement of plasma parameters in both the plume and spot modes of cathode operation, which has made the results of this study (particularly those downstream of the cathode tip) invaluable in any discussion of mode transition. Only a synopsis of some their results is presented here with a more detailed discussion deferred to chapter 7.

The results for 0.31mg/s at several values of discharge current are shown in figures 2.6 and 2.7. Upstream of the orifice, the values found for the electron temperature

were similar to those by Fearn and Philip [146] and were in the range of 0.5-0.8 eV. The plasma properties upstream were independent of discharge current when the cathode was operating in the spot mode. Decreasing the discharge current in the plume mode, however, caused a reduction in the plasma density and an increase in the other parameters. The electron temperature, for a given discharge current, stayed approximately constant upstream of the cathode orifice, with values of 0.5eV estimated in the spot mode. Once the plume mode is reached by decreasing current, the electron temperature increases with decreasing discharge current reaching a value of approximately 0.8eV at 0.5A. The plasma potential experiences a steady increase as the cathode tip is approached, with values ranging from 4V at 15mm to 8V at 5mm from the tip. The electron density exhibited a sharp increase with decreasing distance from the orifice (figure 2.7). The plasma densities were observed to be an order of magnitude greater in the spot mode than in the plume mode. Siegfried and Wilbur estimated densities in the range of 1×10^{16} to 3×10^{20} m^{-3}. All these results for plasma properties seem to indicate that the ionisation rate falls exponentially with distance from the orifice, i.e. that most of the ionisation takes place near or at the orifice.

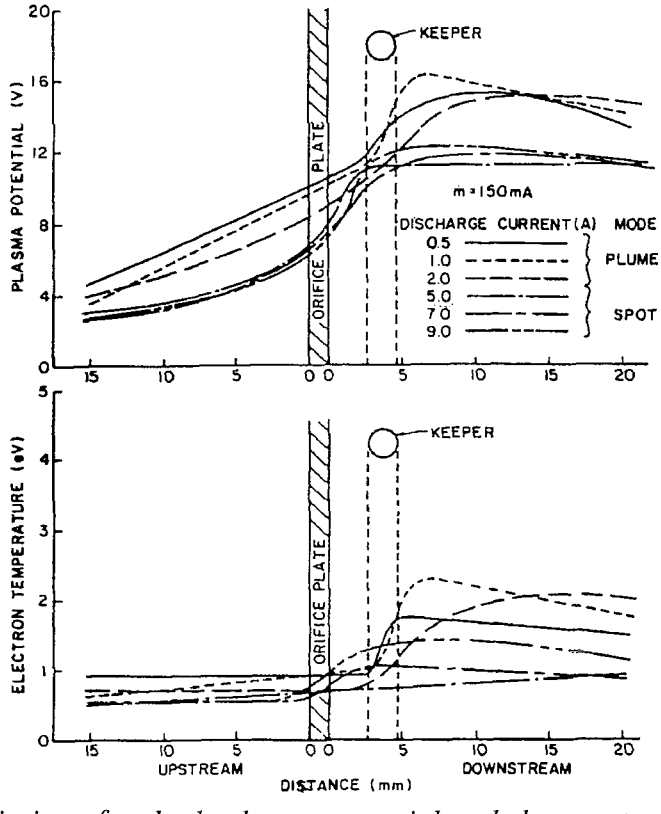

Figure 2.6: Variation of cathode plasma potential and electron temperature profiles with distance from the orifice plate at 0.31mg/s, for several values of discharge current [146].

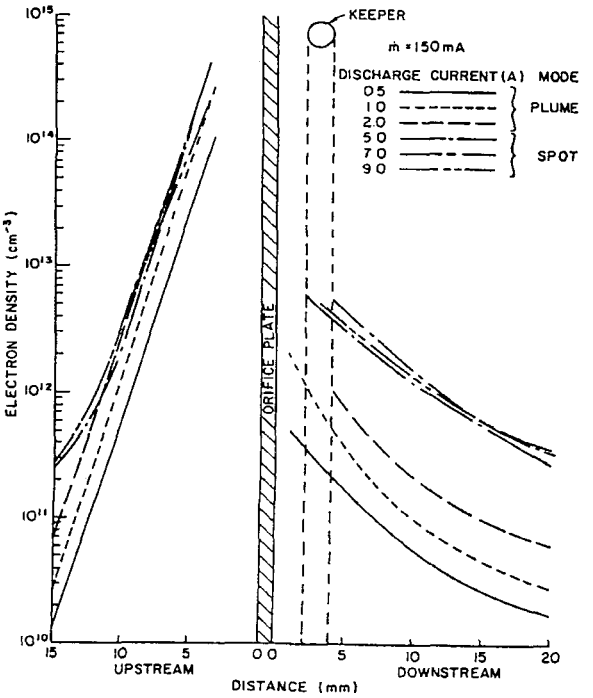

Figure 2.7: Variation in electron density with distance from the orifice at 0.31mg/s, for several values of discharge current [146].

The Langmuir probe measurements reported above did not extend to the immediate vicinity of the cathode tip, which is thought to be the main electron emission and ion production region. The Fearn/Philip results were obtained at 1 to 2mm from the internal face of the tip, and measurements in the Siegfried/Wilbur study were not possible in the region from 4mm upstream to 1 or 2mm downstream of the tip. This was due to the high plasma density in this region. Biasing a probe wherein would lead to intense ion bombardment, resulting in severe erosion and the rapid destruction of the probe.

An even more formidable issue (also recognised by Fearn and Philip [46]) is the considerable perturbation of the internal plasma by the physical presence of a probe. As discussed by Waymouth [167], if the mean free path of the plasma particles is very short, then ions and electrons must diffuse from the undisturbed regions of the plasma to the vicinity of the probe. The density gradients in the plasma might be quite large, and the plasma density and potential in the vicinity of the probe will be substantially different from that of the plasma in its absence. Therefore the plasma parameters derived from a Langmuir probe are unaffected by the physical presence of the probe

only if the plasma mean free paths (for electron-electron (λ_{ee}), electron-ion (λ_{ei}) or ion-ion (λ_{ii}) collisions) are much larger than the probe dimensions, i.e. [185]:

$$\lambda_{ee} \approx \lambda_{ei} \approx \lambda_{ii} >> r_p \tag{2.4}$$

where r_p is the probe radius and the plasma mean free path can be given approximately by [64, 66, 145]:

$$\lambda_{ee} \approx 1.45\times10^{12} \frac{T_e^{\,2}}{n_e} \tag{2.5}$$

In their upstream measurements, Siegfried and Wilbur [146] used Langmuir probes of 0.04mm and 0.13mm radius. Although Fearn and Philip [46] did not discuss their probe dimensions, they are expected to be within the range above. For a plasma of 1eV electron temperature and 10^{14}cm^{-3} density, we calculate a plasma mean free path of only 0.1mm. As the mean free path is of the same order (or may even be less than) the probe dimensions, the condition in (2.4) is not satisfied, and the probe severely perturbs the ambient plasma. If no account of this is taken in the data reduction, this will lead to large errors in estimates of plasma parameters. This puts into serious question the reliability of any Langmuir probe measurements of the HC internal plasma.

2.2.4.2 Measurements in hollow cathodes operating on xenon

The more recent studies avoided the problems of probe perturbation by resorting to non-intrusive remote spectroscopic measurements of the plasma parameters. Using a UK-25 hollow cathode in diode configuration operated on xenon, Monterde *et al.* [115, 116] observed the light emission from the operating cathode via an MgF_2 window located at the upstream end of the cathode tube (figure 2.8). The plasma light emission was collected and then spectrally resolved using a monochromator-photomultiplier tube system. The resulting spectrum was dominated by the xenon neutral and first ionisation emission lines. Monterde constructed a Collisional-Radiative (C-R) model of the HC plasma and, by comparing experimental line ratios at different ionisation stages to the model's predictions, obtained values of electron

temperature of 1.1±0.1eV for the spot mode and a slightly lower value of 1±0.1eV for the plume mode. The model was however incapable of resolving the electron density to less than five orders of magnitude, predicting that the density lies in the range 10^{17} to $10^{22}m^{-3}$. Monterde estimated that a density of $10^{20}m^{-3}$ was probably the most likely value.

Malik [101], using the same experimental set-up as Monterde, later carried out more spectroscopic investigations using xenon propellant on the UK-25 cathode internal plasma. He employed a relative continuum intensities method for assessing the electron temperature, which he estimated, in agreement with Monterde, at around 1.1eV. Using an LTE method (which is not strictly valid for the HC plasma) the electron density was calculated at approximately $10^{20}m^{-3}$.

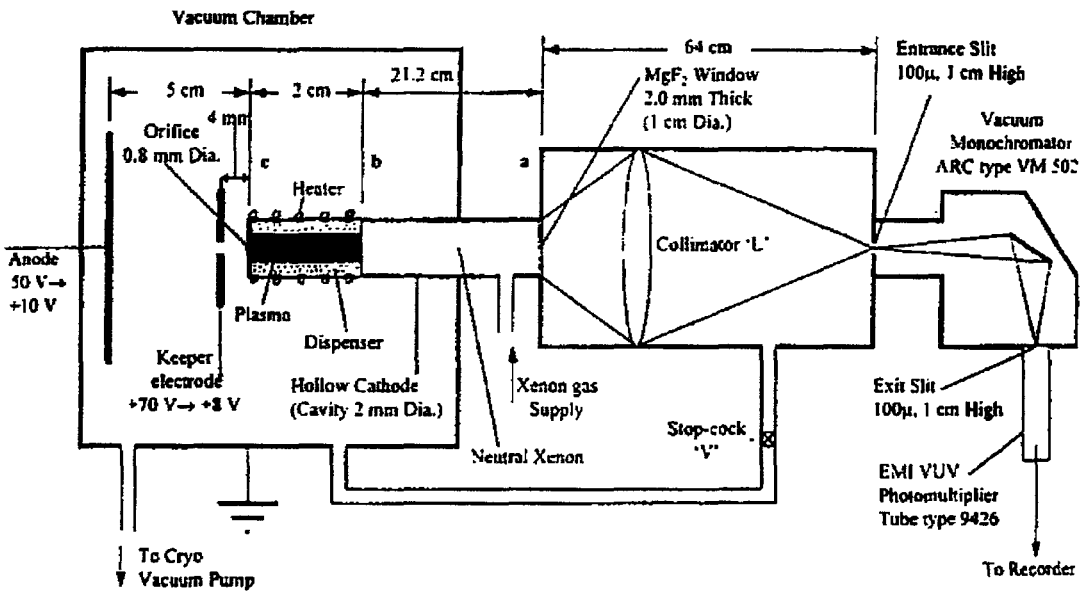

Figure 2.8: Experimental set-up for the spectroscopic investigations in the UK-25 hollow cathode operating on Xe [101].

It is important to note that the system employed in both studies, and illustrated in figure 2.8, does not allow spatial resolution of the plasma properties, i.e. the values of electron temperature and density were essentially averaged out over the entire length of hollow cathode. To the author's knowledge, no HC plasma measurements have been attempted using inert gas propellants other than xenon.

From the preceding discussion it is intuitive to recognise the benefits of using the instrumented HC in conjunction with the high-temperature sapphire optical fibre probes developed in this work (Appendix A), combining the non-intrusive nature of optical diagnostics with in-situ spatially resolved measurements of the plasma parameters. During the subsequent change in this project's direction, it was decided to retain the ability for non-intrusive measurement. Thus, an on-axis optical fibre was used to observe the HC plasma. It is interesting to compare the complexity and cost of the experimental apparatus used in the Monterde/Malik studies, particularly the vacuum system for the optics (figure 2.8), with the setup used in this work and described in chapter 4.

2.2.5 Hollow cathode discharge initiation (Starting)

A crucial requirement for the HC is the ability for a reliable, rapid initiation of the discharge under all possible circumstances. This includes the capacity to initiate the discharge when the cathode is new or after thousands of hours of operation, after exposure to air, and the provision for routine initiation under vacuum in the laboratory or in space [124]. In electron bombardment ion thrusters, the ability to initiate the discharge is largely dependent on the HC. It is thus surprising that this important aspect of HC operation has received little attention, with only a few studies conducted on HC starting characteristics. The picture that emerged is of a highly complex process, dependent on a large number of parameters and partially random in nature. In what follows these experiments and their results are presented in detail.

2.2.5.1 Experience with mercury

Investigations of hollow cathode starting phenomena were conducted using several cathode geometries by Fearn *et al.* [48, 46, 119] at Farnborough, Culham and Philips laboratories. These investigations were carried out during the 1970s and hence used mercury as propellant. Their work was the first systematic examination of the discharge initiation phase, and an attempt to form a comprehensive understanding of

the physical processes involved. All the cathodes used were based on the UK T4 cathode. The tests were carried out in diode configuration, a schematic of the cathode and assembly is shown in figure 2.9.

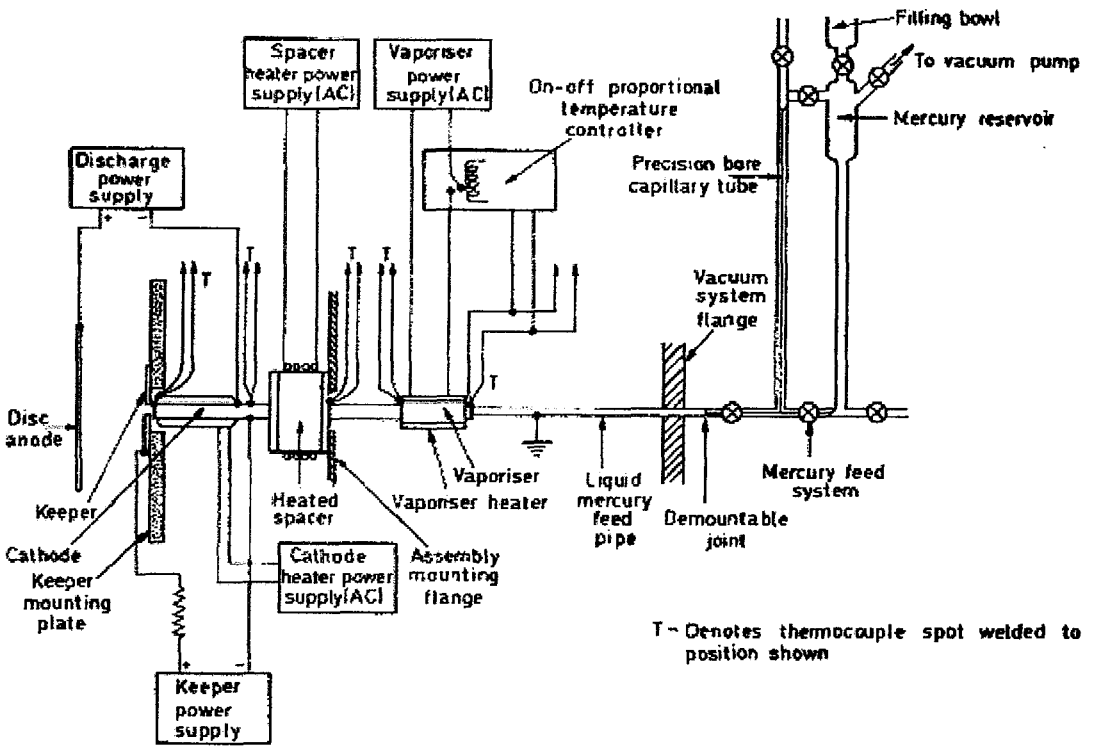

Figure 2.9: Detailed schematic of the diode system employed in the mercury starting experiments [48].

It was expected, based on general physical principles, that the factors that will have the most dominant effect over the discharge ignition of fixed geometry hollow cathodes will be: i) the keeper voltage V_k, ii) the cathode tip temperature T and iii) the propellant flow rate $\dot{m}$ (which determines the pressure distribution inside the cathode body). Other factors expected to come into play were the temperature distribution over the insert and orifice surfaces, the tip material and its surface finish, the previous discharge history and the presence of contaminants (expected to be air and pump oil in this case). Geometrical factors thought to be of significance in these experiments were the cathode-keeper separation, the cathode and keeper orifice diameters and the shape of the insert and the orifice plate. It was not possible in the work to investigate all these parameters and emphasis was placed on V_k, T and $\dot{m}$ along with the factors that might affect the rate of dispensation of barium, such as the orifice shape and the

insert type. Also, the diameters of the cathode orifice and the keeper orifice were varied over a restricted range. Regarding the other parameters that were not investigated, attempts were made by the investigators to keep them as constant as possible during the course of their study.

a) ***The dependence of the discharge initiation on V_k, T and $\dot{m}$***

It was found that the discharge initiation phenomena was more complex than initially thought from gaseous breakdown considerations, due probably to several of the factors mentioned above coming into play. It was found that the keeper voltage required for breakdown was not reproducible, but fell within a certain range, the magnitude of which depended strongly on temperature and flow rate.

Investigations were carried out on a cathode with an orifice diameter $d = 0.3$ mm, and a tubular insert having a triple carbonate mix coating. To investigate the initiation dependence on temperature, the value of $\dot{m}$ ~0.12mg/s was selected, the results are shown in figure 2.10. Discharge initiation was possible below 1000°C with keeper voltages well below 50V, but to be sure of ignition the upper envelope of the data had to be exceeded.

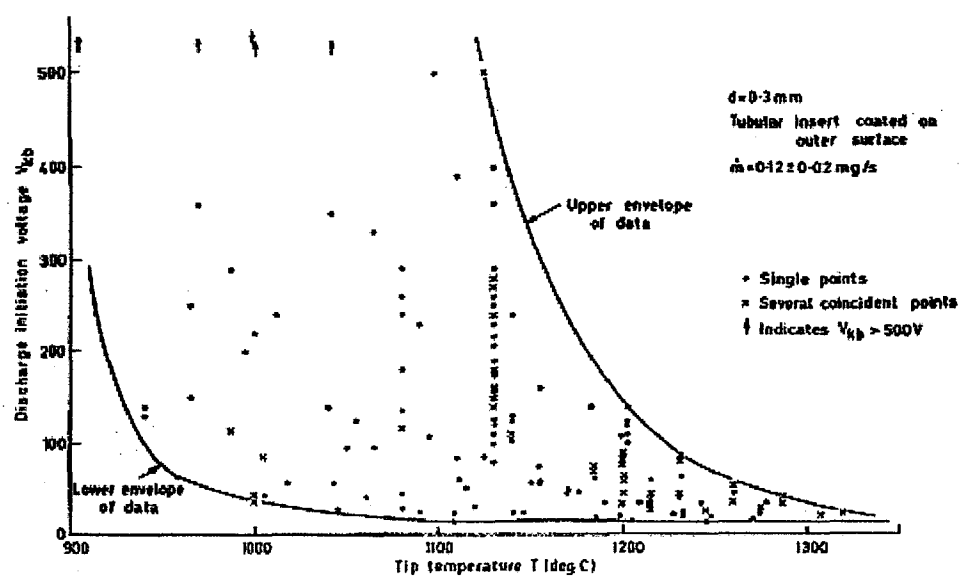

Figure 2.10: Discharge initiation data for a cathode containing tubular insert at $\dot{m}$ ~0.12mg/s [48].

The same experiments were repeated keeping tip temperature fixed and varying the mercury flow rate. Data collected in the range 0.003 to 0.9mg/s are shown in figure 2.11. The variation of the upper limit of the envelope in figure 2.11 seems to be less rapid than that for the same variation in temperature. This indicated to Fearn that discharge initiation is less sensitive to variations in mass flow rate than to those in temperature. The common trend between the two figures is that both the maximum value of V_{bk} and the voltage range decreased if either temperature or mass flow rate were increased until discharge initiation was almost reproducible at low potentials.

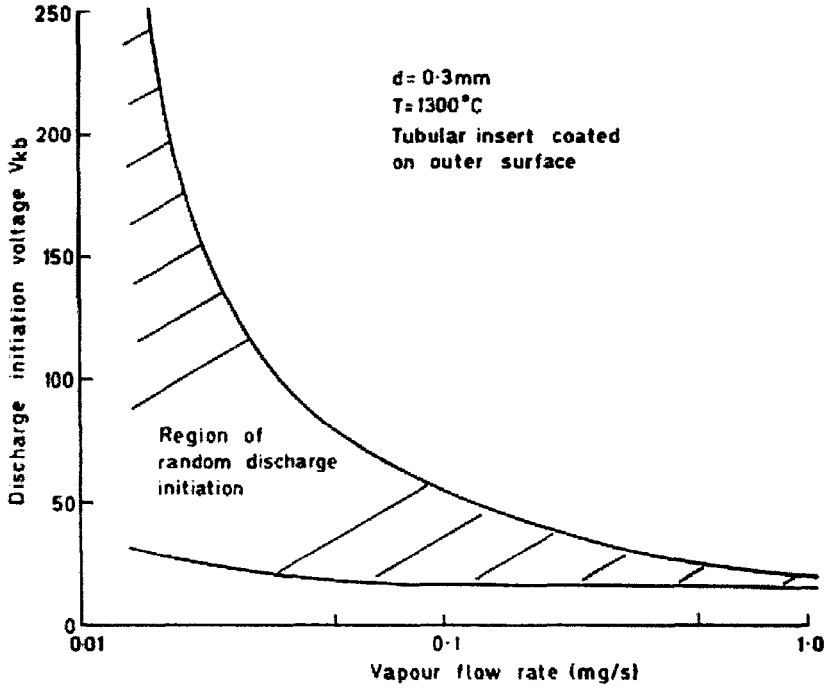

Figure 2.11: Envelopes of discharge initiation data as a function of mass flow rate for T =1300°C [48].

b) ***Dependence of discharge initiation on dispenser configuration:-***

Starting experiments were carried out using rolled foil dispensers to compare their starting behaviour with those of tubular inserts. The results seemed to indicate that the general behaviour was qualitatively similar to the tubular insert case but that discharge initiation occurred at lower values of tip temperature. This is illustrated in figure 2.12, where the curves for the tubular insert are shown superimposed to highlight the shift to lower tip temperatures.

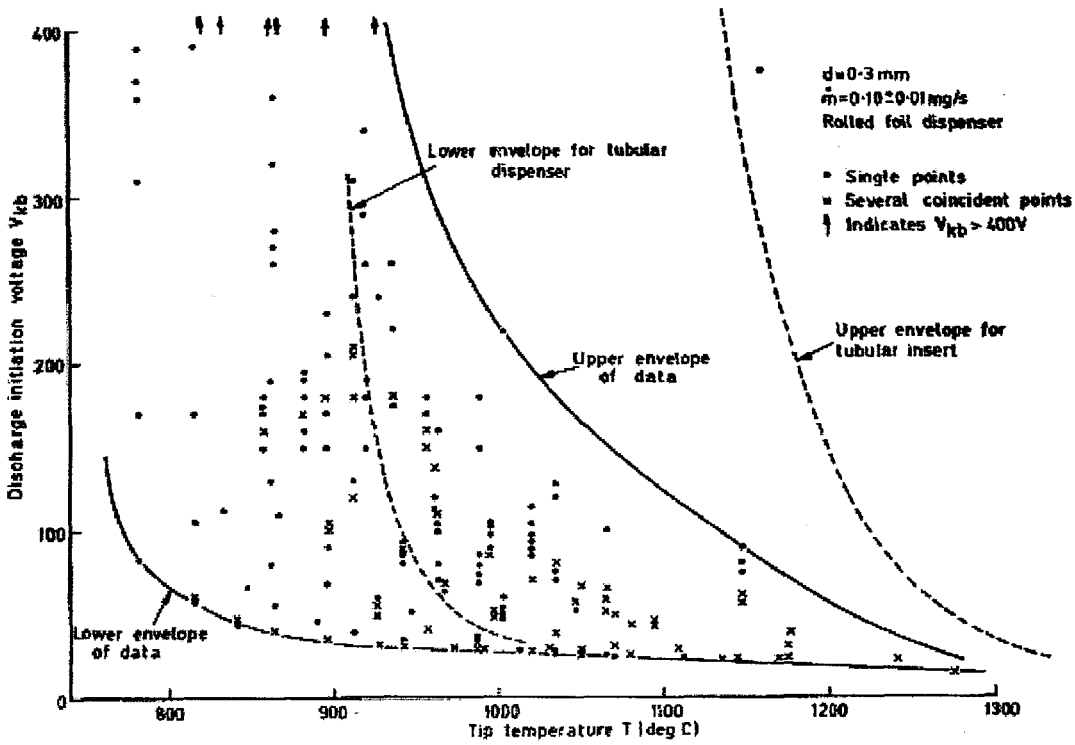

Figure 2.12: The discharge initiation behaviour cathode containing rolled foil insert, superimposed are the results for a tubular insert cathode [48].

c) ***Dependence of discharge initiation on cathode orifice shape***

Several special cathodes were constructed to test the various aspects of proposed cathode emission theories. One such cathode contained a curved orifice plate, which eliminated the sharp edges between the dispenser and the orifice plate. An illustration of this cathode is shown in the inset to figure 2.13. The triple carbonate mix was painted on the inner wall of the cathode body.

The discharge behaviour of the curved orifice cathode is shown in figure 2.13. The device exhibited extreme ease in starting the discharge. The shape of the curves in figure 2.13 indicates a behaviour similar to that observed in previous cases, but the values of breakdown voltages were shifted to lower values. Values of V_{bk} lower than 200V were observed even at flow rates as low as 0.05mg/s and tip temperature as low as 800°C. Increasing $\dot{m}$ led to a narrowing of the random breakdown region. This caused starting to become almost completely reproducible for T >1000°C and $\dot{m}$ ~0.17mg/s, where values of V_{bk} below 30V were always recorded. These excellent

starting characteristics could not be matched by cathodes employing tubular inserts and an angular orifice plate.

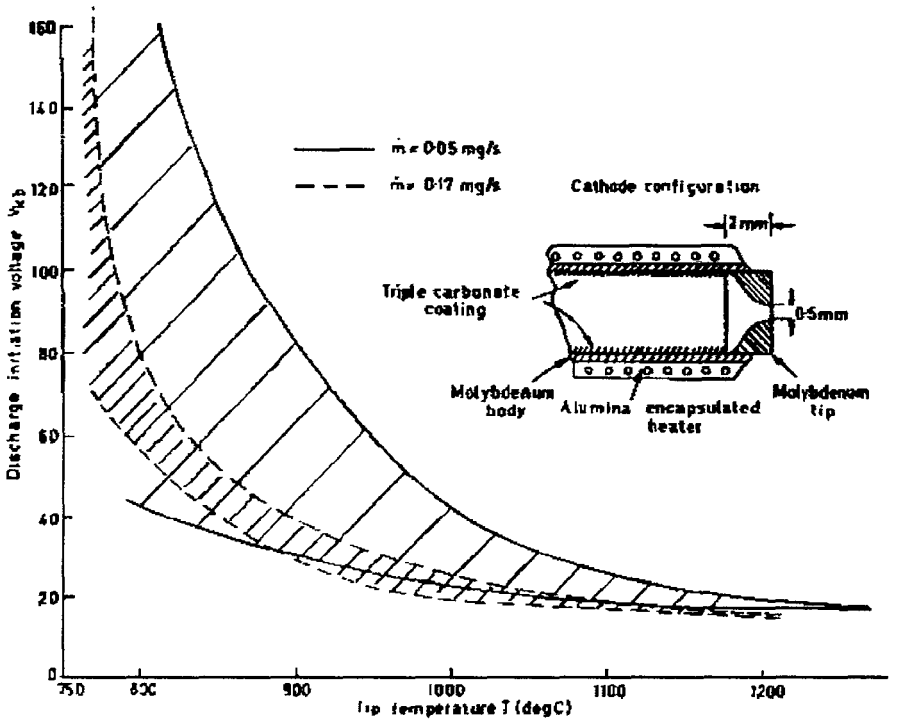

Figure 2.13: Discharge initiation behaviour of curved orifice cathodes [48].

d) *Dependence of discharge initiation on low work function material*

The emission of the 'first' electrons depends on the work function of the emissive surface. The triple-carbonate mix containing barium is hence thought to have an important part in determining the starting and operational characteristics of hollow cathodes. To test this hypothesis, the investigators constructed a cathode, illustrated in figure 2.14, with no provision for a low work function material.

The cathode's performance in steady state was far removed from other cathodes. The cathode was operating at much higher tip temperatures than those encountered in the standard bariated versions; the difference was usually about 200°C. The discharge voltages were also much higher and the plume mode was encountered under conditions where it was previously absent in cathodes of similar geometry.

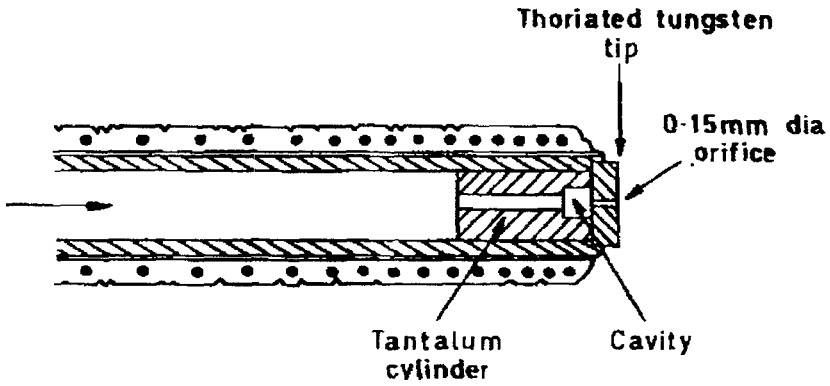

Figure 2.14: Insert configuration used in the non-bariated cathode tests [48].

The starting characteristics of this cathode were also investigated and were found to be inferior to those of cathodes with the same geometry. Breakdown occurred, under the same conditions of flow rate and cathode dimensions, at values of tip temperature about 350°C higher than those for cathodes containing a triple carbonate emissive mix. This is illustrated in figure 2.15. These results were also supported by an investigation in the U.S.A., in which Zuccaro [176] also reported that extremely high temperatures and voltages were required to start a non-bariated cathode.

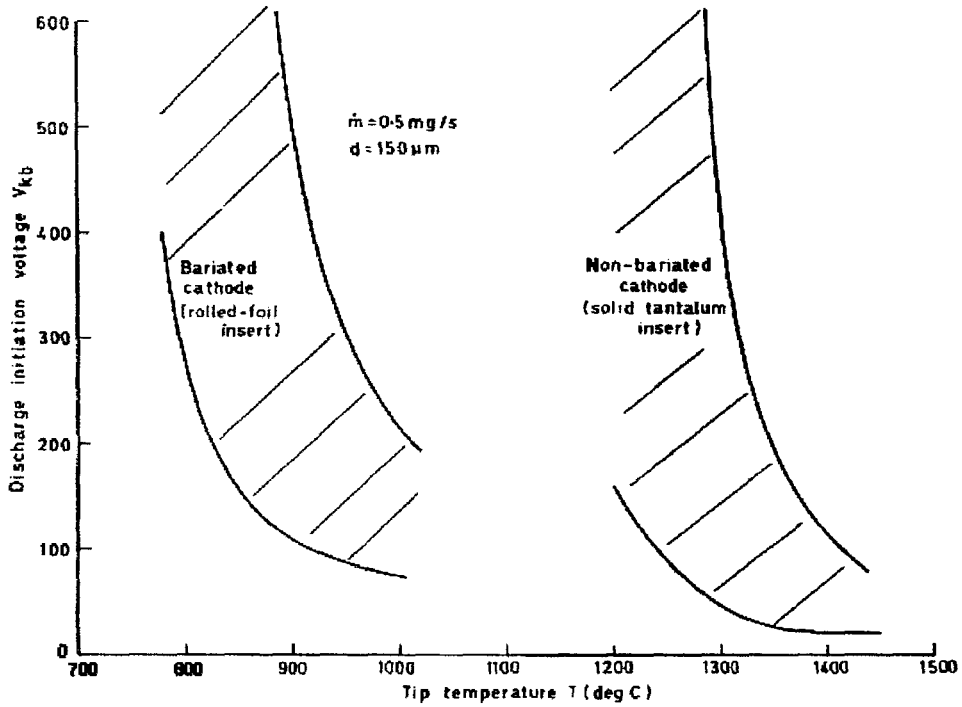

Figure 2.15: Discharge ignition behaviour with and without barium [48].

e) *Dependence of discharge initiation on cathode orifice size*

Experiments conducted for two cathode orifice diameters (0.15mm and 0.3mm) have indicated that orifice diameter, in that restricted range, had only a small effect on discharge initiation when compared to a variation of the same order of magnitude in mass flow rate. The results for the two orifice diameters are shown superimposed in figure 2.16. Their most appreciable features are that the minimum breakdown voltage is displaced to higher values for the 0.15mm diameter orifice, and that at high temperatures (>1000°C) the upper envelope of the results for the two orifices coincided.

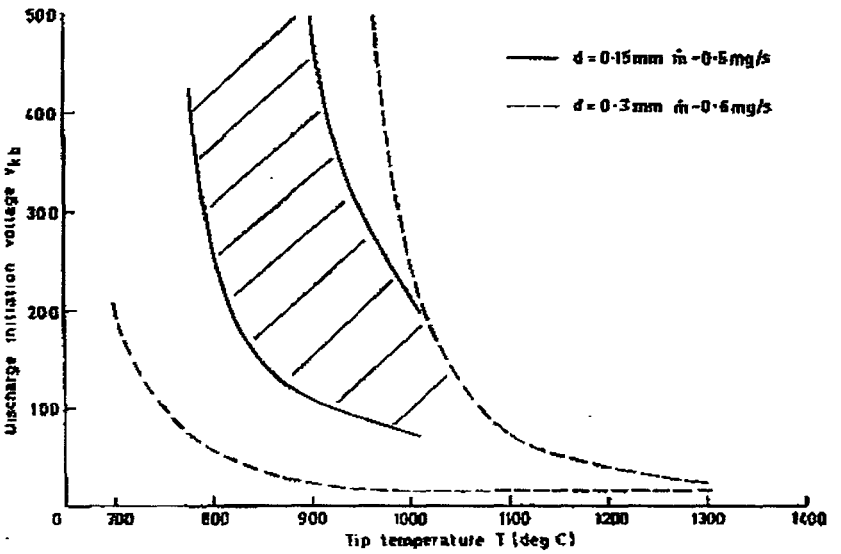

Figure 2.16: Variation in discharge ignition behaviour with change in orifice size [48].

However, as pointed out by Fearn [48], the range of orifice sizes in these experiments was limited. There was also some evidence from a related study [128] that an orifice size of 0.5mm or larger gave improved starting ability. The larger orifice size is thought to lead to a greater field penetration into more deeply seated emission sites, but it must be remembered that this effect might be offset by the concurrent change in the local pressure distribution inside the hollow cathode cavity.

2.2.5.1.1 Proposed HC initiation theory based on the mercury results

In order to explain the results described above, Fearn [48] endeavoured to clarify the discharge initiation mechanisms of relevance to ion thruster hollow cathodes. At the outset it was thought that the starting process would resemble high voltage gaseous breakdown. But, as figures 2.10 and 2.11 show, the situation is more complex than initially thought. Thus, a comprehensive theory of discharge initiation was a difficult aim, as any theory would have to explain the randomness of the data obtained, the dependence of the discharge on T and $\dot{m}$, the effects of orifice shape and barium dispensation mechanisms on starting.

Barium dispensation

The presence of barium, in the form of a triple carbonate mix, on the surface of an emitting insert has been shown to have the effect of lowering the amount of energy required to produce thermionic emission of electrons (figure 2.15).

Comparison of the results has shown that the rolled foil insert was the more copious in barium production from the triple carbonate mix when compared with tubular inserts (refer to figure 2.12). This is thought to be due to the greater contact surface area between the tantalum and the emissive mix and the ready availability of barium in the spiral insert case. Having said that, the cathode containing a curved orifice has demonstrated even better starting abilities (figure 2.13). This seems to indicate that the position of the active barium is of more importance than its rate of dispensation. The curved orifice cathode can conceivably provide an easier migration path for the active barium (by surface or gas phase migration) from the dispenser to the main emission sites, as it eliminates the sharp edges found in a standard hollow cathode orifice.

Newson *et al.* [119] have demonstrated that, for a given set of conditions, discharge initiation occurs at a constant value of pre-discharge current (defined as the current drawn from the keeper prior to the discharge striking). The time taken to achieve this value was however observed to vary. This temporal variation is attributed to the loss

of barium from the emission site after starting due to evaporation or ion bombardment. The replenishment process (for the next start) is limited by the rate of diffusion of barium to these sites, which is in turn dependent on factors that are difficult to assess such as how much barium is needed for replenishment and the location of the available barium, the degree of contamination of the system (the better the vacuum system the smaller this factor), the surface condition of the orifice, and chemical reactions taking place in the dispenser. This seems to qualitatively explain the dependence of starting characteristics on previous discharge history.

Fearn also pointed out that, although a good starting ability might seem desirable, the requirement of rapid dispensation of barium will have the adverse effect of decreasing the life expectancy of the cathode. Thus, the spiral insert and the curved orifice cathodes might prove to be unsuitable options for space operations.

Breakdown

From the results of the investigation described above, Fearn suggests that thermionic emission from the tip is necessary to start the discharge. The first thermionic electrons are emitted from the vicinity of the cathode orifice. These are then accelerated by the applied electric field, which penetrates a short distance into the tip. The electrons cause collisional ionisation of the propellant gas, which leads to multiplication of the electron number. At the same time, the ions produced are accelerated towards the tip, with the ion bombardment of the surface causing secondary emission of electrons. These two processes increase the keeper current (I_k), and as the value of the keeper potential (V_k) increases, a point is reached where the Townsend breakdown criteria is satisfied, and the value of the pre-discharge current grows abruptly to much higher values.

Calculations based on this model were done by Fearn [48] for high flow rates (~1mg/s). The results for the breakdown voltage were close to the upper limits of the experimental results. The results were found to be extremely sensitive to the location of the accelerating electric field in the HC cavity.

This model, however, implicitly implies that the mean free path for ionisation is much less than the orifice dimensions, which is only the case for high values of mass flow rate. It cannot explain the occurrence of breakdown in the large range of values of pressure and temperature at low potentials. It cannot explain, in particular, the occurrence of discharge at very low values of mass flow rate where the internal pressure is too low for collisional ionisation to occur.

A multi-step collisional ionisation process, via electron collisions with metastables, was invoked in order to explain breakdown in the medium to low pressure range. However, with initiation successfully achieved at $\dot{m}$ as low as 0.01mg/s, it is unlikely that collisional processes are responsible for breakdown at these very low pressures. This has forced the investigators to consider vacuum arc mechanisms, involving field emission from micro-projections on the surface, to explain HC breakdown at extremely low cathode pressures.

The Fearn *et al.* [48] study has served to highlight the complexity of HC breakdown and the attendant difficulty of producing a comprehensive theory to explain all the processes involved.

2.2.5.2 Experience with xenon

Patterson and Fearn [124] conducted a recent study to characterise the discharge initiation processes in hollow cathodes operating on xenon. Their experiments utilised a T6 hollow cathode with an open keeper mounted in diode configuration. The T6 cathode was designed to provide higher discharge currents than those of the earlier mercury tests, and was therefore considerably larger. The Patterson/Fearn T6 cathode had an orifice diameter of 1.6mm, an outer diameter of 7mm, and contained an insert 20mm long having an inner diameter of 2mm.

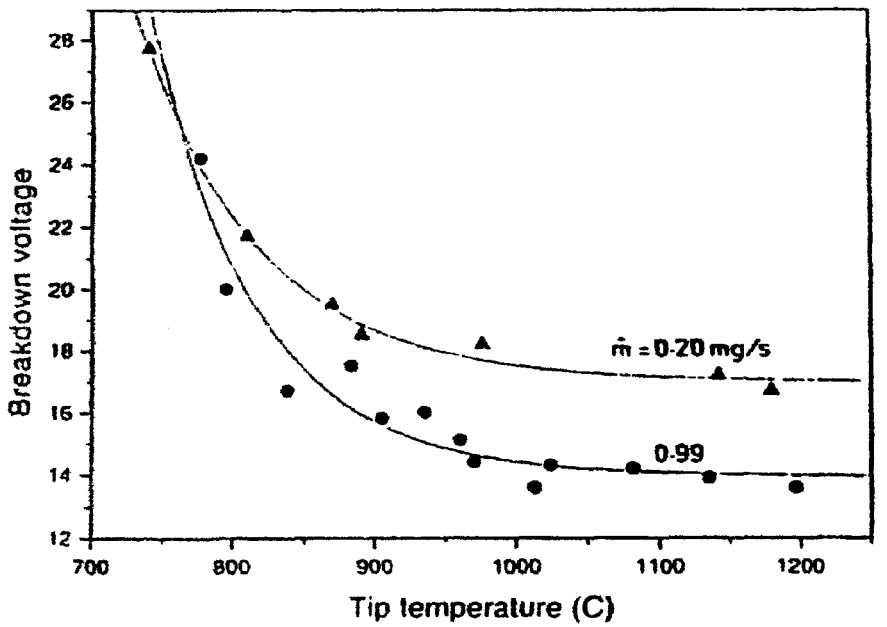

Figure 2.17: V_{bk} as a function of cathode tip temperature for different values of $\dot{m}$ [124].

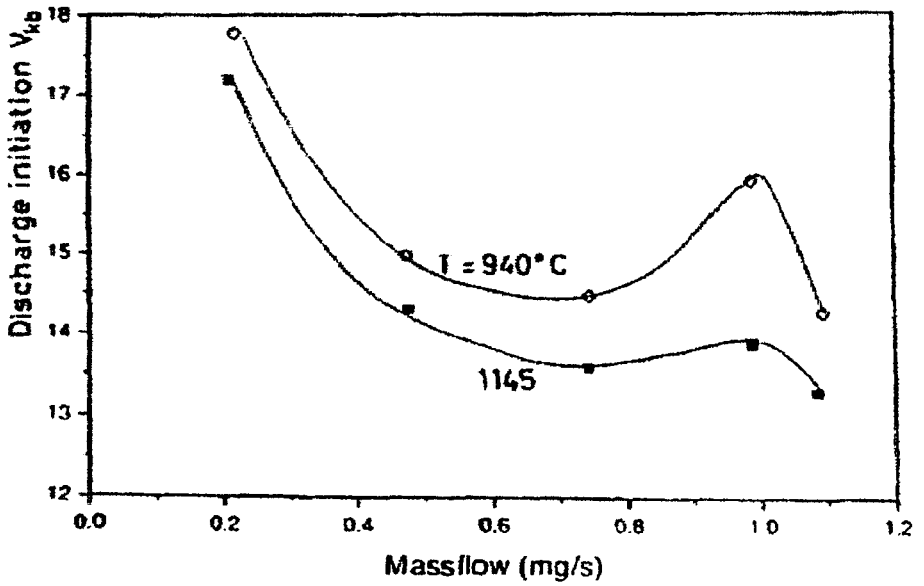

Figure 2.18: V_{bk} as a function of $\dot{m}$ for different values of T [124].

Figures 2.17 and 2.18 illustrate the results obtained for breakdown voltage dependence on tip temperature and mass flow rate respectively. There are two notable features to the results: First, very low potentials (< 30V) were required to ensure reliable initiation of the T6 discharge under all conditions, with initiation possible at under 14V for T >1100°C and $\dot{m}$ = 0.99mg/s. Second, the results do not seem to exhibit the randomness of previous mercury experience and seem to be completely

reproducible over the entire range of the experiments carried out, indicating that discharge initiation might not be as random a process as previously suggested. Of considerable interest is the unexplained severe departure of the results in figure 2.18 from the expected Paschen breakdown behaviour. The breakdown voltage decreased as flow rate was increased to above Img/s, whereas it would be expected from theory to continue to increase.

This work was part of a wider study to characterise and optimise the performance of the T6 HC. Although not as extensive as the earlier mercury work, it constitutes the only systematic study on the breakdown behaviour of hollow cathodes operating on xenon, and, to the author's knowledge, no study has investigated the breakdown behaviour of other inert gases.

Several possible explanations have been proposed for the disparity between the T6 results and those of the earlier mercury tests [124]: -

- *The degree of contamination of the vacuum system*:- The work conducted in the 1970's employed an oil diffusion pump producing a background pressure in the low 10^{-6} Torr region. It was recognised that contamination of the vacuum system due to poor vacuum will have an influence on the results [48], as poisoning of the activated surface (which contains hot reactive barium) can readily occur due to oxidising gases such as O_2, CO_2 and H_2O. Moreover, in the case of the 1970's experiment, pump oil will also be present in the vacuum system, leading to the deposition of a layer of organic contaminant on the electrode surfaces.

  An experiment was undertaken by Fearn [51] to determine the effects of a constant air leak in the propellant feed system on xenon discharge characteristics. The results of the experiment have shown that for low mass flow rates, the spot mode discharge changed into a plume mode 15 minutes after the leak was introduced, indicating that contamination alters the emission behaviour in steady state. It is conceivable that it might also have an effect on reproducibility in the starting phase.

In the more recent Patterson/Fearn investigation this was all taken on-board: A cryo-pumped vacuum chamber was employed, with an ultimate vacuum pressure of about 5×10^{-8} Torr. The experiment also used oxygen absorbers in the propellant feed lines and all the joints in the feed system below atmospheric pressure were either welded, brazed or contained in an auxiliary vacuum chamber thus eliminating the contaminants and probably leading to the more reproducible results.

- *The change of propellant*:- Xenon has a higher first ionisation potential than mercury. Its metastable energy levels are very different from those of mercury and under a given set of conditions will have different creation rates. These two gases will consequently interact differently with the emitting insert, having for example different electron yields per impacting ion or metastable. Moreover, the reactivities of the two gases are far removed. Hence, the change in the atomic characteristics of the propellant gas might be responsible for the change in breakdown behaviour.

- *The cathode orifice size*:- It is thought that a large cathode orifice may facilitate discharge initiation because of the deeper penetration of the electric field allowing current to be drawn from more deeply seated emission sites. Fearn and Patterson used a cathode with an orifice more than five times larger than the one employed in the mercury work. As no study has been previously done using such a large orifice, it is conceivable that the larger orifice can help make discharge initiation easier (and probably more reproducible). A large orifice would, however, also modify the cathode pressure distribution. Therefore, a change in this parameter will have a complex effect on cathode breakdown.

Any one or a combination of these factors might be responsible. More work, specifically more empirical data, is certainly required to understand the physics of breakdown in ion thruster hollow cathodes.

Chapter 3

THEORETICAL BACKGROUND

Introduction

This chapter presents the theoretical background necessary for this thesis. It focuses on two main areas, the plasma spectroscopy carried out on the hollow cathode and the description of the underlying physics of hollow cathode discharges both in the transient and steady state phases of operation.

In the first section the various models of the plasma state and the relevant techniques for interpretation of the spectra are reviewed. The second section is concerned with gaseous breakdown and its application to the starting phase of hollow cathode operation. And the final section reviews relevant models of the physical processes occurring in the steady state hollow cathode discharge.

3.1 Plasma spectroscopy

Spectroscopy entails the observation and interpretation of the radiation emitted or absorbed by a collection of atoms. Due to its non-intrusive nature, Atomic-Emission-Spectroscopy (AES) was selected as the most suitable candidate for investigating the small hollow cathode cavity, where its restricted nature and the expected high plasma density render in-situ measurement techniques difficult [115, 101, 33].

The radiation produced by a plasma is inexorably linked to the composition of the gas and the plasma parameters (electron temperature and electron density). To be able to interpret the plasma spectrum to arrive at an estimate of the desired parameters, a

certain notion of the state of the plasma is required. Thus theoretical models of the plasma state and the selection of an appropriate model for the plasma in question form the basis for any interpretation of the raw spectra.

This section begins with a description of the generally accepted theoretical plasma models, from which we will select an appropriate model for the hollow cathode plasma. Based on the selected model, various techniques described in the literature for interpretation of the spectra in terms of the plasma parameters will then be discussed. The scope and complexity of the subject renders it impossible to fully review the literature and only a brief overview is attempted here, for more details reference should be made to standard texts [59, 65, 94].

3.1.1 Plasma radiation

A plasma is generally composed of electrons, neutral atoms and ions. Each of these contributes to the observed radiation by changes in their respective energy states. These changes are produced by electrons making different types of transitions, such as: bound-bound transitions, free-bound transitions and free-free transitions.

The continuum emission observed in a spectrum is due to free-free and free-bound transitions. Continuum emission or absorption can result when a charged particle is accelerated or decelerated. For example, bremsstrahlung radiation is emitted whenever a free electron is accelerated or decelerated by a long range collision with an ion. As this electron is not bound to the field of an ion or atom the initial and final electron energies can occupy a continuum of possible energy levels. The transitions are hence known as free-free transition and the emitted radiation is a continuum.

Another source of continuum emission is free-bound transitions, where a free electron is captured by an ion (also known as recombination). As the emitted radiation is a function of the initial free electron energy, which can again occupy a continuum of energy levels, the emitted radiation is a continuum, according to equation (3.1):

$$h\nu_{uq} = E(\infty) + \frac{1}{2}mu^2 - E(q) \qquad (3.\ 1)$$

Where $E(\infty)$ is the ionisation energy, $E(q)$ represents the energy at bound energy level q, $mu^2/2$ is the kinetic energy of the electron prior to recombination and $h\nu_{uq}$ is the energy of the emitted photon with h being Planck's constant and ν_{uq} the frequency of the emitted radiation.

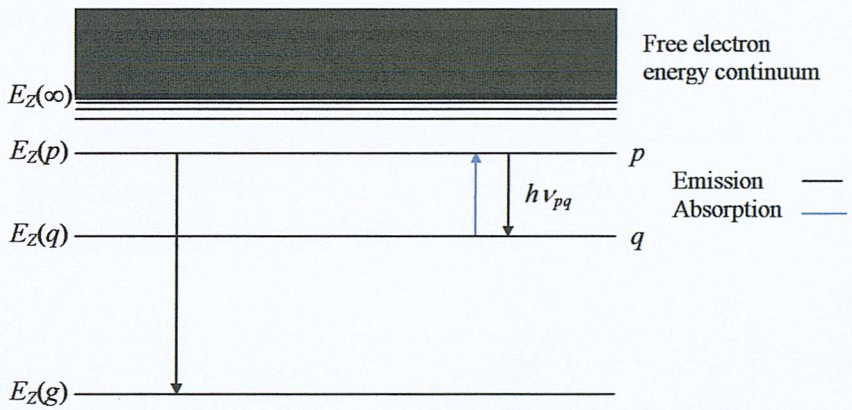

Figure 3.1: Energy level diagram for a hydrogenic species of charge Z

Bound-bound transitions are associated with electrons in atoms and ions where they are allowed to fill only discrete energy levels, as opposed to free electrons which can occupy a continuum of possible energy levels.

When an electron makes a transition between two energy levels (p and q), see figure 3.1, a photon is emitted or absorbed. The emitted photon from a bound-bound transition has an energy:

$$h\nu_{pq} = E(p) - E(q) \qquad (3.\ 2)$$

Where $E(p)$ and $E(q)$ represent the energy at levels p and q respectively, and ν_{pq} is the frequency of the emitted photon in a p-q transition.

The observed intensity of the emission line is basically the sum of the contributions of all the atoms or ions undergoing the same transition at the same instant in time over the instrument's line of sight. The emitted intensity thus depends on:

(a) The probability of an electron being present in the upper level of the transition
(b) The atomic probability of the transition of interest occurring, and
(c) The probability of the produced photon escaping from the plasma without being reabsorbed.

If the interaction of the radiation and the plasma (process (c)) is neglected, considerable mathematical simplification of the problem is achieved. The plasma is then said to be "optically thin"; in the discussion that follows the assumption of an optically thin plasma is assumed to hold. The validity of this assumption in terms of the hollow cathode plasma is discussed in more detail in section 3.1.2.3.

Calculation of the transition probability (process (b)) is a matter of atomic quantum mechanics. Transition probabilities for some emission lines of the noble gases used in this work can be found in the literature [177, 178, 179, 180, 181].

The population of a certain bound level, or more generally the distribution of electron population among available energy levels (process (a)), is dictated by collisions with other particles and radiative processes, which are described by the plasma equilibrium model.

For a complex many-electron atom or ion, the structure of the available energy levels becomes more complex than that shown in figure 3.1. The electrons couple with each other to form a greater number of possible transitions for an excited atom/ion. A further complicating factor is the presence of a plasma in the vicinity of the atom/ion, where the energy level distribution does not necessarily correspond to that in an isolated atom/ion. The energy levels are shifted by long range Coulomb interactions with nearby charged particles, thus not only affecting the emitted radiation but also the energy distribution of its originating levels.

3.1.2 Plasma models and types of equilibrium

The various elementary processes of excitation/de-excitation and ionisation/ recombination in atoms or ions caused by collisions with particles and photo-

processes are listed below [115]:

(i) Three-body recombination to state p of S_Z: $S_{Z+1} + e + e \rightarrow S_Z(p) + e$

(ii) Collisional ionisation, the inverse of (i): $S_Z(p) + e \rightarrow S_{Z+1} + e + e$

(iii) Radiative recombination: $S_{Z+1} + e \rightarrow S_Z(p) + h\nu$

(iv) Photo-ionisation, the inverse of (iii): $S_Z(p) + h\nu \rightarrow S_{Z+1} + e$

(v) Collisional de-excitation: $S_Z(p) + e \rightarrow S_Z(q) + e$

(vi) Collisional excitation, the inverse of (v): $S_Z(q) + e \rightarrow S_Z(p) + e$

(vii) Spontaneous emission: $S_Z(p) \rightarrow S_Z(q) + h\nu$

(viii) Photo-excitation, the inverse of (vii): $S_Z(q) + h\nu \rightarrow S_Z(p)$

Where S_Z represents an atom or ion of charge $+Ze$ and S_{Z+1} represents a species of a higher ionisation stage $+(Z+1)e$, $h\nu$ is the energy of the emitted photon and $p > q$. The electron temperature determines the rate coefficients for all the above processes. Interactions between atoms and ions are not normally included in the above processes because of the low probability of their occurrence.

For total thermodynamic equilibrium to occur, the kinetic and radiative energies need to be conserved in the plasma, therefore all the above processes (i) to (viii) need to be balanced by their inverse process by the principle of detailed balance. The free electrons will have a Maxwellian velocity distribution characterised by a temperature (T_e) and the energy is distributed over all the particles according to Boltzmann's distribution law.

In laboratory plasmas the kinetic energy is transferred by electron collision processes (excitation, de-excitation, ionisation and recombination). Radiative equilibrium is more difficult to achieve as the photon mean free path is generally longer than the plasma dimensions for a laboratory plasma. This is clearly demonstrated by the observation of radiation from the plasma, this very fact makes the realisation of complete thermodynamic equilibrium difficult. Notwithstanding, some useful approximate models for equilibrium can be used instead, and are the subject of the following sections.

3.1.2.1 Local Thermodynamic Equilibrium (LTE) model

For a plasma in LTE, the distribution of electron population densities is determined exclusively by collisional processes and the radiative processes are neglected. The frequency of these collisions is assumed to be high enough to result in instantaneous changes in the distribution. This leads to the creation of a "local" equilibrium at any instant and point in space between the collisional excitation and ionisation processes and their inverse processes.

For the free electrons, the velocity distribution function is given by the Maxwellian distribution. Therefore, the number density of electrons with a velocity between u and $u + du$ is given by [65]:

$$dn_u = 4\pi n_e \left(\frac{m_e}{2\pi k T_e} \right)^{3/2} u^2 \, exp\left(-\frac{m_e u^2}{2kT_e} \right) du \tag{3.3}$$

where n_e is the total number density of electrons and T_e is the electron temperature.

The ratio of bound electron population for two energy levels of the same species is given by the Boltzmann relation [65]:

$$\frac{n_Z(p)}{n_Z(q)} = \frac{g_Z(p)}{g_Z(q)} exp\left(-\frac{E(p) - E(q)}{kT_e} \right) \tag{3.4}$$

$n_Z(p)$ and $n_Z(q)$ are the population densities of the levels identified by the quantum numbers p and q, and ion charge Z. The term $g_Z(p)$ is the statistical weight of the designated level and $E(p)$ represents the energy of that level.

By the principle of mass action, the Saha equation gives the ratio of the number density of species of subsequent stages of ionisation in the ground level [65]:

$$\frac{n_e n_{Z+1}(g)}{n_Z(g)} = \frac{g_{Z+1}(g)}{g_Z(g)} 2 \left(\frac{2\pi m_e kT_e}{h^2} \right)^{3/2} exp\left(-\frac{E_{\infty Z}(g)}{kT_e} \right) \tag{3.5}$$

where $n_Z(g)$ and $n_{Z+1}(g)$ represent number densities of the ground level population of species of charge Z and $Z+1$ respectively and $E_{\infty Z}(g)$ is the ionisation potential of species Z from its ground level g. The total electron number density can be given by the assumption of plasma quasi-neutrality, i.e.:

$$n_e = \sum_{Z=0}^{Z} Z n_Z \tag{3.6}$$

These four equations, (3.3)-(3.6), describe the state of electrons (free and bound) in an LTE plasma.

3.1.2.2 Corona model

As the plasma density is lowered, the rate of radiative processes becomes comparable or even greater than collisional processes, and only the strongest collisions have any influence on the population densities. To illustrate this we consider the collisional ionisation process and its inverse, three body recombination; the two processes in an LTE plasma must take place at equal rates to maintain equilibrium:

$$S_Z + e \rightleftharpoons S_{Z+1} + e + e \tag{3.7}$$

The ionisation process rate is proportional to the electron number density n_e, while the rate of three-body recombination is proportional to n_e^2. The competing process of radiative recombination for the ions is given by:

$$S_{Z+1} + e \longrightarrow S_Z + h\nu \tag{3.8}$$

The reaction proceeds at a rate proportional to n_e, thus at sufficiently low plasma density radiative recombination becomes more significant than three body recombination.

Hence for a low density plasma the equilibrium is between radiative recombination (and spontaneous radiative decay) and ionisation (and excitation) by electron collision. Because the plasma is optically thin, the radiation density is low and thus

the radiative excitation/ionisation processes are neglected. A plasma where such conditions are satisfied is described as a corona model plasma.

The equations describing the corona model are described below:

(a) The free electrons are again assumed to obey a Maxwellian distribution, i.e. equation (3.3) also applies here.

(b) Assuming that the number density of ions in the excited states is negligible when compared to their densities in the ground state, the ionisation and radiative recombination equilibrium can be described with:

$$n_e n_Z(g) S_{Z,g\to\infty} = n_e n_{Z+1}(g) \alpha^{RR}_{z+1,g} \tag{3.9}$$

or equivalently:

$$\frac{n_Z(g)}{n_{Z+1}(g)} = \frac{\alpha^{RR}_{z+1,g}}{S_{Z,g\to\infty}} \tag{3.10}$$

where $S_{Z,g\to\infty}$ is the collisional ionisation coefficient for an atom of charge Z from the ground level to the continuum and $\alpha^{RR}_{z+1,g}$ is the radiative recombination coefficient (the equations describing these coefficients are given in section 3.1.2.4). Interestingly, this shows that, in contrast to the LTE case, described by the Saha equation, the ionisation ratio in a coronal plasma is independent of electron density.

(c) The population densities of the excited levels are given by the equilibrium between the rate of collisional excitation and the rate of spontaneous radiative decay:

$$n_e n_Z(g) X_{g\to p} = n_Z(p) \sum_{q<p} A(p,q) \tag{3.11}$$

or equivalently:

$$\frac{n_Z(p)}{n_Z(g)} = \frac{n_e X_{g\to p}}{\sum_{q<p} A(p,q)} \tag{3.12}$$

where $X_{g\to p}$ is the collisional excitation coefficient from the ground level to level p. $A(p,q)$ is the atomic transition probability for a radiative transition between

levels p and q, which is summed for all the levels between level p and ground to give the total radiative transition probability out of the p level.

3.1.2.3 Validity criteria

The validity criteria for each model are determined by the atomic processes that determine the thermodynamic equilibrium:

The major conditions for the existence of a plasma LTE are that:

- The free electrons have to have a Maxwellian velocity distribution.
- The equilibrium is created exclusively by electron collisions, implying that the collision rate is much greater than the rate of radiative decay.

The above are necessary but not however sufficient conditions for the existence of a plasma in LTE, for example if the electron temperature changes too rapidly, the plasma will fail to achieve LTE even if the above conditions were satisfied [65].

The major conditions for the existence of a plasma in corona equilibrium are that:

- The free electrons are again assumed to follow a Maxwellian distribution
- The collisional de-excitation (and three-body recombination) rate is negligible, so that the only mechanism of decay is by the emission of radiation.

Validity of the assumption of a Maxwellian electron population in a hollow cathode plasma

The free electrons in a hollow cathode can be assumed to be Maxwellian when two conditions are satisfied. The first is that the Spitzer electron-electron relaxation time t_{ee} is less than the energy decay time for continuum radiation t_{rad}. t_{rad} is given by the ratio of energy density to the bremsstrahlung emission coefficient for a fully ionised plasma. The above condition gives rise to the following inequality [173, 101]:

$$\frac{0.3\ T_e^{3/2}}{n_e\ ln\Lambda} << 1.4\times10^{11}\frac{T_e^{1/2}}{n_e} \qquad (3.13)$$

or $$T_e << 5\times10^{11}\ ln\Lambda$$

Where T_e is in °K and $ln\Lambda$ is a slowly varying function of n_e and T_e of the order of 10. Thus, it can be expected that the electrons will have a Maxwellian electron distribution if $T_e << 5\times10^{12}$ °K, a condition invariably satisfied under all possible conditions of hollow cathode operation.

The second condition is that $t_{ee} << t_{cont}$, where t_{cont} is the particle containment time. Following the analysis in reference [116] for the conditions expected in the HC (1eV, 10^{14}cm^{-3}), the drift velocity can be taken as ~10^6cm/s. This implies t_{cont} in a cathode of 1cm length is 10^{-6}s, compared to t_{ee} ~ 10^{-10}s.

Since these two conditions are satisfied in the HC internal plasma, the free electrons can be assumed to possess a Maxwellian velocity distribution. It has to be mentioned here that attempting to incorporate the non-Maxwellian, mono-energetic electron beam accelerated through the sheath potential would result in significant complication of the plasma model.

Range of validity of the LTE and corona plasma models

As stated above, for LTE to be applicable, collisional processes must dominate radiative processes. McWhirter [65], suggested that this would occur when the collisional de-excitation rate is at least an order of magnitude greater than the radiative decay rate, i.e. for all levels p and q:

$$n_e n_Z(p) X_{p\to q} \geq 10 n_Z(p) A(p,q) \qquad (3.14)$$

where $X_{p\to q}$ is the de-excitation coefficient between levels p and q and is given by (in units of cm^{3}sec^{-1}):

$$X_{p\to q} = \frac{6.5\times10^{-4}}{(E(p)-E(q))T_e^{1/2}} f(q,p) exp\left(-\frac{(E(p)-E(q))}{kT_e}\right) \qquad (3.15)$$

$(E(p)-E(q))$ represents the excitation potential of level p from level q (in eV), T_e is in units of °K and $f(q,p)$ is the absorption oscillator strength. The criterion (equation (3.14)) can be reduced by relating the radiative transition probability to the absorption oscillator strength giving (n_e is in units of cm^{-3}):

$$n_e \geq 1.6\times10^{12} T_e^{1/2} (E(p)-E(q))^3 \qquad (3.16)$$

For the plasma to be represented by a corona model, the only mechanism of de-excitation (and recombination) must be by radiative processes and collisional de-excitation processes must be negligible. McWhirter [65] expresses this condition by:

$$\sum_{s<p}^{g} A(p,s) \geq n_e X_{q\to p} \qquad (3.17)$$

It has to be noted that in equation (3.17) there is always a value of p for which this criterion is not satisfied regardless of how low the density is. This is because as the quantum number increases the probability of radiative decay decreases and that of the collisional process increases. A value of $p = 6$ is usually selected [65] for hydrogenic atoms, where the value of $\sum A$ in the inequality can be calculated from tabulated values for hydrogen like ions.

A simpler condition for the corona model was given by Wilson [173]. As the quantum number for a level increases, the probability of collisional processes becomes greater and the probability of radiative processes decreases. Defining a level p^* above which all levels are in LTE, the corona model is satisfied when the rate coefficients α_{p*} and S_{p*} for the LTE levels are ten times smaller than the corresponding rate coefficients for the continuum. This condition is described by:

$$n_e \leq 1.5\times10^{10} (kT_e)^4 (E(p)-E(q))^{-1/2} \qquad (3.18)$$

For the hollow cathode plasma studied in this work, three gases were subjected to spectroscopic analysis, namely argon, krypton and xenon. Applying the validity conditions, equations (3.16) and (3.18), and using [173, 115] $E(p)-E(q)=E_\infty(g)$ the ionisation potential of the gas (12.13, 14 and 15.76eV for Xe, Kr and Ar respectively) the validity limit curves shown in figure 3.2 were constructed. They show, for all

gases, that the LTE model is applicable at electron densities above $10^{17}cm^{-3}$, and the corona model is applicable only for electron densities below $10^{11}\ cm^{-3}$.

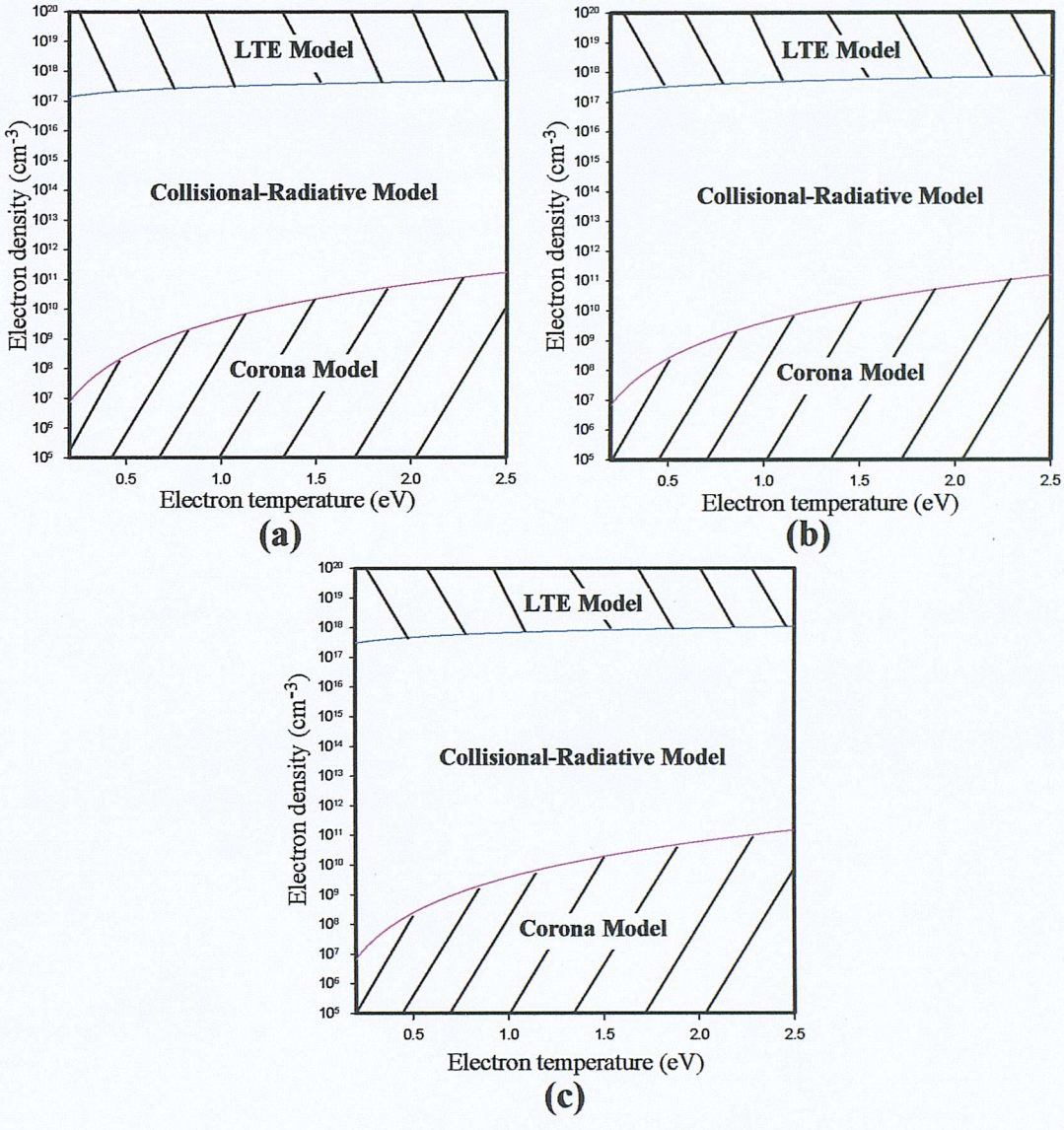

Figure 3.2: Validity limits of LTE and corona models for **(a)** *xenon,* **(b)** *krypton, and* **(c)** *argon plasma*

In a typical ion thruster hollow cathode the plasma parameters are expected to be T_e= 1eV and $n_e \approx 10^{14}cm^{-3}$ [101, 115], so from the validity conditions it is apparent that the cathode is neither in LTE nor in coronal equilibrium for all the gases to be investigated, in agreement with Monterde's [115, 116] conclusion on xenon. Thus the condition in the hollow plasma requires description by a model in-between the LTE and corona domains. Such a model is known as a collisional-radiative model and is the subject of section 3.1.2.4.

HC plasma optical depth

The implicit assumption of a plasma that is optically thin to all frequencies above the plasma frequency, which underpinned the previous discussion of plasma models, is assessed in this section. Radiation produced in the plasma interior interacts with the plasma on its way to the plasma edge. This modifies the population densities of the various energy levels and the observed intensity is then not simply a sum of intensities from infinitesimal volume elements.

The equation for radiative transfer gives the rate of change of radiation intensity $I(\nu,x)$ with respect to distance as [24]:

$$\frac{dI}{dx} = -I(\nu,x)\chi(\nu,x) + J(\nu,x) \tag{3. 19}$$

where $I(\nu,x)\chi(\nu,x)$ represents the decrease in intensity by absorption over a distance dx with $\chi(\nu,x)$ being the absorption coefficient. And the increase in intensity over a distance dx is represented by $J(\nu,x)$ the emission coefficient. Equation (3.19) can be expressed in terms of the optical depth (τ) given by:

$$\tau(\nu,x) = \int_0^D \chi(\nu,x)dx \tag{3. 20}$$

Equation (3.19) can thus be re-written as:

$$\frac{dI}{d\tau} = -I(\nu,x) + \frac{J(\nu,x)}{\chi(\nu,x)} \tag{3. 21}$$

where the ratio $J(\nu,x)/\chi(\nu,x) = S(\nu,x)$ is known as the source function.

The optical depth (τ) defines the criteria for optical thickness of the plasma. When $\tau >> 1$, the plasma is optically thick, and the region of the plasma from which radiation escapes becomes more and more concentrated at a progressively thinner layer at the plasma surface. So that finally the observed intensity of a given emission line is defined solely by the temperature at the surface and the intensity approaches that of a blackbody at the same surface temperature. Assuming a uniform plasma, we

can define the mean optical depth ($\bar{\tau}_o$) at the central frequency of the emission line at ν_o by:

$$\bar{\tau}_o = \chi(\nu_o)D \tag{3.22}$$

where $\chi(\nu_o)$ is the absorption coefficient at the line centre and D is a characteristic linear dimension generally taken to be half the shortest dimension of the plasma [65, 94], for a cylindrical plasma case (as in the hollow cathode), D is given by the radius of the cylinder [12, 161].

Griem [59] gives an approximate relation for the optical depth in terms of the angular frequency ω for discrete line emission, neglecting the effect of induced emission:

$$\bar{\tau}_o \approx 2\pi^2 r_o c\, f_{pq} L_{pq}(\omega) N_i D \tag{3.23}$$

where r_o is the classical electron radius ($\approx 2.818\times10^{-15}$m), c is the speed of light, N_i is the ground state density averaged over the line of sight. f_{pq} is the oscillator strength for a line of wavelength λ, given by the relation:

$$f_{pq} = 1.499\times10^{-8}\lambda^2 \frac{g(p)}{g(q)} A(p,q) \tag{3.24}$$

All that is left now for us to estimate $\bar{\tau}_o$, is determining the line shape factor $L(\omega)$. Which, for a Doppler broadened emission line in a Maxwellian plasma, has a peak value at the line centre given by (3.25) [59] (for a discussion of spectral line profiles and broadening mechanisms refer to appendix C):

$$L(\omega_{pq}) = \left(\frac{Mc^2}{2\pi kT_i}\right)^{1/2} \frac{1}{\omega_{pq}} \tag{3.25}$$

ω_{pq} is the emission line frequency, M is the radiator mass and T_i is the ion temperature. Combining equations (3.23) and (3.25) and simplifying gives [59]:

$$\bar{\tau}_o \lesssim 4.7515\times10^{-3}\left(\frac{1}{kT_i}\right)^{1/2} \frac{f_{pq}}{\omega_{pq}} N_i D \tag{3.26}$$

For a plasma to be considered optically thin, the absorbed radiation must be less than

10% of the emitted intensity [24, 115]. Cooper [24] expresses this condition for any given wavelength as $\tau < 0.2$. Substituting in equation (3.26) the conditions expected in a hollow cathode: $N_i = 10^{20} m^{-3}$, D =1mm (internal radius of the T6 cathode), two values were used for the ion temperature: T_i = 1eV where it is assumed to be equal to the electron temperature, and T_i = 0.1eV where it is assumed to be equal to the cathode wall temperature, the real value of T_i is expected to lie somewhere between these two extremes. This was used to construct table 3.1, in which the optical depth for xenon, argon and krypton first ionisation and neutral excitation lines were calculated. From inspection of table 3.1 it can be concluded that Cooper's validity criterion is satisfied by the entire line spectrum used in this work and that the hollow cathode plasma is indeed optically thin.

Element	Wavelength (nm)	f_{pq}	$\bar{\tau}_o$ (T_i=T_s=0.1eV)	$\bar{\tau}_o$ (T_i=T_e=1eV)
XeII	418.010	0.576	0.188974	0.0608
	433.052	0.525	0.178282	0.0573
	441.480	0.292	0.101194	0.0325
	460.300	0.260	0.09405	0.0302
XeI	450.100	1.13×10^{-3}	3.99×10^{-4}	1.28×10^{-4}
	452.470	6.45×10^{-4}	2.29×10^{-4}	7.36×10^{-5}
KrII	425.058	0.0325	0.010838	3.49×10^{-3}
	429.2923	0.265	0.08932	0.0287
	435.5477	0.379	0.129559	0.0417
	443.1685	0.530	0.184247	0.0592
	443.6812	0.390	0.135584	0.0436
	458.2978	0.160	0.057357	0.0184
KrI	427.3969	7.12×10^{-3}	2.39×10^{-3}	7.68×10^{-4}
	436.2641	1.44×10^{-3}	4.92×10^{-4}	1.58×10^{-4}
	437.6121	5.36×10^{-3}	1.84×10^{-3}	5.92×10^{-4}
	439.9965	9.67×10^{-3}	3.34×10^{-3}	1.07×10^{-3}
	441.03685	1.28×10^{-3}	4.44×10^{-4}	1.43×10^{-4}
	445.3917	3.87×10^{-3}	1.35×10^{-3}	4.34×10^{-4}
	446.3689	6.87×10^{-3}	2.41×10^{-3}	7.74×10^{-4}
	450.2353	4.66×10^{-3}	1.65×10^{-3}	5.29×10^{-4}
ArII	401.3856	0.025361	7.985×10^{-3}	2.568×10^{-3}
	405.292	0.329984	0.104913	0.033736
	407.2004	0.144177	0.046055	0.01481
	407.9573	0.019794	6.335×10^{-3}	2.037×10^{-3}
	408.2387	7.246×10^{-3}	2.32×10^{-3}	7.46×10^{-4}
	413.1723	0.108769	0.035254	0.011336
	427.7528	0.146297	0.049091	0.015786
	434.8064	0.442527	0.15094	0.048537
	435.2205	0.060201	0.020553	6.609×10^{-3}
	436.2066	0.023534	8.053×10^{-3}	2.59×10^{-3}
	437.5954	0.029425	0.010101	3.248×10^{-3}
	437.9666	0.288714	0.099192	0.031897
	440.0986	0.066204	0.022856	7.35×10^{-3}
	442.6001	0.359906	0.124959	0.040182
	447.4759	0.043527	0.015279	4.913×10^{-3}
	448.181	0.137016	0.048172	0.01549
	454.5052	0.145865	0.052007	0.016723
	457.9349	0.251507	0.090349	0.029053
	458.9898	0.31457	0.113263	0.036421
	460.9567	0.335111	0.121176	0.038966
ArI	415.8591	3.63×10^{-3}	1.18×10^{-3}	3.81×10^{-4}
	418.1884	4.41×10^{-3}	1.45×10^{-3}	4.65×10^{-4}
	419.8317	2.26×10^{-3}	7.46×10^{-4}	2.40×10^{-4}
	420.0675	3.58×10^{-3}	1.18×10^{-3}	3.79×10^{-4}
	425.9362	3.61×10^{-3}	1.21×10^{-3}	3.88×10^{-4}
	427.2169	2.18×10^{-3}	7.31×10^{-4}	2.35×10^{-4}
	430.0101	1.74×10^{-3}	5.88×10^{-4}	1.89×10^{-4}
	451.0733	1.20×10^{-3}	4.25×10^{-4}	1.37×10^{-4}

Table 3.1: Optical depth of xenon, krypton & argon first ionisation and neutral excitation lines assuming Doppler line broadening

3.1.2.4 Collisional- Radiative (C-R) model

The collisional-radiative model attempts to tackle some of the constraints in the corona model. Specifically, in the C-R model the possibility of stepwise collision processes causing transitions in upper levels (including three-body recombination) is included in the plasma model. The plasma is still assumed to have negligible radiation trapping, i.e. it is optically thin. For a plasma described by a C-R model the following assumptions apply [65]:

(a) The free electrons follow a Maxwellian velocity distribution given by equation (3.3).

(b) Ionisation proceeds by electron collision from any bound level of the atom or ion. This is balanced by three-body recombination and radiative recombination into any bound level. The rate of collisional ionisation out of any bound level p of an atom/ion (process (ii) in section 3.1.2) is given by $n_e\, n_Z(p)\, S_{Z,p\to\infty}$ cm^{-3}s^{-1}, where $S_{Z,p\to\infty}$ is the collisional ionisation coefficient for an atom of charge Z from the p level to the continuum. The rate of three-body recombination from a ground state ion of charge Z+1 to an excited (in a quantum level p) atom/ion of charge Z is given by $n_e^2\, n_{Z+1}(g)\, \alpha^3_{Z+1,g}$ cm^{-3}s^{-1}, where $\alpha^3_{Z+1,g}$ is the three-body recombination coefficient for a ground state ion recombining with a free electron to form an excited atom/ion in an excited level p.

(c) Collisions with free electrons induce transitions between pairs of bound levels, the rate of collisional de-excitation out of any level p is given by $n_e\, n_Z(p) X_{Z,p\to q}$ cm^{-3}s^{-1}.

(d) The sources for radiative emission from the plasma are: (1) Spontaneous decay from an excited level p to a lower lying energy level q (process (vii) section 3.1.2), the rate for this process is defined by $n_Z(p) A_{p\to q}$ cm^{-3}s^{-1}, and (2) Radiative recombination with a free electron performing a collisionless transition to a bound level p (process (iii) section 3.1.2), whose rate is given by $n_e\, n_{Z+1}(g)\, \alpha^{RR}_{z+1,g}$ cm^{-3}s^{-1}.

The above assumptions form the basis for the construction of a quantitative description of the rates at which the bound levels are populated. For any level p, the rate of change of the population density of level p is given by:

$$\frac{dn_Z(p)}{dt} = -\eta + \kappa \tag{3.27}$$

η is the rate of destruction of species of charge Z in quantum level p by collisional ionisation out of level p, collisional excitation/de-excitation out of level p and radiative spontaneous decay out of level p into a lower lying level q. κ is the rate of production of species in a quantum level p due to radiative recombination into the p level, collisional excitation/de-excitation into level p and three-body recombination into level p. Substituting the rate equations for these various processes into (3.27), we arrive at:

$$\frac{dn_Z(p)}{dt} = -n_Z(p)\left\{n_e S_{Z,p\to\infty} + n_e \sum_{q\neq p} X_{Z,p\to q} + \sum_{q<p} A(p,q)\right\} + n_e \sum_{q\neq p} n_Z(q)\, X_{Z,q\to p}$$
$$+ \sum_{q>p} n_Z(q)\; A(q,p) + n_e n_{Z+1}(g)\;\left\{n_e \alpha^3_{Z+1,p} + \alpha^{RR}_{Z+1,p}\right\} \tag{3.28}$$

The summations are taken for all possible q within the indicated limits. The above equation is applied to all p levels and this leads to an impractically large number of simultaneous differential equations to be solved over an equally large summation over q levels. However, one advantage of the C-R model is that, as the quantum number of the energy level increases, the spacing between the energy levels becomes closer. This leads to the probability of the collisional processes becoming greater and the probability of radiative processes becoming smaller. Thus, there will always exist an energy level above which the radiative processes can be neglected and the population densities can be described by a modified form of the Saha equation:

$$\frac{n_e n_{Z+1}(g)}{n_Z(p)} = \frac{g_{Z+1}(g)}{g_Z(p)} 2\left(\frac{2\pi m_e kT_e}{h^2}\right)^{3/2} exp\left(-\frac{E_{\infty Z}(p)}{kT_e}\right) \tag{3.29}$$

with $E_{\infty Z}(p)$ being the ionisation potential of a species of charge Z from level p, where $p > p_s$ the level above which the modified Saha equation can be used.

Consideration of the relaxation times for the population densities reveals that the relaxation times associated with ground level populations are orders of magnitude larger than those for inter-excited level transitions [65]. Thus the transitions between excited bound levels can be considered instantaneous when compared to the observation time (negligible numbers of atoms/ions are in their excited levels when compared with the ground level) and only processes involving ground level populations need be considered [115]. Hence, the processes that need to be considered are reduced to:

- Collisional ionisation out of ground state $S_Z(g)+e \rightarrow S_{Z+1}+e+e$
- Three-body recombination into ground state $S_{Z+1}+e+e \rightarrow S_Z(g)+e$
- And radiative recombination into ground state $S_{Z+1}+e \rightarrow S_Z(g)+h\nu$

Collisional excitation/de-excitation and spontaneous radiative transition processes are neglected. This is known as the "ladder approximation" [115].

For a pure (single gaseous element) plasma composed of free electrons, neutral atoms (denoted by the subscript I), ions in the first ionisation stage (II) and ions in the second ionisation stage (III), the population rate equation (3.28) can be simplified to:

$$\begin{aligned}
\frac{dn_{I,g}}{dt} &= -S_{I\rightarrow II}n_e n_{I,g} + \alpha^{RR}_{II\rightarrow I}n_e n_{II,g} + \alpha^{3}_{II\rightarrow I}n_e^2 n_{II,g} \\
\frac{dn_{II,g}}{dt} &= S_{I\rightarrow II}n_e n_{I,g} - \alpha^{RR}_{II\rightarrow I}n_e n_{II,g} - \alpha^{3}_{II\rightarrow I}n_e^2 n_{II,g} - S_{II\rightarrow III}n_e n_{II,g} \\
&\quad + \alpha^{RR}_{III\rightarrow II}n_e n_{III,g} + \alpha^{3}_{III\rightarrow II}n_e^2 n_{III,g} \\
\frac{dn_{III,g}}{dt} &= S_{II\rightarrow III}n_e n_{II,g} - \alpha^{RR}_{III\rightarrow II}n_e n_{III,g} - \alpha^{3}_{III\rightarrow II}n_e^2 n_{III,g}
\end{aligned} \tag{3.30}$$

Empirical relations for the collisional ionisation coefficient (S) and the radiative recombination coefficient (α^{RR}) were derived by McWhirter [65]:

$$S_{Z\rightarrow Z+1} = 2.34\times10^{-7}\frac{\zeta_Z T_e^{1/4}}{E_{\infty Z}(g)^{7/4}}\exp\left(-\frac{E_{\infty Z}(g)}{kT_e}\right)\ (\mathrm{cm^3\,s^{-1}}) \tag{3.31}$$

$$\alpha^{RR}_{Z+1\rightarrow Z} = 2.05\times10^{-12}\frac{E_{\infty Z}(g)}{T_e^{1/2}}\ (\mathrm{cm^3\,s^{-1}}) \tag{3.32}$$

And the three-body recombination coefficient (α^3) is defined by Elwert [36] as:

$$\alpha^3_{Z+1\to Z} = 3.9\times10^{-28}\frac{\xi_{Z+1}}{E_{\infty Z}(g)^{7/4}(kT_e)^{5/4}} \quad (\mathrm{cm^6\,s^{-1}}) \tag{3.33}$$

where ζ_Z is the number of electrons in the outermost occupied shell (n^*) of species Z and ξ_{Z+1} represents the number of vacancies in the last shell, its value is given by the equation $\xi_{Z+1} = 2(n^*)^2 - \zeta_{Z+1}$. The parameters $E_{\infty Z}(g), \xi_{Z+1}$ and ζ_Z are evaluated in table 3.2 for neutral, first stage ionisation and second stage ionisation species of the rare gases used in this work. As can be seen from equations (3.31)-(3.33) the rate coefficients are functions of the electron temperature and atomic constants only. Although the equations have been designed for hydrogen and hydrogen like ions, the collisional ionisation coefficient has shown fair agreement with published data [63].

Element	$E_{\infty Z}(g)$ (eV)	ζ_Z	ξ_Z
XeI	12.128	8	42
XeII	21.2098	7	43
XeIII	32.1230	6	44
KrI	13.9996	8	24
KrII	24.3599	7	25
KrIII	36.950	6	26
ArI	15.7596	8	10
ArII	27.6297	7	11
ArIII	40.74	6	12

Table 3.2: Atomic properties of the propellant gas atoms and ions

Population equations

The simultaneous equations designated equation (3.30) can be coupled to the condition for plasma quasi-neutrality:

$$n_e = n_{II} + 2n_{III} \tag{3.34}$$

to form a system of 4 equations with 4 unknowns (namely: n_e, n_I, n_{II} & n_{III}) and a free parameter T_e which determines the rate coefficients.

In a steady state situation where the population densities can be assumed to remain constant over the observation period, the population rate $\frac{dn_z}{dt} = 0$. The system of equations (3.30) can be rewritten as [115]:

$$
\begin{aligned}
&-S_{I\to II} n_e n_{I,g} + \alpha^{RR}_{II\to I} n_e n_{II,g} + \alpha^{3}_{II\to I} n_e^2 n_{II,g} = 0 \\
&S_{I\to II} n_e n_{I,g} - \alpha^{RR}_{II\to I} n_e n_{II,g} - \alpha^{3}_{II\to I} n_e^2 n_{II,g} - S_{II\to III} n_e n_{II,g} + \alpha^{RR}_{III\to II} n_e n_{III,g} \\
&+ \alpha^{RR}_{III\to II} n_e n_{III,g} + \alpha^{3}_{III\to II} n_e^2 n_{III,g} = 0 \\
&S_{II\to III} n_e n_{II,g} - \alpha^{RR}_{III\to II} n_e n_{III,g} - \alpha^{3}_{III\to II} n_e^2 n_{III,g} = 0
\end{aligned}
\qquad (3.35)
$$

This can be simplified and solved for n_I, n_{II} & n_{III} in terms of T_e and n_e, thus giving:

$$
\begin{aligned}
n_{I,g} &= \frac{\left(\alpha^{RR}_{II\to I} + n_e \alpha^{3}_{II\to I}\right)}{S_{I\to II}} n_{II,g} \\
n_{II,g} &= \frac{n_e \left(\alpha^{RR}_{III\to II} + n_e \alpha^{3}_{III\to II}\right)}{2S_{II\to III} + \alpha^{RR}_{III\to II} + n_e \alpha^{3}_{III\to II}} \\
n_{III,g} &= \frac{n_e - n_{II,g}}{2}
\end{aligned}
\qquad (3.36)
$$

Figure 3.3 shows the ratio of the population densities of the various xenon species to the total number density (given by $n_T = n_I + n_{II} + n_{III}$) for a range of electron temperatures at $n_e = 10^{14}\,\mathrm{cm}^{-3}$. The figure shows that, for the range of temperatures expected in the hollow cathode, the plasma will consist primarily of atoms in the neutral or first stage of ionisation. This is consistent with the spectroscopic results of this work where XeIII, KrIII and ArIII lines were absent from the spectra. We note however, that although this is in agreement with previous spectroscopic studies on xenon and mercury [101, 115, 116, 146], there is some evidence [202] indicating the presence of XeIII ions in a HC discharge.

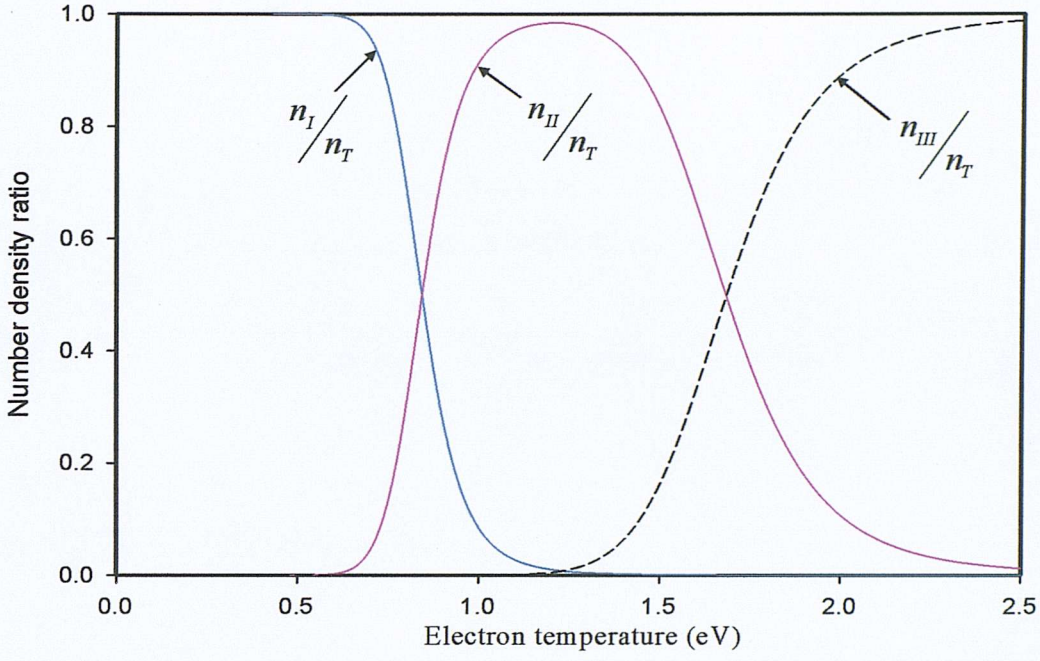

Figure 3.3: Ratio of number densities from theoretical model for $n_e=10^{14}$ cm^{-3}

3.1.3 Spectroscopic methods for plasma parameter evaluation

The purpose of the previous sections was to outline theoretical models for the plasma, this has lead to the selection of the collisional-radiative model as the one most suited to the conditions in the hollow cathode. The objective of this section is to relate the experimentally observable quantities, through the plasma model, to the plasma parameters of T_e and n_e. Three methods of plasma parameter evaluation were applied and are here outlined.

3.1.3.1 Ratio of line intensities

For an optically thin plasma, the spectrally integrated emission line intensity $I(p,q)$ (which will be called 'intensity' for short) arising from a bound-bound transition between levels p and q is given by:

$$I(p,q) = \frac{h\nu_{pq}}{4\pi} A(p,q) \int_0^l n(p)\, dx \tag{3.37}$$

The integration is taken over the depth of plasma (l) viewed by the detector. Assuming a homogeneous plasma, equation (3.37) becomes:

$$I(p,q) = \frac{h\nu_{pq}}{4\pi} A(p,q)\ n(p)\ l \tag{3.38}$$

Ratio of lines of the same species

The ratio of two lines of the same atom/ion produced by transitions from upper levels p and p' to levels q and q' respectively is given by:

$$\frac{I_Z(p,q)}{I_Z(p',q')} = \frac{\lambda_{p'q'}}{\lambda_{pq}} \frac{A(p,q)}{A(p',q')} \frac{n_Z(p)}{n_Z(p')} \tag{3.39}$$

substituting the emission line frequency (ν_{pq}) in equation (3.38) by the emission line wavelength (λ_{pq}). The ratio of the two populations can be given by the modified Saha equation for the collisional-radiative model (equation (3.29)) for levels $p > p_s$ giving:

$$\frac{I_Z(p,q)}{I_Z(p',q')} = \frac{\lambda_{p'q'}}{\lambda_{pq}} \frac{A(p,q)}{A(p',q')} \frac{g_Z(p)}{g_Z(p')} exp\left(-\frac{E(p) - E(p')}{kT_e}\right) \tag{3.40}$$

The electron temperature corresponding to a given line ratio is thus [59]:

$$kT_e = \frac{E(p) - E(p')}{ln\left(\frac{I_Z(p',q')\ \lambda_{p'q'}\ A(p,q)\ g_Z(p)}{I_Z(p,q)\ \lambda_{pq}\ A(p',q')\ g_Z(p')}\right)} \tag{3.41}$$

This method allows for determination of T_e without prior knowledge of electron number density. The accuracy of the temperature estimate requires that the two upper energy levels be separated by as large an energy difference as possible, as the transition probabilities are only known to an uncertainty of $\leq 50\%$. It is however

difficult to increase the energy difference between the selected line upper levels beyond a few eVs in the limited observation range.

For a plasma in LTE, the accuracy of the above method can be greatly enhanced by use of a "Boltzmann plot". In a Boltzmann plot, we plot $ln(I_Z(p,q)\lambda_{pq}/[g_Z(p)A(p,q)])$ as a function of the excitation energy of the upper levels $E_Z(p)$. If the resulting data fall close to a straight line, a more accurate estimate of T_e can be obtained from the slope of the line, which is equal to $(-1/kT_e)$. Any appreciable deviation from this linear behaviour would indicate departure from LTE. The Boltzmann plot method is well established for estimating T_e for LTE plasmas (see for example [59, 71, 118, 165, 174]), but has apparently not been extended to plasmas in the C-R regime, it will be shown here that this method can indeed be applied to C-R plasmas to yield excellent results, thus constituting an interesting feature of this work.

Taking the intensity of an emission line (equation (3.38)) and substituting for the population number density using the modified Saha equation (3.29) for the C-R model gives:

$$I_Z(p,q)=\frac{h}{4\pi}\frac{c}{\lambda_{pq}}A(p,q)\frac{n_{Z+1}(g)\,n_e}{2}\left(\frac{2\pi m_e kT_e}{h^2}\right)^{-3/2}\frac{g_Z(p)}{g_{Z+1}(g)}\exp\left(\frac{E_{\infty Z}(g)-E_Z(p)}{kT_e}\right)l \qquad (3.42)$$

Taking the natural logarithm of both sides of (3.42) gives:

$$\ln\left(\frac{I_Z(p,q)\lambda_{pq}}{A(p,q)g_Z(p)}\frac{8\pi\, g_{Z+1}(g)}{hc\,n_e\,n_{Z+1}(g)\,l}\left(\frac{2\pi m_e kT_e}{h^2}\right)^{3/2}\right)=\frac{E_{\infty Z}(g)-E_Z(p)}{kT_e} \qquad (3.43)$$

The HC plasma is in steady state and will be under the same discharge conditions (anode current and flow rate) for the length of the observation time. Realising that for such a plasma, the electron temperature, electron density and population density of ground state ions of the next ionisation stage ($n_{Z+1}(g)$) will all be constant for a given spectrum throughout the observation time. We can thus rearrange equation (3.43) into:

$$\ln\left(\frac{I_Z(p,q)\lambda_{pq}}{A(p,q)g_Z(p)}\right) = -\frac{E_Z(p)}{kT_e} + \left[\frac{E_{\infty Z}(g)}{kT_e} - \ln\left(\frac{8\pi\, g_{Z+1}(g)}{hcn_e n_{Z+1}(g)\, l}\left(\frac{2\pi m_e kT_e}{h^2}\right)^{3/2}\right)\right] \tag{3.44}$$

By inspection of equation (3.44), we can now recognise that, for a plasma in the C-R regime, if we plot $ln(I_Z(p,q)\lambda_{pq}/[A(p,q)g_Z(p)])$ as a function of energy of the upper level $E_Z(p)$, we will obtain a line whose slope is $(-1/kT_e)$ and whose intercept is given by the term in the square brackets on the right hand side of equation (3.44).

Applying the Boltzmann plot method to a C-R plasma involves the implicit assumption that the modified Saha equation, which is used to derive it, is applicable. The modified Saha equation can only be used for levels p greater than p_s, where p_s can be thought of as a "thermal limit" where the levels above can be envisaged as being in thermal equilibrium with the continuum due to the increased collisional transition rates between the upper levels and free electrons. A great feature of this method is that it is self-consistent, i.e. if the upper levels were not high enough for the modified Saha equation to apply, we will experience large deviations from the expected linear behaviour and a value for T_e will not be obtained.

Ratio of lines of the same element at different stages of ionisation

Another approach to improve the accuracy of the temperature measurement is to use the ratio of lines from two different ionisation stages, as their upper level energies can be very different and yet lie in the same region of the spectrum. This is the approach used by Monterde for evaluation of plasma parameters in UK-25 HC operating on xenon [115,116].

The ratio of the line intensity $(I_{II}(p,q))$ produced by ionic species (at the first ionisation stage) undergoing a $p \rightarrow q$ transition to that of atomic species $(I_I(p',q'))$ undergoing a $p' \rightarrow q'$ transition is given by:

$$\frac{I_{II}(p,q)}{I_I(p',q')} = \frac{\lambda_{p'q'}}{\lambda_{pq}} \frac{A(p,q)}{A(p',q')} \frac{n_{II}(p)}{n_I(p')} \tag{3.45}$$

For a C-R plasma the modified Saha equation can now be used to obtain the excited level population in terms of the ground state population of species in the next stage of ionisation:

$$\frac{I_{II}(p,q)}{I_I(p',q')} = \frac{\lambda_{p'q'}}{\lambda_{pq}} \frac{A(p,q)}{A(p',q')} \frac{n_{III}(g)}{n_{II}(g)} \frac{g_{II}(p)}{g_I(p')} \frac{g_{II}(g)}{g_{III}(g)} \exp\left(\frac{E_{II\infty}(g) - E_{II}(p) - E_{I\infty}(g) + E_I(p')}{kT_e}\right) \tag{3.46}$$

where $g_{II}(g)$ and $g_{III}(g)$ are the ground state statistical weights, and $E_{II\infty}(g)$ and $E_{I\infty}(g)$ are the ionisation potentials from ground level for the singly and doubly ionised species respectively. Now using the ladder approximation from (3.36) to obtain the ratio of ground state populations, we obtain finally:

$$\frac{I_{II}(p,q)}{I_I(p',q')} = \frac{\lambda_{p'q'}}{\lambda_{pq}} \frac{A(p,q)}{A(p',q')} \frac{g_{II}(p)}{g_I(p')} \frac{g_{II}(g)}{g_{III}(g)} \left(\frac{S_{II\to III}}{n_e \alpha^3_{III\to II} + \alpha^{RR}_{III\to II}}\right) \times \exp\left(\frac{E_{II\infty}(g) - E_{II}(p) - E_{I\infty}(g) + E_I(p')}{kT_e}\right) \tag{3.47}$$

It can be seen here that the resulting ratio of intensity is a function of both n_e and T_e. If either T_e or n_e can be measured independently, correlating the experimental results with equation (3.47), the other parameter can be estimated.

3.1.3.2 Continuum methods

The sources of continuum radiation were discussed in section 3.1.1. With the free electrons possessing a Maxwellian distribution, the major sources of continuum radiation in the VIS/UV region are bremsstrahlung and free-bound (recombination) transitions.

Relative continuum intensities

As described by Malik [101], the plasma electron temperature can be assessed, using the intensity ratio of the bremsstrahlung continuum, by:

$$\ln(I_1/I_2) = -hc\,(1/\lambda_1 - 1/\lambda_2)/kT_e \qquad (3.48)$$

where intensities I_1 and I_2 are taken at wavelengths λ_1 and λ_2 respectively.

The continuum measurements represent however a superposition of the radiation due to both bremsstrahlung and recombination processes. To find the regions of the continuum due to bremsstrahlung, we plot $log(I)$ versus λ. The regions exhibiting a linear decay will be representative of bremsstrahlung [101].

3.2 Electrical breakdown in Gases [22, 162]

Here we give a brief overview of the general theory of electrical breakdown in gases. We assume plane parallel electrodes, with a uniform field $E = V/d$ where d is the gap length and V is the potential difference between the electrodes, and that primary electrons are produced at the cathode with a current density j_o. Due to acceleration by the applied field these electrons are multiplied on their way to the anode by ionising the gas. This is described by the first Townsend coefficient α (= ionisation impacts per unit length traversed by the electron). The ions formed are accelerated by the field in the opposite direction towards the cathode giving an ion current j_i that impacts the cathode surface liberating secondary electrons. This process is described by Townsend's second coefficient γ (= number of electrons liberated per impacting ion). The electron current density leaving the cathode region is thus:

$$j_c = j_o + \gamma \times j_i \tag{3.49}$$

As a consequence of the ionisation multiplication effect, the electron current density reaching the anode is

$$j_a = j_c \, exp(\alpha d) \tag{3.50}$$

in other words each electron produces $exp(\alpha d) - 1$ new electrons in traversing the gap. The ion current density is thus given by:

$$j_i = j_a - j_c \tag{3.51}$$

From equations (3.49)-(3.51) the electron current density at the anode can be obtained by:

$$j_a = \frac{j_o \, exp(\alpha d)}{1 - \gamma[exp(\alpha d) - 1]} \tag{3.52}$$

α is connected to the electron mean free path for ionisation λ_e by the relation:

$$\alpha = \frac{1}{\lambda_e} exp\left(-\frac{V_i}{E\lambda_e}\right) \tag{3.53}$$

λ_e is related to the pressure P (or more appropriately the density $N = P/(kT)$) by the relation $1/\lambda_e = N\sigma_i$ (σ_i is the ionisation cross-section). Equation (3.53) becomes:

$$\frac{\alpha}{P} = A\,exp\left(-\frac{CP}{E}\right) \tag{3.54}$$

where $A = 1/(P\lambda_e) = \sigma_i/(kT)$, and $C = AV_i$.

Breakdown of the gap takes place when there is a sudden, sharp rise in the current of several orders of magnitude at the breakdown voltage. This condition occurs when the denominator of equation (3.52) is zero, i.e. when:

$$\gamma[exp(\alpha d)-1]=1 \tag{3.55}$$

With $E = V/d$, we obtain from (3.54) and (3.55) the breakdown voltage V_{bk} as a function of the product (Pd)

$$V_{bk} = \frac{C(Pd)}{ln\left(\frac{A(Pd)}{ln\left(1/\gamma+1\right)}\right)} \tag{3.56}$$

Equation (3.56) is known as Paschen's law. Figure 3.4 shows experimental results illustrating Paschen's law for various gases [162]. The value of the breakdown voltage minimises for a unique value of (Pd) known as Paschen's minimum, which can be obtained by differentiating equation (3.56) and equating it to zero to give:

$$(Pd)_{min} = \frac{2.718}{A} ln\left(\frac{1}{\gamma}+1\right) \tag{3.57}$$

$$(V_{bk})_{min} = C(Pd)_{min} \tag{3.58}$$

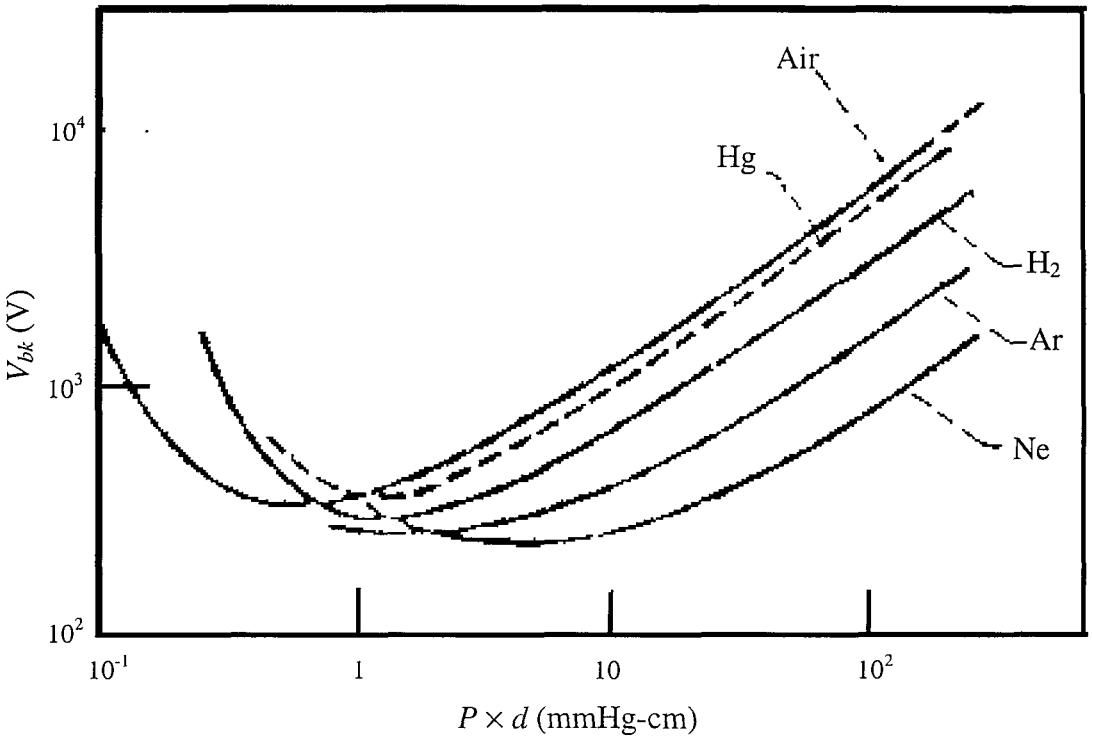

Figure 3.4: Breakdown voltage as a function of ($P \times d$) for several gases [162].

Classical breakdown theory, as described by Paschen's law, is very well understood for plane parallel electrodes with a static gas and uniform pressure profile. But breakdown in an orificed ion thruster hollow cathode differs in several ways [124]:

- The non-planar nature of the geometry
- The high flow velocities
- The high pressure gradient between the electrodes
- The use of a heated cathode with a low work function insert
- The variable surface conditions at the insert due to ion bombardment and Ba loss.

These differences may lead to a departure from the standard Paschen behaviour and hence justify the attempts made in this study to obtain empirical data on HC breakdown and to explain any differences that may arise due to the unique nature of the orificed HC discharge.

3.3 Hollow cathode discharge modelling

A complete analytical description of the phenomena occurring in hollow cathode discharges has been hampered by lack of experimental data and the complexity of the processes involved. Emission from the cathode can take place via several mechanisms (thermionic, field-enhanced thermionic, photo-electric, secondary emission etc..) or even by a combination of these mechanisms. The HC physical surfaces and the interior plasma can interact in complex ways, and in addition, these processes influence the gasdynamics of the flow through the cathode. The development of HC models has attempted to bridge the gap in our understanding, in the absence of a substantial body of experimental data, by making simplifying assumptions to the description of the discharge (for example favouring a certain emission process or assuming a homogeneous HC plasma). The model's predictions of the observed cathode behaviour can be used to indicate the relative importance of the many possible processes in HC discharges.

Any review of theoretical models of hollow cathodes must begin with those presented for the more generic open channel hollow cathode arcs [81]. In 1978 Ferreira and Delcroix [186] proposed what can be considered as the first detailed, self-consistent description of the underlying physics of open channel hollow cathode arcs. Their model describes analytically, for an argon plasma, the gas flow in the cathode, the cathode wall emission mechanism and energy balance, the formation of the plasma and the radial and axial transport of plasma ions and electrons. For an argon plasma, they predict equal contribution to the total discharge current from surface emitted electrons and secondary electrons produced by volume ionisation. Field-enhanced thermionic emission was assumed to be the only mechanism of electron emission from the surface. This assumption, although suitable for orificed hollow cathodes [140, 147], might not be applicable in the open channel case (see Krishnan *et al.* [86]). The model, in spite of its analytical rigour, relies on experimental determination of the cathode wall temperature profile as input to obtain the corresponding surface current density profile. This information is usually not available, and moreover, due to the extreme sensitivity of the current density to wall temperature, any slight error in wall temperature determination will lead to large errors in the calculated current density.

More recently, Kennedy [81] presented a 1-D theoretical model for low-pressure hollow cathode arcs, with the aim of determining the cathode surface current density and wall temperature. The model assumes no net mass flow. For the cathode energy balance he presents arguments similar to Siegfried (see next section) but neglects cathode power gain by excited species and photon flux, and also ignores energy loss by radiation. To achieve an energy balance of the cathode internal plasma, the model uses a differential approach, whereby the cathode region is divided into thin slices of length *dx*, see figure 3.5.

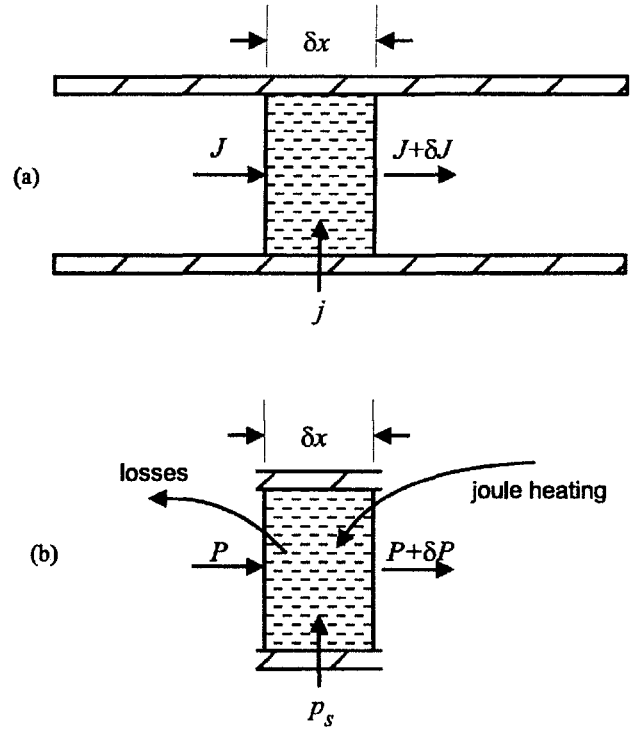

Figure 3.5: Illustration of cylindrical slices of the arc adjacent to HC surface used in the Kennedy model: (a) current balance at steady state, (b) power balance [81].

Kennedy writes for $P(x)$, the power deposited into the volume element at x:

$$\frac{dP}{dx} = (p_{cs} - p_{loss})2\pi R + p_j \qquad (3.59)$$

where p_{cs} is the net power deposited by the cathode surface electrons accelerated by the sheath per unit area, p_{loss} is the power lost by collisions per unit area, p_j is the Joule heating term and R is the cathode radius. Assuming a constant axial electric field, Kennedy formulates an expression for the variation of electron temperature with

x, which can be solved iteratively to obtain the electron temperature $T_e(x)$, the surface current density $j_s(x)$ and also $T_s(x)$ the wall temperature. The model, when compared to experiments, succeeds in predicting the extent of the active zone, which the Ferreira and Delcroix model fails to do. This agreement with experiment is however qualitative, as the predicted current densities were about twice as those measured experimentally [81]. Moreover, the model uses thermionic emission as the surface emission mechanism, and this leads to extremely high cathode temperatures. When using parameters from Fearn and Patterson [44] on the T6, Kennedy predicted wall temperatures in excess of 3000°K for 5-10A discharge currents, which are again approximately twice the expected value.

Moving on to the models specifically designed for orificed hollow cathodes, the model proposed by Siegfried (1984) formed the first and simplest model of underlying physical behaviour, which gave good agreement with the experimental results. It did suffer, however, from some drawbacks which the more recent Salhi-Turchi model attempted to address.

3.3.1 The Siegfried-Wilbur model

Siegfried and Wilbur [145, 146, 147] carried out a series of experimental investigations on orificed hollow cathodes operating on mercury. Based on the experimental results they developed a phenomenological model to describe the electron emission and plasma production processes in the hollow cathode cavity. The most significant processes are shown in figure 3.6.

The surface electrons originate from a narrow band at the downstream end of the insert, the electron emission mechanism is assumed to be field-enhanced thermionic emission. These electrons are accelerated by the cathode sheath gaining enough energy for multi-step ionisation of the gas. Siegfried and Wilbur introduce an idealised ion production region (IPR) (indicated by the dashed lines in figure 3.6),

which they define as the volume circumscribed by the emitting portion of the insert of length L_e, and where the plasma properties are assumed to be uniform.

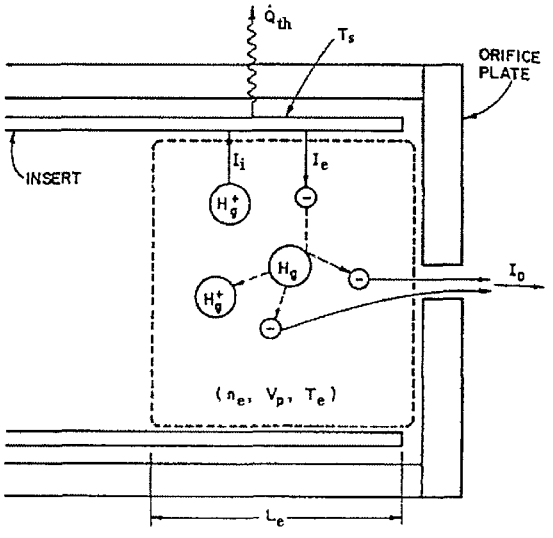

Figure 3.6: Schematic of the ion production region in a hollow cathode operating on Hg, whose boundaries are defined by L_e, the emission length. [145]

The total cathode discharge current I_D is the sum of the electron emission current I_e and the ion current to the surface I_i due to ions produced in the production volume and accelerated through the cathode fall. This ion current provides the energy input to the insert surface necessary to maintain the emission temperature. The current balance is described by equation (3.60).

$$I_D = I_e + I_i = j_{ft} A_e + j_i A_s \tag{3.60}$$

where j_{ft} is the field-enhanced thermionic current density emitted from an insert surface area A_e specified by the emission length L_e and j_i is the Bohm current density of ions crossing the boundary of the IPR of surface area A_s. The surface area of the IPR is given by $A_s = A_e + 2A_c$, where A_c is the area of the end faces of the IPR. Equation (3.60) ignores field emission and secondary emission due to ions, photons and excited states. The model also ignores electron production in the orifice region, which was shown, based on the experimental results, to have a negligible contribution to the total discharge current.

The emission current density j_{ft} from a surface of temperature T_s is given by:

$$j_{ft} = a_o T_s^2 \exp\left(-\frac{e\phi_e}{kT_s}\right) \tag{3.61}$$

where, $a_o = 1.2\times10^6\,\mathrm{Am^{-2}\,{}^oK^{-2}}$ and ϕ_e is the effective surface work function. The effective work function is the surface work function ϕ_s minus the reduction in the work function due to an electric field E_s at the surface due to the presence of the plasma sheath, i.e.:

$$\phi_e = \phi_s - \left(\frac{e|E_s|}{4\pi\varepsilon_o}\right)^{1/2} \tag{3.62}$$

The electric field at the cathode surface is estimated using a double sheath analysis governed by Poisson's equation for a hot cathode emitting thermionic electrons to a plasma. A solution presented by Prewett and Allen [133] was approximated by Siegfried, for conditions in a hollow cathode, to:

$$E_s \approx \left(\frac{n_e kT_e}{\varepsilon_o}\right)^{1/2}\left[2\left(1+2\frac{eV_p}{kT_e}\right)^{1/2}-4\right]^{1/2} \tag{3.63}$$

V_p being the potential drop across the cathode sheath.

An energy balance at the emitting surface is used to estimate the Bohm current density j_i. The balance involves equating the power input due to ion bombardment/neutralisation and de-excitation of excited states to the power loss from the emitting surface by electron emission, conduction and radiation. This is represented by equation (3.64)

$$j_i A_e\left(V_p + V_i - \phi_s\right) + \dot{q}_{dx} A_e + \dot{q}_{ph} A_e = \dot{Q}_{th} + I_e \phi_e \tag{3.64}$$

where V_i is the ionisation potential, the terms $\dot{q}_{dx}A_e$ and $\dot{q}_{ph}A_e$ represent the energy input due to de-excitation of excited atomic states at surface and photon flux to surface respectively. $\dot{Q}_{th}$ is the power loss due to conductive and radiative processes, which is a function of T_s. Siegfried estimates this term for his specific cathode configuration. Neglecting the $\dot{q}_{dx}A_e$ and $\dot{q}_{ph}A_e$ terms (Siegfried estimates the

contribution of the two terms at less than 5% of total current), and expressing j_i in terms of the discharge current I_D, equation (3.64) becomes:

$$j_i = \left(\frac{\dot{Q}_{th}}{\phi_e} + I_D\right) \times \left[2A_c + A_e\left(1 + \frac{\left(V_p + V_i - \phi_s\right)}{\phi_e}\right)\right]^{-1} \tag{3.65}$$

The plasma potential ($=V_p$) can be estimated using an energy balance in the IPR. Energy is convected into and out of the IPR by the various particle species. The particle species do not only transport the energy due to their directed and random kinetic motion across the IPR boundary but they also carry the internal energy due to any excited state they might be in. Assuming the ionised state is the only excited state of consequence and neglecting radiation transport, Siegfried writes for the IPR energy balance:

$$V_p I_e = V_i I_i + \frac{5kT_e}{2e} I_D \tag{3.66}$$

where V_pI_e is the rate of energy input due to surface emitted primary electrons, V_iI_i is the rate of energy loss due to ionised atoms leaving the IPR, and the last term $(5/2)(kT_e/e)I_D$ is the rate of energy loss by convection of Maxwellian electrons through the cathode orifice. Solving (3.66) for V_p we have:

$$V_p = \frac{1}{I_D - j_i A_s}\left(V_i j_i A_s + \frac{5kT_e}{2e} I_D\right) \tag{3.67}$$

To estimate n_e we assume quasi-neutrality ($n_e \approx n_i$), a uniform plasma density throughout the IPR and that the ions leave the IPR at the Bohm velocity. This leads to equation (3.68):

$$j_i = n_e e\left(\frac{kT_e}{m_i}\right)^{1/2} \tag{3.68}$$

The total pressure at any point in the hollow cathode cavity is the sum of the partial pressures of each species. To estimate the total neutral density (n_o) in the hollow cathode cavity we use the ideal gas law, assuming quasi-neutrality and the ions and neutrals to be in equilibrium at the insert temperature:

$$P = n_e kT_e + kT_s(n_e + n_o) \tag{3.69}$$

To complete the model a means of evaluating L_e and P (the cathode pressure) is required. Siegfried uses two empirically derived equations to achieve this:

$$L_e = 2\lambda_{pr} \tag{3.70}$$

where λ_{pr} the primary electron energy exchange mean free path, is given by:

$$\lambda_{pr} = \left[\frac{6.5\times10^{-17} n_e}{V_p^2} + \frac{10^3 n_o V_p}{2.83\times10^{23} - 1.5n_o}\right]^{-1}$$

The pressure is given by an empirical equation derived over a large range of mass flow rates (in mA units), discharge currents and orifice diameters d_o (in mm):

$$P = \frac{\dot{m}}{d_o^2}(13.7 + 7.82 I_D)\times10^{-3} \text{ Torr} \tag{3.71}$$

Inserting the mass flow rate ($\dot{m}$), the insert diameter, the discharge current I_D and the thermal power loss $\dot{Q}_{th}$, the 10 equations ((3.60)-(3.63), (3.65) and (3.67)-(3.71)) can be solved in terms of all the other parameters except T_e, which Siegfried assumed to be constant at 0.7±0.1eV over all the range of normal operating conditions of a mercury hollow cathode.

3.3.2 The Salhi-Turchi model

Salhi and Turchi's [140] main criticism of the Siegfried-Wilbur model is its reliance on empirically derived relations (equations (3.70) and (3.71) in section 3.3.1) and specification of a constant value of T_e obtained from the related experimental program. They present a first principles model for the HC, which can be used to specify cathode properties and operating conditions and can be used as a design tool for hollow cathodes.

The Salhi-Turchi model, like that of Siegfried, assumes field enhanced thermionic emission from the cathode surface, where the surface field is given by the Prewett-

Allen relation. It assumes that the ion flux to the cathode is given by the Bohm criterion and that the pressure at any point inside the cathode is given, for a perfect gas, by the sum of all the partial pressures, with the heavy particle temperature equal to the wall temperature. i.e. Salhi reuses equations (3.61), (3.62), (3.63), (3.68) and (3.69) from Siegfried.

The current balance at the cathode surface (equation (3.60)) was modified by the addition of the term ($-I_e$) to the right hand side of the equation. This term represents the contribution to the total current by plasma electrons with enough energy to overcome the repulsive sheath to impact the cathode surface. Salhi presents an alternative expression for the discharge current:

$$I_D = en_e\left(\frac{kT_e}{2\pi m_e}\right)^{1/2} A_{or} - I_{eq} \tag{3.72}$$

where A_{or} is the orifice area, with the first term representing the electron current escaping through the cathode orifice. I_{eq} is the ion current through the orifice given by $I_{eq} = Ze\dot{m}\beta/m_i$ where β is the ionisation fraction.

The mass flow rate is determined from conditions at the orifice. Assuming an isothermal flow and using a one dimensional momentum equation corrected for viscous effects, leads to equation (3.73) for the mass flow rate:

$$\dot{m} = \frac{Pe^{-1/2}}{\sqrt{\frac{kT_i}{m_i}\left(1+\beta\frac{T_e}{T_i}\right)}}\frac{A_{or}}{2} \tag{3.73}$$

To evaluate the pressure (P) in (3.73) we need to solve equation (3.69), which necessitates a knowledge of the neutral density. Salhi uses a two-temperature Saha equation ($T_e \neq T_i$) to achieve this with θ being the ratio of the partition functions of the ion and neutral:

$$n_e\left(\frac{n_i}{n_o}\right)^{T_i/T_e} = 2\theta\left(\frac{2\pi m_e kT_e}{h^2}\right)^{3/2}\exp\left(-\frac{V_i}{kT_e}\right) \tag{3.74}$$

For the cathode energy balance the model includes, like that of Siegfried, the energy input due to ion bombardment and energy loss due to electron emission. In addition it includes energy loss by emitted electrons in the form of enthalpy, and energy input by high-energy plasma electrons penetrating the cathode sheath. The model gives the terms in the form of integrals over the surface to allow for variations in current density:

$$\int j_{fi}\left(\phi_e + \frac{5kT_s}{2e}\right)dA_e = \int j_i\left(V_i + V_p - \phi_e\right)dA_e + \int j_e\left(\phi_e + \frac{5kT_e}{2e}\right)dA_e + f\,q_r \tag{3.75}$$

where j_e is the plasma electron current density to the surface, q_r is the radiative heat flux and f is the view factor. It is however unclear how Salhi evaluates, if at all, the radiative flux term.

The mechanism of energy input to the plasma in this model is not confined to the electrons accelerated through the cathode fall, but also includes energy input due to Ohmic heating of a plasma with conductivity σ. The energy input is used to heat the electrons and excite and ionise the gas, energy loss is by particles leaving the cavity. This energy balance is expressed by Salhi as:

$$\int j_{fi}\left(V_p + \frac{5kT_s}{2e}\right)dA_e + \int\frac{j^2}{\sigma}dV = \int j_i\left(V_i + \frac{5kT_i}{2e}\right)dA_s + \int j_e\left(\frac{5kT_e}{2e}\right)dA_s + \left(I_D + I_{eq}\right)\left(\frac{5kT_e}{2e}\right) + \frac{I_{eq}}{\beta}\left(\frac{5kT_s}{2e}\right) + q_r \tag{3.76}$$

The plasma conductivity is estimated using the Spitzer formula for a fully ionised gas:

$$\sigma = \frac{1.53\times10^{-2}}{\ln\Lambda}T_e^{3/2} \tag{3.77}$$

where

$$\Lambda = 1.24\times10^{7}\left(\frac{T_e^3}{n_e}\right)^{1/2} \tag{3.78}$$

This model allows two-dimensional variation in plasma properties in an axi-symetric cathode with the assumption of uniform T_e. The plasma potential distribution is

obtained using the Laplace equation, which governs a neutral plasma:

$$\nabla^2 V = 0 \tag{3.79}$$

with appropriate boundary conditions. An interesting consequence of using the Laplace equation is that its solution gives the length of the plasma column (L_e), which Salhi found to scale to one insert diameter [141].

Salhi compared his model with experimental results from Siegfried and Wilbur. His model was found to have, over all the parameters compared (T_e, n_e, V_p and T_s) an overall maximum discrepancy of 30%.

The models described above are relatively simple illustrations of the physical processes in orificed hollow cathodes, which can be applied to this work. More complex, computationally intensive models (see for example the Centrospazio models [138, 160] and the model under development in Southampton [25, 187]) would require a considerable effort to implement and are thus not discussed here.

Chapter 4

EXPERIMENTAL APPARATUS

Introduction

This chapter describes the experimental facility used during the course of this investigation. It first describes the vacuum chamber and associated systems, then goes on to describe the hollow cathode in diode configuration and associated hardware. Finally, it contains a description of the various diagnostics used in the experiments.

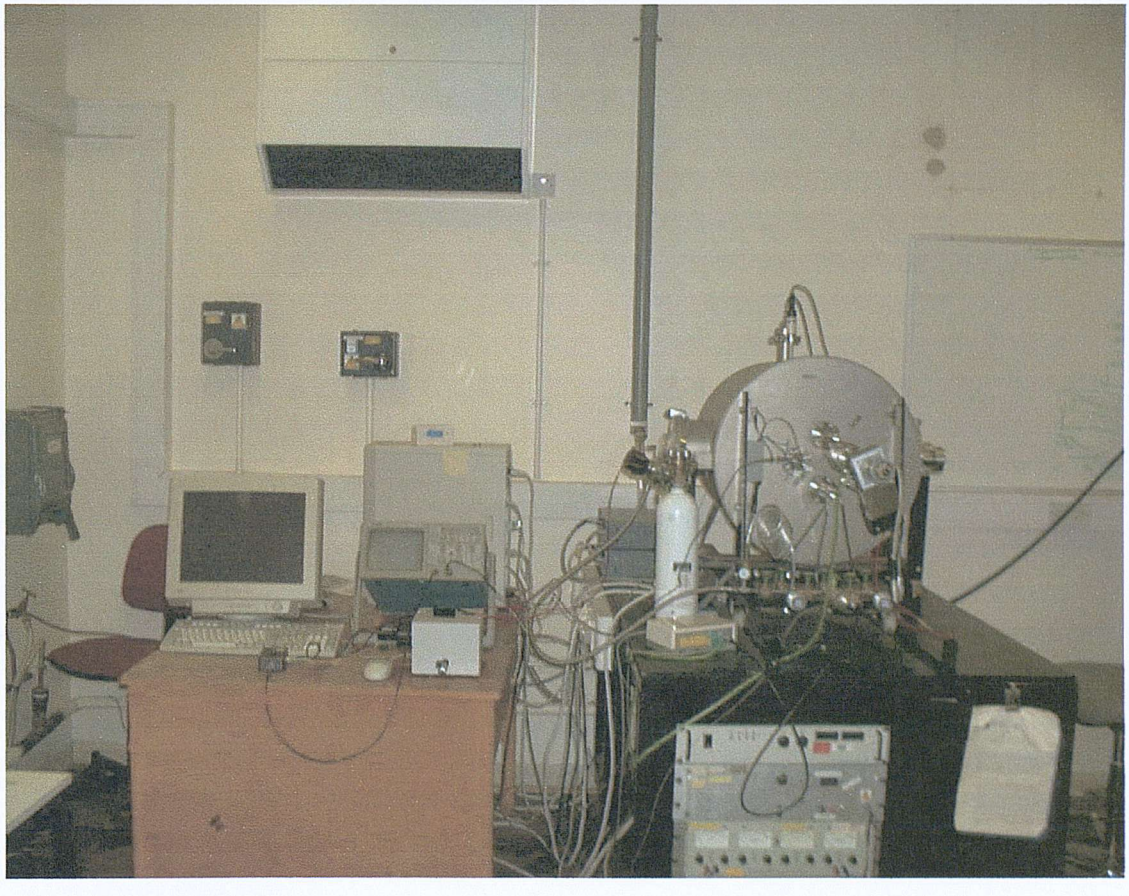

Figure 4.1: The Vacuum chamber with accompanying hardware

4.1 Mechanical system

The vacuum chamber is essentially the one used by Edwards [33] and Milligan [112], with minor modifications, and will be here described in brief (for more details reference should be made to the above works).

4.1.1 Vacuum chamber

For the operation of the hollow cathode a background pressure of the order of 10^{-7} mbar is required. This condition reduces the residual oxygen partial pressure, and hence mitigating the risk of oxygen poisoning of the hollow cathode insert. The vacuum chamber thus needs to be capable of high vacuum.

The stainless steel vacuum chamber is cylindrical in design, 500mm in diameter and 500mm in length a sketch is presented in figure 4.2. One end, an ISO500 flange, doubles as the chamber door and also as the mounting for the propellant feed and the back-plate on which all the vacuum side hardware (the hollow cathode-enclosed keeper assembly, anode, optical fibre mount, mirror and optical fibre shield) are mounted.

The vacuum chamber has several ports (CF35 or ISO160 high vacuum ports) to allow electrical and propellant feeding through the chamber walls. Two of the ISO160 flanges located halfway along the length of the chamber have been changed for the purposes of this investigation. One was drilled to allow the installation of an Ocean Optics FC-VFT-UV200 optical fibre vacuum feedthrough (see section 4.4.1.4), the other had one of the two CF35 flanges on it replaced with a quartz viewport, which facilitated pyrometry of the cathode tip and provided visual access to the inter-electrode space.

The pumping system is a Balzers turbomolecular pump system incorporating a TPH520KGT turbomolecular pump in series with a DUO016B rotary vane pump. The pumping system is fully integrated, which greatly simplifies operation.

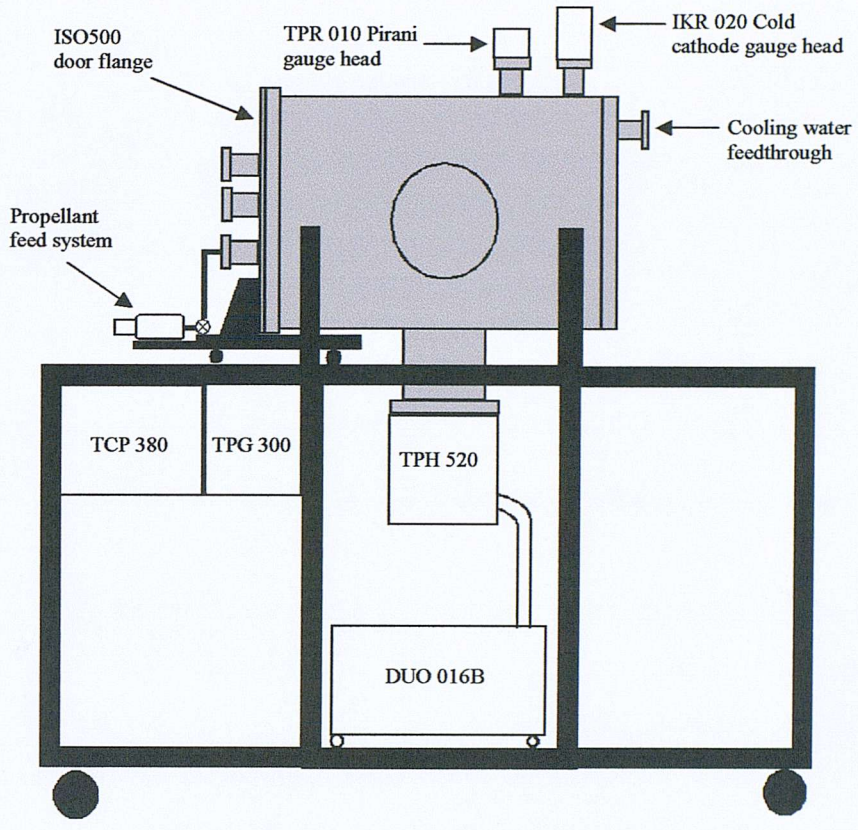

Figure 4.2: Vacuum system schematic [33]

4.2 Experimental subsystems

4.2.1 Hollow cathode in diode configuration

Hollow cathode geometry

The hollow cathode used in this work is a T6 thruster hollow cathode, modified for use in a Hall thruster (ROS2000), on loan from QinetiQ (formerly DERA). A schematic cross section of the cathode is shown in figure 4.3. It is designed to provide the discharge current requirement of the T6 thruster, which is about 17A [45]. However, this cathode has demonstrated a capability of up to 30A [45].

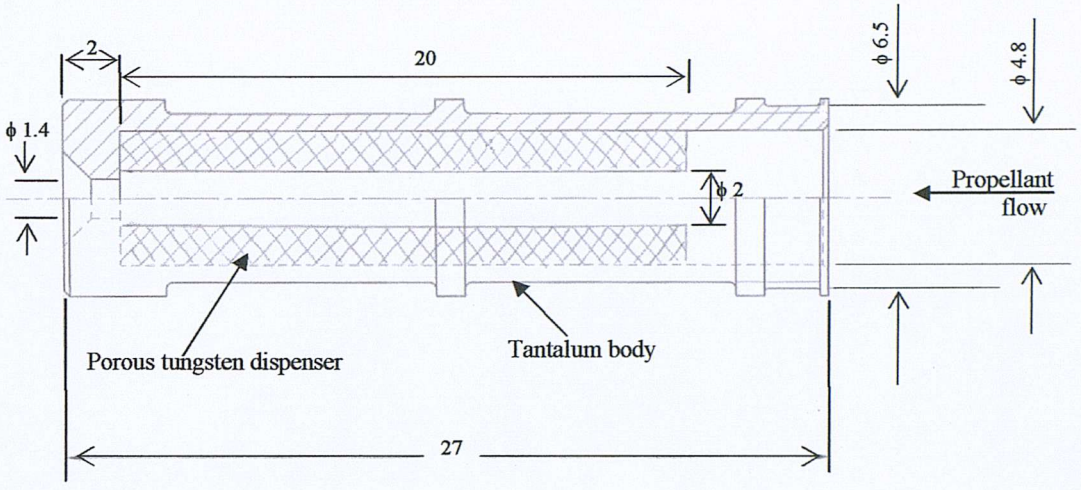

Figure 4.3: T6 hollow cathode dimensions (dimensions in mm)

The cathode body and tip were made by turning a single tantalum rod, reducing the risk of tip weld failure. The cathode body is a tube of 6.5mm outer diameter and 4.8mm inner diameter. The cathode tip is 2mm thick and contains a central orifice of 1.4mm diameter, which is countersunk at 45° to 1mm depth.

A porous tungsten insert of 20mm length and 2mm internal diameter is push fitted flush with the cathode tip's upstream face. It is impregnated with a barium-calcium-aluminate low work function material.

A bifilar tungsten-rhenium heater winding surrounds the cathode body, with a machinable ceramic serving as insulation between them. Radiation shields made of dimpled molybdenum foil surround the complete assembly in the radial direction, while dimpled molybdenum washers perform the same function in the axial direction.

Experimental arrangement in diode configuration

A schematic cross section of the hollow cathode in diode configuration and the associated vacuum side equipment is shown in figure 4.4. All the vacuum side hardware is mounted on the back-plate, which in turn is connected to the main chamber door by a support frame. A picture of the hollow cathode in diode configuration is shown in figure 4.5.

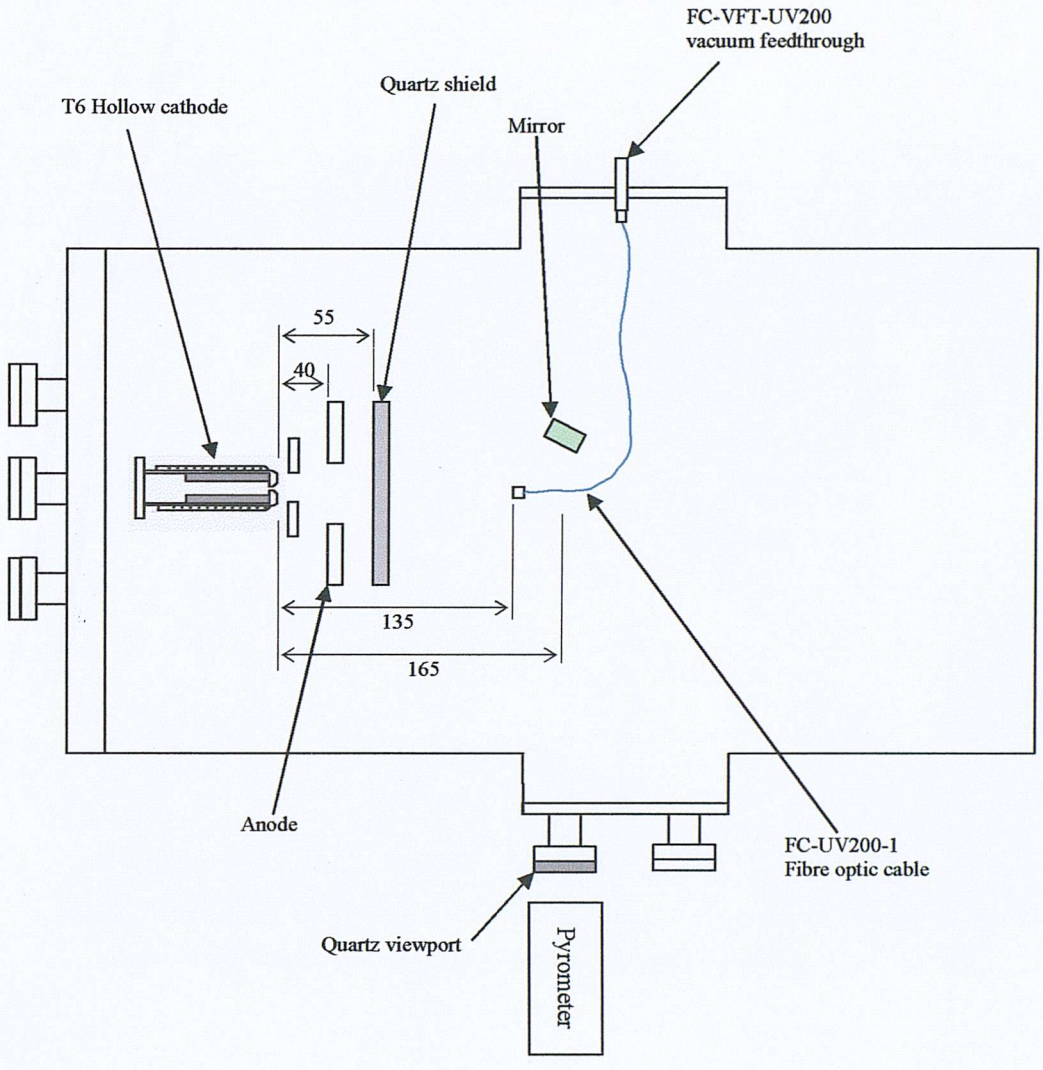

Figure 4.4: Schematic of the hollow cathode arrangement in diode configuration (dimensions in mm)

The hollow cathode used in this work employs a fully enclosed keeper configuration. The keeper is made of carbon and its inner surface is situated 2.5mm away from the cathode tip when cold, with a keeper orifice diameter of 4mm. The anode is a 100mm diameter stainless steel disc with a 50mm diameter hole through its centreline. It is located 40mm from the cathode tip and mounted on insulating ceramic mounts. A quartz disc of 100mm diameter is mounted 55mm from the cathode tip to shield the optical fibre from ion bombardment (see section 4.4.1.4) and the optical fibre itself is situated 135mm from the cathode tip with an unobstructed view of the hollow cathode interior plasma. The optical fibre is connected to a FC-VFT-UV200 vacuum feedthrough, which transmits the light emission to the exterior of the chamber. A mirror is placed 165 mm from the cathode tip at an approximate angle of 45° to the

cathode axis to facilitate cathode tip temperature measurement using an optical pyrometer (see section 4.4.2).

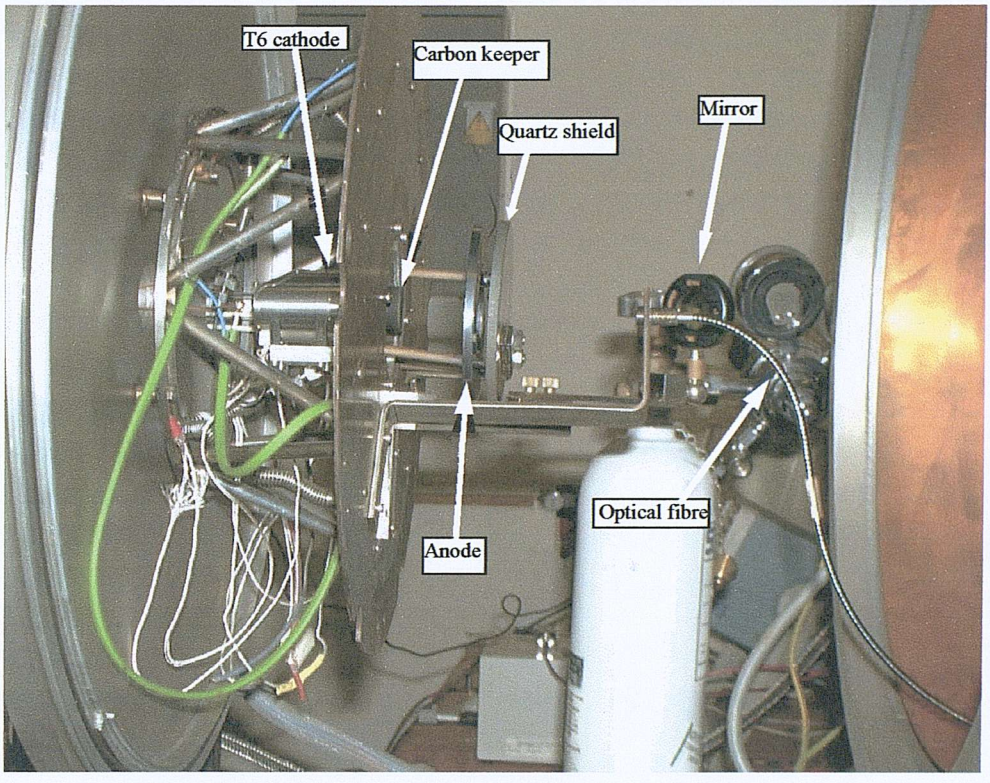

Figure 4.5: Photograph of the hollow cathode in diode configuration

4.2.2 Propellant feed system

A schematic of the propellant feed system is provided in figure 4.6. It operates on the principle that a high purity gas providing a constant upstream pressure to a metered needle valve would provide a constant flow of propellant that can be varied over the entire range of calibration.

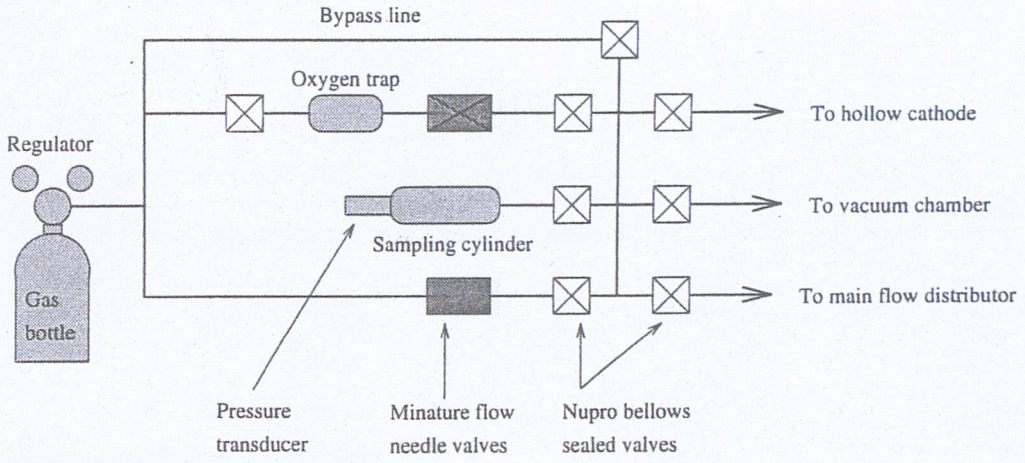

Figure 4.6: The propellant feed system [33]

All the piping used is ¼ inch stainless steel pipes and all the connections are ¼ inch Swagelock® compression fittings. High purity gas is provided through a Spectra Gases 7120 double stage regulator, which allows upstream pressure control of the hollow cathode and discharge chamber feed lines (the chamber feed line is not used in this investigation), control of the gas flow rate was effected by a Negretti VS-MF-1V-4P miniature flow needle valve. An oxygen trap is used on the hollow cathode line upstream of the Negretti valve, along with a bypass line (which is evacuated prior to propellant feeding), to minimise the risk of cathode oxygen poisoning. Nupro HK series valves are used to direct the flow to the sampling cylinder when flow rate calibration is required.

Flow rate calibration is done using a stainless steel sampling cylinder with a known volume. The flow is deflected to this sampling cylinder from the cathode or discharge chamber line, the rate of change of pressure in the cylinder is measured using a Druck PDCR910 pressure transducer, while the temperature of the gas is simultaneously measured by a K-type thermocouple attached to the cylinder.

The mass flow rate can be calculated for a given upstream pressure and Negretti needle setting using (Edwards [33])

$$\frac{dP}{dt} = \dot{m}\frac{RT}{V}$$

This method, in spite of the benefits of its simplicity, makes it impossible to measure the flow rate in real time. A calibration prior to testing is necessary, making this method susceptible to errors due to changes in temperature or upstream pressure during the course of an experiment. By performing pre- and post- test calibration the error was found to be less than ±10%. For more details of the calibration procedure refer to section 5.1.2.

4.3 Electrical supply system

The behaviour of the hollow cathode can be characterised by operating it in diode configuration [28, 40, 115, 146]. This leads to a simplification of the required electrical arrangement when compared to that in a fully operational thruster.

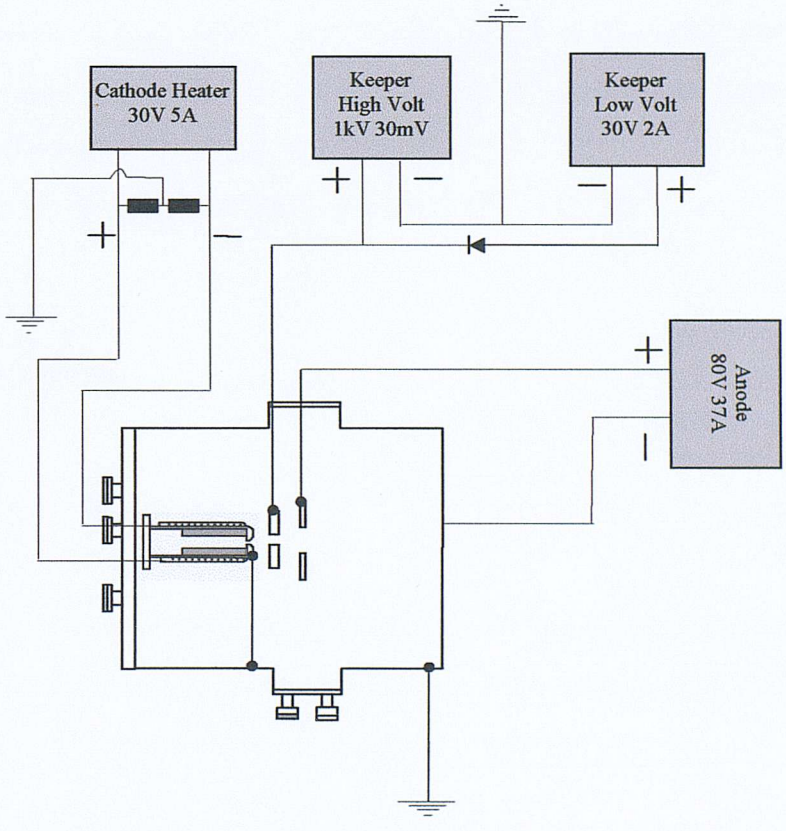

Figure 4.7: Electrical power supply arrangement in diode configuration

The hollow cathode heater power supply is a Powerbox Lab605 (30V, 5A), operated in constant current mode, which can provide the necessary power to bring the cathode to the required discharge initiation temperature. An earth connection was made between the two terminals of the power supply to lower the potential difference between the heater and the cathode body, thus mitigating the risk of heater failure.

The keeper power supply consists of a high voltage power supply for discharge initiation and a low voltage power supply for steady state operation. The high voltage power supply is a pair of Farnell Hivolt PM1/DCP photomultiplier power supplies (1kV, 30mA) which are themselves powered by a pair of Farnell 16RA24012 linear 24V power supplies. The low voltage (post discharge initiation) operation is maintained by a Powerbox Lab622 (30V, 2A), operating in constant current mode. It has a load regulation of ±0.05% (of V_{max}), and an output ripple of 1mV r.m.s. over the frequency range 20Hz-20MHz.

For the main discharge to start, a potential is applied to the anode electrode. This is done using a Glassman LV80-37 (80V, 37A) switch mode power supply, operated in current regulated mode. It has a load regulation of ±0.1% (of V_{max}), and an output ripple of 20mV r.m.s. over the frequency range 20Hz-20MHz.

4.4 Diagnostics

4.4.1 Optical diagnostics

The optical diagnostic systems include a photomultiplier tube, a spectrometer/CCD array system, a monochromator and an optical fibre system used to guide the light from the vacuum chamber interior to the various detectors.

4.4.1.1 Spectrometer and CCD array

The spectrometer used in this work is an Oriel Instruments MS127i imaging

spectrograph. It utilises a Czerny-Turner design with an astigmatism correcting mirror (see figure 4.8) to improve spectral and spatial resolution and to render multi-channel spectroscopy possible. It is a versatile instrument with the ability to rotate and interchange gratings enabling it to cover a wide range of wavelengths (180nm-25μm) and resolving powers.

The spectrograph has an input focal length of 127mm, an F/number of 3.8 and a spectral resolution of 0.4nm (with a 1200l/mm grating). A 25μm entrance slit was used throughout this study.

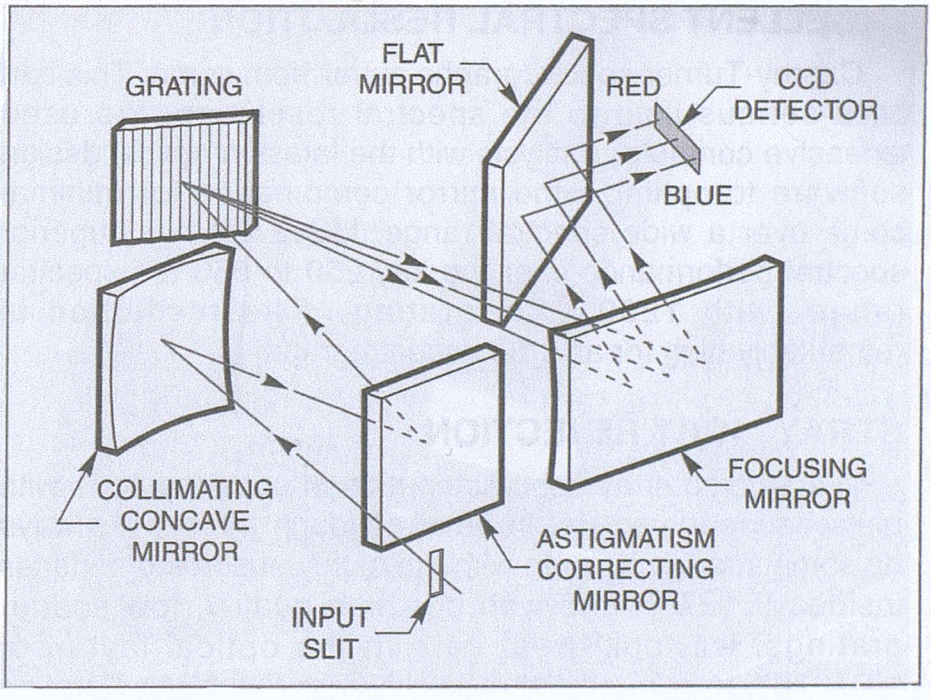

Figure 4.8: The Oriel MS127i spectrograph's optical design [157]

Two gratings were used in this investigation. A 300l/mm ruled grating blazed at 300nm, which is useable in the range 180-1000nm. Its transmission properties are shown in figure 4.9. It is a coarse grating with a wide wavelength range (giving a band pass of 681nm for a 25mm CCD array field and a spectral resolution of approximately 1.7nm). This grating is used here primarily to gain an overview of the spectra and to determine which regions are of primary interest and are thus candidates for further study using a 2400l/mm grating. This denser grating is a holographic grating blazed at 250nm with a useable wavelength range between 175-610nm. Its

transmission properties are shown in figure 4.10. This grating has an array band pass of just 67nm and a high resolving power (approximately 0.2nm), allowing positive identification of the majority of the lines in the discharge spectrum.

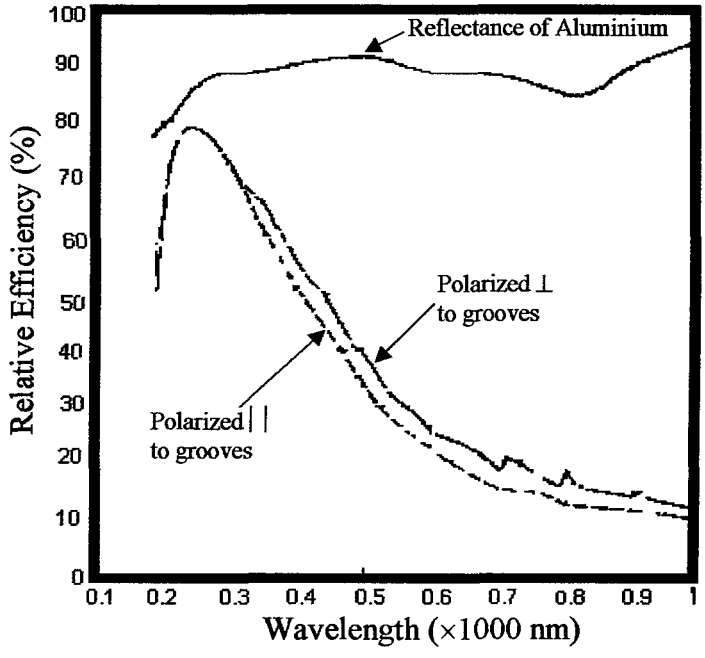

Figure 4.9: Grating efficiency plot for 300l/mm grating

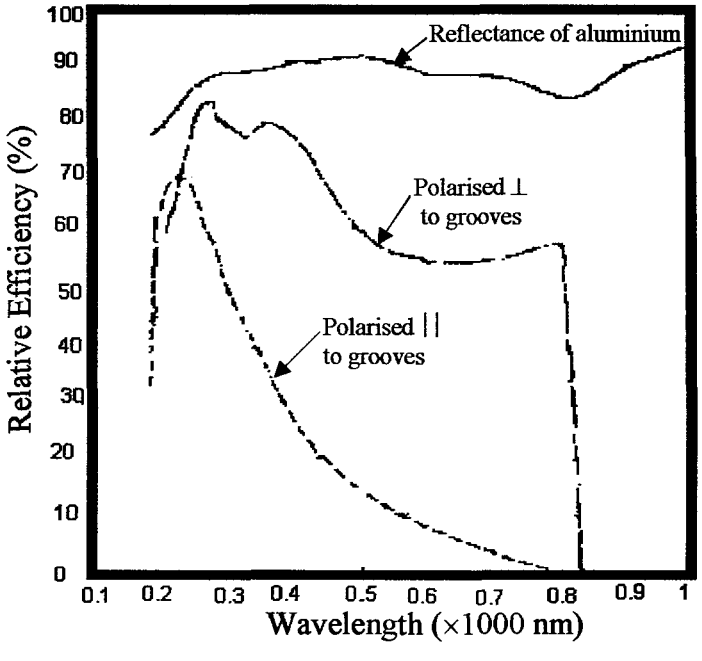

Figure 4.10: Grating efficiency plot for 2400l/mm grating

The CCD array is an Andor Technologies InstaSpec IV CCD detector. It consists of a

2-Dimensional array of 1024×256 elements. The Quantum efficiency (QE) of the CCD array in the range 150-1150nm is shown in figure 4.11.

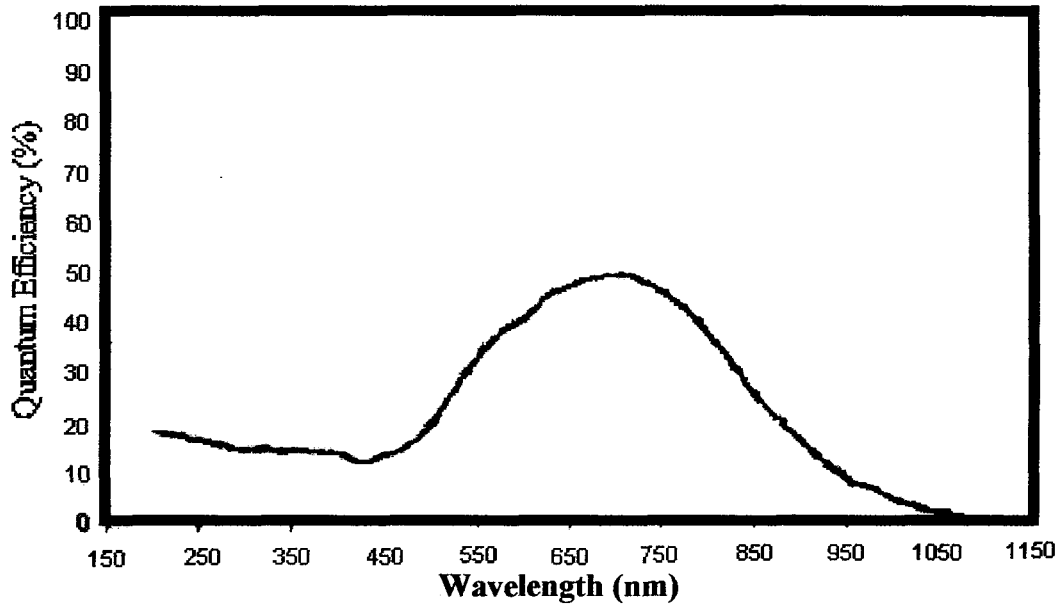

Figure 4.11: Quantum efficiency plot of Instaspec IV CCD array

4.4.1.2 Photomultiplier tube

The photomultiplier tube (PMT) used for the discharge initiation studies is a Hamamatsu H6780 photosensor module. It is a compact, lightweight unit consisting of a photomultiplier and the associated high voltage power supply in the same package. It has high sensitivity, wide dynamic range, short rise time and an operating range of 300-650nm (see figure 4.12 for its frequency response curve). The unit is powered by a low voltage desktop power supply (+12V). Its sensitivity can be varied using a 0-0.8V control voltage.

Radiant sensitivity (@ 420nm)	21μA/nW
Dark current	0.5nA
Induced ripple in signal	0.6mV peak-peak
Rise time (@ +0.8V control voltage)	0.65ns
Detector Area	$0.64cm^2$
Sensitivity adjustment range	$1:10^4$

Table 4.1: Manufacturer's specifications for the H6780 photosensor module

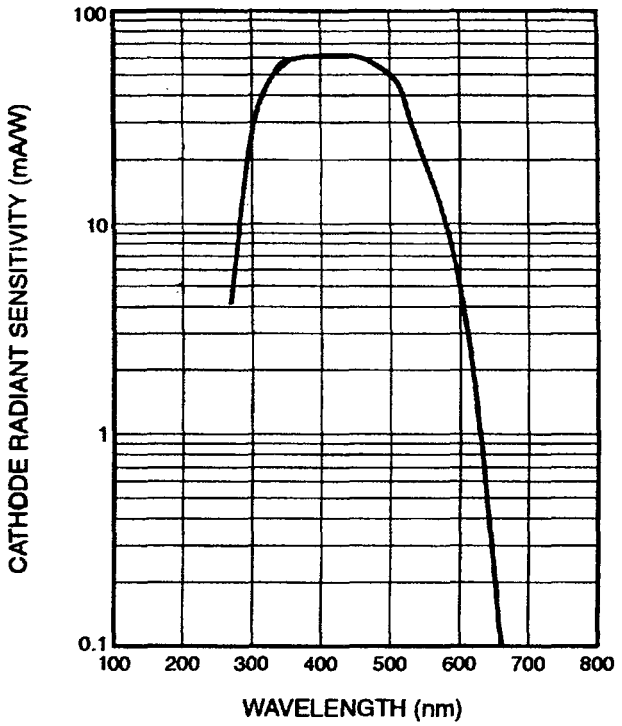

Figure 4.12: H6780 photosensor module frequency response curve

The H6780 photosensor also comes with an optional optical fibre SMA 905 adapter, which allows direct coupling of the light from the discharge chamber to the photomultiplier tube for the broadband discharge initiation studies.

4.4.1.3 Monochromator

A monochromator was used to spectroscopically resolve the plasma light emission during the breakdown phase of hollow cathode operation. The monochromator of choice was a Thermo-Jarrel-Ash Monospec18 monochromator with a focal length of 156mm, a resolution of 0.6nm (with a 1200l/mm grating) and a crossed Czerny-Turner design. The Monospec 18 model has an aperture ratio of F/3.8, and the entrance and exit slits used here were both 25μm wide.

Figure 4.13 shows the grating efficiency curve for the 1200l/mm grating used with the monochromator.

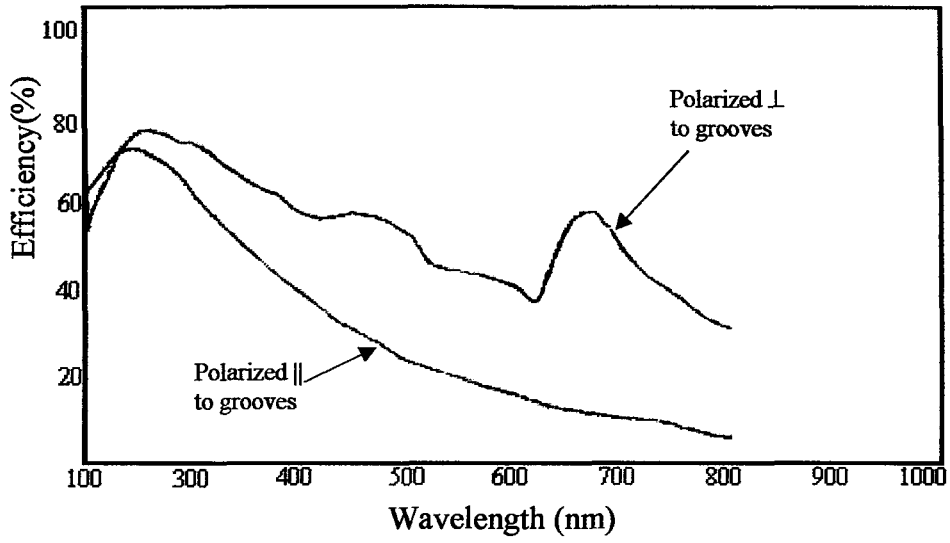

Figure 4.13: Grating efficiency plot for monochromator 1200l/mm grating

An optical fibre adaptor and an F/number matcher (to decrease stray light inside the monochromator and increase throughput) were mounted on the monochromator's entrance slit, while an H6780 photomultiplier tube was mounted on the exit slit to act as a detector.

4.4.1.4 Optical fibre and optical fibre shield

Optical fibres were used to guide the light from the hollow cathode interior to the intended detector. For the discharge initiation work, two Ocean Optics FC-UV200-1 quartz optical fibres were employed, one for the air side and the other for the vacuum side, with SMA905 connectors at both ends of each fibre for coupling and for ease of assembly. Both fibres were of 200μm diameter, 1m in length with a numerical aperture (NA) of 0.22 and a wavelength range of 200-750nm. The optical fibre used on the vacuum side had a flexible metal sheathing to minimise outgassing and the SMA905 end facing the hollow cathode was especially modified for high temperature use. A plot of the transmission properties of the optical fibre is shown in figure 4.14.

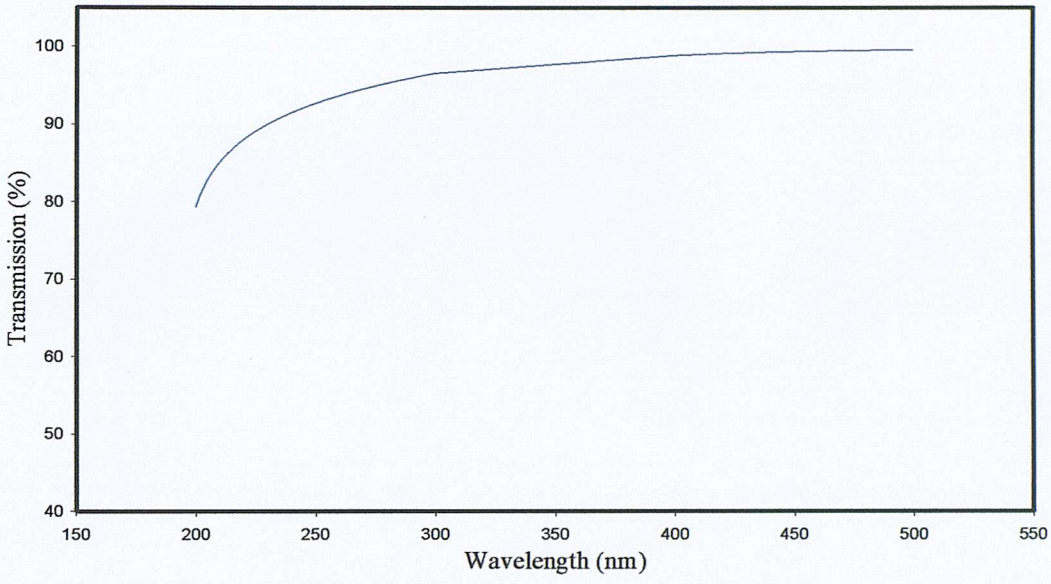

Figure 4.14: Transmission properties of the FC-UV200-1 optical fibre

In order to transmit the light through the vacuum wall, an Ocean Optics FC-VFT-UV200 vacuum feedthrough was used. It is essentially a FC-UV200 optical fibre (with the same transmission properties as in figure 4.14) in an M12 bolt housing with a Viton O-ring and two SMA fibre optic interconnects. The fibre has a metal buffer which makes a hermetic seal with the housing possible. It has a minimum vacuum operating pressure of 1×10^{-7} mbar.

For the steady state side of this work employing the MS127i spectrograph, the air side optical fibre was replaced by an Oriel 77678 Multi-track optical fibre bundle with three branches, of which only the central branch was used in this study. Each track is composed of a 200μm fibre, with their common end terminated, vertically aligned, in a ferrule which couples to the spectrograph entrance using an Oriel 77863 mounting adapter. The input side of the fibre is terminated by an SMA905 connector, allowing coupling to the vacuum feedthrough. Figure 4.15 shows the transmission plot of this fibre.

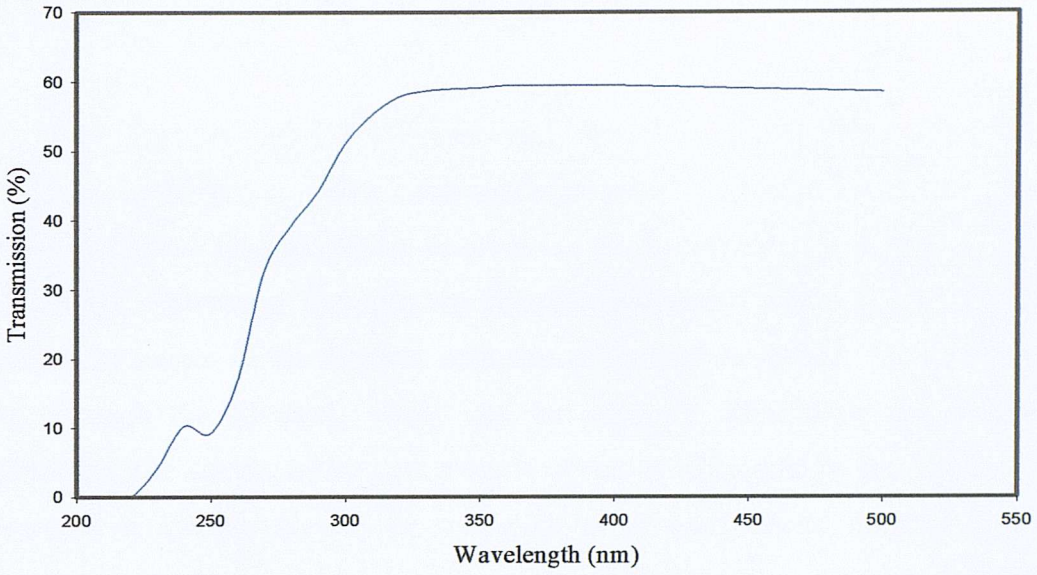

Figure 4.15: Transmission properties of the Oriel 77678 Multi-track optical fibre bundle

Severe ion bombardment damage to the optical fibre tip has been experienced at the start of these investigations, due to this, an optical fibre shield was installed upstream of the optical fibre. This is a quartz disc of 100mm diameter and 6mm thickness mounted 55mm from the cathode tip. This eliminated the problem. The shield's transmission properties are shown on figure 4.16.

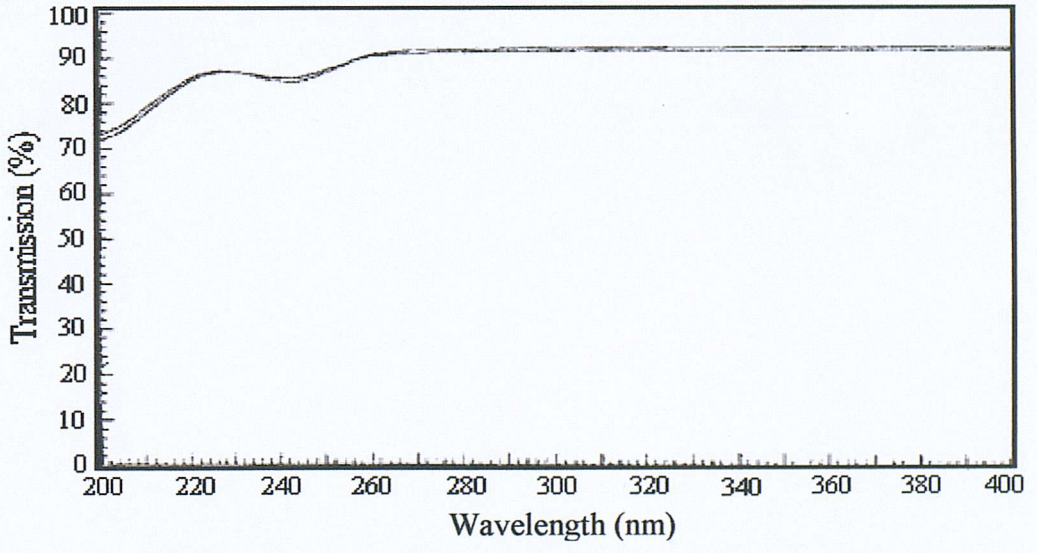

Figure 4.16: Transmission properties of the quartz shield

4.4.2 Hollow cathode tip temperature measurement

One of the main variables in the discharge initiation investigation is the hollow cathode tip temperature, which determines thermionic emission from the cathode surface. In order to measure the tip temperature during the discharge initiation phase, a Cambridge Instrument disappearing filament pyrometer was used. It works by matching the colour of the filament with that of the hollow cathode tip. The current going through the filament, which can be adjusted, determines the filament's temperature. The reading of the pyrometer is of course influenced by the emissivity of the cathode tip and the transmission properties of the quartz shield, mirror and quartz viewport. These effects were accounted for by calibration using an R-type (platinum-platinum/rhenium) thermocouple inserted into the tip orifice of the cathode when not operating. The cathode is heated, with no gas flow, and the temperature measured by both the pyrometer and the thermocouple, the results are shown in figure 4.17. The results of the calibration indicate a linear relationship between the pyrometer and thermocouple readings. The pyrometer measured temperatures were then corrected based on the calibration results. The measured temperature will be within $\pm 10^{\circ}C$ of the actual value, with the measurement accuracy degrading as the tip temperature is reduced.

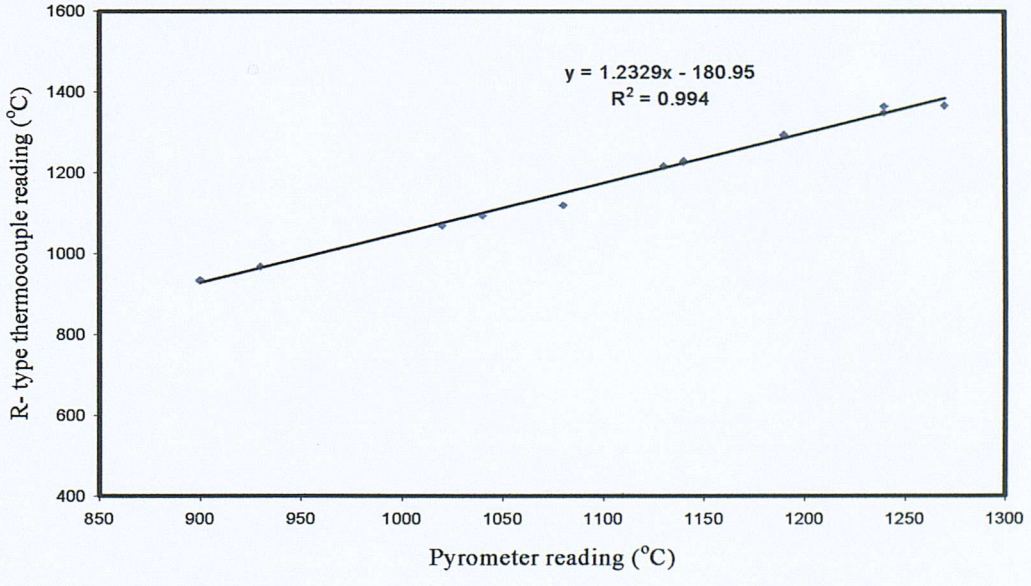

Figure 4.17: Optical pyrometer calibration

Chapter 5

EXPERIMENTAL PROCEDURES

Introduction

This chapter describes the experimental set-ups and procedures used in obtaining the results of this work. The experimental equipment is described in chapter 4 and the results in chapter 6.

The T6 hollow cathode was operated using several inert gas propellants, namely xenon, krypton, argon and a krypton/xenon mixture in the natural ratio (i.e. 12:1 ratio by volume).

The investigation was divided into two sections: a) discharge initiation and b) steady-state experiments. In the discharge initiation experiments emphasis was placed on investigating the effects of cathode operating parameters on breakdown potential. This was further augmented by a study of the optical emission from the hollow cathode interior plasma during breakdown for all the gases used. The steady state study focused on investigating the discharge dependence on operating parameters. To gain a better understanding of the underlying physics of HC operation, a spectroscopic study of the steady-state discharge was undertaken using the pure inert gases.

5.1 General experimental procedure

5.1.1 Vacuum system

The pumping system's drive unit controls the turbomolecular pump, the rotary vane

pump, the vent valve and the cooling water valve. This integrated nature renders operating the pumping system and the achievement and maintenance of the required vacuum simply a matter of pressing the start button. The drive unit also continuously monitors the condition of the pumping system, and any disruption of electrical power or cooling water would lead to a safe shut down.

The target ultimate background pressure of $1\text{-}5\times10^{-7}$ mbar can be achieved in about 12 hours with the hollow cathode in diode configuration, but the system is usually left to pump down for a minimum of two days to allow any trapped gases to outgas, and to mitigate the risks of oxygen poisoning of the hollow cathode insert.

5.1.2 Propellant flow rate calibration

The propellant flow rate calibration procedure was similar to that of Edwards [33] and Milligan [112] and is stated here briefly.

As the system does not allow real time measurement of flow rate, the calibration of the propellant flow rate was carried out prior to testing for the entire range of flow rates to be utilised. The vacuum line and bypass line (figure 4.6) are used to evacuate the system prior to calibration and experiments. At the beginning of every set of experiments, following evacuation of the feed lines, calibration was performed by setting the upstream pressure and the Negretti needle valve to the desired number of turns. The flow is then directed to an evacuated sampling cylinder, where a pressure transducer measures the rate of change of pressure in the range 100-250 mbar, and transmits the data to a personal computer where the mass flow rate is calculated. The results of this calculation are plotted for the entire range of flow rates to be used in the tests. A polynomial interpolation is then carried out, from which all the valve settings for the desired flow rates can be read off.

This calibration procedure was applied, as mentioned above, prior to every test for each of the propellants used. If the previous test had been carried out using a different propellant, a period of 10-15 minutes of flushing with the new propellant was allowed

to eliminate any traces of the previous test. The upstream pressure was usually set at 195kPa for xenon, krypton and the krypton/xenon mix, while it was set at 150kPa in the case of argon. Calibration was also done after each of the tests in order to determine the effect of drifts in temperature and upstream pressure on the needle valve setting. It was found that the deviation was less than ±10% for all the range of flow rates and propellants used.

A general calibration was done prior to this work to compare the values acquired to those obtained by Edwards and Milligan using xenon. The results are shown in figure 5.1. They seem to be in good agreement and the differences between them can be attributed to temperature effects.

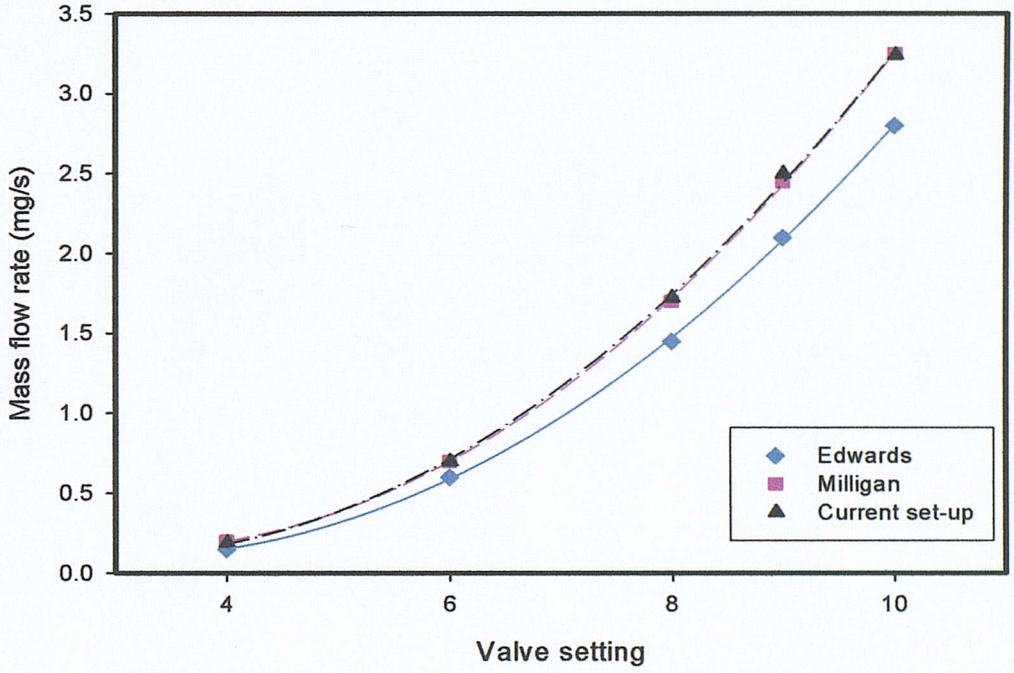

Figure 5.1: Comparison between calibration data for Edwards [33] Milligan [112] and the current set-up

Throughout this work the propellant flow rate is expressed in either mg/s or Aequiv units, Aequiv measures the number of charge carriers in each gas. Conversion between these two units can be achieved by using the ion charge to mass ratio:

$$\dot{m}(Aequiv) = \frac{e}{m} \times 10^{-6} \dot{m}(mg/s) \tag{5.1}$$

5.2 Discharge initiation experiments

Discharge initiation experiments were carried out on the T6 cathode in diode configuration. Several factors are thought to influence the breakdown behaviour of the hollow cathode. Mainly, the propellant flow rate ($\dot{m}$), tip temperature (T), keeper voltage (V_k), cathode orifice diameter, cathode-keeper separation (d_k) and, to a lesser degree, the degree of atmospheric contamination and the previous discharge history. Due to the enclosed keeper design the investigation of the cathode-keeper separation was rendered impossible. Emphasis was therefore placed on investigating the effects of keeper voltage, propellant flow and tip temperature, while attempts were made to keep the other factors constant throughout the experimental program. For example, to remove any dependence on previous discharge history, the same start-up procedure was applied following any long periods of inactivity or exposure to air, and the discharge was run at the same discharge current for a set length of time in all the tests.

The discharge initiation investigation was divided into three sections: First, an investigation into the effects of V_k, T and $\dot{m}$ on breakdown potential was performed. Then a photomultiplier tube investigation of the broadband breakdown radiation and its dependence on breakdown parameters was conducted. Finally, a spectroscopic investigation of the breakdown radiation was attempted.

5.2.1 Range of experiments

Breakdown investigations were carried out for xenon, krypton, argon and for the krypton/xenon mix with mass flow rates ranging from 0.2-1.1 mg/s at constant tip temperature (929°C and 1299°C), and tip temperatures ranging from 916-1422°C at constant propellant flow rate (0.2 mg/s and 1mg/s). A systematic investigation of the effect of varying these parameters over the entire range was conducted and will be described in the next sections.

5.2.2 Breakdown voltage dependence on propellant flow rate and tip temperature

Experimental set-up

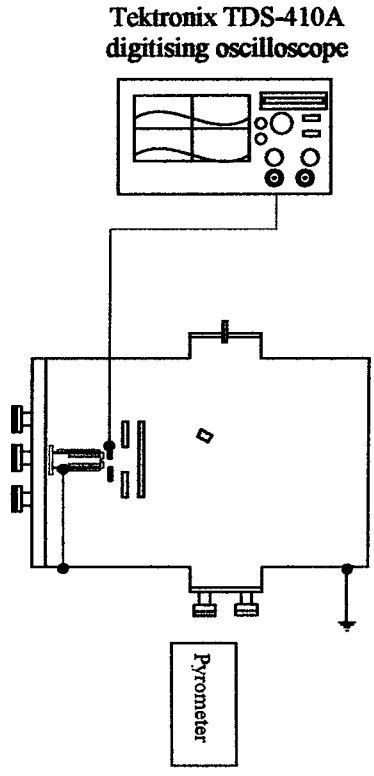

Figure 5.2: Experimental set-up for investigation of breakdown voltage dependence on flow rate and tip temperature

Figure 5.2 shows the diagnostics used in determining the dependence of breakdown voltage on hollow cathode operating parameters. A Tektronix TDS-410A digitising scope was used to measure and record the keeper voltage temporal behaviour, which is then used to determine the breakdown potential (V_{bk}). The scope trace is digitised and stored on disc for later analysis. The optical pyrometer is used to determine the cathode tip temperature.

Experimental procedure

Following the calibration of the propellant flow rate, the low voltage keeper power

supply current limit is set at 0.5A, the anode power supply current limit is set at 1A and the power supply is put on stand-by. Both supplies are operated in constant current mode. A cathode flow rate of 1mg/s is initiated, the cathode heater is then switched on and operated in constant current mode with 3A heater current for 15 minutes till a tip temperature of around 1299°C is reached. The low voltage keeper power supply voltage is then increased gradually till breakdown occurs, indicated by a rapid drop in keeper voltage and the onset of a discharge. The heater is then switched off to prevent overheating the cathode. If no breakdown occurs using the keeper low voltage power supply, the high voltage power supply is brought on line and the potential gradually increased until the gas has broken down. The discharge is then transferred to the anode and run for 5 minutes at 0.5A keeper current and 5A discharge current. This is done to allow regeneration of the insert surface barium prior to the next start in order to have reproducible results. The discharge is then switched off, the mass flow rate adjusted to the required setting and the heater switched on to bring the cathode to the required temperature and the above process is repeated. The first start of the day is not considered as typical due to the oxidation of the free barium by the residual oxygen in the vacuum system

To investigate breakdown potential dependence on mass flow rate, the above process was applied for 0.2, 0.5, 0.7, 0.9, 1 and 1.1mg/s at constant temperature (around 929 and 1299°C) for xenon, krypton, argon and the krypton/xenon mix. To investigate breakdown voltage dependence on tip temperature the above procedure was applied in the range 916-1422°C using approximately 100°C intervals at constant mass flow rate (0.2 and 1mg/s) for all the propellants tested.

Reproducibility of breakdown behaviour has been a major concern from the outset, due to the results of the discharge initiation tests on mercury [48] (see section 2.2.5.1), thus it was decided to conduct at least three measurements of V_{bk} for each set of parameters.

5.2.3 Discharge initiation optical emission studies

5.2.3.1 Broadband discharge initiation optical emission study

Experimental set-up

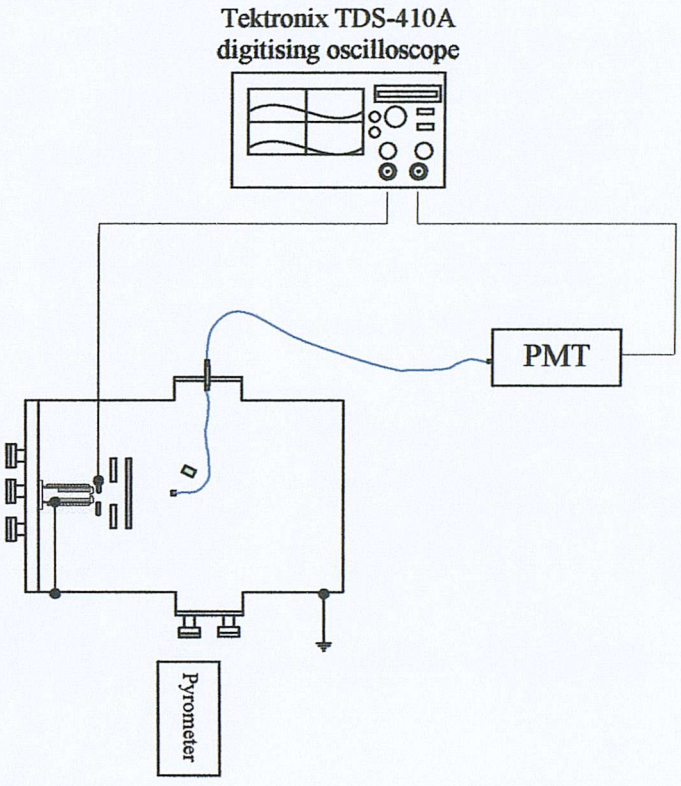

Figure 5.3: Experimental set-up for breakdown broadband optical emission studies

Figure 5.3 shows the experimental set-up used to investigate the temporal behaviour of the breakdown plasma optical broadband emission. The set-up is essentially the same as that discussed in section 5.2.2 with two differences: 1) The addition of the optical fibre system and photomultiplier tube with optical fibre interconnector to accept the light emission conducted from the vacuum chamber interior. 2) Method of data acquisition; the oscilloscope trace acquisition was triggered by the falling edge of the keeper voltage (V_k). The scope acquired V_k as well as the photomultiplier tube behaviour with 10% of the length of the time record dedicated to the pre-trigger period, thus giving a record of the keeper and breakdown plasma behaviour prior to, during and after breakdown.

Experimental procedure

The procedure used in investigating the broadband breakdown emission is virtually the same as that used in obtaining the breakdown potential dependence on discharge characteristics (see section 5.2.2).

The experiments were carried out for all the propellants with the exception of the krypton/xenon mix. To investigate breakdown optical emission behaviour dependence on propellant flow rate, experiments were carried out at 0.2, 0.5, 0.7, 0.9, 1 and 1.1mg/s while keeping the tip temperature constant at 1299°C. To investigate breakdown optical emission behaviour dependence on tip temperature, experiments were carried out in the range 916-1422°C while keeping the flow rate constant at 1mg/s. The photomultiplier control voltage was set at 0.553V.

To check reproducibility of the optical emission signature, the experiments were carried out at least three times for a given set of parameters.

5.2.3.2 Spectroscopic discharge initiation optical emission study

Experimental set-up

Figure 5.4 shows the set-up used to carry out time-resolved spectroscopy of the breakdown plasma. A Thermo-Jarrel-Ash monochromator is used to spectrally resolve the hollow cathode optical emission, with a photomultiplier tube being employed as a detector. A pulse amplifier circuit was constructed to amplify the breakdown signal from the selected emission line. Unfortunately, during testing, the amplifier circuit did not behave as expected due to several factors, particularly the low signal to noise ratio. Thus, due to time constraints, the experiment was abandoned and no useful data was obtained.

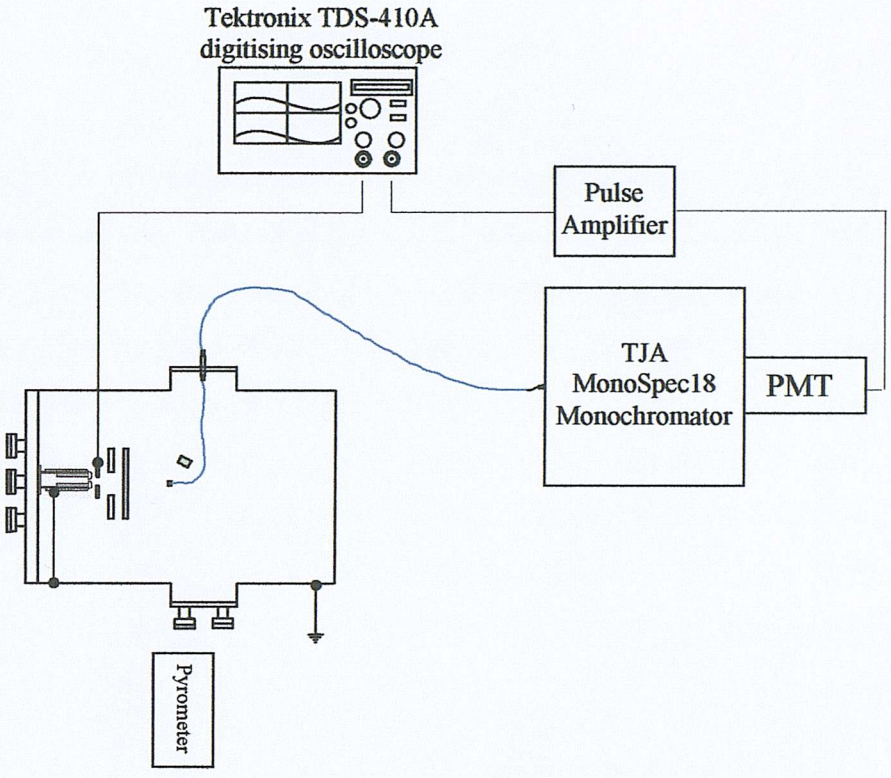

Figure 5.4: Experimental set-up for discharge initiation spectroscopy

5.3 Steady state spectroscopy

The initial aim of the steady state spectroscopy experiments was to identify the most suitable lines for investigation during discharge initiation. However, the aims of the investigation were gradually extended until the steady state investigation became a complete and independent test program in its own right, covering all the gases used in the starting experiments (i.e. argon, krypton, xenon and the krypton/xenon mix) under a wide range of test conditions.

5.3.1 Range of experiments

5.3.1.1 Range of Propellant flow rates

Voltage-current characteristics and spectroscopic data were recorded for xenon with flow rates ranging from 0.147 - 2.415 Aequiv (0.2 - 3.61mg/s). For krypton no discharge could be maintained below 0.92 Aequiv (0.8mg/s) so the investigation was carried out in the range 0.92 – 4.83 Aequiv (0.8 - 4.2mg/s). For Argon no discharge could be maintained below 1.932 Aequiv (0.8mg/s) so the investigation was carried out in the range 1.932 – 8.453 Aequiv (0.8 - 3.5mg/s). In the case of the krypton/xenon mix no discharge could be maintained below 0.92 Aequiv (0.83mg/s) so the investigation was carried out in the range 0.92 – 4.83 Aequiv (0.83 - 4.38mg/s). The lower flow rate limit in the alternative gases could possibly be decreased by use of a higher voltage anode power supply.

The variation of V_a, V_k and the spectral characteristics with mass flow rate experiments were carried out at a discharge current (I_a) of 5A and a keeper current (I_k) of 1A.

5.3.1.2 Range of discharge currents

Voltage-current characteristics were recorded for xenon propellant operating at cathode flow rates of 0.3675 (0.5), 0.5145 (0.7), 0.735 (1), 1.15 (1.56) and 2.415 (3.29) Aequiv(mg/s). The keeper and anode voltages were recorded over a discharge current (I_a) range of 0.5 - 5A. For krypton the same discharge current range was investigated for flow rates of 1.15 (1), 1.725 (1.5), 2.415 (2.1), 3.623 (3.15) and 4.83 (4.2) Aequiv (mg/s). For argon the same discharge current range was investigated for flow rates of 2.415 (1), 3.623 (1.5), 4.347 (1.8), 4.83 (2) and 8.211 (3.4) Aequiv (mg/s). And finally, in the case of the krypton/xenon mix, the same discharge current range was investigated for flow rates of 1.15 (1.04), 2.415 (2.19), 3.623 (3.28) and 4.83 (4.38) Aequiv (mg/s). The keeper current was kept constant at 1A for all the above experiments.

The discharge current was limited to 5A due to a problem with the cathode earth return cable, which caused the cable to fail if the discharge current exceeded 6A. The T6 cathode is capable of producing 30A of discharge current but, due to time constraints, the wiring problem rendered it impossible to investigate the whole region of discharge current achievable in a T6 hollow cathode.

5.3.2 Experimental set-up

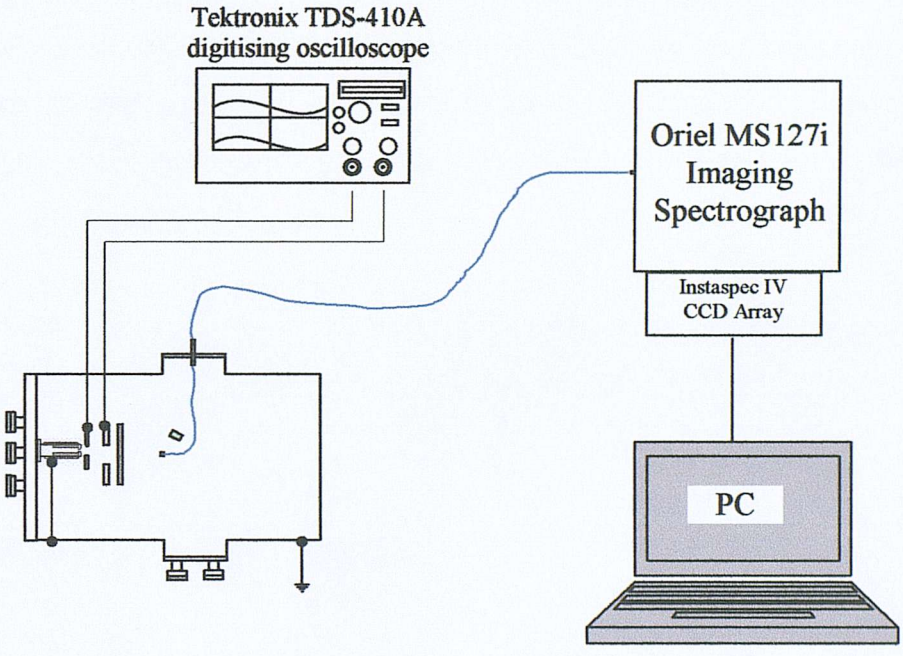

Figure 5.5: Experimental set-up for steady state discharge investigations

Figure 5.5 shows the set-up used in the steady state discharge investigations to be described in the following sections. The digitising oscilloscope was used to record the keeper and anode voltage characteristics. For the spectroscopic investigation, a personal computer was used to record the data from the Instaspec IV CCD array.

5.3.3 Hollow cathode start-up and thermal equilibrium

Following propellant flow rate calibration, the hollow cathode discharge is initiated.

The hollow cathode flow rate is first set to a value of Img/s and a heater current of 3A is applied for 15 minutes. At this point the hollow cathode has reached an appropriate temperature for discharge initiation. The low voltage keeper power supply is switched on and voltage increased until discharge initiation occurs, and the discharge is then transferred to the anode. If the discharge did not start, the keeper high voltage power supply is brought on line and the applied voltage increased until discharge initiation occurs, following which the low voltage power supply takes over.

After discharge initiation and transfer to the anode, the discharge becomes self-sustaining and the heater power supply is then switched off to prevent excessive heating of the cathode. The hollow cathode is run for half an hour to an hour to allow the cathode to achieve thermal equilibrium, which is indicated by the power supply voltages achieving steady state. The usual values of the control parameters during this period are I_a = 5A, I_k = 1A and $\dot{m}$ =1mg/s.

The hollow cathode parameters are then set to the required values for the first test and left for 15 minutes to stabilise before commencing any experiment.

5.3.4 Discharge characterisation

It was necessary, before commencing spectroscopic investigations of the hollow cathode discharge, to establish the discharge behaviour and points of mode change (from spot to plume) for each of the propellants used. Three parameters are thought to control discharge transitions: Anode current (I_a), keeper current (I_k) and propellant flow rate ($\dot{m}$) [28, 40, 115, 126]. The discharge transition dependence on keeper current is the least significant [115], therefore it was left out in favour of concentrating on the other two parameters.

To investigate discharge dependence on anode current, the propellant flow rate is set to the desired value (see section 5.3.1.2 for details of flow rates used for each propellant) with the keeper current fixed at 1A throughout the testing program. The anode current is then increased from 0.5A to 5A in steps of 0.5A every minute, while

the anode and keeper voltages are monitored using the digitising scope where the data is saved in digital format and stored for later analysis.

To investigate discharge dependence on propellant flow rate, the anode current was fixed at 5A while the keeper current was set to 1A. In order to compare the different gases used in the discharge, a system was developed to compare them in both mass flow rate and Aequiv units. The conversion between the two units is simply a matter of multiplying by a constant for an individual gas (see equation 5.1). The constant, however, is not the same for every gas as the propellant species' charge to mass ratio varies from gas to gas. This is further complicated by the fact that the discharge could not be maintained in the case of argon for flow rates of less than 1.932Aequiv and for flow rates less than 0.92Aequiv in the case of krypton and the krypton/xenon mix. Moreover, initial experiments seemed to show that transitions from spot to plume mode occurred at much higher flow rates for argon when compared to the other gases. This necessitated the use of a larger step size to fully characterise its discharge behaviour. All these factors mean that a variable step size is needed for each propellant in order for a meaningful comparison between them to be possible. A system for investigation was devised, see figure 5.6.

Mass flow rate in mg/s was used to determine the maximum envelope for each gas (3.5 mg/s for argon, 4.2 mg/s for krypton, 4.38 mg/s for krypton/xenon mix and 3.61 mg/s for xenon). Starting with argon, in the region where there is an overlap in the flow rates (in Aequiv) a step size of 0.2415Aequiv was used (refer to figure 5.6). In the region beyond that a step size of 0.483Aequiv was used. Moving on to krypton, in the region where it overlaps with both argon and xenon a step size of 0.2415Aequiv was used. In the region below that (shared with xenon only) a step size of 0.115Aequiv was used. The same applies to the krypton/xenon mix, which occupies the same region in the chart. For xenon, the regions shared with the other gases have the same step size as those mentioned above for each gas. In the region below that, however, a step size of only 0.0735Aequiv was used.

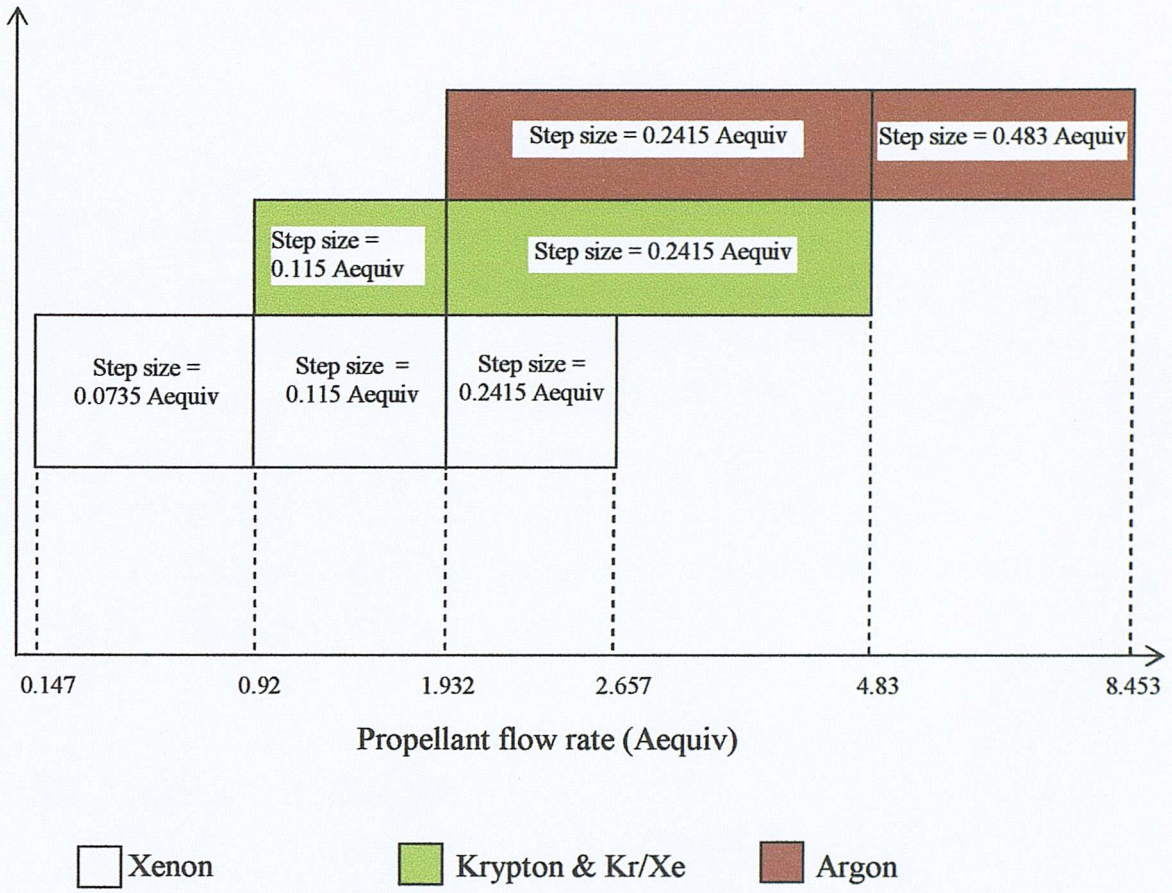

Figure 5.6: Illustration of the system used to compare propellant flow rate for different gases

To illustrate the above procedure, xenon is used here as an example. After thermal equilibrium of the cathode is achieved at 0.147Aequiv (0.2mg/s) (I_a = 5A and I_k = 1A), the propellant flow rate is increased in steps of 0.0735Aequiv every minute till a flow rate of 0.92Aequiv (1.25mg/s) is reached. From 0.92 Aequiv to a flow rate of 1.932 Aequiv (2.63mg/s) the propellant flow rate is increased in steps of 0.115Aequiv every minute. From a flow rate of 1.932Aequiv to 2.657Aequiv (3.61mg/s) the propellant flow rate is increased in steps of 0.2415 Aequiv. The process is then reversed with the flow rate decreased by the amount indicated in each interval every minute till a value of 0.6615Aequiv (0.9mg/s) is reached, the experiment is then terminated. The same procedure applies to all the other propellants using their respective step values, illustrated in figure 5.6.

5.3.5 Spectroscopic investigation

The characterisation of the T6 hollow cathode discharge in diode configuration with the different propellants and the establishment of the envelopes for the operating modes were a precursor to a spectroscopic investigation of the steady state discharge. Two approaches were adopted. The first approach was to acquire the complete discharge optical emission spectra for each of the gases at different discharge modes in order to observe variations in hollow cathode internal plasma properties with changes from spot to plume mode. The second approach was to tag three lines of one species and, using the CCD array in chart recorder mode, observe the effect of variation of discharge parameters (propellant flow rate and discharge current) on the optical emission lines in real time.

5.3.5.1 Spectral calibration

A mercury- argon Hg(Ar) lamp was used to calibrate the CCD array. It produces a pencil beam of very narrow spectral lines, which extend from the UV to the IR. A typical calibration spectrum (with the 300l/mm grating) is shown in figure 5.7.

The Instaspec IV software controls all the functions of the array from hardware, data acquisition and data manipulation. Calibration of the CCD array is simply a matter of acquiring the spectra from the Hg(Ar)lamp, then manually entering the wavelength values (in nm) of the known calibration lines. They are then used by the software to construct a cubic polynomial, which fits all the pixel element numbers to the more meaningful unit of wavelength (in nm).

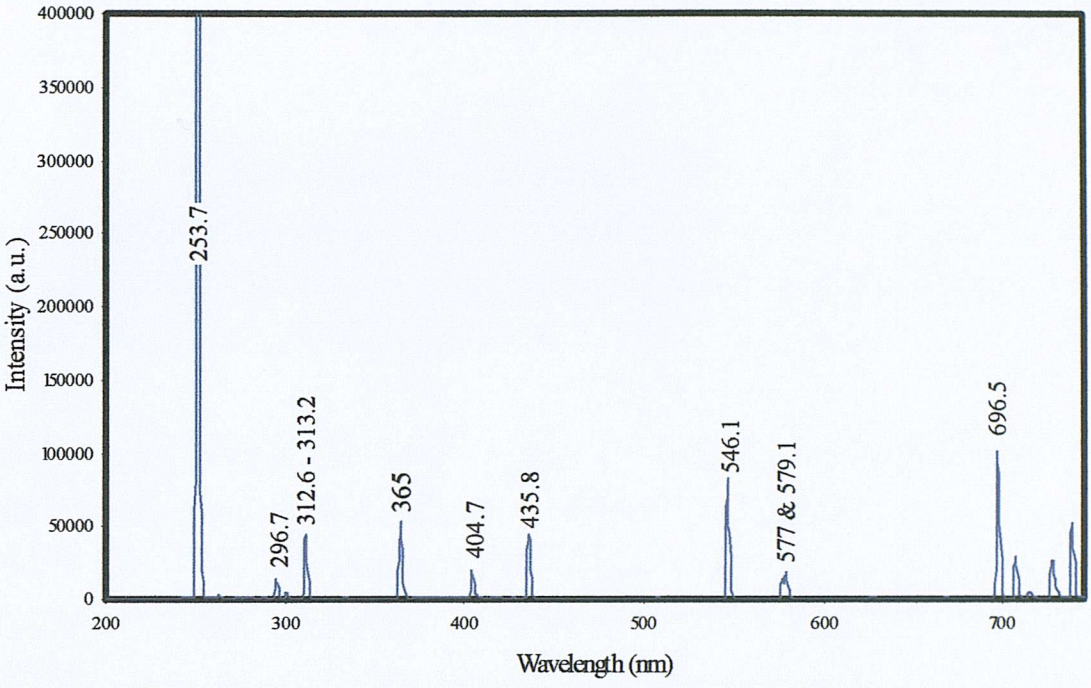

Figure 5.7: Line output of Hg(Ar) spectral calibration lamp

5.3.5.2 Full optical emission spectra experiments

To investigate the plasma properties (electron temperature and density) for different hollow cathode operating modes and propellants, a full optical emission spectra was obtained.

Initially, the 300l/mm grating was used to obtain a spectrum in the range 200-750nm for each of the gases and test conditions. From this spectrum, a certain range was selected for a more detailed investigation using the 2400l/mm grating which has greater spectral resolving powers. The region of interest was usually 400-463nm.

Once thermal equilibrium of the hollow cathode has been achieved, a spectrum of the discharge conditions can be taken. All the spectra were taken at I_a = 5A and I_k = 1A, while the discharge mode change was achieved by varying the propellant flow rate.

The CCD array is cooled to –10°C, to reduce dark current shot noise. A background reading is always taken prior to spectrum acquisition, which is then subtracted

automatically by the software to give the resulting spectrum in "Intensity (background corrected)" units.

The CCD takes 100 readings of the spectrum and integrates them (thus enhancing the signal to noise ratio) with an exposure time of 1s. A note of the keeper and anode voltages is made. The flow rate is then changed to the next setting and left for 5min to stabilise before taking the next spectrum.

The same procedure applies to all the propellants used: xenon, argon and krypton. No spectroscopic work was performed on the krypton/xenon mix. A spectrum was taken at 0.735(1), 1.15(1.56) and 2.415(3.29) Aequiv (mg/s) flow rates for xenon. For krypton discharges a spectrum was taken at 1.15(1), 2.415(2.1) and 4.347(3.78) Aequiv(mg/s). For Argon discharges a spectrum was taken at 2.415(1), 3.623(1.5), 4.347(1.8), 4.83(2) and 8.211(3.4) Aequiv(mg/s) flow rates.

5.3.5.3 Variation of emission line intensity with propellant flow rate and discharge current

The InstaspecIV software allows different acquisition modes of data from the CCD detector. One of these modes is the chart record mode which allows for tagging of up to three emission lines simultaneously and the recording of their temporal behaviour. This allowed for an interesting set of experiments where three lines from the same species (neutral lines, first ionisation lines or impurity lines) were tagged and the line intensity dependency on discharge current and flow rate was investigated.

The CCD array was operated at $-10^{\circ}C$, with an exposure time of 0.5s and four integrations per point. A background reading was always taken prior to acquisition and was used to correct the spectrum.

The same procedure used for discharge characterisation (section 5.3.4) was applied here. The experiments were also carried out over the same discharge current and flow

rate ranges used in the discharge characterisation experiments. A digitising scope was used to record the anode and keeper voltage behaviour.

Chapter 6

RESULTS

6.1 Introduction to the results

This chapter describes and presents the results of the experimental investigation carried out in this work. The experimental apparatus and procedures are described in chapters 4 and 5 respectively.

The initial aim of the experimental program was to investigate the T6 hollow cathode discharge initiation using several inert gases. This is the subject of the following section, which details the results of several methods employed to that end.

The second area of investigation was a spectroscopic study of the steady-state discharge from a T6 cathode, using the same inert gases utilised in the starting study. This involves establishment of the hollow cathode operating modes in diode configuration, which has never been done before for some of the gases employed, the acquisition of spectra at several discharge conditions and the determination of the effect of variation of discharge conditions on emission line intensity.

6.2 Starting results

In order to achieve a better understanding of the hollow cathode breakdown phenomena, two approaches were successfully employed. First, an investigation of the dependence of the breakdown voltage on cathode parameters. Second, an investigation into the broadband optical emission from the hollow cathode plasma during breakdown and its dependence on cathode parameters.

It has to be mentioned here that a third approach was also attempted, namely, to spectrally resolve the optical emission from the hollow cathode breakdown plasma, and to determine the temporal behaviour of a given emission line during breakdown. Regretfully, this was unsuccessful for the reasons mentioned in section 5.2.3.2.

6.2.1 Breakdown voltage (V_{bk}) dependence on propellant flow rate and tip temperature

As previously mentioned, hollow cathode breakdown behaviour is thought to depend on several factors, chief amongst which are tip temperature and propellant flow rate, which are the subjects of this section

6.2.1.1 V_{bk} dependence on mass flow rate

Figures 6.1-6.4 show the dependence of breakdown voltage (V_{bk}) on propellant flow rate for xenon, krypton, argon and Kr/Xe mix, with the error bars indicating the spread in the values obtained. The experiments were carried out for mass flow rates in the 0.2 mg/s to 1.1 mg/s range at two values of tip temperature, 929°C and 1299°C.

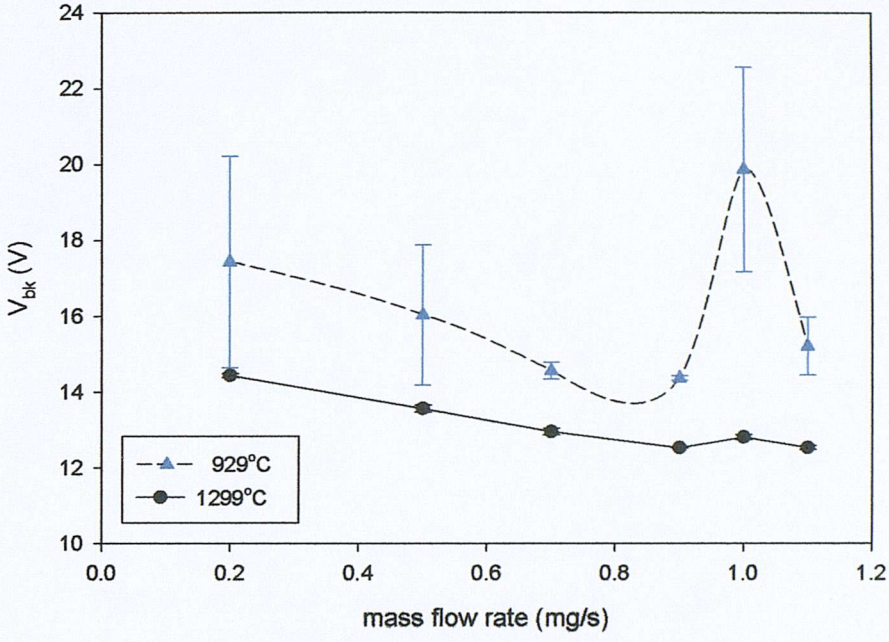

Figure 6.1: Discharge initiation voltage as a function of propellant flow rate (Xe)

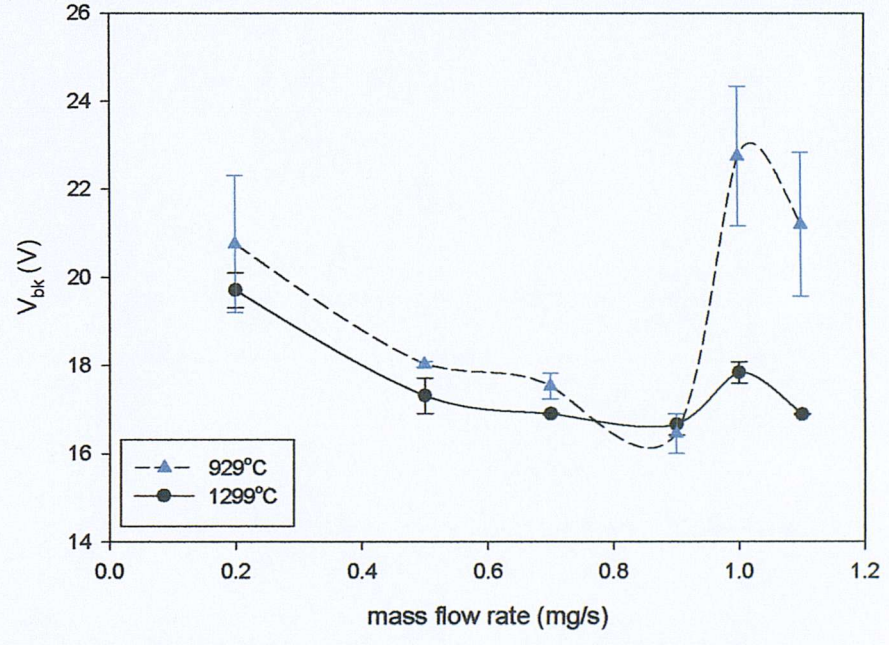

Figure 6.2: Discharge initiation voltage as a function of propellant flow rate (Kr)

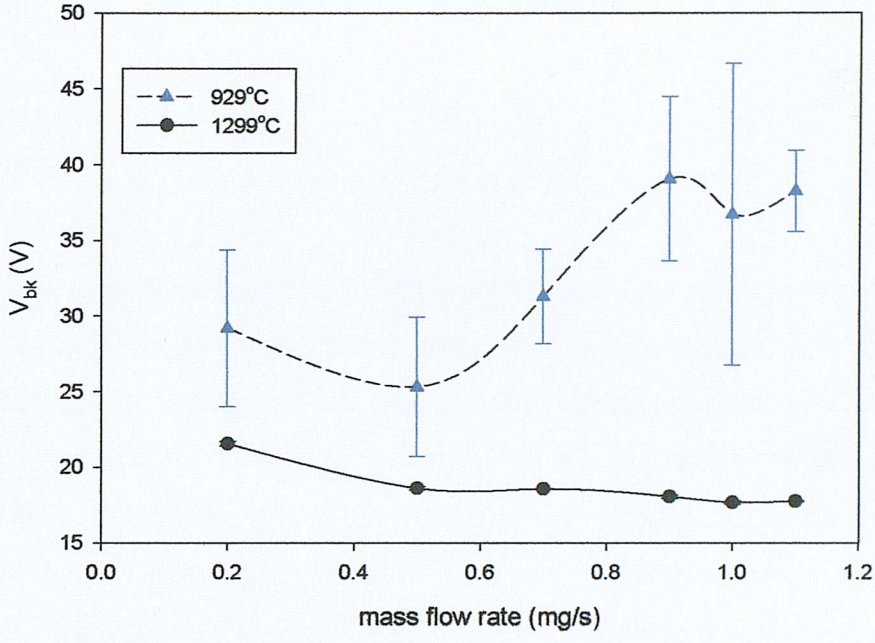

Figure 6.3: Discharge initiation voltage as a function of propellant flow rate (Ar)

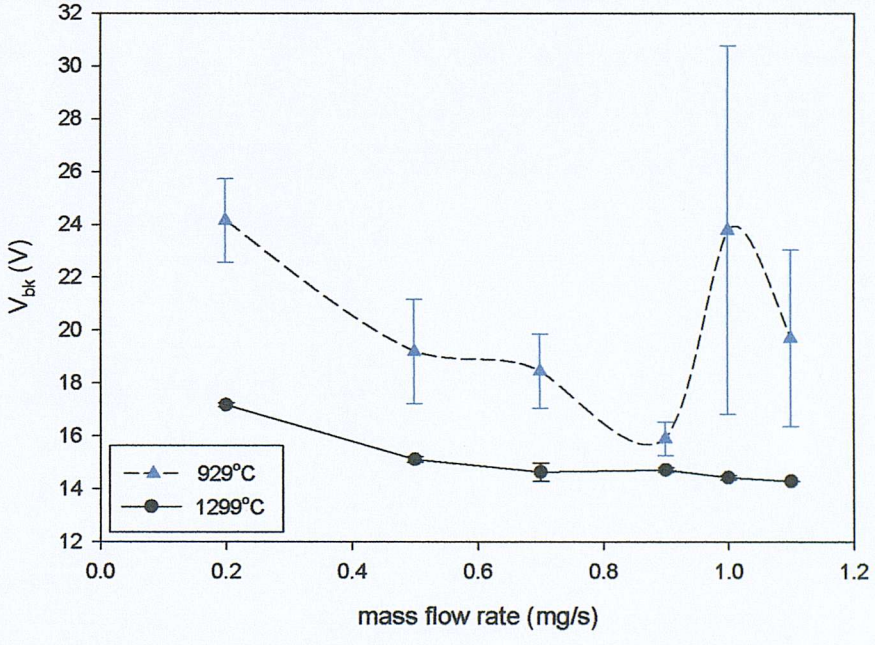

Figure 6.4: Discharge initiation voltage as a function of propellant flow rate (Kr/Xe)

Breakdown voltages were surprisingly low, with discharge initiation occurring at potentials lower than 22V for xenon, 25V for krypton, 50V for argon and 32V for Kr/Xe even at 929°C. The xenon results showed lower breakdown voltages than those found in mercury tests [48] and they were also lower than those carried out on the open keeper T6 [124]. The results were found to be more reproducible at 1299°C than

they were at 929°C. In general, the results were much more reproducible than expected, with a maximum standard deviation of 2.8V for xenon, 1.6V for krypton, 10V for argon and 7V for Kr/Xe at 929°C. Compare these with the envelope of several hundred volts found in mercury tests (figures 2.12 - 2.15).

Numerical simulation of the cathode flow has shown that pressure is an approximately linear function of $\dot{m}$ (see figure B.6 of appendix B). This coupled with the fact that the cathode-keeper separation was kept constant throughout the tests leads to the conclusion that the $\dot{m}$ vs. V_b plots will approximate the Paschen breakdown curves for the above gases. The gases, however, seem to exhibit anomalous breakdown behaviour. Argon (figure 6.3) possesses a double minimum instead of the expected one from Paschen's law. For the other gases we observe an increase in the breakdown potential at around 1mg/s followed by a decrease. We can then infer that the double minimum must exist for the other gases as well, as V_{bk} is expected to increase at higher $\dot{m}$ due to the decreasing electron mean free path not allowing primary electrons to gain enough energy for ionisation. Departure from Paschen behaviour is observed to be more pronounced at 929°C. This anomalous behaviour was also noted in the T6 open keeper work with xenon [124] (see also figure 2.18), and is here demonstrated to exist for all the gases investigated.

6.2.1.2 V_{bk} dependence on tip temperature

Figures 6.5 through to 6.8 illustrate the results of the investigation into the dependence of V_{bk} on tip temperature (T). Experiments were carried out, except in the case of the Kr/Xe mix, at two values of propellant flow rate for tip temperatures in the 916°C to 1422°C range.

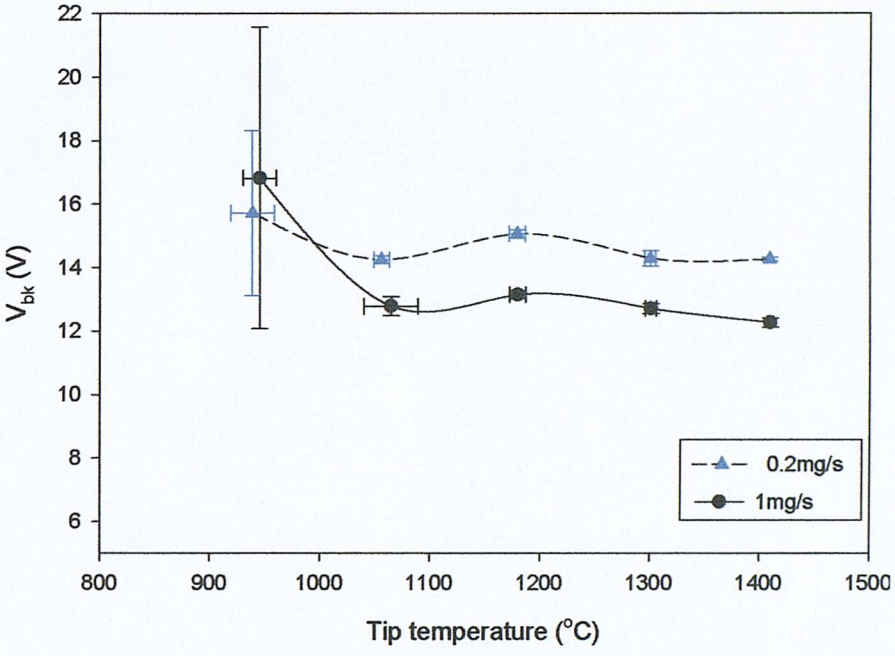

Figure 6.5: Discharge initiation voltage as a function of cathode tip temperature (Xe)

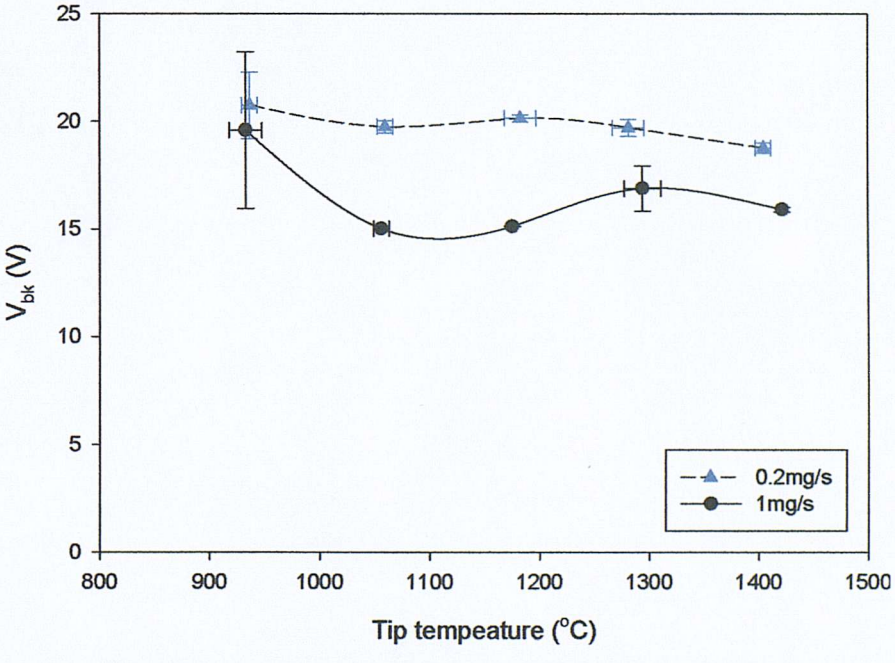

Figure 6.6: Discharge initiation voltage as a function of cathode tip temperature (Kr)

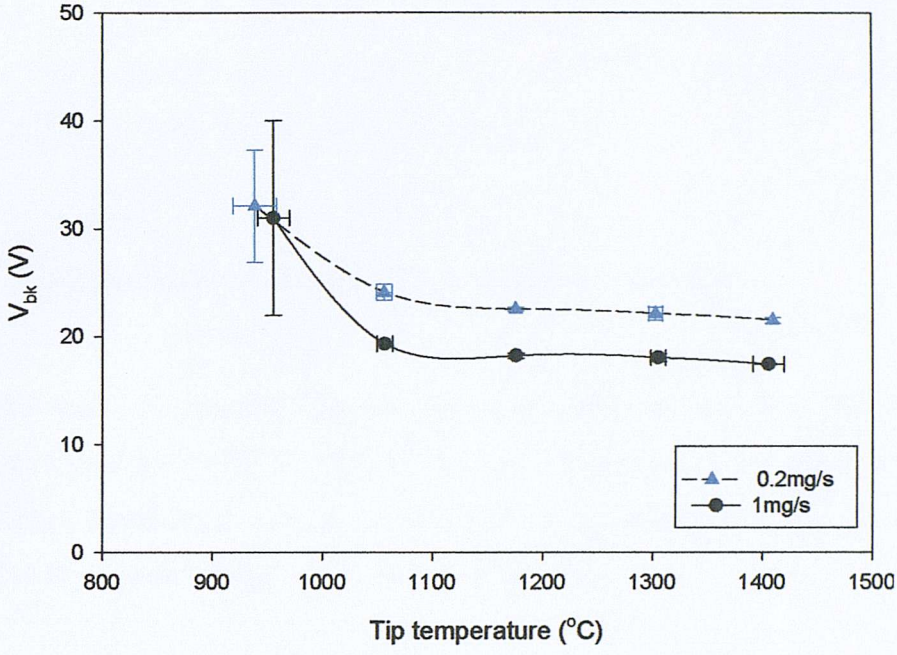

Figure 6.7: Discharge initiation voltage as a function of cathode tip temperature (Ar)

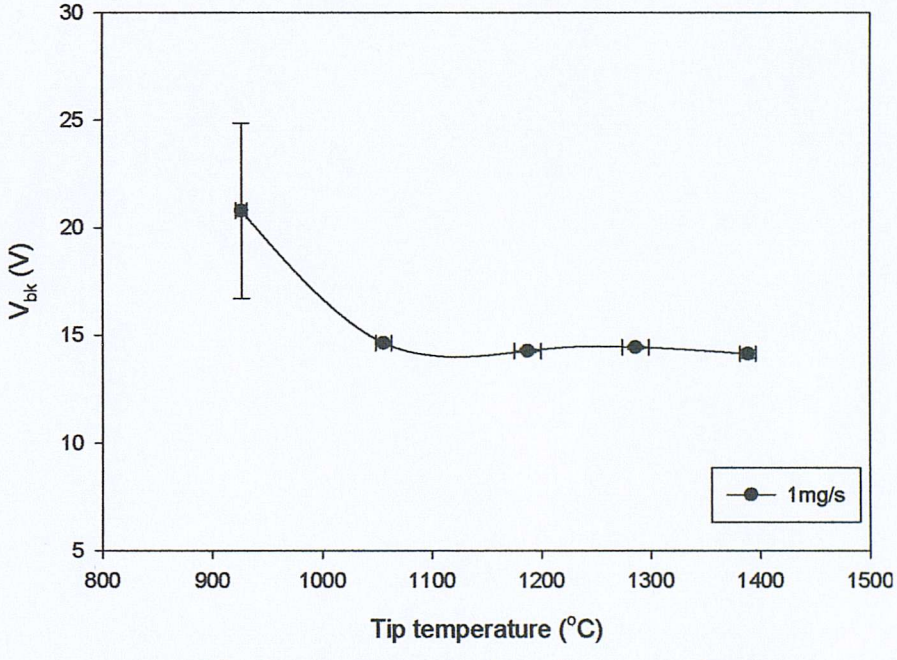

Figure 6.8: Discharge initiation voltage as a function of cathode tip temperature (Kr/Xe)

In general, for tip temperatures above 1100°C, the tip temperature has little to no effect on breakdown potential. When tip temperature is reduced below 1100°C, there is a dramatic increase in breakdown potential, which is also associated with an increase in the spread in the results. For T >1100°C in Ar and Xe, the higher mass

flow rate curve is at lower breakdown voltages. However the situation is unexpectedly reversed when tip temperature is brought below 1100°C. This is again consistent with results from the T6 open keeper work (refer to figure 2.17).

6.2.1.3 Comparison of the results for different gases

Figures 6.9 and 6.10 directly compare V_{bk} dependence on mass flow rate for all the propellants tested at 1299°C and 929°C respectively. Figures 6.11 and 6.12 compare the results of breakdown voltage dependence on tip temperature for all the gases involved at 1mg/s and 0.2mg/s flow rates respectively.

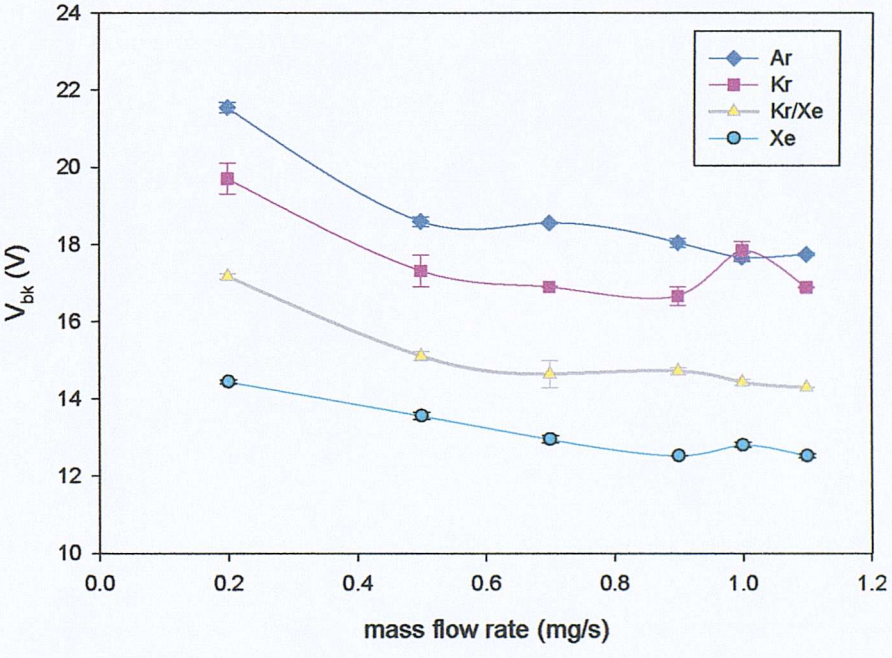

Figure 6.9: Comparison of V_{bk} as a function of $\dot{m}$ for Xe, Kr, Ar and Kr/Xe (at 1299°C tip temperature)

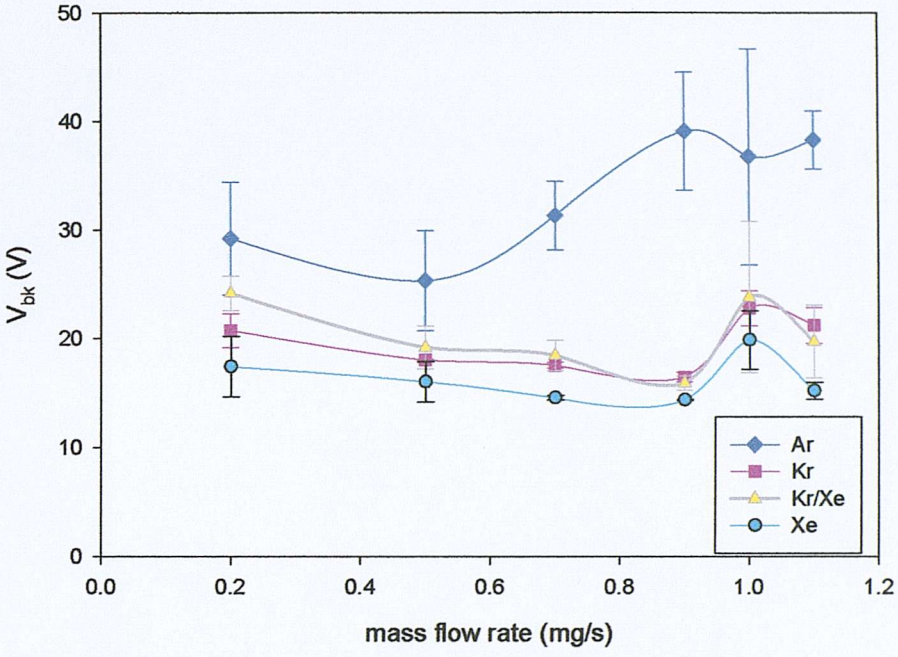

Figure 6.10: Comparison of V_{bk} as a function of $\dot{m}$ for Xe, Kr, Ar and Kr/Xe (at 929°C tip temperature)

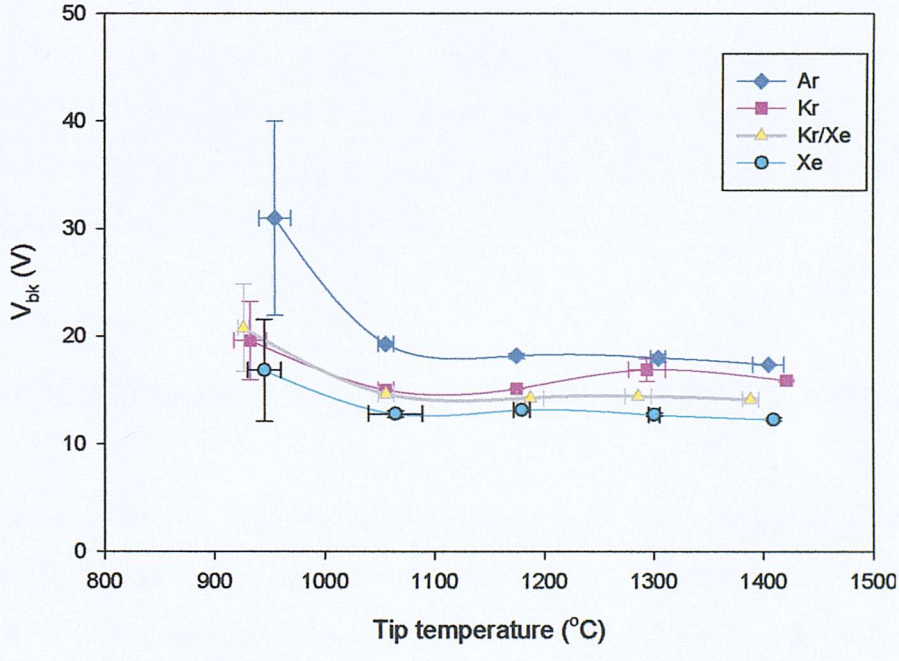

Figure 6.11: Comparison of V_{bk} as a function of T for Xe, Kr, Ar and Kr/Xe (at 1mg/s propellant flow rate)

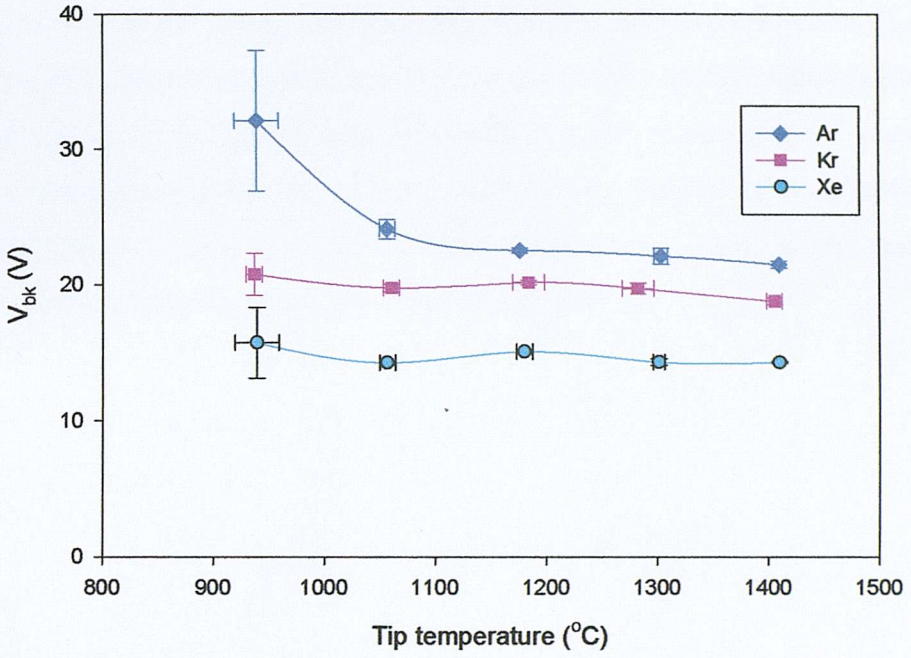

Figure 6.12: Comparison of V_{bk} as a function of T for Xe, Kr and Ar (at 0.2mg/s propellant flow rate)

The breakdown voltages are generally arranged, as would be expected, in the same order as the ionisation potentials of the gases: with xenon the lowest, followed by the Kr/Xe mix, then krypton and finally argon having the highest breakdown voltage for a given mass flow rate and tip temperature.

6.2.2 Hollow cathode breakdown plasma broadband optical study

Optical emission from the hollow cathode breakdown plasma was investigated using a photomultiplier tube. The PMT control voltage was initially set to maximum sensitivity (0.8V), then it was reduced to a value of 0.553V to prevent saturation of the detector.

6.2.2.1 Breakdown broadband emission dependence on $\dot{m}$ and T

Figure 6.13 shows a typical plot of plasma broadband optical emission and the keeper voltage behaviour during breakdown and the subsequent achievement of a stand-by

discharge (between the keeper and cathode) which is later transferred to the anode. Acquisition of data is triggered by the first negative slope on the keeper trace, which marks the onset of HC breakdown. The variation of photomultiplier signal with cathode conditions ($\dot{m}$ and T) is investigated for xenon, krypton and argon propellants. All the gases seem to exhibit similar trends, thus, in the interest of brevity, only the results for argon are shown in this section.

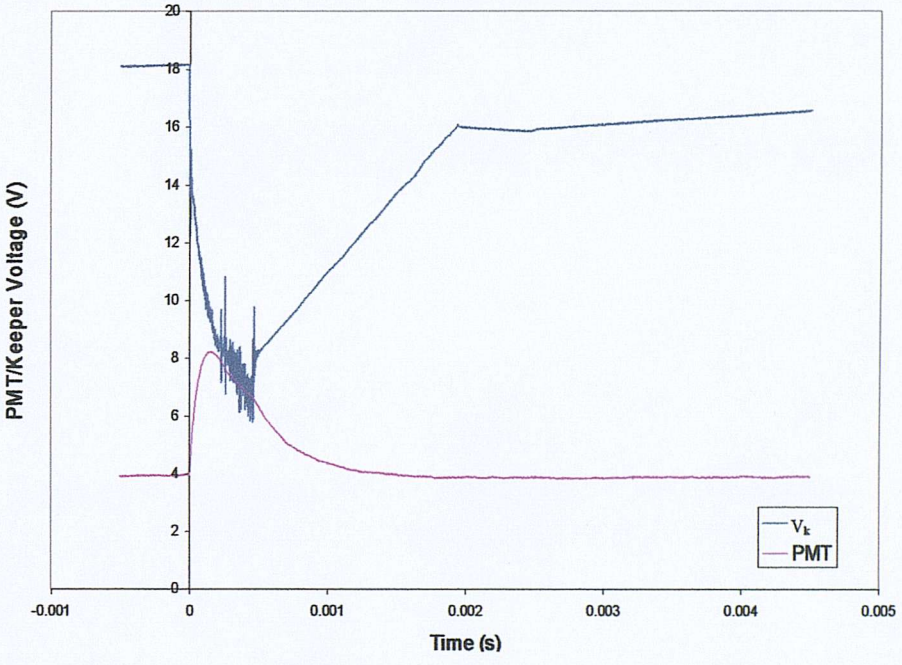

Figure 6.13: Plot of a typical result from PMT investigation of breakdown in argon (Art289, $\dot{m}$ =1mg/s and T=1299°C)

6.2.2.1.1 Optical emission dependence on mass flow rate

In this section breakdown optical signature and V_k variation with mass flow rate were investigated at constant tip temperature (1299°C), the results are shown in figure 6.14 and 6.15. The keeper voltages required for discharge initiation follow the trend shown in figure 6.3.

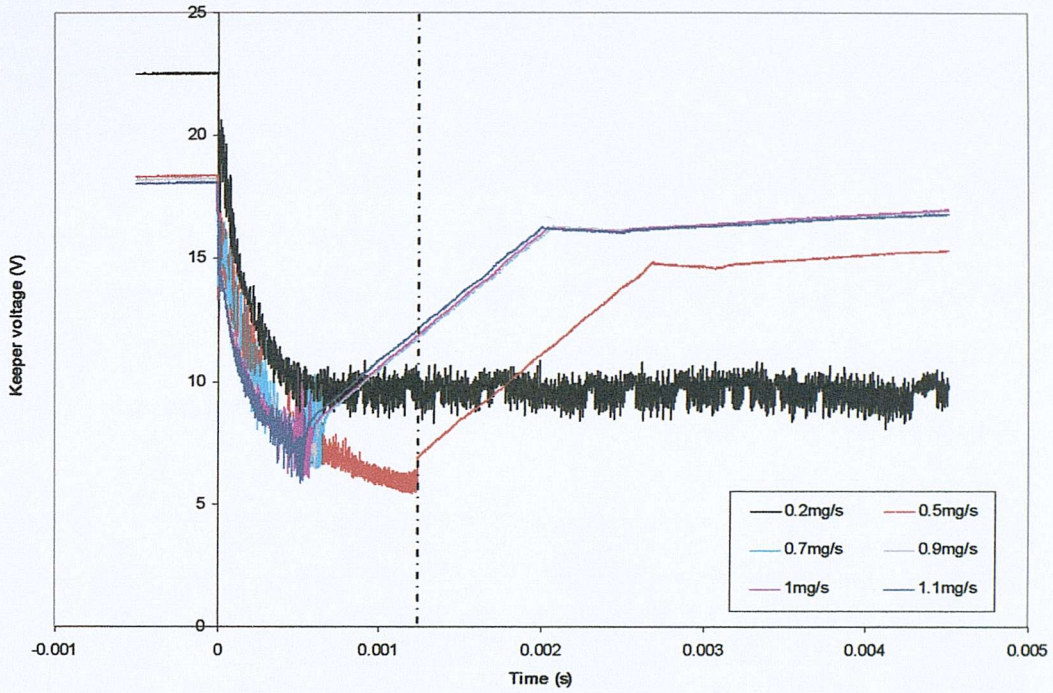

Figure 6.14: Plot of the dependence of V_k temporal behaviour on mass flow rate during breakdown (1299°C)

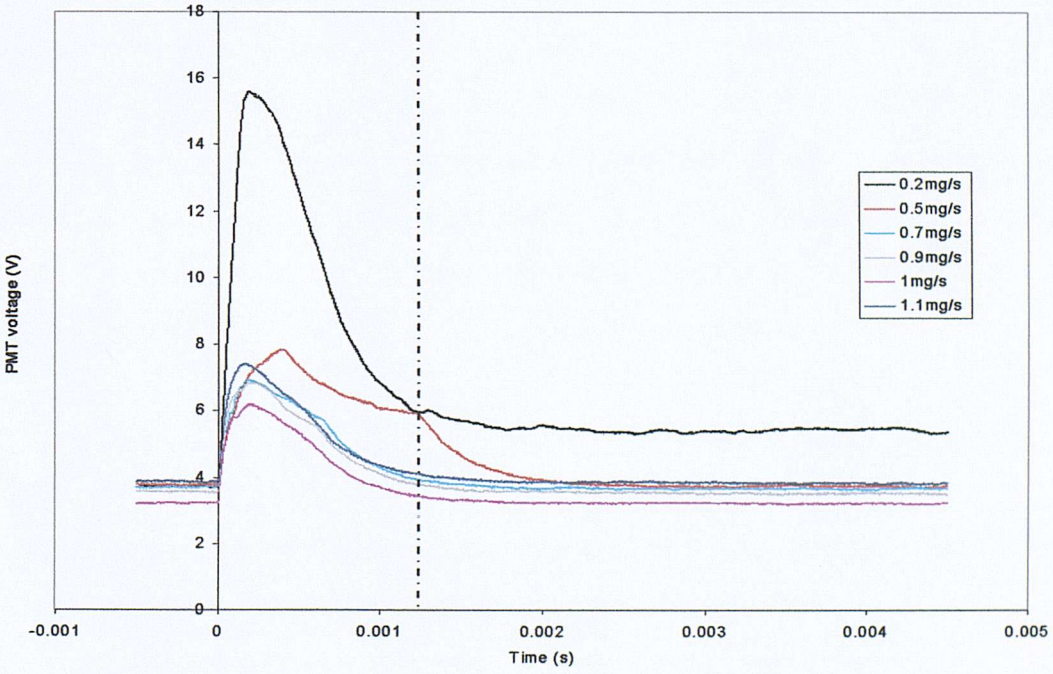

Figure 6.15: PMT output voltage during breakdown, dependence on mass flow rate (1299°C)

Following breakdown, the V_k trace goes through two distinct regimes before achieving a stand-by discharge. The first region constitutes a rapid and noisy drop in V_k. The discharge experiences this noisy region for a period that can last from 0.4ms to over 5ms (= the total observation time of the experiment). The length of time spent in the noisy period seems to be inversely proportional to $\dot{m}$, decreasing as $\dot{m}$ is increased. The second phase involves a linear, quiescent increase (recovery) in V_k, till voltage levels required to maintain a stand-by discharge are achieved. The rate of recovery (i.e. the slope of V_k in the recovery phase) is virtually the same regardless of $\dot{m}$ or T, and has a value of approximately 5.46V/ms with a standard deviation of only 0.6% of the average value. The total time required to achieve a stand-by discharge is again found to be inversely proportional to $\dot{m}$.

The photomultiplier output signals corresponding to those of V_k at the specified mass flow rates are shown in figure 6.15. The pre-breakdown section of the plot shows the PMT signal due to the blackbody emission from the hot cathode. The experiments were carried out at approximately constant tip temperature, thus the pre-breakdown section for all $\dot{m}$ are close to each other in value. Post-breakdown, the light emission from the plasma depends on V_k behaviour. If the duration of the noisy region in the V_k trace is less than 0.8ms, the PMT output reaches a maximum in 0.5ms or less and then decreases smoothly to approximately pre-breakdown levels. When the duration of the noisy region is around 0.8ms or more, the PMT trace increases in a similar fashion to the first case till it reaches a maximum. The subsequent decrease in the PMT trace takes place in a two step process. It first decreases to a value intermediate between the maximum and pre-breakdown levels and remains at that value until the noisy region in the V_k trace ends. At exactly the same time the PMT output commences a second decrease until it achieves pre-breakdown levels. This is shown in figures 6.14 and 6.15 for 0.5mg/s, where the dashed line indicates the end of the noisy region for V_k in figure 6.14 and the corresponding, concurrent decrease in PMT output. Note also that in cases where the duration of the noisy region exceeds the observation time, such as the curves for 0.2mg/s, we only observe the first step of the above process and the PMT trace does not return to pre-breakdown levels.

The 0.2mg/s PMT trace seems to have a significantly higher maximum than the rest. One probable explanation is that this is due to a combination of the higher initial energy input to breakdown the gas (see figure 6.14) and the decreased radiation trapping with the lower neutral number density leading to the stronger signal. However, this cannot be determined without measurement of the growth of breakdown current and spectroscopic data on the growth of breakdown plasma.

6.2.2.1.2 Optical emission dependence on tip temperature

Figure 6.16 and 6.17 show the V_k and the corresponding PMT records for the investigation carried out to determine the effect of variations in tip temperature on optical emission from breakdown plasma. Tip temperature has a similar effect to $\dot{m}$ on V_k, with both the duration of the noisy part of V_k and the total time to achieve a stand-by discharge being inversely proportional to T. The recovery phase of the V_k trace again proceeds at the same rate regardless of T till stand-by levels are achieved.

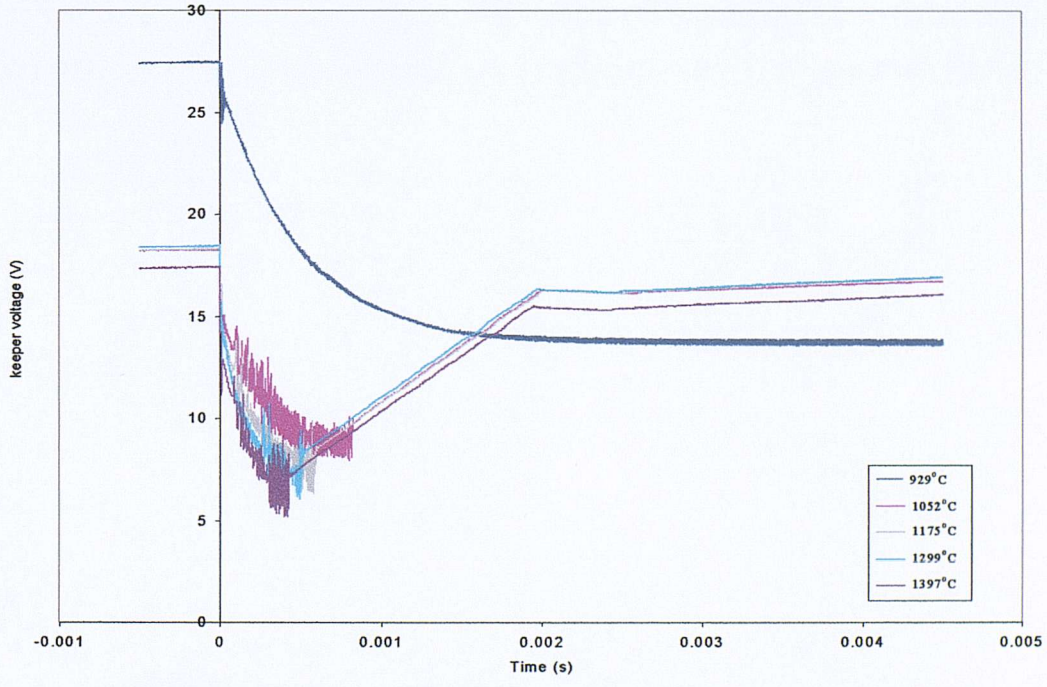

Figure 6.16: Plot of the dependence of V_k temporal behaviour on tip temperature during breakdown (1mg/s)

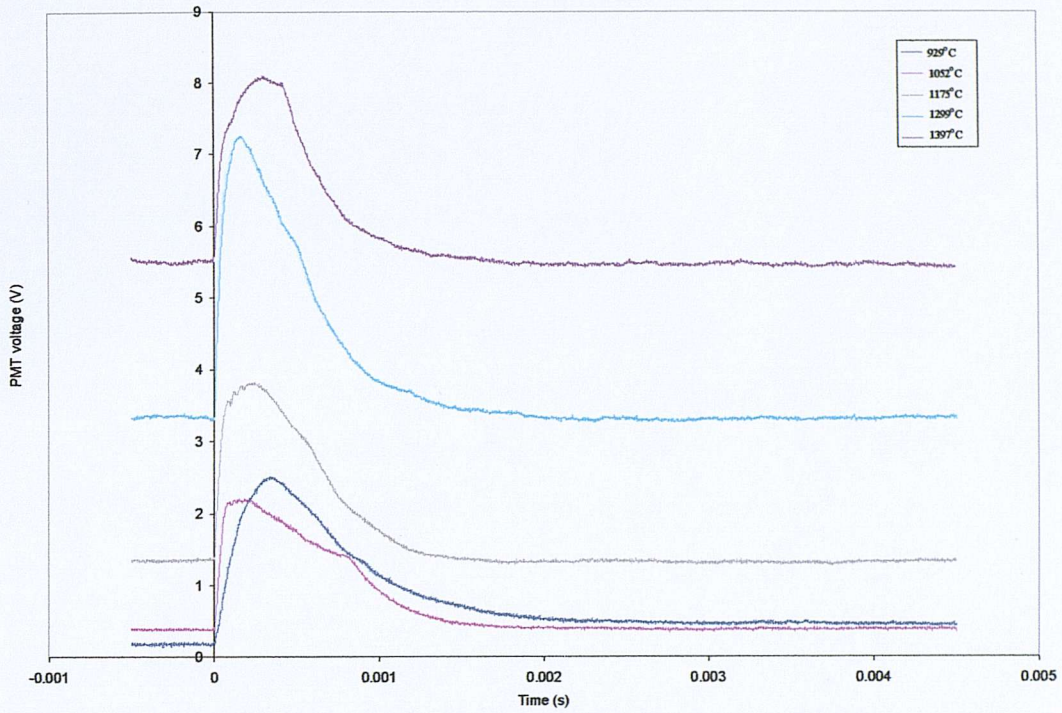

Figure 6.17: PMT output voltage during breakdown, dependence on tip temperature (1mg/s)

The pre-breakdown sections of the PMT signals are clearly arranged, as expected, according to the tip temperature of the hollow cathode. The PMT trace exhibits the same behaviour as previously encountered in the $\dot{m}$ results, with the section immediately following breakdown increasing to a maximum, followed by a decrease, dependent on the character of the V_k trace, to approximately pre-breakdown levels.

6.3 Steady-state results

Initially the aim of investigating the T6 hollow cathode in steady state was to identify the emission lines most suitable for breakdown spectroscopy. However, the investigation grew into an independent test program involving the characterisation of the discharge, the acquisition of emission spectra of the discharge over a wide wavelength range and the determination of the effect of the cathode operating characteristics on emission line behaviour. These tests were carried out over a wide range of test conditions and utilised all the gases used in discharge initiation experiments (i.e. argon, krypton, xenon and the krypton/xenon mix)

6.3.1 Discharge characterisation

As mentioned in chapter 2, the hollow cathode has two clearly distinct modes of operation: Namely, the spot and plume modes, with the spot mode being the more stable and less noisy of the two. It was therefore necessary, prior to any spectroscopic work being carried out, to establish under which conditions these modes occur for all the propellants involved.

There exists a considerable body of data on the discharge characteristics of alternative inert gas propellants in full thruster geometry [33, 104, 112, 150, 188, 190], however, a smaller number of studies has directly compared the different inert gases [33, 189 , 190]. Moreover, in full geometry, the plume mode is suppressed and no plume to spot transition is observed, only a couple of studies compared the various gases in diode configuration [51, 191] and observed the associated dual-mode operation. No previous work has utilised a Kr/Xe mix (or any mixture of inert gases) as propellant. In addition, particularly for the T6, the krypton and argon results of this work are unique.

A detailed analysis of the discharge behaviour, in particular that of the plume phase of operation, will be left for the next chapter, where it will be utilised in the formulation of a theoretical description of the plume and spot modes. We will concentrate here

mostly on describing trends and salient features of the *V-I* and *V-ṁ* characteristics in the spot mode.

6.3.1.1 Discharge voltage-current characteristics

The discharge current was increased in steps of 0.5A every minute from 1 to 5A and the process was then reversed, with keeper current kept at 1A throughout. Due to the wiring problem mentioned in section 5.3.1.2 the discharge current range investigated was limited to the 1-5A range. This limited current range complicated matters by not allowing a plume to spot transition to be observed on the *V-I* characteristics at every given value of mass flow rate. So a compromise was reached by investigating the discharge characteristics at several values of mass flow rate, where keeper (V_k) and anode (V_a) voltage dependence on discharge current (I_a) was observed separately, in the plume mode at low values of $\dot{m}$, and in the spot mode at high values of $\dot{m}$. Figure 6.18 shows the complete time trace of two such experiments for xenon discharge variation of V_a and V_k with I_a.

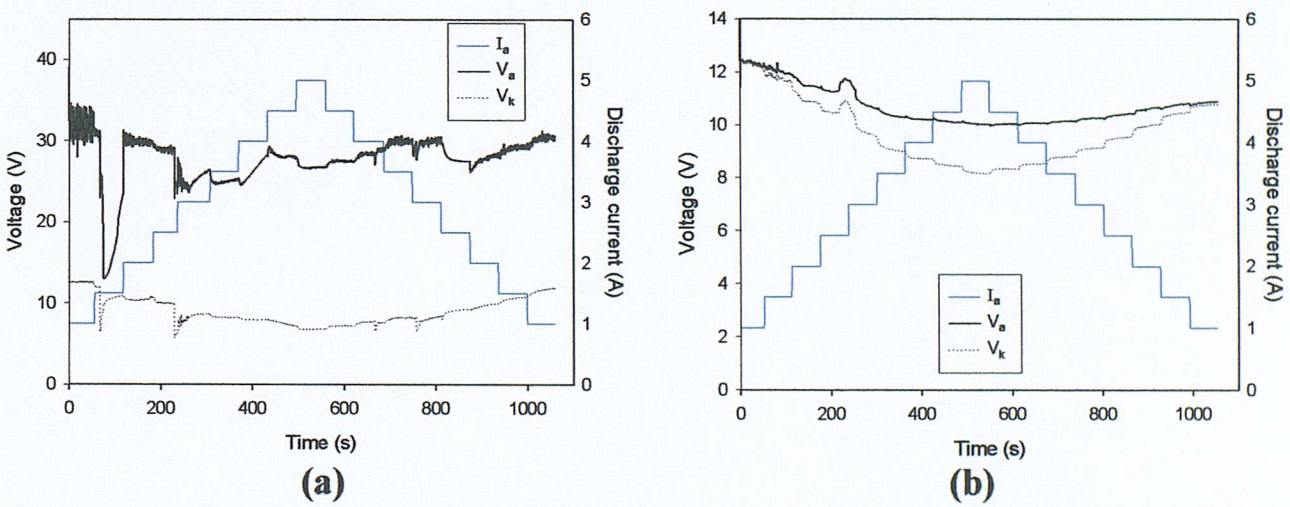

Figure 6.18: Discharge voltage dependence on I_a for xenon discharge at **(a)** *1mg/s (plume mode) and* **(b)** *3.29mg/s (spot mode)*

The plume mode (figure 6.18(a)) is characterised by its high noise levels and high anode potentials. There also appears to be a hysteresis effect: the voltage values are not reproducible. The spot mode (figure 6.18(b)), on the other hand, shows a more

stable discharge with lower noise levels. Moreover, the anode potentials are reduced to approximately keeper levels. Again, a hysteresis effect is present. The discharge seems to exhibit a negative *V-I* characteristic, i.e. the discharge impedance in spot mode seems to decrease with increasing discharge current.

The most widely accepted reason for hysteresis is that the cathode does not reach thermal equilibrium during the one minute it is allowed. The power (*I*×*V*) supplied to the cathode controls the cathode wall temperature, which in turn is thought to control electron production. If the power requirement is changed prior to re-establishing thermal equilibrium, a dependency on the previous power setting (i.e. whether the cathode is being heated up or cooled down) is introduced into the results and hence the hysteresis effect [40, 115].

Anode *V-I* characteristics are demonstrated graphically, for a number of flow rates, in figures 6.19-6.22 for the xenon, krypton, argon and Kr/Xe mix propellants. Figure 6.23 compares the spot mode voltage-current characteristics of the various gases.

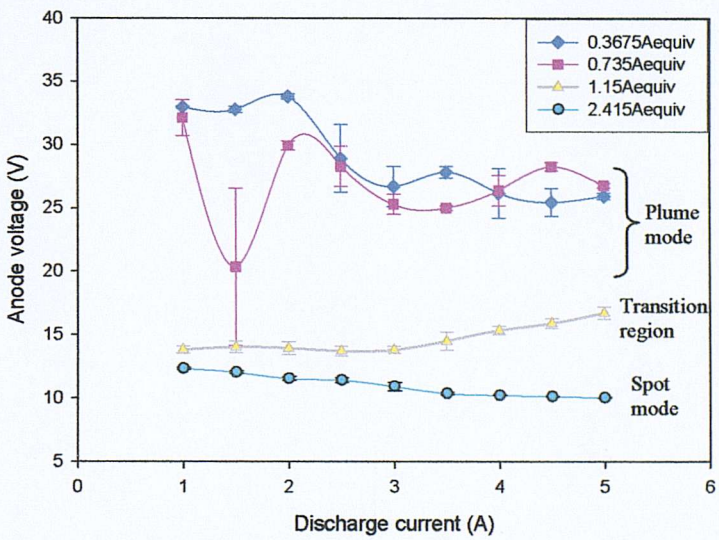

Figure 6.19: Anode V-I characteristics for the T6 operating on xenon

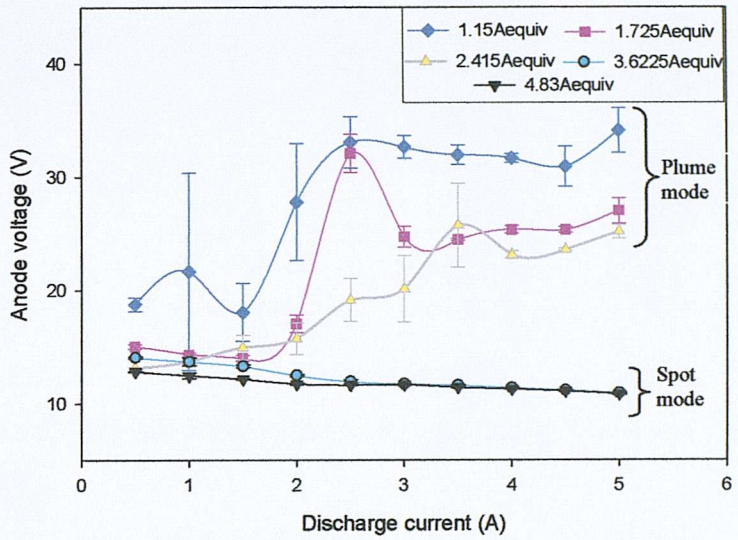

Figure 6.20: Anode V-I characteristics for the T6 operating on krypton

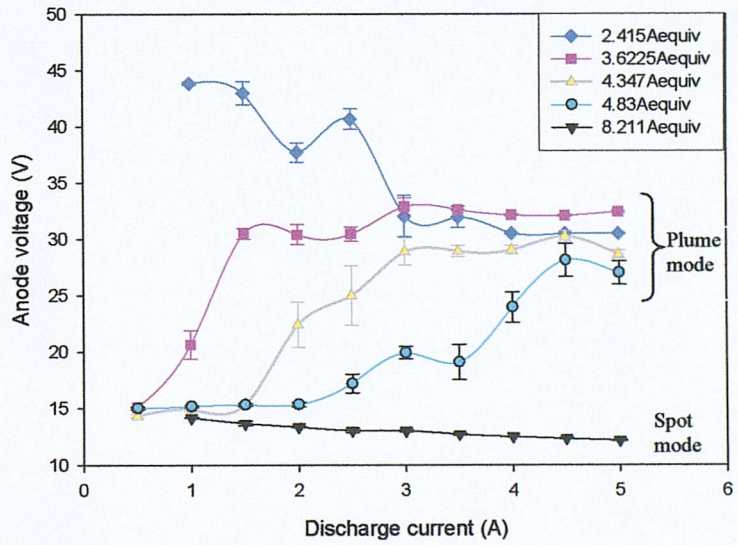

Figure 6.21: Anode V-I characteristics for the T6 operating on argon

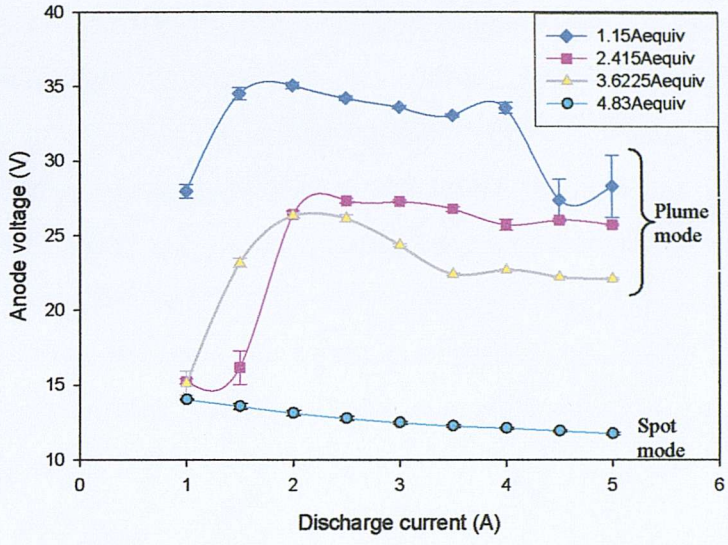

Figure 6.22: Anode V-I characteristics for the T6 operating on Kr/Xe

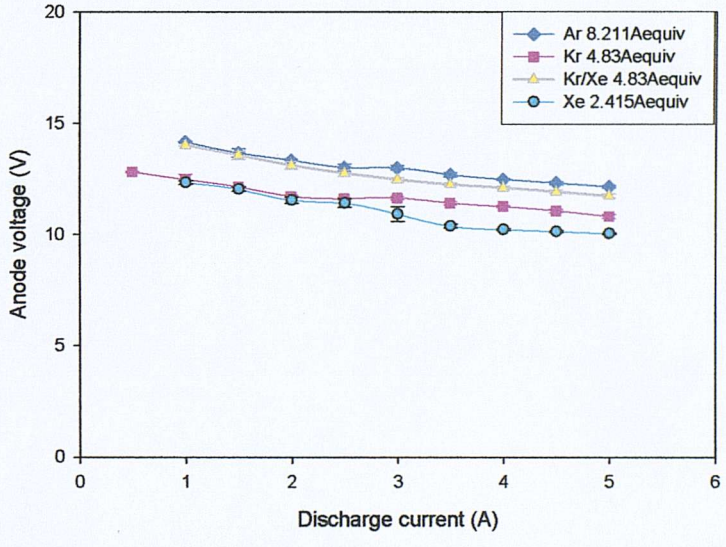

Figure 6.23: Comparison of anode V-I characteristics for all gases in the spot mode

All the gases indeed exhibited the same overall behaviour experienced in the past with xenon and mercury, i.e. the discharge exhibits high discharge potentials accompanied by significant noise levels at low $\dot{m}$ (plume mode), when the flow rate is increased beyond a certain value, the *V-I* characteristic showed an abrupt large drop in anode potential with almost negligible noise levels indicating the onset of the spot mode of operation. The anode characteristics in the spot mode show a negative voltage current characteristic for all the gases. The gradient of the *V-I* curve is steepest at low discharge currents, with the slope reducing with increasing current. It has been determined that the establishment of the spot mode required progressively higher flow

rates and discharge potentials as the propellant atomic mass is reduced. For the pure gases, the discharge potential was arranged according to the ionisation potential of the gas, with xenon lowest, followed by krypton and highest for argon. It is interesting to note that the discharge characteristics of the Kr/Xe mix were actually higher than those of krypton, while they were expected to be intermediate between those of krypton and xenon. However, it has to be emphasised that, notwithstanding the large difference in the flow rate required for the spot mode between say argon and xenon, the difference between the operating anode potentials although tangible is actually quite small (<2.3V).

Figure 6.24 shows the dependence of the keeper potential (V_k) on discharge current for xenon plasma under the discharge conditions shown previously in figure 6.19. The results for the other gases show qualitatively similar behaviour as figure 6.24 and are not shown here. In general, V_k was virtually independent of flow rate, showing an overall negative voltage-current behaviour regardless of the mode in which the discharge is operating, with the only indication of transition being a reduction in the noise on the keeper trace.

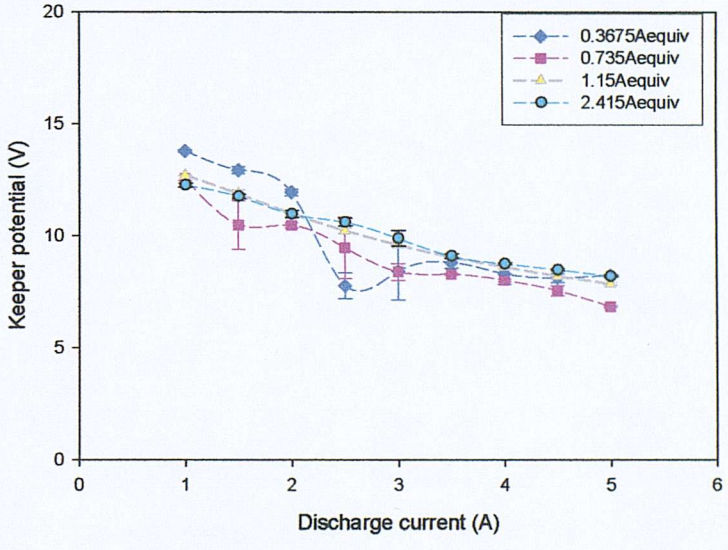

Figure 6.24: Keeper V-I characteristics for the T6 operating on xenon

6.3.1.2 Discharge voltage dependence on $\dot{m}$

With the limitations on the range of discharge current, the only possible means for

observing the plume to spot transition is by variation of the flow rate at constant discharge current. Figure 6.25 shows the complete time trace of such an experiment for xenon discharge variation of V_a and V_k with $\dot{m}$, where the discharge and keeper currents were set at 5A and 1A respectively.

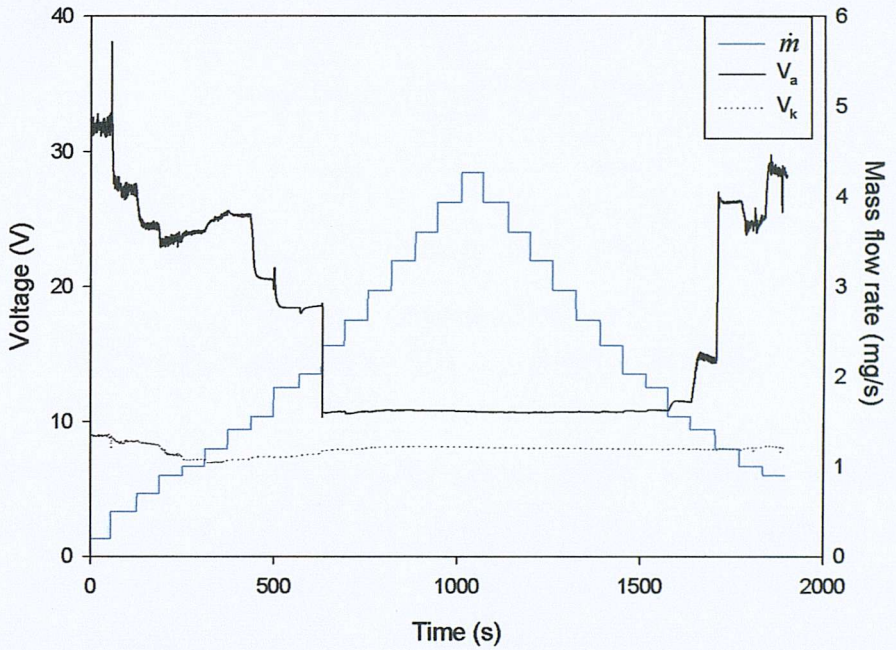

Figure 6.25: Discharge voltage dependence on $\dot{m}$ for xenon discharge at 5A anode current

The mass flow rate is investigated in the range 0.2 - 3.61mg/s, with a variable step size to allow comparison with other propellants (this is described in more detail in section 5.3.4). As the mass flow rate is increased, mode change occurs at 2.35mg/s. When, after reaching maximum, the mass flow rate is decreased, the change back to plume mode occurs at 1.2mg/s, i.e. we experience hysteresis much in the same way as the *V-I* characteristics. There is a change of around 10V in discharge voltage when mode change occurs. The keeper voltage does not seem to be strongly influenced by the transition from spot to plume mode, with the only clear indication of a mode change being a reduction in keeper noise.

Figure 6.26 compares the anode voltage flow rate dependence for the various gases.

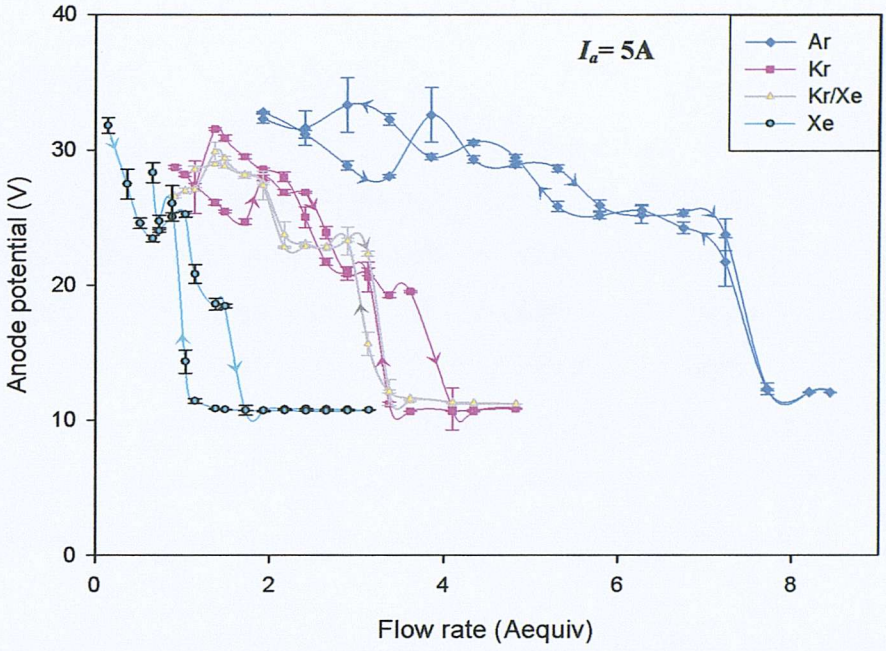

Figure 6.26: Comparison of V_a as a function of $\dot{m}$ for all gases

With reference to figure 6.26, we note that the plume to spot transition is species dependent, with higher values of $\dot{m}$ required to achieve spot mode as the species atomic weight is reduced. Transition in all gases show a hysteresis effect, with the spot mode extending to lower flow rates as $\dot{m}$ is reduced. When in spot mode the anode potential of the various gases are arranged, like those for the *V-I* characteristics, according to their ionisation potentials, with the Kr/Xe mix again showing discharge potentials higher than those for krypton and xenon.

6.3.2 Full optical emission spectra experiments

This section deals with the qualitative determination of the plasma chemical composition from emission line identification for argon, krypton and xenon discharges. Quantitative treatment of the spectra through the determination of plasma parameters and comparison of spectra at different modes and discharge conditions is left for later discussion. As described in section 5.3.5.2, the discharge was first investigated using a 300l/mm grating in the 200nm to 750nm range (Only results for the xenon discharge with 300l/mm grating are displayed here) and then a 2400l/mm grating was used to resolve the finer details of the spectrum. The choice of the 400 to 463nm range for the finer grating was based on various considerations, such as the availability of spectroscopic data and the spectral efficiency of the grating.

6.3.2.1 Xenon results

Optical emission from xenon plasma in a hollow cathode was recorded over the ranges specified above using both gratings. Figure 6.27 shows the spectrum obtained using the 300l/mm grating over the 200nm to 760nm range, at 1mg/s (0.735Aequiv) flow rate and 5A discharge current. The keeper current was set at 1A and the discharge voltage was 24.2V. Figure 6.28 shows the spectrum obtained using the 2400l/mm grating in the 400 - 463nm range. The cathode was operated here at 5A discharge current, 1A keeper current, 1mg/s propellant flow rate and 24.4V discharge voltage. In both the above cases the discharge was in the plume mode.

The spectra shown here are the calibrated results. They, however, are not corrected for the spectral transmission properties of the optics and the spectral response of the detector.

Both spectra are dominated by xenon emission lines (I & II), with some impurity (BaII) lines, superimposed on a weak continuum (not visible in the plots). 40 lines were identified in the spectrum shown in figure 6.28, with table 6.1 listing some of these lines. The first column in table 6.1 identifies the emitting species. The next column lists the calibrated emission line wavelength detected by the CCD. The third column lists the wavelength of the identified lines obtained from various sources [177, 178, 179, 180, 181]. The next two columns give the difference in nanometres between the observed and tabulated wavelength of the identified line, followed by the degree of confidence in identification: whether it is positive or tentative. We then give the tabulated relative intensity of the line from the literature. The last six columns are dedicated to the atomic properties of the emitting species associated with the transition, detailing in the following order: the atomic transition levels, the atomic transition probability of the radiative transition, the statistical weights of the lower and upper levels and finally the energies of the lower and upper levels.

Spectra were also obtained for xenon discharges at 1.56mg/s (1.15Aequiv) and 3.29mg/s (2.415Aequiv) flow rates.

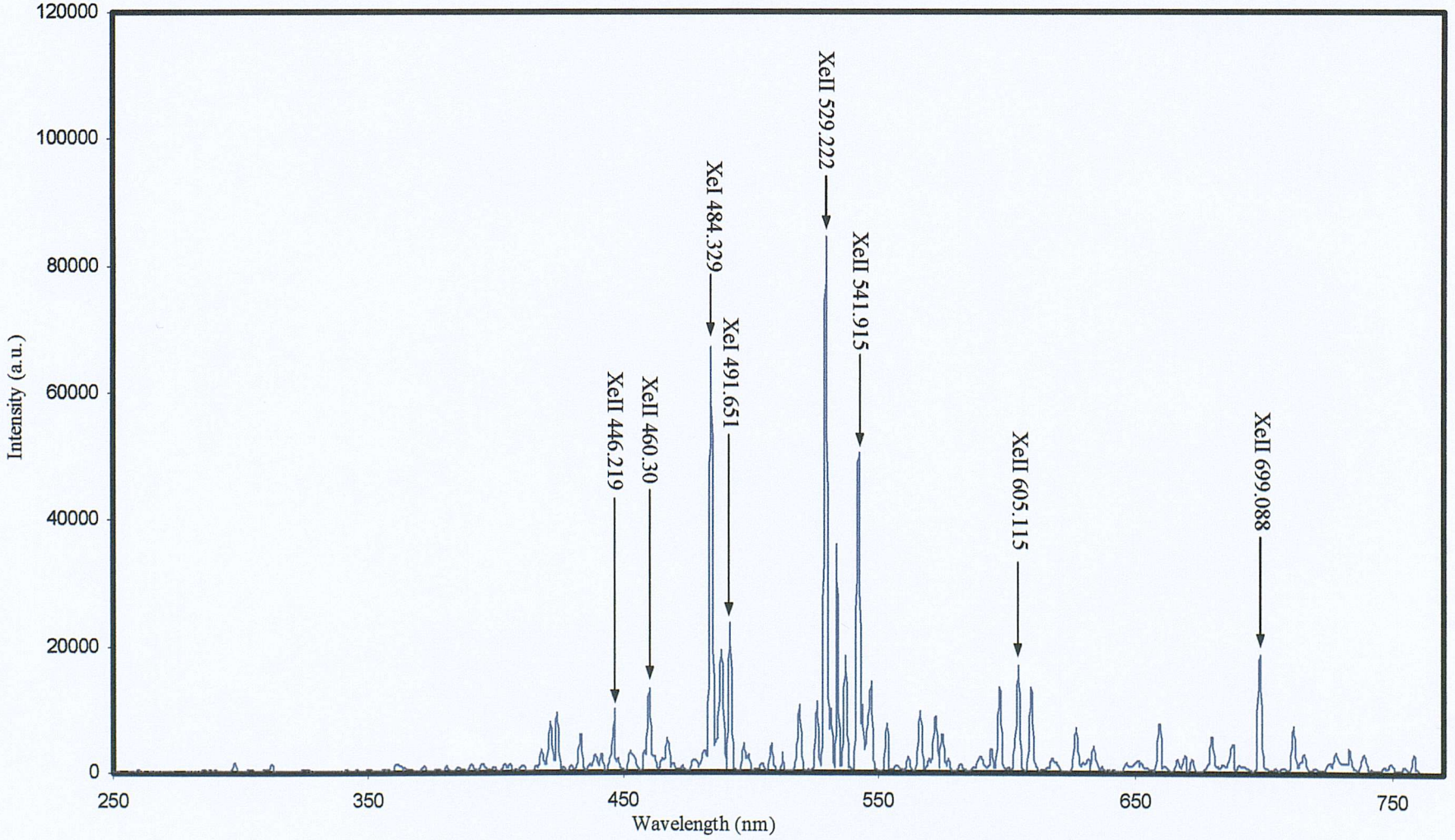

Figure 6.27: Optical emission spectrum from the hollow cathode internal plasma with xenon at 1mg/s and 5A discharge current (300l/mm grating)

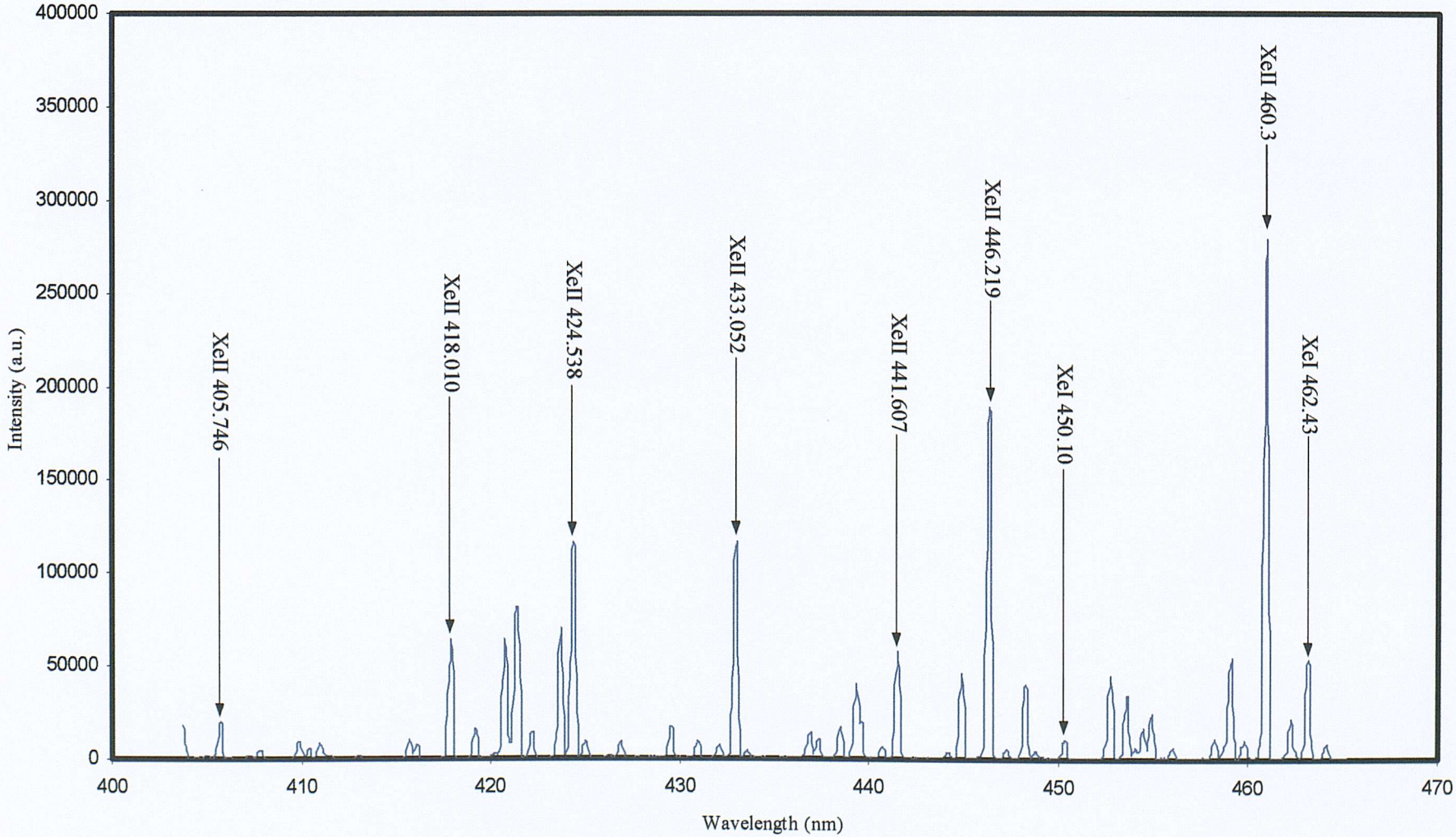

Figure 6.28: Optical emission spectrum from the hollow cathode internal plasma with xenon at 1mg/s and 5A discharge current (2400l/mm grating)

Element	Observed Wavelength (nm)	Tabulated Wavelength* (nm)	Δ Wavelength (nm)	Identification (Positive, Tentative)	Relative Intensity*	Transition*	A_{pq}* ($\times 10^8$ s^{-1})	g(q)*	g(p)*	E(q)* (eV)	E(p)* (eV)
XeII	403.6222	403.759	-0.1368	P	100	6p $^2S^o$ - 6d ^2D	--------	2	4	15.02	18.09
XeII	405.6786	405.746	-0.0674	P	200	6p $^4P^o$ - 6d ^4F	--------	6	8	13.89	16.93
XeII	409.8257	409.889	-0.0633	P	100	6p $^4P^o$ - 12	--------	2	4	14.09	17.12
XeII	415.6891	415.804	-0.1149	P	200	6p $^2S^o$ - 6d ^2P	--------	2	2	15.02	18.00
XeII	417.9367	418.010	-0.0733	P	1000	6p $^4P^o$ - 6d ^4D	2.2	4	4	13.86	16.82
XeII	419.2421	419.315	-0.0729	P	500	--------	--------	--------	--------	--------	--------
XeII	420.7906 →	420.848	-0.0574	T	300	6p $^4P^o$ - 6d ^4D	--------	4	6	13.86	16.80
XeII		420.947	-0.1564	T	100	6p $^4P^o$ - 6d ^4D	--------	6	4	13.89	16.82
XeII	421.4084 →	421.372	0.0364	T	300	6p $^4D^o$ - 6d ^4P	--------	2	4	14.93	17.87
XeII		421.560	-0.1516	T	100	6s ^4P – 6p $^4D^o$	--------	6	4	11.54	14.48
XeII	422.2101	422.300	-0.0899	P	300	6p $^2P^o$ - 14	--------	4	6	15.28	18.22
XeII	423.7472	423.825	-0.0778	P	400	6p $^4P^o$ - 6d ^4D	--------	6	6	13.89	16.80
XeII	424.4216	424.538	-0.1164	P	500	6p $^4P^o$ - 6d ^4D	--------	6	8	13.89	16.80
XeII	425.0949	425.157	-0.0621	P	100	6p $^2P^o$ - 6d' ^2D	--------	2	4	15.44	18.36
XeII	429.5943	429.640	-0.0457	P	500	6p $^4P^o$ - 7s ^4P	--------	4	2	13.86	16.74
XeII	430.9821	431.051	-0.0689	P	500	6p $^2D^o$ - 7s' ^2D	--------	6	6	15.26	18.14
XeII	432.9646	433.052	-0.0874	P	1000	6p $^4D^o$ - 6d ^4F	1.4	6	8	14.07	16.93
XeII	436.839	436.920	-0.081	P	200	6p $^4P^o$ - 18	--------	2	2	14.09	16.93
XeII	437.313	437.378	-0.065	P	100	6p $^4D^o$ - 6d ^4F	--------	4	4	14.48	17.31
XeII	439.321 →	439.320	0.001	T	500	6p $^4S^o$ - 6d ^2D	--------	4	6	15.08	17.90
XeII		439.577	-0.256	T	500	6d' ^2F – 6f' ^2F	--------	6	8	14.23	17.05
XeII	440.6731	440.688	-0.0149	P	200	6p $^2P^o$ - 6d ^2D	--------	4	4	15.28	18.09
XeII	441.4937 →	441.484	0.0097	T	300	5d ^2D – 6p' $^2D^o$	1.0	6	6	13.58	16.39
XeII		441.607	-0.1133	T	150	6p $^2D^o$ - 14	--------	4	6	15.41	18.22
XeII	444.7571	444.813	-0.0559	P	500	--------	--------	--------	--------	--------	--------
XeII	446.2044	446.219	-0.0146	P	1000	--------	--------	--------	--------	--------	--------
XeII	448.1057	448.086	0.0197	P	500	6p $^4D^o$ - 6d ^4F	--------	4	6	14.48	17.24
XeI	450.1108	450.100	0.0108	P	500	6s [3/2]^o – 6p' [1/2]	6.2×10^{-3}	5	3	8.31	11.07
XeII	452.4448 →	452.186	0.2588	T	100	6p' $^2D^o$ – 6d' ^2F	--------	4	6	16.36	19.10
XeII		452.421	0.0238	T	200	6s ^4P – 6p $^2P^o$	--------	2	4	12.54	15.28
XeI		452.47	-0.0252	T	400	6s [3/2]^o – 6p' [3/2]	2.1×10^{-3}	5	5	8.31	11.05
XeII	460.4600	460.30	0.16	P	600	6s ^4P – 6p $^4D^o$	8.2×10^{-1}	4	4	11.79	14.48
XeI	462.5571	462.43	0.1271	P	1000	6s [3/2]^o – 7p [3/2]	7.2×10^{-3}	5	5	8.31	10.99
BaII	426.9253	426.795	0.1303	T	800	--------	--------	--------	--------	--------	--------
BaII	455.663	455.403	0.26	T	65000	--------	1.17	2	4	0.00	2.72

Table 6.1: Identified emission lines for xenon discharge (2400l/mm grating)
** [177, 178, 179, 180, 181]*

6.3.2.2 Krypton results

Figure 6.29 shows the optical emission from a T6 krypton discharge. The spectrum was obtained by using the 2400l/mm grating in the 400-460nm range. The cathode was operated at 5A discharge current, 1A keeper current and 1mg/s (1.15Aequiv) propellant flow rate, the discharge voltage was 28V. The discharge was in the plume mode.

The spectrum is the calibrated result, but like the xenon case it is not corrected for the spectral transmission properties of the optics and the frequency response of the detector. The spectrum is dominated by krypton species (I & II) superimposed on a weak continuum. Barium emission lines were again detected. From figure 6.29, 45 lines were identified, table 6.2 lists some of those lines and is arranged in a fashion similar to table 6.1.

Spectra of krypton plasma were also obtained at 2.1mg/s (2.415Aequiv) and 3.78mg/s (4.347Aequiv) flow rates.

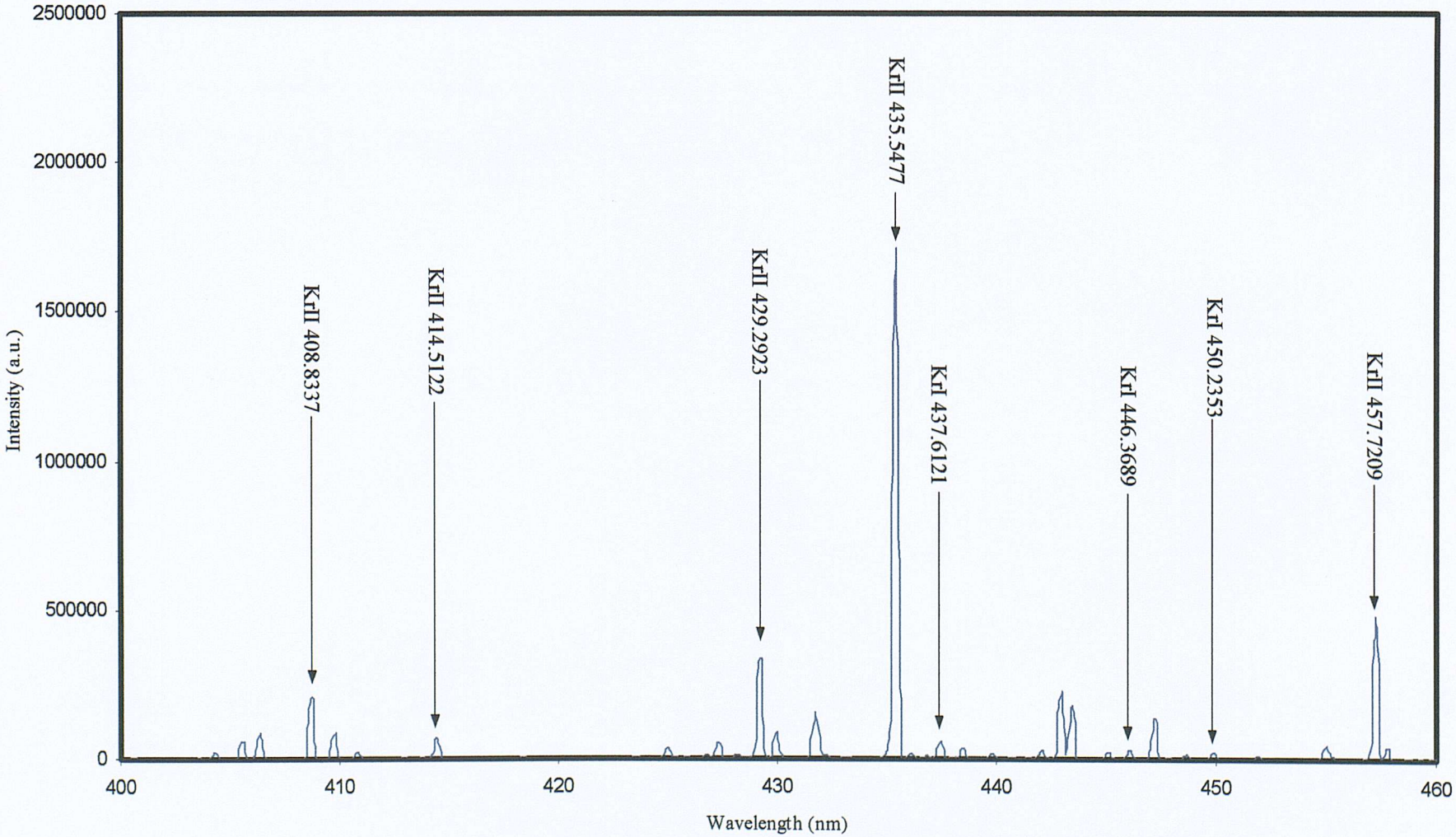

Figure 6.29: Optical emission spectrum from the hollow cathode internal plasma with krypton at 1mg/s and 5A discharge current (2400l/mm grating)

Element	Observed Wavelength	Tabulated Wavelength* (nm)	Δ Wavelength (nm)	Identification (Positive, Tentative)	Relative Intensity*	Transition*	A_{pq}* ($\times 10^8$ s^{-1})	g(q)*	G(p)*	E(q)* (eV)	E(p)* (eV)
KrII	405.7448	405.7037	0.0411	P	300	$5s'\ ^2D - 5p'\ ^2P^o$	--------	4	2	15.82	18.87
KrII	406.5087	406.5128	-0.0041	P	300	$5s'\ ^2D - 5p'\ ^2D^o$	--------	4	4	15.82	18.87
KrII	408.8562	408.834	0.0225	P	500	$5s'\ ^2D - 5p'\ ^2D^o$	--------	6	6	15.85	18.88
KrII	409.8675	409.8729	-0.0054	P	250	$5s\ ^4P - 5p\ ^2D^o$	--------	2	4	14.58	17.60
KrII	410.9395	410.9248	0.0147	P	100	$5s'\ ^2D - 5p'\ ^2D^o$	--------	6	4	15.85	18.87
KrII	414.5148	414.512	0.0026	P	250	$5s\ ^4P - 5p\ ^4S^o$	--------	2	4	14.58	17.57
KrII	425.0653	425.058	0.0073	P	150	$5s\ ^2P - 5p\ ^2D^o$	1.2×10^{-1}	4	4	14.69	17.60
KrI	427.3741	427.3969	-0.0228	P	1000	$5s\ [3/2]^o - 6p\ [3/2]$	2.6×10^{-2}	5	5	9.91	12.82
KrI	428.3424	428.297	0.0457	P	100	$5s\ [3/2]^o - 6p\ [3/2]$	--------	5	3	9.91	12.81
KrII	429.3083	429.2923	0.016	P	600	$5s\ ^4P - 5p\ ^4D^o$	9.6×10^{-1}	4	4	14.27	17.16
KrII	430.0915	430.049	0.0425	P	200	$5s\ ^2P - 5p\ ^4S^o$	--------	4	4	14.69	17.57
KrI	431.9528	431.855	0.0977	T	400	$5s\ [3/2]^o - 6p\ [5/2]$	--------	5	5	9.91	12.78
KrI		431.958	-0.0051	T	1000	$5s\ [3/2]^o - 6p\ [5/2]$	--------	5	7	9.91	12.78
KrII	432.3121	432.298	0.0141	P	150	$5s''\ ^2S - 5p''\ ^2P^o$	--------	2	4	18.08	20.94
KrII	435.5902	435.5477	0.0425	P	3000	$5s\ ^4P - 5p\ ^4D^o$	1.0	6	8	13.99	16.83
KrI	436.3018	436.2641	0.0377	P	500	$5s\ [3/2]^o - 6p\ [1/2]$	8.4×10^{-3}	5	3	9.91	12.76
KrII	437.0121	436.969	0.0431	P	200	$5p'\ ^2F^o - 4d''\ ^2D$	--------	6	4	18.49	21.33
KrI	437.6621	437.6121	0.05	P	800	$5s\ [3/2]^o - 6p\ [1/2]$	5.6×10^{-2}	3	1	10.03	12.86
KrII	438.7234	438.654	0.0694	P	300	$5p\ ^4P^o - 6s\ ^4P$	--------	4	6	16.65	19.47
KrI	440.0752	439.9965	0.0787	P	200	$5s'\ [1/2]^o - 6p'\ [3/2]$	2.0×10^{-2}	3	5	10.64	13.46
KrI	441.0752	441.03685	0.0383	P	50	$5s'\ [1/2]^o - 6p'\ [1/2]$	4.4×10^{-3}	3	3	10.64	13.45
KrII	442.4148	442.27	0.1448	P	100	$5s'\ ^2D - 5p'\ ^2P^o$	--------	4	4	15.82	18.62
KrII	443.2303	443.1685	0.0618	P	500	$5s\ ^4P - 5p\ ^4D^o$	1.8	2	2	14.58	17.38
KrII	443.7536	443.6812	0.0724	P	600	$5s\ ^4P - 5p\ ^2P^o$	6.6×10^{-1}	2	4	14.58	17.37
KrI	445.4926	445.3917	0.1009	P	600	$5s\ [3/2]^o - 6p\ [3/2]$	7.8×10^{-3}	3	5	10.03	12.82
KrI	446.4745	446.3689	0.1056	P	800	$5s\ [3/2]^o - 6p\ [3/2]$	2.3×10^{-2}	3	3	10.03	12.81
KrII	447.6263	447.5014	0.1249	P	800	$6s'\ ^2D - 5p'\ ^2P^o$	--------	6	4	15.85	18.62
KrII	449.1183	448.988	0.1303	P	400	$5p'\ ^2F^o - 4d''\ ^2D$	--------	8	6	18.56	21.32
KrI	450.376	450.2353	0.1407	P	600	$5s\ [3/2]^o - 6p\ [5/2]$	9.2×10^{-3}	3	5	10.03	12.78
KrII	452.4814	452.314	0.1674	P	400	$5p\ ^4P^o - 4s\ ^4P$	--------	2	4	16.83	19.57
KrII	457.9983	457.7209	0.2774	T	800	$5s'\ ^2D - 5p'\ ^2F^o$	9.6×10^{-1}	6	8	15.85	18.56
KrII	458.5564	458.2978	0.2586	T	300	$5p\ ^4D^o - 6s\ ^4P$	7.6×10^{-1}	6	4	16.87	19.57
BaII	455.7007	455.403	0.2977	T	65000	--------	1.17	2	4	0.00	2.72

Table 6.2: Identified emission lines for krypton discharge (2400l/mm grating)
** [177, 178, 179, 180, 181]*

6.3.2.3 Argon results

A similar investigation was also carried out on argon. Figure 6.30 shows the spectrum obtained using the 2400l/mm grating. The cathode was operated at 5A discharge current, 1A keeper current and 1mg/s (2.415Aequiv) propellant flow rate. The discharge voltage was 30.5V and the discharge was in the plume mode.

The spectrum is the calibrated result, but like xenon and krypton it is not corrected for the spectral transmission properties of the optics and the frequency response of the detector. The spectrum is dominated by argon species (I & II) superimposed on a weak continuum. Barium emission lines were also detected. From figure 6.30, 72 lines were identified, with table 6.3, arranged in the same manner as the preceding tables 6.1 and 6.2, listing some of the identified lines.

Spectra were also obtained for argon at 1.5mg/s (3.6225Aequiv), 1.8mg/s (4.347Aequiv), 2mg/s (4.83Aequiv) and 3.4mg/s (8.211Aequiv).

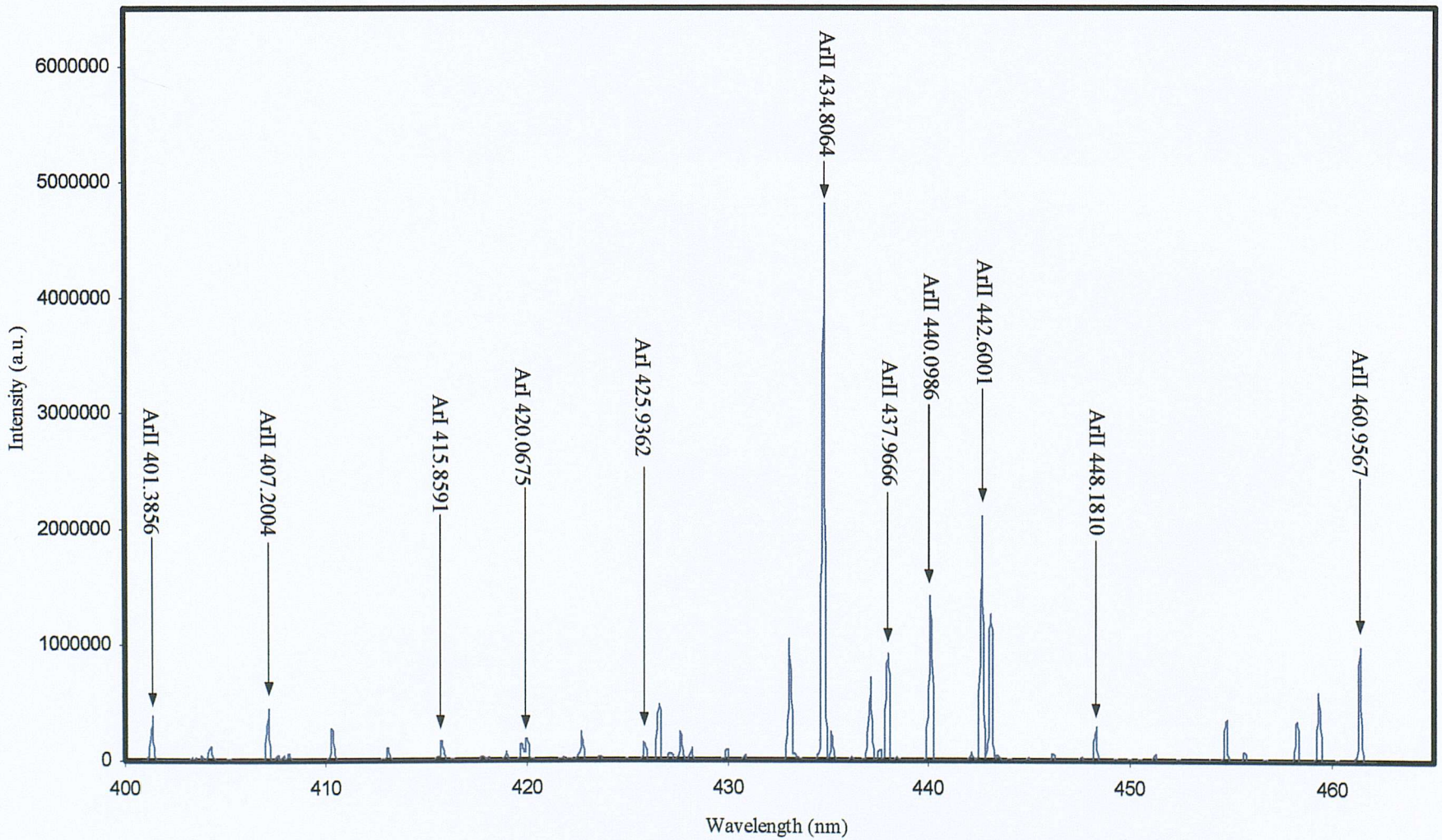

Figure 6.30: Optical emission spectrum from the hollow cathode internal plasma with argon at 1mg/s and 5A discharge current (2400l/mm grating)

Element	Observed Wavelength	Tabulated Wavelength* (nm)	Δ Wavelength (nm)	Identification (Positive, Tentative)	Relative Intensity*	Transition*	A_{pq}* ($\times 10^8$ s^{-1})	g(q)*	g(p)*	E(q)* (eV)	E(p)* (eV)
ArII	401.3395	401.3856	-0.0461	P	50	$3d\ ^4D - 4p\ ^4D^o$	1.05×10^{-1}	8	8	16.40650	19.49454
ArII	405.2368	405.2921	-0.0553	P	100	$4d\ ^2S - 4p\ ^2P^o$	6.7×10^{-1}	2	4	20.74355	23.80182
ArII	407.142	407.2004	-0.0584	T	200	$4s\ ^2D - 4p\ ^2D^o$	5.8×10^{-1}	6	6	18.45412	21.49805
ArII		407.2385	-0.0965	T	70	--------	--------	--------	--------	--------	--------
ArII	407.6488	407.6628	-0.014	P	25	$4p\ ^4D^o - 5s\ ^4P$	8×10^{-1}	2	2	19.64258	22.68307
ArII	407.902	407.9573	-0.0553	P	35	$4s\ ^2D - 4p\ ^2D^o$	1.19×10^{-1}	6	4	18.45412	21.49241
ArII	408.1551	408.2387	-0.0836	P	25	$4s\ ^4P - 4p\ ^2D^o$	2.9×10^{-2}	6	6	16.64386	19.68005
ArII	410.3007	410.3912	-0.0905	P	150	$4p\ ^4D^o - 5s\ ^4P$	1.2	8	6	19.49454	22.51481
ArII	413.1256	413.1723	-0.0467	P	300	$4s\ ^2D - 4p\ ^2P^o$	8.5×10^{-1}	4	2	18.42655	21.42649
ArI	415.8092	415.8591	-0.0499	P	400	$4s\ [3/2]^o - 5p\ [3/2]$	1.4×10^{-2}	5	5	11.54835	14.52891
ArII	417.7963	417.9297	-0.1334	P	35	$4p\ ^4D^o - 5s\ ^4P$	1.3×10^{-1}	6	6	19.54901	22.51481
ArI	418.106	418.1884	-0.0824	P	50	$4s\ [1/2]^o - 5p\ [1/2]$	5.61×10^{-3}	1	3	11.72316	14.68712
ArI	419.7747	419.8317	-0.057	P	200	$4s\ [3/2]^o - 5p\ [1/2]$	2.57×10^{-2}	3	1	11.62359	14.57595
ArI	420.0215	420.0675	-0.046	P	400	$4s\ [3/2]^o - 5p\ [5/2]$	9.67×10^{-3}	5	7	11.54835	14.49905
ArI	425.8415	425.9362	-0.0947	P	200	$4s\ [1/2]^o - 5p\ [1/2]$	3.98×10^{-2}	3	1	11.82807	14.73812
ArI	426.5713	426.6287	-0.0574	P	100	$4s\ [3/2]^o - 5p\ [3/2]$	3.12×10^{-3}	3	5	11.62359	14.52891
ArI	427.1785	427.2169	-0.0384	P	150	$4s\ [3/2]^o - 5p\ [3/2]$	7.97×10^{-3}	3	3	11.62359	14.52491
ArII	427.6637	427.7528	-0.0891	P	550	$4s\ ^2D - 4p\ ^2P^o$	8×10^{-1}	6	4	18.45412	21.35180
ArI	429.9611	430.0101	-0.049	P	100	$4s\ [3/2]^o - 5p\ [5/2]$	3.77×10^{-3}	3	5	11.62359	14.50607
ArII	434.7582	434.8064	-0.0482	P	800	$4s\ ^4P - 4p\ ^4D^o$	1.171	6	8	16.64386	19.49454
ArII	435.1754	435.2205	-0.0451	P	50	$3d\ ^4D - 4p\ ^4P^o$	2.12×10^{-1}	2	2	16.45738	19.30535
ArII	436.1869	436.2066	-0.0197	P	25	$3d\ ^2D - 4p\ ^2D^o$	5.5×10^{-2}	4	6	18.65652	21.49805
ArII	437.0774	437.0753	0.0021	T	200	$3d\ ^2D - 4p\ ^2D^o$	6.6×10^{-1}	4	4	18.65652	21.49241
		437.1329	-0.0555	T	70	$3d\ ^4D - 4p\ ^4P^o$	2.21×10^{-1}	6	4	16.42558	19.26109
ArII	437.6107	437.5954	0.0153	P	50	$4s\ ^2P - 4p\ ^2S^o$	2.05×10^{-1}	4	2	17.14003	19.97254
ArII	437.966	437.9666	-0.0006	P	150	$4s\ ^4P - 4p\ ^4D^o$	1.004	2	2	16.81247	19.64258
ArII	440.0909	440.0096	0.0813	T	70	$3d\ ^4D - 4p\ ^4P^o$	1.60×10^{-1}	4	4	16.44412	19.26109
ArII		440.0986	-0.0077	T	200	$3d\ ^4D - 4p\ ^4P^o$	3.04×10^{-1}	8	6	16.40650	19.22290
ArII	442.6149	442.6001	0.0148	P	400	$3s\ ^4P - 4p\ ^4D^o$	8.17×10^{-1}	4	6	16.74853	19.54901
ArII	447.6165	447.4759	0.1406	P	100	$3d\ ^2D - 4p\ ^2P^o$	2.90×10^{-1}	4	2	18.65652	21.42649
ArII	448.3095	448.1810	0.1285	P	200	$3d\ ^2D - 4p\ ^2D^o$	4.55×10^{-1}	6	6	18.73244	21.49805
ArI	451.2412	451.0733	0.1679	P	100	$4s\ [1/2]^o - 5p\ [1/2]$	1.18×10^{-2}	3	1	11.82807	14.57595
ArII	454.776	454.5052	0.2708	T	400	$4s\ ^2P - 4p\ ^2P^o$	4.71×10^{-1}	4	4	17.14003	19.86716
ArII	458.2786	457.9349	0.3437	T	400	$4s\ ^2P - 4p\ ^2S^o$	8×10^{-1}	2	2	17.26583	19.97254
ArII	459.3456	458.9898	0.3558	T	400	$4s\ ^2D - 4p\ ^2F^o$	6.64×10^{-1}	4	6	18.42655	21.12704
ArII	461.3589	460.9567	0.4022	T	550	$4s\ ^2D - 4p\ ^2F^o$	7.89×10^{-1}	6	8	18.45412	21.14308
BaII	455.683	455.403	0.28	T	65000	--------	1.17	2	4	0.00	2.72

Table 6.3: Identified emission lines for argon discharge (2400l/mm grating)
** [177, 178, 179, 180, 181]*

6.3.3 Dependence of emission line intensity on propellant flow rate and discharge current

This section is concerned with describing the effects of varying the discharge parameters and propellant flow rate on the spectrally resolved light emission from the hollow cathode. This set of experiments was carried out by tagging a set of three emission lines of the same species (neutral, first ionisation or impurity lines) using the CCD array operated in chart recorder mode for xenon, krypton and argon discharges.

6.3.3.1 Dependence of gas species emission line intensity on discharge current

The results from experiments carried out on three KrII lines (the 408.834, 435.5477 and 405.7209nm lines) are shown in figure 6.31, where the discharge is in spot mode and, as mentioned in section 6.3.1.1, showing a negative *V-I* characteristic indicating that in the spot mode the discharge has negative impedance. The discharge current is increased from 0.5A to 5A and back again to 0.5A, at 2.1mg/s mass flow rate. The increase or decrease of power to the discharge seems to have an instantaneous effect (in terms of the observation time) on the ionisation process (represented by the KrII line intensity), where the energy for ionisation is provided by the power supplies.

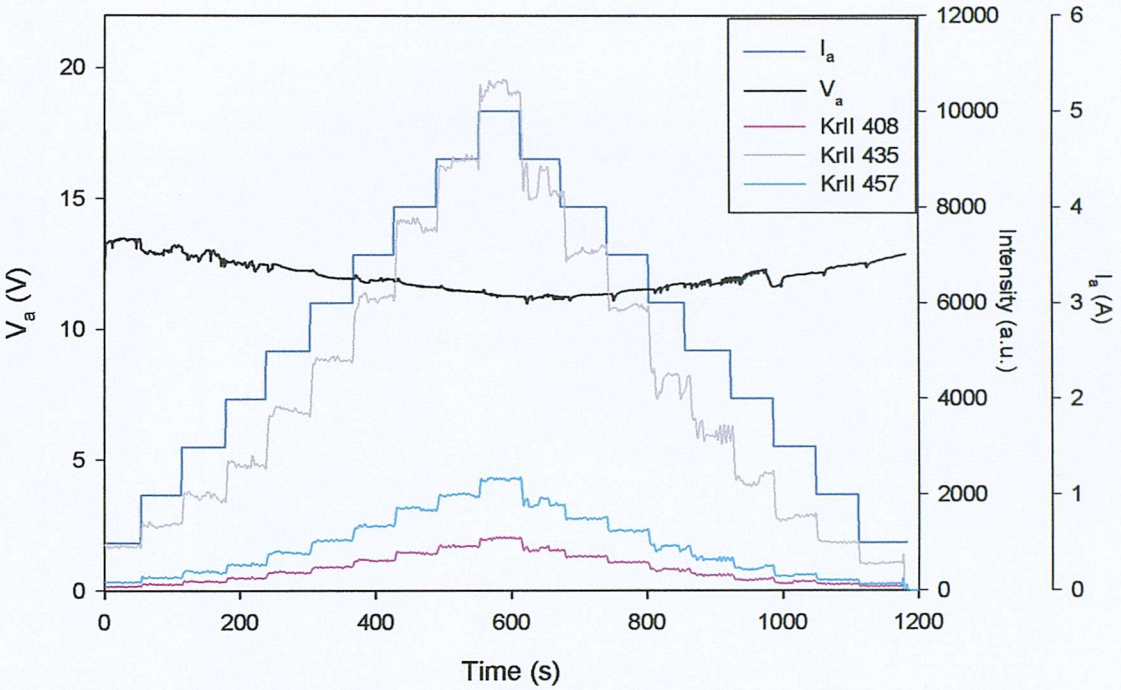

Figure 6.31: Time trace of KrII line intensity as a function of discharge current in spot mode (2.415Aequiv)

In order to facilitate comparison of the emission line behaviour as a function of I_a for: lines of the same species, lines at different stages of ionisation of the same element and lines from different propellants, the intensity of an emission line is normalised with respect to the highest intensity achieved during the test (which is always the intensity at maximum discharge current). Figure 6.32 is a reconstruction of figure 6.31 in terms of averaged normalised intensity for the KrII lines. It shows that behaviour of emission lines of a given species is virtually identical, this is mirrored in the argon and xenon results. The discharge power (P_D) is also plotted in figure 6.32 to show that, although V_a is decreasing, the power deposited in the discharge actually increases with increasing current, thus leading to the monotonic increase in intensity.

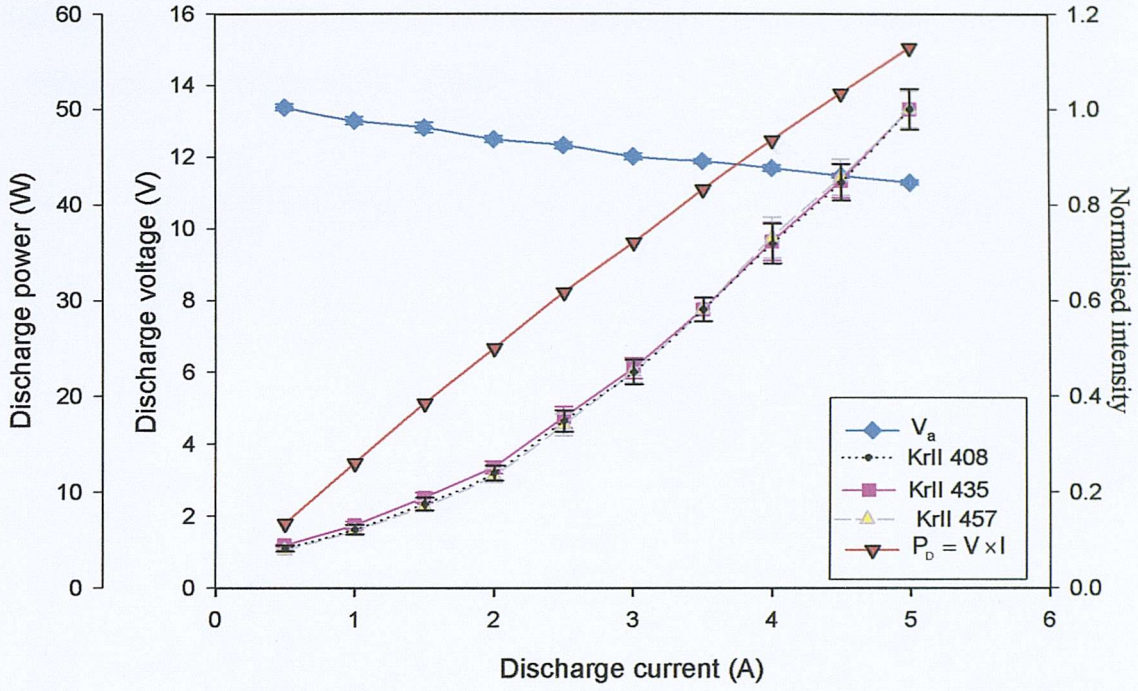

Figure 6.32: Normalised intensity of KrII lines as a *function of I_a in spot mode, $\dot{m}$ = 2.415Aequiv*

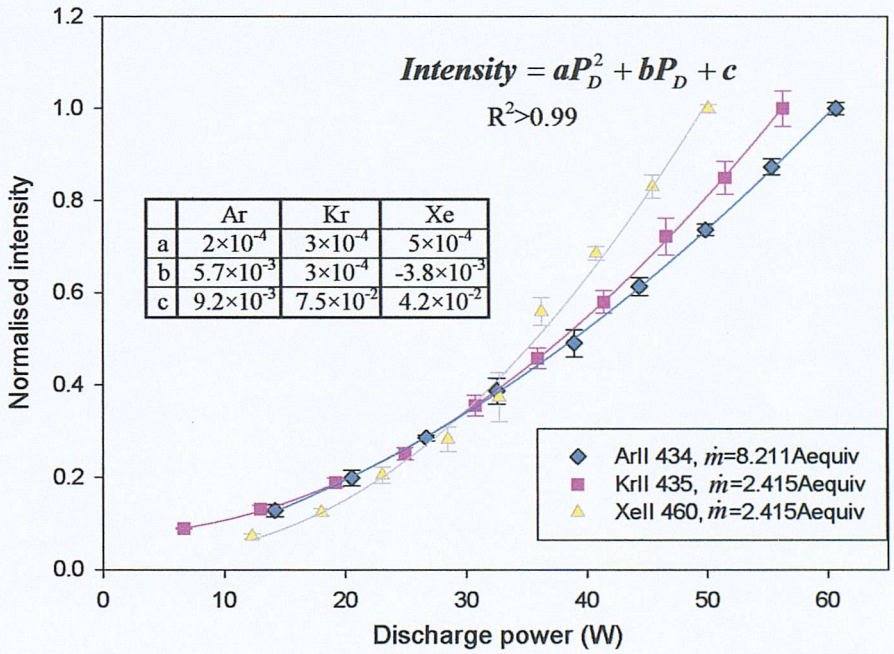

	Ar	Kr	Xe
a	2×10^{-4}	3×10^{-4}	5×10^{-4}
b	5.7×10^{-3}	3×10^{-4}	-3.8×10^{-3}
c	9.2×10^{-3}	7.5×10^{-2}	4.2×10^{-2}

Figure 6.33: Comparison of Ar, Kr & Xe normalised first ionisation emission line intensity as a function of discharge power in spot mode

Figure 6.33 illustrates the dependence of emission line intensity on discharge power for argon (ArII 434.8064nm), krypton (KrII 435.5477nm) and xenon (XeII 460.300nm) first ionisation lines in spot mode. It shows that the relationship between

line intensity and P_D can be very well described by a quadratic polynomial, with the coefficients for each gas shown in the inset.

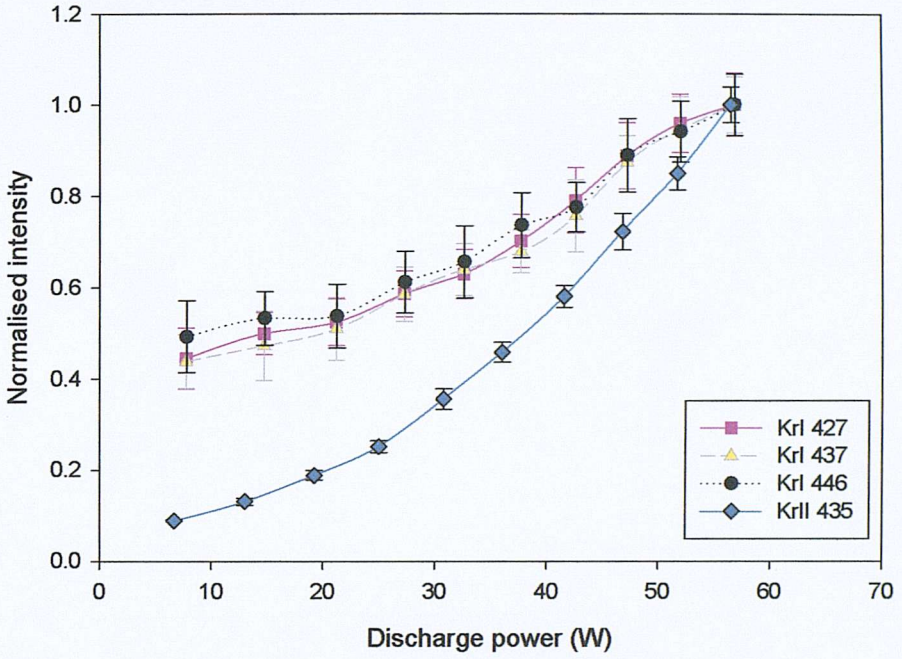

Figure 6.34: Comparison of KrII and KrI normalised line intensity as a function of P_D in spot mode

The neutral emission lines (KrI 427.3969, 437.6121 & 446.3689nm), as illustrated by figure 6.34, are far less sensitive to discharge current (and power) than first ionisation lines. The neutral lines showed an increase of about 120%, compared to an increase of 1025% for the first ionisation lines, when the discharge power was increased from 7W to 57W. This indicates an increasing degree of ionisation of the propellant gas as discharge power is increased in the spot mode. Furthermore, the intensity (non normalised) of the neutral lines was in general one to two orders of magnitude less than that for the first ionisation lines, when the cathode operated in the spot mode.

6.3.3.2 Dependence of gas species emission line intensity on propellant flow rate

Figure 6.35 shows the time trace of the variation of the intensity (in arbitrary units) of three KrII lines (the 408.834, 435.5477 and 405.7209nm lines) with $\dot{m}$ in the range

0.8mg/s to 4.2mg/s, with the anode and keeper current fixed at 5A and 1A respectively. The left hand side of the graph represents the anode voltage while the right hand side represents the KrII line intensity in arbitrary units and the outer right hand side represent mass flow rate in mg/s.

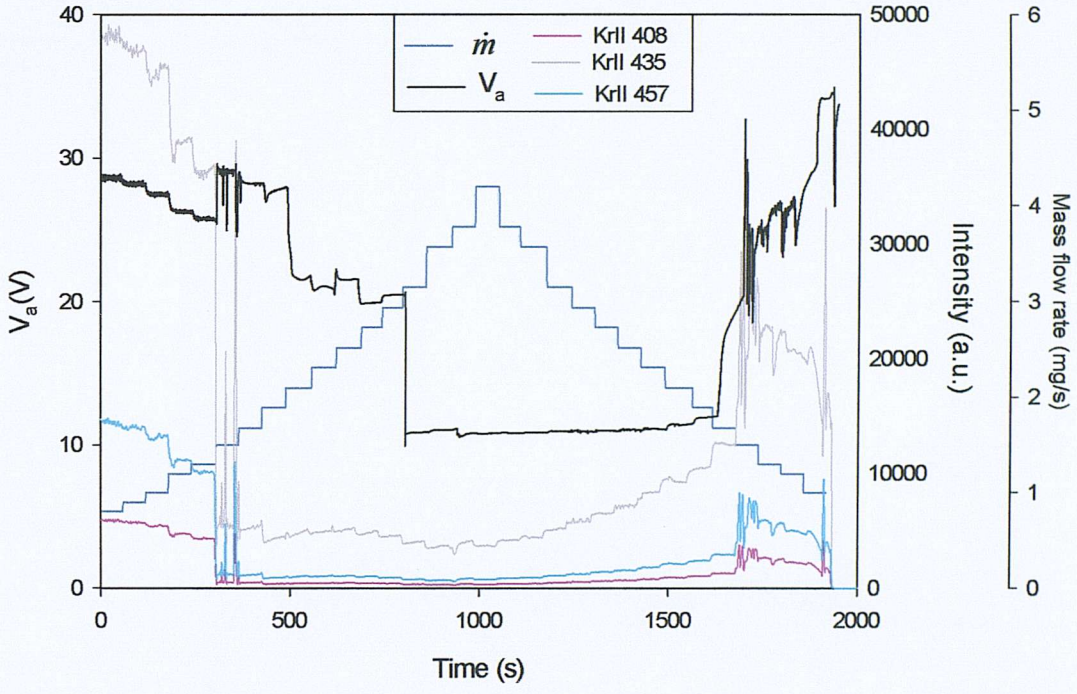

Figure 6.35: Time trace of the line intensity of three KrII emission lines as a function of ṁ (I_a=5A)

In keeping with previous sections, we concentrate on the results associated with the spot mode operation, leaving the plume mode for later discussion. When the discharge is in the plume mode, changes in V_a usually accompany $\dot{m}$ variations and make decoupling the effect of the two variables difficult. Observation in the spot mode allows us to determine the effect of flow rate independently of variations in P_D (in the spot mode, with I_a = 5A throughout and V_a not changing appreciably, discharge power is thus approximately constant, see figure 6.36). The emission line dependence on flow rate is shown in figure 6.36 for normalised XeI (the 450.10 & 462.43nm) lines and XeII (405.746, 446.219 & 460.30nm) lines, with the discharge in the spot mode. It can be seen that the light intensity of the XeI and XeII lines seems to decrease with increasing $\dot{m}$. With the higher neutral density, which is a product of increasing flow rate, the mean free path for electrons between collisions decreases increasing the collision frequency. The electrons thus gain less energy between collisions and the

first ionisation and neutral excitation emission line intensity decreases. This trend was also reproduced in argon and krypton spot mode emission line behaviour.

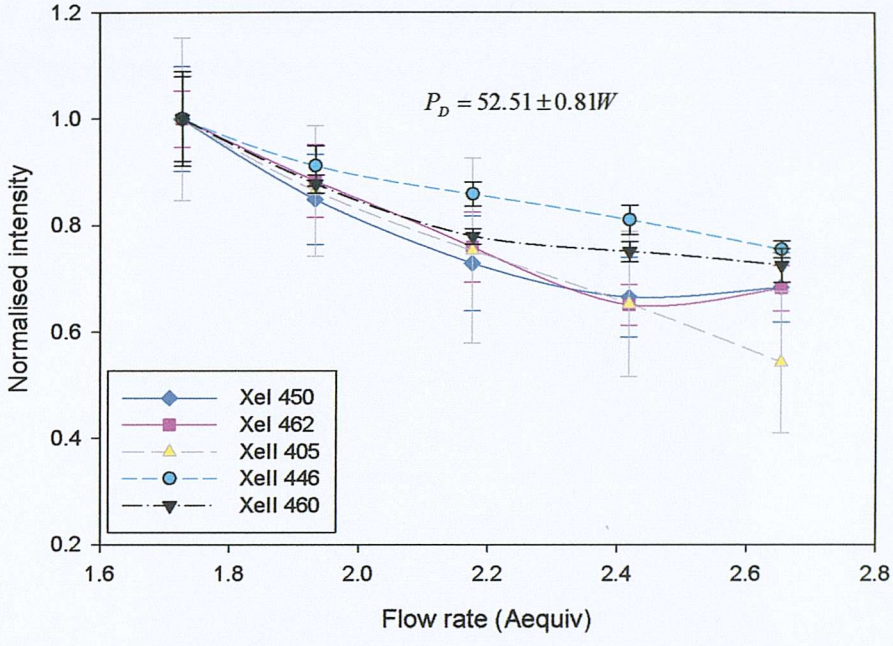

Figure 6.36: Comparison of XeII and XeI line intensity as a function of $\dot{m}$ in the spot mode where the electrical set up is kept approximately constant

6.4 Anode deposit

At the end of the experimental program, the various components of the set-up were examined. It was observed that the anode had acquired a thin layer of deposited material in the vicinity of the hole in the anode centreline, as shown in figure 6.37.

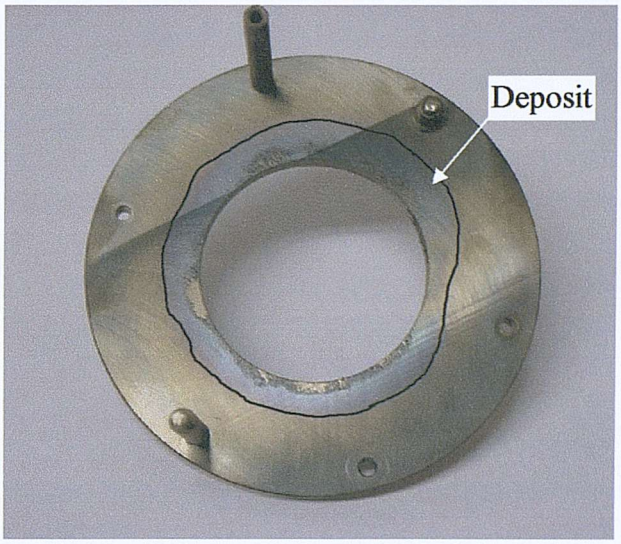

Figure 6.37: Photograph of anode with area of deposit indicated

Samples of the deposit were taken for further analysis to determine its chemical composition. The first step was to take a picture of the deposit using a Scanning Electron Microscope (SEM), shown in figure 6.38.

The deposit was then analysed using Energy Dispersive X-ray Fluorescence (ED-XRF) spectrometry. ED-XRF is illustrated in figure 6.39, it works by aiming an x-ray beam at the surface of a sample. The beam's interaction with the surface leads to emission of secondary x-rays (i.e. fluorescence). The energy of the fluorescent beam is a characteristic of the elements present in the sample. Plotting the spectrum (energy versus intensity) gives not only the elements present in the sample, but also quantifies the relative abundance of each element. The spectrum obtained from the anode deposit is shown in figure 6.40, with table 6.4 showing the relative abundance of each element in the deposit in terms of both percentage of weight and number of atoms.

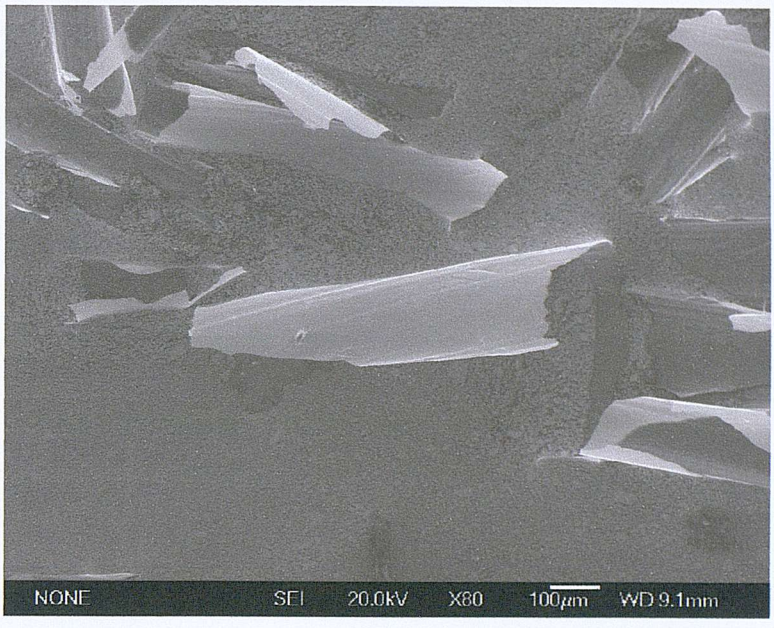

Figure 6.38: SEM of deposited material

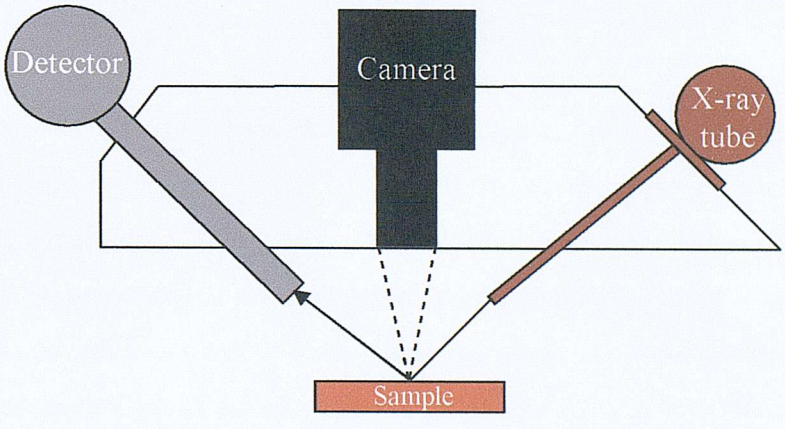

Figure 6.39: Illustration of ED-XRF [192]

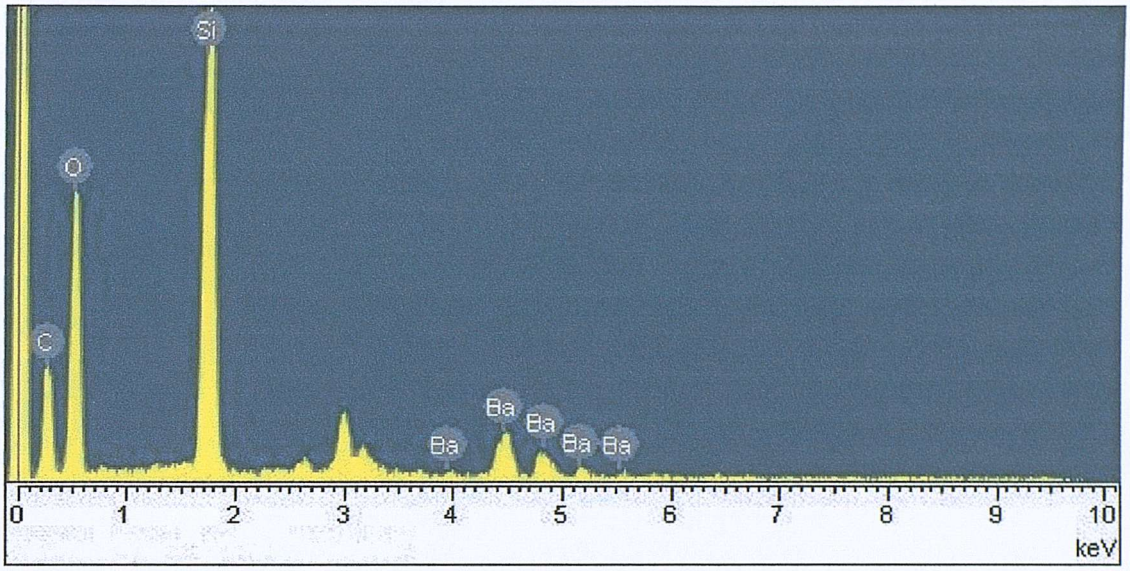

Figure 6.40: ED-XRF spectrum of deposit

Element	Weight %	Atomic %
Carbon	29.35	41.55
Oxygen	44.41	47.20
Silicon	16.60	10.05
Barium	9.64	1.19

Table 6.4: Relative abundance of elements

It was discovered that only four elements constituted the deposit: Carbon, oxygen, silicon and, interestingly, barium. The carbon is thought to come from ion bombardment of the graphite keeper. The source of the silicon and oxygen is the quartz shield downstream of the anode, which is expected to experience some ion bombardment. Barium can only come from the insert of the hollow cathode, it is evaporated from the insert when heated by the activation of the triple carbonate mix, this barium is then deposited on the surfaces downstream of the cathode.

Chapter 7

DISCUSSION

7.1 Hollow cathode breakdown

Most breakdown investigations utilise cold cathodes, and hence the number of electrons liberated by an impacting ion, Townsend's secondary process γ, is expected to be low (O ~ 0.1). As reference [124] describes, in the hollow cathode due to the low work function of the emitting surface and the heating of the cathode, thermionic emission dominates, and leads to a higher effective γ (>1), which results in the lower breakdown voltages in HC.

7.1.1 Anomalous HC breakdown & Penning ionisation

A consequence of Paschen's Law is that a unique minimum breakdown voltage exists for each gas at a unique value of $(P \times d)$ known as the Paschen minimum. However, HC breakdown curves seem to exhibit an anomalous increase in V_{bk} leading to the formation of a double minimum instead of the expected one (fig. 6.3). This departure from Paschen behaviour was also observed with xenon in the open keeper T6 [124], and is demonstrated here to exist for *all* the inert gases employed. It is proposed here that these empirical results can be explained by invoking the 'Penning Effect'.

Gas atoms are excited by inelastic collisions to energy states which can fall short of complete ionisation. If spontaneous radiative decay from the excited level is prohibited by the selection rules of quantum mechanics, the atom is then in a "metastable" state. The lifetime of these metastable states is very long, of the order of milliseconds or occasionally even seconds [158], compared to the expected

lifetime of a normal excited state which is of the order of just 10^{-8}s. Their long lifetime and their ability to diffuse against an electrical gradient make metastable atoms a notable contributor to the gas discharge through cumulative ionisation processes and secondary electron emission by metastable impact on the cathode surface. The ionising effect of metastable atoms has been demonstrated to be of paramount importance in mixtures of gases satisfying certain conditions. Penning [125] showed that, for a rare gas (A) with a small amount of admixed gas molecules (B), excitation of the rare gas atoms often brings them into a metastable state A_m, with high energy V_{Am} and a long lifetime. When the admixed molecules have an ionisation energy V_{Bi} satisfying the condition:

$$V_{Bi} < V_{Am} \tag{7.1}$$

The metastable atoms of the main gas can then ionise the molecules of the admixture by the reaction:

$$A_m + B \rightarrow A + B^+ \tag{7.2}$$

The probability of this ionisation process (also known as "Penning ionisation") is so large that extremely small amounts of admixtures are required for an appreciable effect (the Penning Effect was detectable in Ne-Ar mixtures with argon concentrations as low as 10^{-4} % ! see figure 7.1). A consequence of this extra ionisation mechanism is the formation of a double minimum in the breakdown curves of a Penning mixture as will be seen next.

Kruithof and Penning [88] conducted experiments on determining Townsend's first ionisation coefficient (α) in several Ne-Ar mixtures. The results of their investigation are illustrated in figure 7.1, where η (= α/E) is plotted as a function of E/P_o (where E is the electric field and P_o is the pressure of the gas reduced to 0°C). Kruithof and Penning in using η (units V^{-1}), instead of the more common α/P_o, relate the ionisation more directly to the breakdown potential V_{bk} . The quantity η is hence an *efficiency function* representing *the ions produced per unit of energy available from the electric field.*

For the pure gases, η, giving the efficiency of ionisation for a given imposed field, is

low at low E/P_o due to the high electron energy losses to excitation relative to ionisation. As E/P_o increases, this loss decreases relative to ionisation and is reflected in an increasing η until a maximum is reached η_{max} (η_{max} for argon is $0.022V^{-1}$ occurring at E/P_o = 200V/cm×mmHg, and η_{max} for Ne is $0.015V^{-1}$ occurring at E/P_o = 80 V/cm×mmHg, from figure 7.1). With further increase in E/P_o the electrons continue to gain energy, however, the ionisation cross-section (and hence the probability of the ionisation process) ultimately decreases with primary electron energy. As an electron cannot dissipate its energy in ionisation, the extra energy is deposited at the anode. This results in the subsequent decrease in η with increasing E/P_o in the pure gases.

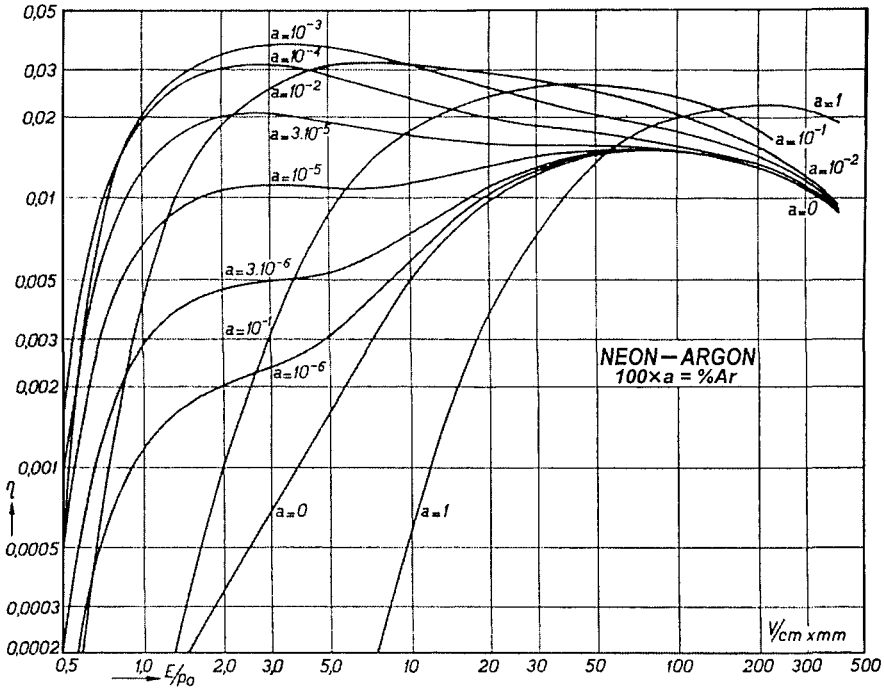

Figure 7.1: Ionisation coefficient η as a function of E/P_o for several Ne-Ar mixtures where 100×a= argon percentage (thus a=0 is pure Ne, and a=1 is pure Ar) [88]

Turning our attention to the Ne-Ar mixtures, the highest ionisation level of any Ne-Ar mixture (η_{max} = 0.037 V^{-1}) occurs for Ne + 0.1 % Ar at $E/P_o \approx$ 3 V/cm×mmHg. For lower values of argon concentration ($a < 10^{-3}$), there is very little chance of excitation or ionisation of the Ar atoms by direct electron impact due to their low concentration. Most of the electron energy is thus expended in ionising and exciting the main gas constituent Ne, and in the corresponding curves η has two maxima. The maximum at E/P_o = 3V/cm×mmHg corresponds to the peak cross-section (probability) of

excitation for the Ne metastable levels per volt potential difference. At low E/P_o, The energy stored in the metastable Ne states is converted directly, by the Penning Effect, to ionisation of the small amount of readily ionised admixture, effectively eliminating electron energy loss to excitation. The electrons produced by Penning ionisation add to those produced by the direct action of electron impact ionisation of the main gas, thus contributing to further ionisation and excitation. It follows that, at E/P_o = 3 V/cm×mmHg, Penning ionisation causes η to increase manyfold, leading to the formation of the maximum at low E/P_o.

As E/P_o is decreased below 2 V/cm×mmHg, η experiences a steep fall. The metastable states in rare gas atoms constitute their lowest possible excitation levels. With decreasing electron energy, the electron population start losing energy in *elastic* collisions with the atoms. The electrons will need to travel large distances to gain enough energy to ionise or excite the Ne atoms and hence the fall in η with decreasing E/P_o.

Increasing E/P_o above 3V/cm×mmHg in the $a < 10^{-3}$ mixtures results in a slight decrease in η. This is due to the decrease in the probability of formation of metastable states with increasing electron energy (refer to figure 7.3) and the onset of excitation of higher, short lived Ne levels, which are far less efficient at Ar ionisation than the metastables. With increasing E/P_o, a second maximum occurs at approximately 80 V/cm×mmHg, which is due to the increasing probability of direct ionisation of the Ne atoms by electron impact.

At extremely low concentrations of Ar, the rarity of the Ar atoms causes only a modest increase in ionisation. Ionisation is observed to increase with Ar concentration. This continues until a concentration of 0.1 % Ar is reached. From thereon the argon atoms are numerous enough for direct excitation of the Ar by electrons at energies about or below the excitation potentials of Ne. The Ar atoms thus dissipate the energy of the electron swarm reducing the excitation of Ne atoms. The excitation of the Ar atoms does not contribute to ionisation, thus η decreases as the Ar concentration exceeds 0.1 %. Direct ionisation of Ar atoms does not become significant unless high Ar concentrations are reached, and even then it is not as effective, or efficient, as metastable action.

In the case of the pure gases, where no complicating factors arise such as two ionisation mechanisms acting simultaneously like the Penning Effect, the peak of the η - E/P_o curves fixes the minimum breakdown potential. In Penning mixtures the enhanced ionisation causes significant reduction in the sparking potential, as illustrated in figure 7.2. The breakdown voltage for Penning mixtures can even be lower than either of the constituent gases.

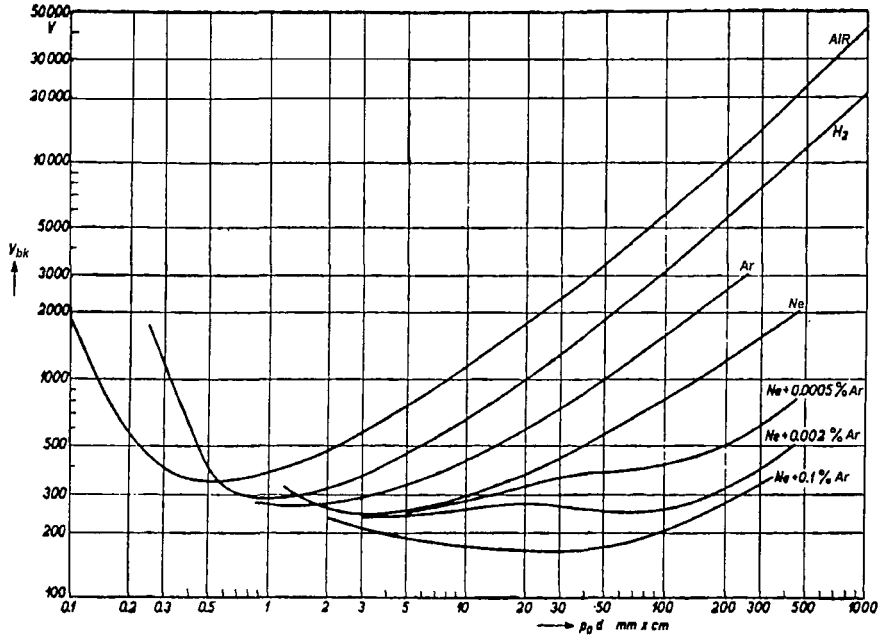

(a)

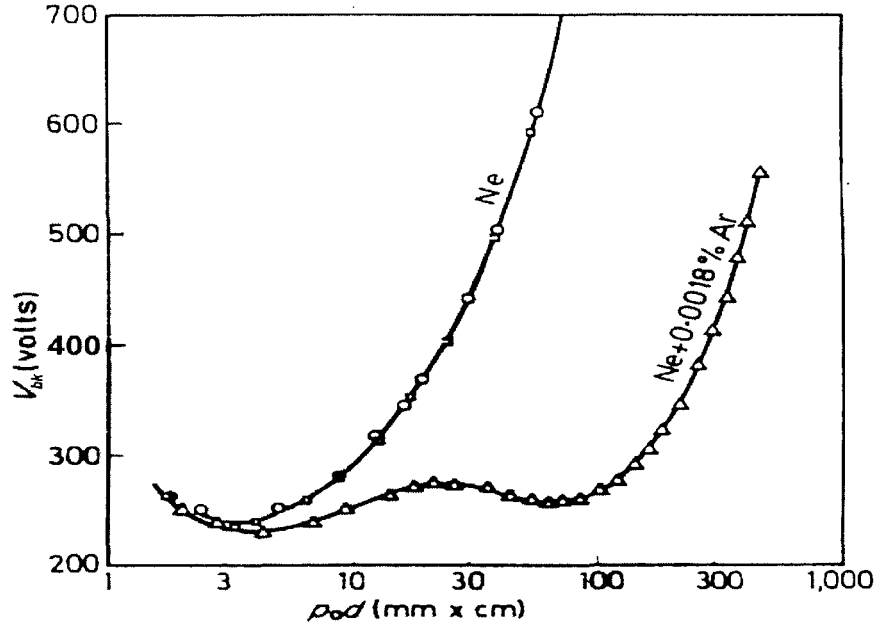

(b)

Figure 7.2: **(a)** *Breakdown voltage dependence on $P_o \times d$ for several gases and Ne-Ar mixtures [32], formation of a double minimum due to Penning ionisation better illustrated in figure* **(b)** *[125]*

In figure 7.2(b) the breakdown curve for Ne + 0.0018 %Ar exhibits a double minimum corresponding to the two maxima observed in the η - E/P_o curve for approximately the same gas mixture (figure 7.1). The first V_{bk} minimum at low $P_o \times d$ corresponds to that due to direct ionization of the rare gas atoms by electrons (similar to the minimum in the pure rare gas), while the second minimum corresponds to the increase in the ionization coefficient due to Penning ionization of the admixed molecules by the metastables. Due to the profound effect Penning ionisation has on the characteristics of gas mixtures, some effort was put in to quantify the cross-sections for ionisation of several admixed molecules by metastable rare gas atoms. Biondi [8] measured the ratio σ_{iP} / σ_d of the cross-section of Ar ionisation by metastable Ne (σ_{iP}) to the cross-section for de-excitation of Ne metastables by collisions with other Ne atoms (σ_d), which he found to be large (2.9×10^3). Biondi also measured the ratio σ_{iP} / σ_d in He-Hg mixtures (also known as Heg) where he found it to be even larger (1.5×10^6).

Gas	$E_{\infty Z}(g)$ (eV)	Energy level of metastable state (eV) $^3P_2$	$^3P_0$
Neon	21.56	16.62	16.80
Argon	15.76	11.55	11.72
Krypton	13.99	9.92	10.56
Xenon	12.13	8.32	9.45

Table 7.1: Metastable energy levels and Ionisation potentials of the rare gases [105]

From the preceding discussion we infer that the occurrence of Penning ionisation in the hollow cathode can indeed explain the double minimum in the experimental breakdown curves of sections 6.2.1.1 and 6.2.1.3. However, since all the gases employed were of high purity, it was initially difficult to see the source of the easily ionised trace element required for the Penning Effect (we note here that in the case of a 'pure' Kr/Xe mixture no Penning ionisation is expected to take place since the metastable levels of one constituent are never higher than the ionisation potential of the other, refer to table 7.1).

Barium, which evaporates from the insert during its activation process, is identified as the source of the Penning Effect, as will be discussed in section 7.1.1.2. Prior to this, the presence of metastable states in the hollow cathode discharge is demonstrated in the following section.

7.1.1.1 Estimation of metastable population in the propellant gases

In ordinary gas discharges, metastable atoms maybe present in relatively high concentrations, which are comparable with the concentration of positive ions in the discharge [22, 23]. This section aims to produce a similar, order of magnitude estimate for an orificed HC discharge.

For a discharge in equilibrium, the number density of metastable states is determined by the respective rates of their generation and loss processes. Assuming that the main process for metastable generation is by electron collision and that de-excitation at the cathode surface is the only active destruction process we can write [55]:

$$n_e\, n_o\, \sigma_m\, \bar{c}_e = \frac{n_m \bar{c}_o}{r_c} \tag{7.3}$$

where n_m is the metastable density, r_c is the cathode radius, $\bar{c}_o$ is the mean thermal velocity of the atoms. σ_m is the cross-section for excitation from the ground state into the metastable state and $\bar{c}_e$ is the mean electron velocity.

The total cross-sections for excitation into the metastable state for the inert gases were obtained from the experimental measurements of Mason and Newell [108] and are illustrated in figure 7.3. By the 'total' cross-section we mean the sum of the cross-sections for excitation into the $^3P_2$ and $^3P_0$ metastable levels. The experimental points are then fitted by Weibull 5-parameter distribution where the correlation coefficient was greater than 0.98 in all the gases.

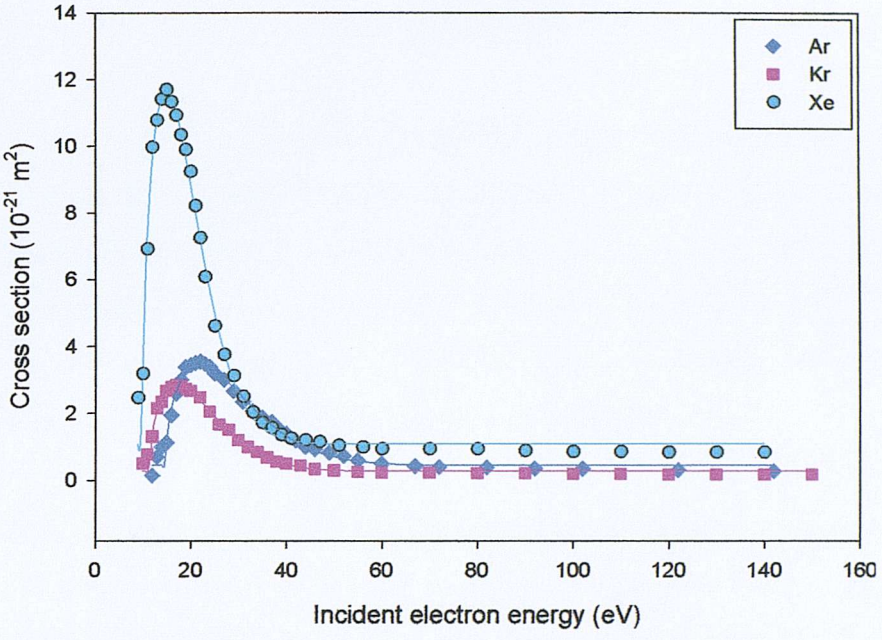

Figure 7.3: Total cross-sections for the metastable excitation in Ar, Kr and Xe [108]

The metastable cross-section is, as expected, dependant on the velocity of the incident electron. In order to obtain an average for the velocity dependant product $\sigma_m(c_e) \times c_e$ in the production term we integrate over the electron Maxwellian velocity distribution using the standard integral:

$$\int_{c_t}^{\infty} c_e \, \sigma_m(c_e) f(c_e) dc_e \qquad (7.4)$$

where the lower limit of the integration c_t defines a threshold primary electron energy for the reaction, and $f(c_e)$ is the non-directional Maxwellian velocity distribution function given by:

$$f(c_e) = 4\pi \left(\frac{m_e}{2\pi k T_e} \right)^{3/2} c_e^2 \exp\left(-\frac{m_e c_e^2}{2kT_e} \right) \qquad (7.5)$$

Using $\bar{c}_o = (8kT_s / \pi m_o)^{1/2}$, where atoms of mass m_o are assumed to be in equilibrium at the insert temperature $T_s \approx$ 1273K. Combining equations (7.3) to (7.5) and using the spot mode spectroscopic measurements of T_e and n_e for each gas (section 7.2.2), solving the integral numerically, and using r_c = 1mm we obtain the ratios:

For Xenon: $\frac{n_m}{n_o} = 3\%$ for Argon: $\frac{n_m}{n_o} = 0.3\%$ for Krypton: $\frac{n_m}{n_o} = 5.7\%$

The result suggests that a significant number of atoms in the discharge exist in a metastable state. With neutral densities in the $10^{23}m^{-3}$ range expected in the HC (Appendix B), this indicates metastable densities of the order of $10^{20}m^{-3}$ ($10^{14}cm^{-3}$) which are indeed comparable to the positive ion concentration in the HC. The above prediction is in good agreement with Trindade's [30] order of magnitude estimate of $10^{14}cm^{-3}$ in the more generic open channel hollow cathodes.

However, the use of equation (7.3) ignores metastable destruction by electron impact excitation and ionisation out of the metastable levels, metastable destruction by inter-atomic collisions (including Penning ionisation) and metastable production by electrons cascading from higher states, with the net result probably being an overestimation of the metastable density. Nevertheless, tests in open channel hollow cathodes have shown metastable yields two orders of magnitude greater than any glow discharge [30], which resulted in their widespread use in numerous studies as a metastable source (see for example [11, 62, 72, 144]).

7.1.1.2 Presence of barium in inert gas

Free barium is formed when the insert is activated by heating via a reaction between the barium-calcium-aluminate and the tungsten insert matrix [33]. The chemical reaction between the impregnate, which is found to consist of three phases ($Ba_3Al_2O_6$, $Ba_2\ Ca\ Al_2\ O_6$ and $Ca\ O$), and the tungsten insert occurs at the cathode operating temperature and probably proceeds by the equation [27]:

$$W + 3Ba_3\,Al_2\,O_6 + 6Ca\,O \rightleftharpoons 3Ba_2\,Ca\,Al_2\,O_6 + 3Ba + Ca_3\,W\,O_6 \qquad (7.6)$$

The barium then sublimates from the insert and mixes with the inert propellant gas. With an ionisation potential of 5.2 eV, which is lower than the potential energy of the metastable states of all the noble gases (table 7.1), barium is found to indeed satisfy the prime requisite for Penning ionisation to occur, and the resulting mixture is hence a Penning mixture. As previously mentioned, only very small amounts of barium are

required for an appreciable Penning Effect, owing to the very high probability of the process.

Due to its decisive impact on the performance and durability of dispenser cathodes, evaporation rates from a barium-calcium-aluminate dispenser have been the subject of a substantial body of work [27], most notably that by Brodie and Jenkins [14, 15]. Figure 7.4 exhibits the barium evaporation as a function of temperature for a dispenser impregnated in the 4:1:1 ratio, similar to that in the T6.

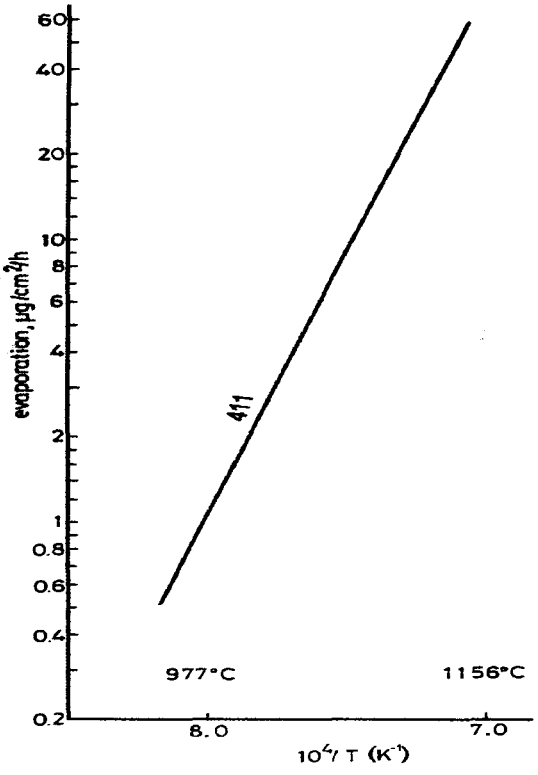

Figure 7.4: Barium evaporation rate as function of temperature for a 'new' 4:1:1 dispenser cathode [27]

The research demonstrated a strong dependence of evaporation rate on cathode life, falling very rapidly early in life with cathode length of operation. Thus, the data collected are only beneficial if it is known at what point in the cathode life they were taken. However, some fundamental principles have been established for the barium evaporation rate. Brodie and Jenkins [14, 15] formulated, as was later confirmed by other authors [30], that, for a cathode of a given age, the rate of barium evaporation (E_{Ba}) is related to the cathode temperature by a relationship of the form:

$$\log E_{Ba} = C - \frac{5040\Omega}{T} \qquad (7.7)$$

where Ω is the activation energy for evaporation in eV and C is a constant. Accordingly, increasing T would result in a higher barium evaporation rate. Analysis by Katz *et al.* [204, 205] showed that the predicted barium emission rates and insert lifetimes from these vacuum devices are consistent with experimental results in HC's.

Returning to the T6 hollow cathode, the presence of barium traces in the gas was conclusively demonstrated by the detection of BaII lines in the spectra of the various gases (section 6.3.2) and by the detection of barium in the anode deposit (section 6.4). We can infer from the above discussion on dispenser cathodes that the rate of evaporation of barium from the T6 dispenser would increase substantially with increasing cathode temperature. This would result in a higher barium concentration at a given mass flow rate. From figures 7.1 and 7.2, significantly increasing the concentration of admixed gas in a Penning mixture would lead to two effects: decreasing the required breakdown voltage and producing a less pronounced double minimum, which is *exactly* what is observed in the V_{bk} vs $\dot{m}$ plots (section 6.2.1) when the HC tip temperature is increased from 929°C to 1299°C. We estimate from equation (7.7) and from plots in reference [15] that the rate of barium evaporation increases by roughly three to four orders of magnitude when cathode temperature increases from 929°C to 1300°C. Note here that a decrease in V_{bk} with increasing T can also be attributable to increased thermionic emission, the change in the shape of the curve however is not. This effect was also observed in the open keeper T6 work [124], and further confirms that the Penning effect is operational in the HC.

To the author's knowledge, *this work constitutes the first observation of barium Penning ionisation and it is the first time this mechanism has been invoked to describe the HC phenomena*. The available literature reported observations of Penning ionisation in monatomic mixtures containing two inert gases (He or Ne as the main gas with Ar or Kr or Xe as the admixture [8, 32, 62, 96]) or in mixtures containing an inert gas with: mercury [9], alkali metals such as caesium [197], nitrogen [182], copper [198], some rare earth metals (La, Sm, Gd, Er, Yb, Lu and U) [72], and, more importantly calcium [144]. The significance of the observation of Penning ionisation

in an inert gas/calcium mixture is in that Ca shares the second group of alkaline earth metals with barium and, consequently, shares many of its characteristics.

Shuker *et al.* [144] conducted the investigation into the Ne-Ca Penning ionisation using a commercial hollow cathode lamp discharge. They employed an Optogalvanic Effect spectroscopy (OGE) technique to study the plasma. This technique involves shining a laser on the discharge, which induces changes in the ionisation equilibrium, affecting the electrical resistivity of the plasma and hence altering the voltage current characteristics of the discharge. These effects can be monitored electrically, resulting in an electrical characterisation of optical effects and hence the name. Conducting their experiments in steady state, Shuker *et al.* proceeded by shining a laser into the hollow cathode at frequencies known to excite Ne electrons out of the metastable levels and into nonmetastable higher levels, effectively depopulating the discharge of metastables. Ca, sputtered from the cathode surface by the action of Ne^+ ions, is then ionised by the Ne metastables via the Penning process. The resulting higher number of charge carriers and the high efficiency of the process lowers the potential required to sustain a steady state discharge when compared to the case of pure Ne. Depopulation of the metastable states by laser irradiation hence causes a reduction in the ionisation rate, increases the discharge resistance and subsequently leads to a rise in discharge potential. By studying the post laser pulse discharge voltage history, Shuker *et al.* calculated the Penning cross-section (on the order of $10^{-14}cm^2$), the relevant relaxation times and the Penning rate. Moreover, they also established the range of discharge currents for which the Penning Effect is important.

In ion thruster hollow cathodes, barium plays a dominant role in discharge initiation through enhanced thermionic emission and, as demonstrated here, through Penning ionisation. The role of the low work function material in steady state operation is however less clear [48, 46]. Philip and Fearn [46, 126] proposed secondary emission by metastable impact as a mechanism to explain the high current densities in HC discharges, and noted that this emission mechanism is not dependant on the presence of Ba and the cathode should thus operate successfully in its absence. When they conducted experiments on non-bariated cathodes, they however found that significantly higher voltages and tip temperatures were required to operate the HC. This lead Philip to suggest that "a mechanism requiring the coating normally operated

in conjunction with that dependent on metastable (impact)" [130]. If metastable related processes are significant, then the Penning effect can indeed provide such a mechanism, and the parallels with the Shuker *et al.* [144] Ne-Ca experiment certainly do suggest that this is probable. Having said that, it is not possible to ascertain the significance of the process in the discharge due to lack of information on the relevant cross-sections, relaxation times and concentrations of Ba and the range of currents and pressures in which Penning ionisation is important in cathodes such as the T6. A similar OGE study is necessary to determine the role of Penning ionisation and, more generally, that of metastable atoms in the steady-state operation of ion thruster HC's.

7.1.2 The role of the cathode orifice and breakdown statistics

Figure 7.5 compares the results of the breakdown work on the xenon part of this study to the early work by Fearn *et al.* [48] on mercury with a T4 cathode. The T4 work employed a cathode with an orifice diameter of 0.3mm at a temperature of 1300°C, the cathode insert was coated on its outer surface with a triple carbonate mix. The dashed lines indicate the upper and lower limits of the region where, for a given $\dot{m}$, breakdown can be expected to occur at random, with breakdown being assured only if V_k exceeds the upper envelope of this region.

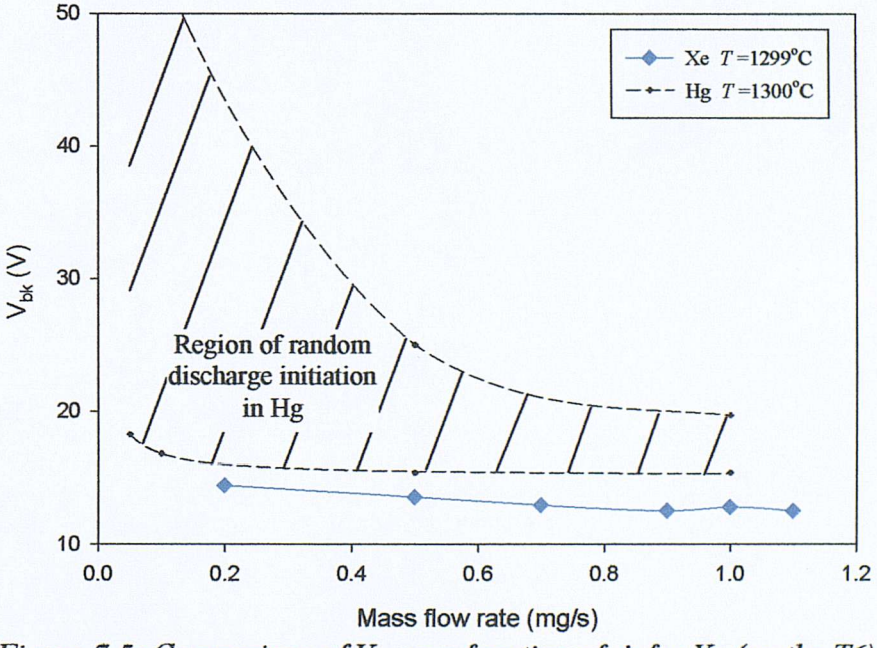

Figure 7.5: Comparison of V_{bk} as a function of $\dot{m}$ for Xe (on the T6) and Hg (on the T4) [48]

It can be seen from figure 7.5 that a remarkable improvement in reproducibility has been achieved in changing from the T4 cathode to the T6. The results from the open-keeper T6 work [124] have also demonstrated this improved reproducibility. The breakdown voltages were slightly higher in the open-keeper T6, this can be attributed to the higher inter-electrode pressure expected in the enclosed-keeper case.

It is important here to note that in the T4 study, time was an additional factor that greatly influenced the breakdown results. Quoting from reference [48], "with $\dot{m}$ =0.14mg/s and T =1220°C, rapidly increasing V_k to 500V did not initiate a discharge, but one occurred after leaving the keeper at this potential for about 1min. On the next attempt, with $\dot{m}$ and T at the same values, the discharge started with V_{bk} =140V. On extinguishing this discharge and waiting for 2min, a further start could not be achieved, even with 500V applied for some while. Later, a discharge was obtained with V_{bk}=220V, yet immediately afterwards the application of 500V was not effective". This indeed highlights the considerable effort undertaken to map the breakdown behaviour of the T4.

It is also interesting to note, from figure 7.5, that the breakdown voltages for xenon are consistently lower than those for mercury for all the mass flow rates investigated. This is in spite of mercury having the lower ionisation potential: the first ionisation potential of mercury is 10.4 V, compared to xenon's 12.13V. Several reasons have been put forward to account for the greater reproducibility in the T6 (see section 2.2.5.2 and reference [124]): i) the change of propellant species ii) contamination of the vacuum system in the T4 study and iii) the larger orifice size in the T6 cathode. Of these the effect of orifice size was thought to be the more likely (and easiest to investigate) of the three, and was hence subjected to greater scrutiny.

To both qualify and quantify the effect of the cathode orifice on electric field penetration, the Crawford/Gabriel model (Appendix B) was used to simulate in 3-D the electric field in the vicinity of the cathode tip for a range of keeper voltages. Results for different orifice sizes and tip configurations are shown in figure 7.6.

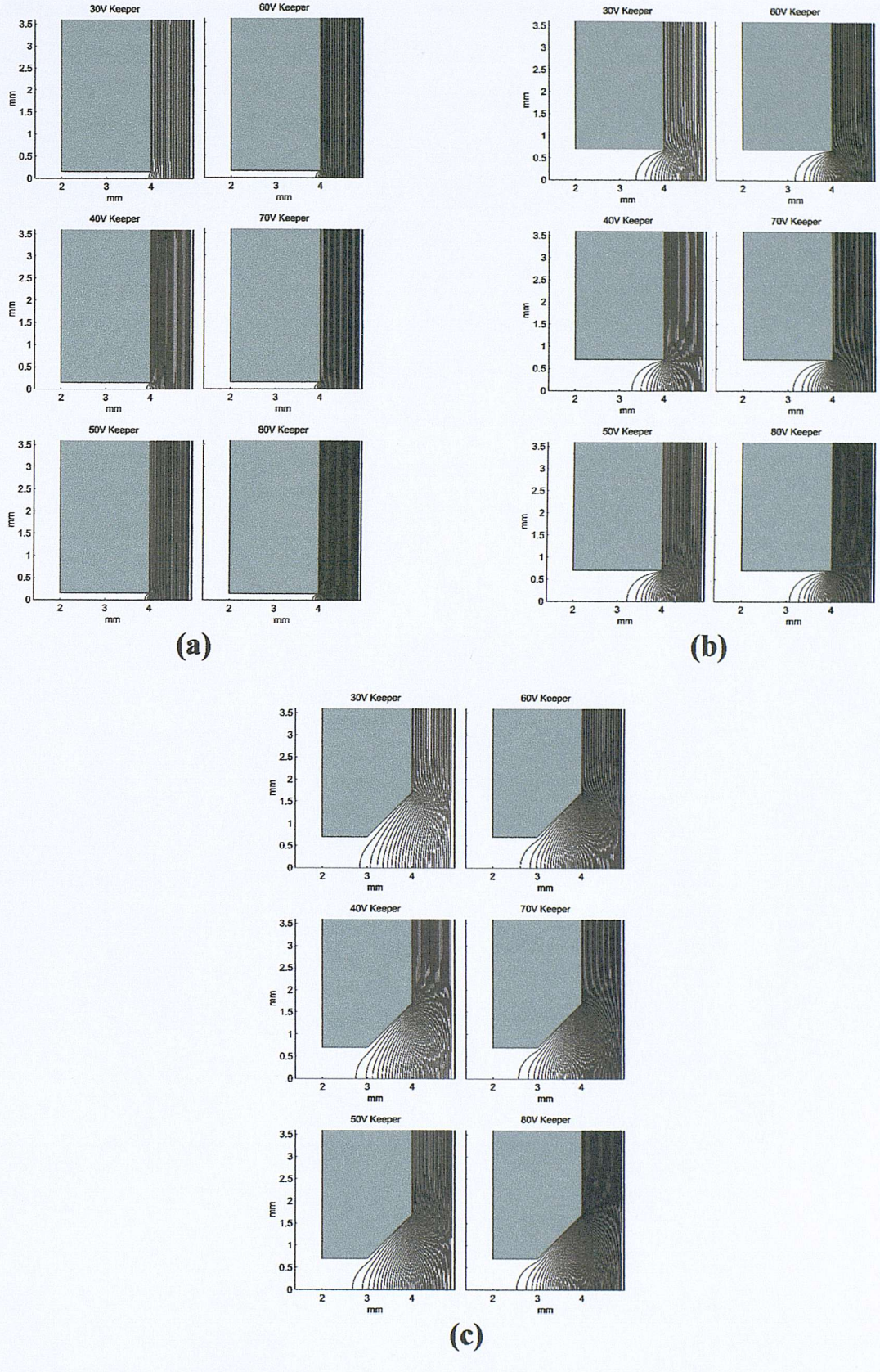

Figure 7.6: 1V contours of electric potential for: **(a)** *a flat 0.3mm dia. tip (similar to the T4 Hg case [48]).* **(b)** *a flat 1.4mm dia. tip.* **(c)** *a bevelled 1.4mm dia. tip (similar to the T6 case), for several keeper potentials*

Figure 7.6(a) represents the T4 hollow cathode used to obtain the mercury breakdown data in figure 7.5, with a flat tip surface and a 0.3mm orifice [48]. Figure 7.6(c) represents the T6 cathode used in this work, with a 1.4mm diameter orifice countersunk at 45° to 1mm depth. Figure 7.6(b) represents a cathode with the same dimensions as the T6 but without a bevelled orifice plate, to evaluate the effect of countersinking on the electric field profile.

The results show that for the T4 case the electric field only penetrated 0.13mm into the cathode tip at the highest simulated keeper potential of 80V (for 30V keeper potential the electric field only penetrated to 0.053mm into the cathode tip). The results for the unnotched T6 cathode showed a great improvement with 0.635mm penetration at only 30V keeper potential. For the bevelled T6 tip, the field penetration was deeper still, with 1.164mm at 30V keeper potential. The results show that, not only is the orifice diameter important in determining the electric field penetration, but that the hollow cathode tip configuration also has an appreciable effect. The penetration of the electric field has a determining effect on the time lags and statistics of the cathode breakdown, as will be discussed next.

For breakdown to occur, two conditions must be satisfied simultaneously [109]: 1) At least one suitably placed free electron must exist in the gap to initiate the discharge. 2) The applied electric field must be of sufficient strength and duration to guarantee that this electron produces a sufficient series of successful electron avalanches to achieve breakdown. If sufficient initiatory electrons are unavailable, it is necessary to wait for a period of time before the discharge develops. The waiting period preceding breakdown is known as the total time lag of spark breakdown t_{tot}. It is made up of two distinct and well-defined parts; the initiatory or statistical time lag t_s and the formative time lag t_f, i.e. $t_{tot} = t_s + t_f$.

It is important here to clarify that the values of the breakdown voltage quoted in the literature for the variety of gases and conditions is known as the static or steady state sparking potential (V_s) and is obtained under steady state conditions with a constant static field (E is constant) and sufficient electron production (by for example irradiation from a UV source) to ensure the presence of initial electrons. V_s is thus

fairly reproducible and well defined. However, if there is an impulsive increase in voltage (even at low rate (pg. 205 [162])), and if insufficient electrons are produced, the breakdown voltage is found to be subject to statistical variation. In this case V_s forms a minimum value below which it is impossible to achieve breakdown.

- *Dependence of the statistical time lag on the electron production rate*: The statistical time lag is the time elapsing between the application of a voltage in excess of V_s and the appearance of the electron that initiates breakdown. The mean statistical time lag $\bar{t}_s$ is the inverse of the rate of electron liberation (I_{pr})[109]:

$$\bar{t}_s = 1/I_{pr} \tag{7.8}$$

The number of times (n_t) that the statistical time lag exceeds a time t for a large number of trials N can be given by:

$$\frac{n_t}{N} = \exp(-I_{pr}\, t) \tag{7.9}$$

Also, if the voltage V never greatly exceeds V_s (i.e. the breakdown criteria is just satisfied), then there is a significant number of unsuccessful avalanches (as will be discussed in the next paragraph) and several primary electrons will have to appear, following the attainment of V_s, before breakdown occurs. The statistical time lag is hence also dependent on the excess voltage (or "overvoltage"), with t_s increasing as the applied voltage is decreased towards the critical value V_s [109]. Thus we need to replace I_{pr} in equations (7.8) and (7.9) with ($P_r \times I_{pr}$) where P_r gives the probability of a successful avalanche at the given excess voltage.

- *The formative time lag and avalanche statistics*: The collisional processes leading to the formation of sparks and the establishment of a discharge are essentially chance phenomena governed by the laws of probability. Townsend's primary (α) and secondary (γ) coefficients represent the average values for the statistically fluctuating quantities, with the magnitude of these fluctuations having an important bearing on the breakdown criteria. The breakdown condition, equation (3.55) ($\gamma[exp(\alpha d)-1]=1$), represents the condition of an uninterrupted series of avalanches flowing indefinitely between electrodes maintained at an inter-electrode

voltage $V=V_s$. Under these conditions, the α and γ processes ensure replenishment of electrons and ions lost to the electrodes, and hence lead to a self-sustaining discharge.

However, as mentioned previously, the primary and secondary replenishment processes are statistical in nature. The initial electron moving in an electric field may or may not gain enough energy to ionise a gas atom in an '*average*' distance of $1/\alpha$. Once it has gained ionising energy, there is a chance it will ionise only after several impacts have taken place, with the associated risk of it losing its energy before doing so. This statistical picture also applies to secondary emission from the cathode by ion bombardment or otherwise. Because of the large fluctuations about the mean, it is possible that at some stage in the electron avalanche, the breakdown criteria is not satisfied (by greater loss than gain of charged particles) and the avalanche is "interrupted" [109]. The current hence ceases in spite of V being maintained equal to V_s. The probability (P_r) of an uninterrupted avalanche initiated by a single electron is [109]:

$$P_r = 0 \qquad for \quad Q < 1$$

$$P_r = 1 - \frac{1}{Q} \qquad for \quad Q > 1 \tag{7.10}$$

$$\text{with } Q = \gamma\left[exp(\alpha d) - 1\right]$$

Q =1 represents the static breakdown condition with $V=V_s$. When $V < V_s$ and $Q < 1$ breakdown is not possible and hence $P_r = 0$. However, even when $V > V_s$ ($Q > 1$), P_r is less than unity for voltages significantly greater V_s and hence it is not guaranteed that a current will flow uninterrupted. As illustrated in figure 7.7, a significant excess voltage or overvoltage must be applied to ensure an uninterrupted avalanche produced by a single electron. Overvoltage, ΔV, is here defined as the difference between the applied voltage and the static voltage V_s expressed as a fraction of V_s [109], i.e. $\Delta V = (V - V_s)/V_s$.

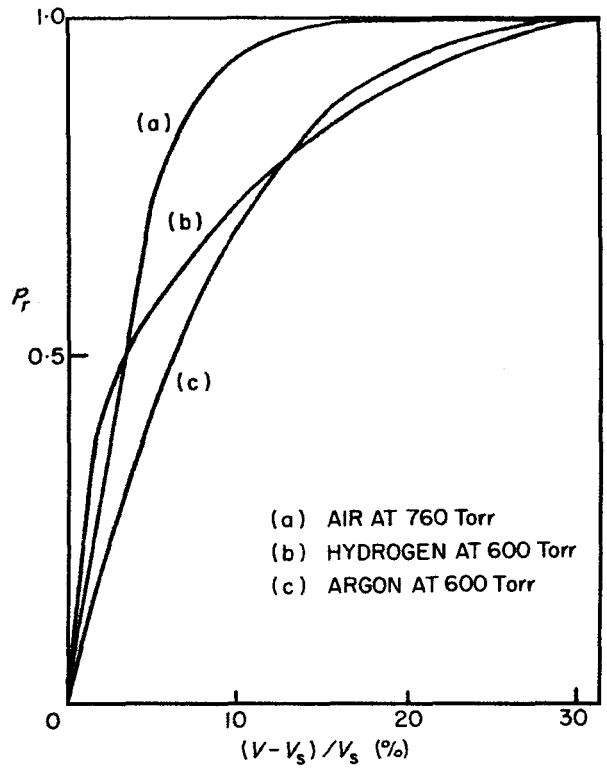

Figure 7.7: Probability of an uninterrupted sequence of electron avalanches initiated by a single electron as a function of overvoltage [109].

If more than one electron is used to initiate breakdown the probability of interruption decreases markedly. If N electrons are used to initiate N avalanches, the probability of an uninterrupted sequence is now [109]:

$$P_r(N) = 1-(1-P_r)^N \qquad (7.11)$$

Thus, to ensure *reliable* and rapid breakdown, a large number of initiating electrons and a large overvoltage are required.

The formative time lag is the time taken by initiating electrons to break down the gap and establish a discharge. Hence, it is dependent on the applied overvoltage, the nature and pressure of the gas, the electrode material and the number of initiating electrons.

We now turn our attention back to hollow cathodes and proceed to describe the behaviour of the Fearn *et al.* [48] Hg HC (described earlier and in section 2.2.5) at a given value of T and $\dot{m}$. In the HC, primary electrons are produced by thermionic

emission from the cathode insert. However, most of the electrons will be found in the cathode interior, and relatively few electrons will diffuse through the aperture, via random collisions, into the orifice region. At a low applied voltage, V equal to or slightly greater than V_s, the field only penetrates a very small distance into the cathode orifice. The probability of an electron arriving at the *right location* to be accelerated by the field is hence expected to be low. Due to the small overvoltage, the probability of an uninterrupted avalanche by one electron is also low (see figure 7.7), and consequently the probability of uninterrupted avalanches by a small number of electrons, as described by the relation (7.11), is also low. There is thus little chance of the necessary prerequisite conditions being simultaneously satisfied at low overvoltage and breakdown is highly unlikely.

Increasing the overvoltage to intermediate values, at constant T and $\dot{m}$, raises the chances of a successful breakdown both in terms of enhancing the probability of a non-arrested avalanche and increasing the penetration depth to where there is a higher probability of finding initiatory electrons. Increasing the overvoltage hence brings us to the envelope of random breakdown described by Fearn *et al.* [48]. The occurrence of breakdown in this region is dependent on the rate of arrival (and number) of initiating electrons at a suitable location and the probability of them producing an uninterrupted breakdown. Hence, due to the large possible fluctuations in these quantities for a given run, there will be a large scatter in the observed breakdown voltage. Moreover, as observed by the investigators, this statistical behaviour will also manifest itself, not only in the value of the breakdown voltage, but also in the unpredictable nature of the time required from the application of the voltage to the achievement of breakdown.

The number of electrons required to initiate a spark decreases with increasing overvoltage applied to the gap [109]. By further increasing the applied voltage, a point is reached when the probability of an uninterrupted avalanche reaches unity (figure 7.7). This point forms the upper envelope of the Fearn *et al.*'s data. At and above this point the electron avalanche cannot be arrested and the breakdown criteria is always satisfied. As the investigators observed, to ensure breakdown of the HC, V_k has to exceed the upper envelope of the region.

The above description indeed simultaneously explains: the higher breakdown voltages observed in the Hg cathode, the presence of a region of irreproducibility in the breakdown voltage results, and the random nature of the time lag between application of the voltage and the onset of breakdown. Two factors will dictate the extent of the random discharge region a) the cathode temperature and b) the mass flow rate (i.e. gas pressure). Increasing the cathode temperature results in a higher rate of electron production by thermionic emission as described by the Richardson-Dushman equation (equation 2.1). At the field location, this results in an increase in the number of initiating electrons (N) and hence, by equation (7.11), increases the probability of an uninterrupted sequence of avalanches for a given overvoltage. Accordingly, the range of voltages for which the breakdown voltage is irreproducible is reduced as temperature is increased. Ultimately, at high cathode temperature, the initial electrons are so numerous that the probability of interruption is zero, the breakdown criteria is always satisfied and breakdown is reproducible, as observed experimentally (figure 2.12). The gas flow rate influences the breakdown statistics via a different mechanism. Raising the gas pressure (at low to medium pressure) increases the total collision cross-section and hence the gas multiplication for a given overvoltage and number of initiating electrons. Increasing the gas pressure thus increases the probability of an uninterrupted sequence P_r for each individual avalanche, and hence reduces the overvoltage required for reliable breakdown. Consequently, we expect that increasing the propellant flow rate will reduce the envelope of the random breakdown region, which is indeed the experimental observation (figures 7.11 and 2.13).

In the case of the T6 cathode, the larger orifice size yields two benefits: The first, which was demonstrated earlier, is the increased electric field penetration for a given applied voltage, which increases the probability of finding an electron at the field locality and also increases the distance travelled by the electron (and hence its terminal energy) while being accelerated by the field. The second is that the increased orifice size also increases the number of electrons diffusing into the orifice region. The combined effect leads to a more reproducible breakdown behaviour. Moreover, we note that, in accordance with the theory, there was an increase in the spread of breakdown results when the T6 operating temperature was reduced from 1299°C to 929°C for all the gases (figures 6.1-6.4). This is due to the reduction in the electron

production rate, nevertheless, owing to the beneficial effects of the larger orifice, the spread in results was far less than that encountered in the Hg tests.

The strongest evidence that the orifice size is solely responsible for the observed irreproducibility actually comes from the mercury study itself. Fearn *et al.* [48] in their investigation conducted some test using auxiliary internal electrodes to initiate the discharge. Biasing the internal electrode positive with respect to the cathode, the breakdown characteristic shown in figure 7.8 was obtained. It was found that the discharge exhibited superior breakdown ability, at 1200°C and 0.8mg/s a potential of *only 6V* was required to initiate the discharge. This cathode had almost exhausted its barium supply and usually required a keeper potential of 500V to start! Note also that even at the very low cathode temperature of 520°C, the electrodes only required 30V to start. Most significantly this behaviour was *reproducible*.

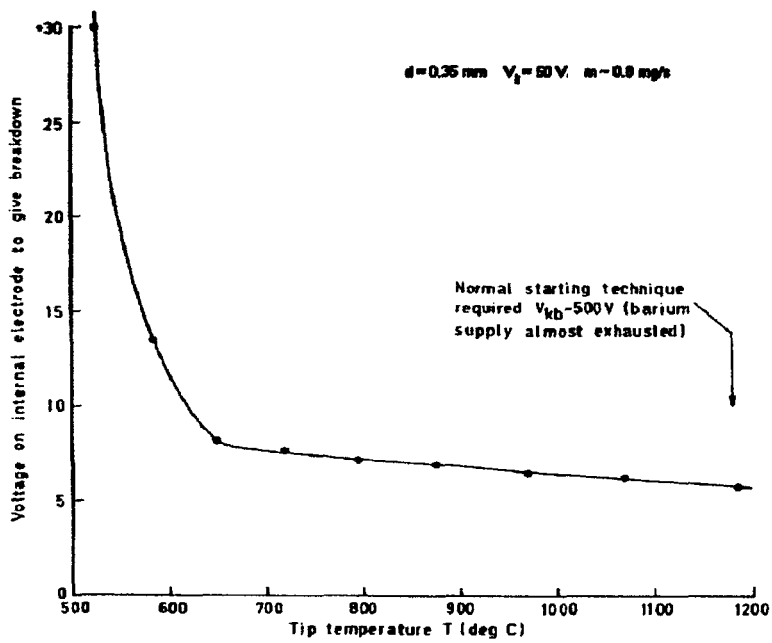

Figure 7.8: Discharge initiation characteristics using an internal electrode [48]

The internal electrode achieved this in two ways: 1) It accelerated a large number of the electrons emitted from the cathode insert in its vicinity. 2) The high neutral density in the HC interior ensured that the probability of interruption for the large number of avalanches expected was virtually zero. Note here that, in comparing the experiments with and without the auxiliary internal electrodes, the degree of

contamination and the operating gas are the *same*. The only difference being ***the location of the accelerating field***.

The results of this section are highly significant, as they imply that judicious design of the cathode tip will eliminate the need for a high voltage keeper power supply. The discharge initiation voltages will not only be low but also reproducible. Discarding the HV keeper supply will result in the concurrent benefits of a reduction in thruster mass, complexity and associated hardware.

7.2 Spectroscopic results

7.2.1 Discussion of analysis methods employed

As discussed in section 3.1.3, three methods were employed to evaluate the plasma parameters T_e and n_e: a) the ratio of lines of the same species, b) the ratio of lines of the same element at different stages of ionisation and c) the ratio of continuum intensities.

The ratio of lines of the same species method is used to estimate the electron temperature for a plasma in the C-R regime using a simple Boltzmann plot method developed in this work and discussed in section 3.1.3.1. The results for the various propellants are presented in the next section, figures 7.12 -7.17.

The continuum method formed an alternative approach to estimating T_e, and has been previously employed to that end in a Kaufmann type UK-25 HC xenon discharge [101]. The spectra was first corrected for the transmission of the optics and the frequency response of the detector in a region of the spectrum ranging from 280-310nm. In this region the density of discrete emission lines is low. By plotting log (I) against λ, and by judicious removal of any traces of superimposed emission lines, plots such as figure 7.9 were produced.

This method is subjective in nature as it requires the identification of the region of linear decay due purely to bremsstrahlung processes. Limiting the application of equation (3.48) to this region gives the electron temperature. As can be seen from figure 7.9, the spread in results (due to the low signal to noise ratio attributable to the relatively low transmissivity and frequency response of the optics/detector assembly in that wavelength range) makes such a subjective assessment difficult. Furthermore, the spread makes for a low degree of confidence in the selection of a best fit line. This has rendered the application of this method unsuccessful and precluded its use in the estimation of T_e.

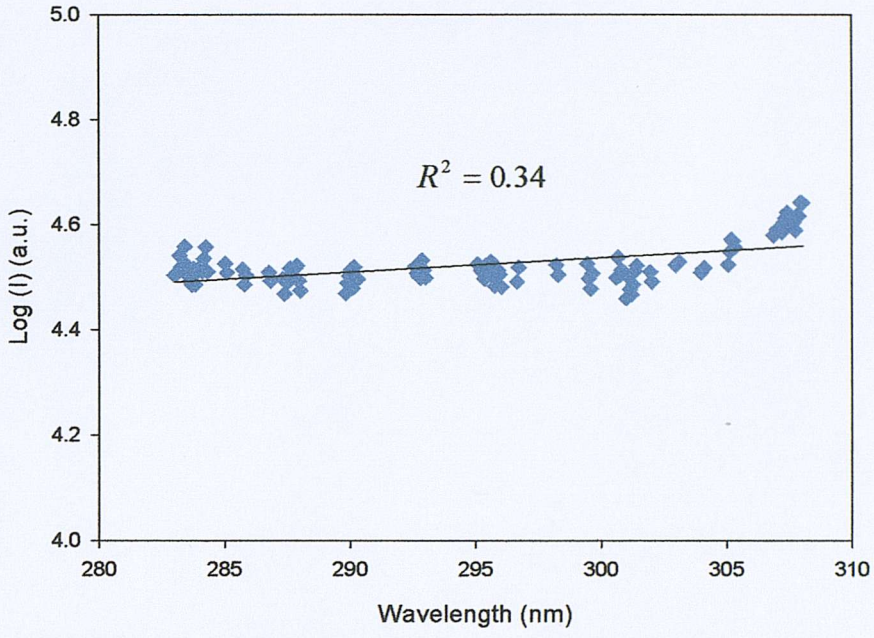

Figure 7.9: Log I vs λ for continuum in a xenon discharge, $\dot{m}$ =1mg/s, I_a=5A

The strategy envisaged for estimation of n_e is as follows: T_e is first calculated by the aforementioned ratio of lines of the same species method. The ratio I_{II}/I_I of a first ionisation and a neutral line of the gas is then calculated from the spectrum. These two parameters, along with the relevant atomic data, are then inserted into equation (3.47) to yield n_e.

Figure 7.10 shows the theoretical ratio of intensities of two xenon emission lines (the XeII 433.052nm line over the XeI 450.100nm line) based on the C-R model described by equation (3.47) as a function of T_e for several values of n_e. Due to three body recombination, the ratio of line intensities at different stages of ionisation should (theoretically) depend on electron density. However, as can be seen from figure 7.10, this dependence on n_e is very weak in the range of T_e expected in our plasma, with a five orders of magnitude change in n_e (from 10^{11} to 10^{16}cm^{-3}) occurring when T_e is changed by only 0.1eV from 1.1 to 1.2eV. This is in agreement with a previous spectroscopic study on xenon which employed this method (Monterde *et al.*[115, 116]), which concluded that due to this insensitivity, n_e could not be precisely determined and indeed quoted a value for n_e in the 10^{11} to 10^{16}cm^{-3} range. Thus, even a small uncertainty in estimating T_e precludes any determination of n_e to an acceptable accuracy.

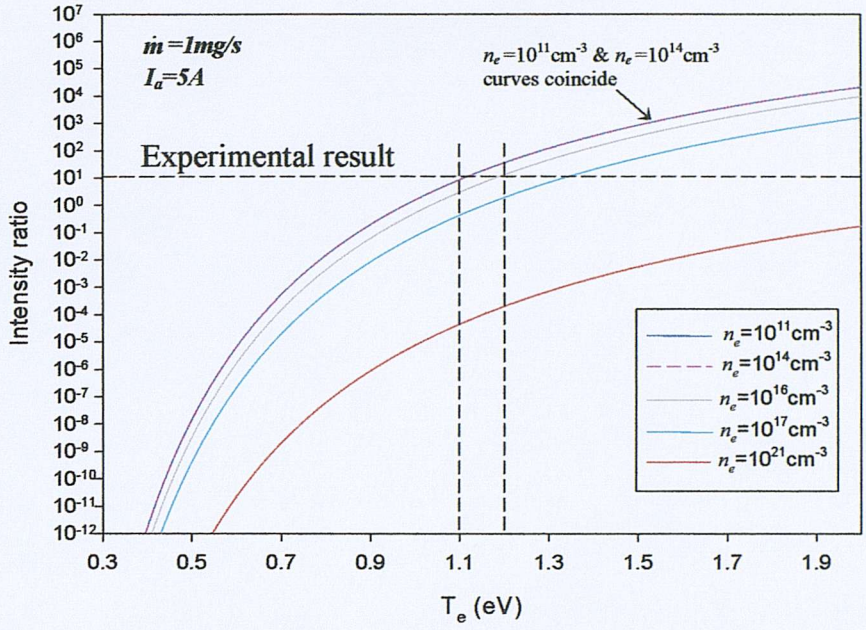

Figure 7.10: Intensity ratio of the XeII 433.052nm and XeI 450.100nm lines as a function of electron temperature for several n_e values

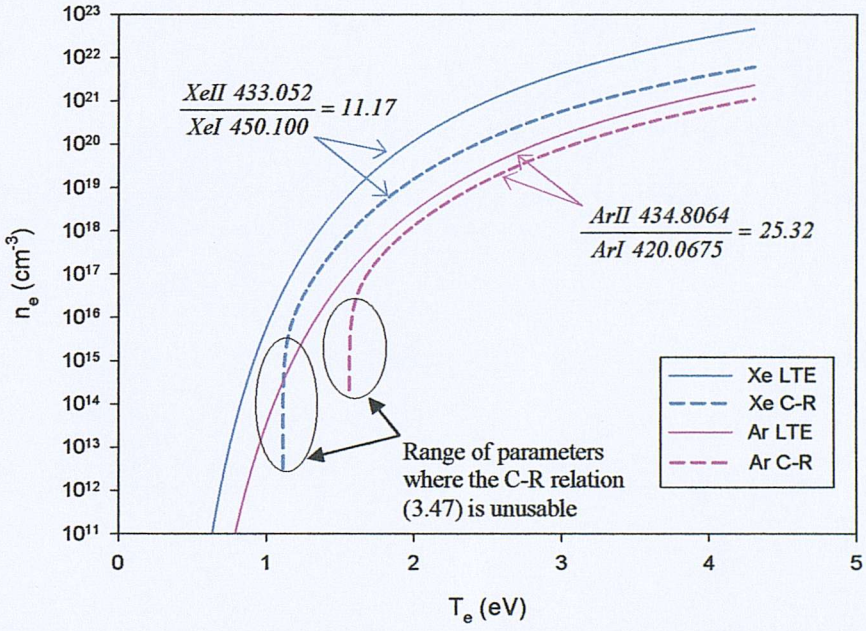

Figure 7.11: n_e as a function of T_e predicted by both LTE model and equation (3.47) for the C-R model in xenon and argon discharge, $\dot{m}$ = 1mg/s and I_a = 5A in both gases

An alternative approach had to be adopted for estimating the electron density. Using the relative intensity of lines at different stages of ionisation method for a plasma in LTE gives the following relation for electron density [59, 94]:

$$n_e = 2\times\frac{I_I(p',q')}{I_{II}(p,q)}\frac{\lambda_{p'q'}}{\lambda_{pq}}\frac{A(p,q)}{A(p',q')}\frac{g_{II}(p)}{g_I(p')}\left(\frac{2\pi m_e kT_e}{h^2}\right)^{3/2}\times exp\left(-\frac{E_{II}(p)-E_I(p')+E_{I\infty}(g)}{kT_e}\right)$$

(7. 12)

The predicted dependence of n_e on T_e from this LTE relation is compared to that in equation (3.47) for a C-R plasma in figure 7.11. This is done for xenon at the experimentally measured relative intensity of *XeII 433.052/XeI 450.100 = 11.17* at the discharge conditions: $\dot{m}$ = 1mg/s and I_a = 5A, as well as for argon at the experimentally measured relative intensity of *ArII 434.8064/ArI 420.0675 = 25.32* for an argon discharge at $\dot{m}$ = 1mg/s and I_a = 5A. From figure 7.11, in the range of T_e where equation 3.47 is useful, the LTE estimate of electron density is, as expected, greater than that of the C-R model. Moreover, in this region, the difference between the predicted values of n_e at a given T_e appears to be approximately constant; for xenon $n_{e,LTE} = (6.64 \pm 0.09)\times n_{e,C-R}$ and for argon the agreement is very good with $n_{e,LTE} = (1.13 \pm 0.14)\times n_{e,C-R}$. In general, assuming that this proportionality between the values of n_e predicted by the LTE and C-R models at higher T_e holds in the region where the simplifications made to the C-R model in obtaining equation (3.47) breakdown, the electron density estimated by using an LTE model (equation (7.12)) overestimates the density in a C-R plasma by no more than one order of magnitude. Thus we can use the LTE relation to give a substantially more accurate estimate of n_e than that of equation (3.47); furthermore, for argon discharges the agreement is expected to improve. In what follows, equation (7.12) is used to estimate n_e. Whenever equation (3.47) is thought to be applicable both values are provided for comparison.

7.2.2 Calculation of electron temperature and density

The plasma electron temperature was determined using the C-R Boltzmann plot method described in detail in section 3.1.3.1. Vital to the successful application of this method is the judicious selection of emission lines belonging to transitions from upper levels of quantum number p greater than p_s the "thermal level" (see sections 3.1.2.4 and 3.1.3.1). Fortunately, it was found that this condition was satisfied in virtually all

the first ionisation emission lines of argon, krypton and xenon, in the 400-463nm wavelength range investigated.

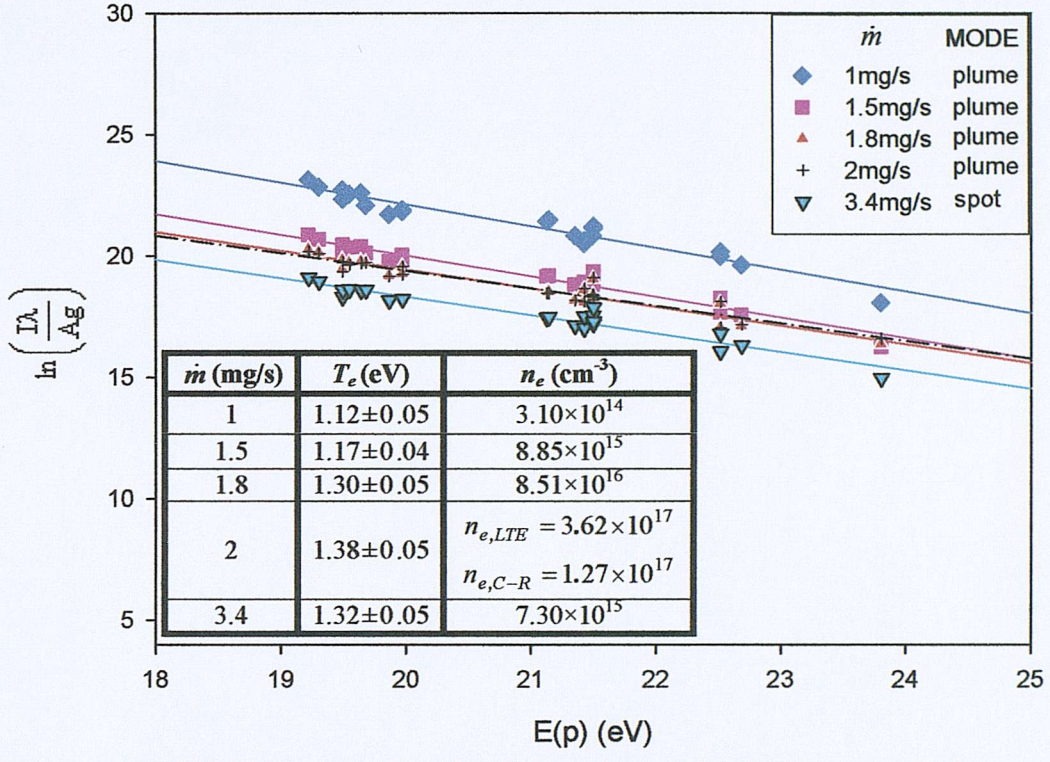

$\dot{m}$ (mg/s)	T_e (eV)	n_e (cm^{-3})
1	1.12±0.05	3.10×10^{14}
1.5	1.17±0.04	8.85×10^{15}
1.8	1.30±0.05	8.51×10^{16}
2	1.38±0.05	$n_{e,LTE} = 3.62\times10^{17}$ $n_{e,C-R} = 1.27\times10^{17}$
3.4	1.32±0.05	7.30×10^{15}

Figure 7.12: C-R Boltzmann plot of ArII lines from T6 cathode argon discharges in both spot and plume modes at several values of $\dot{m}$, I_a=5A, correlation coefficient > 0.92

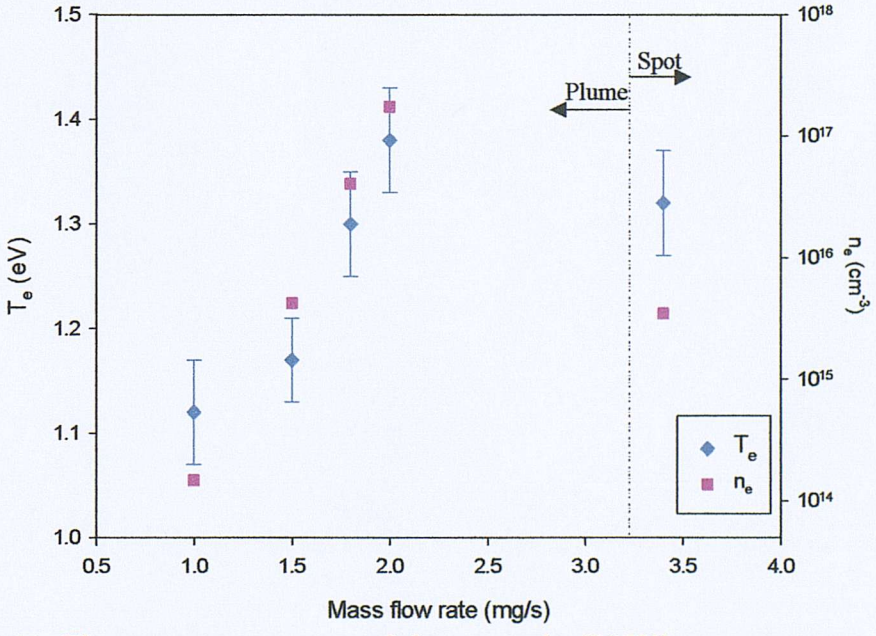

Figure 7.13: Electron temperature and density in the T6 HC operating on argon as a function of $\dot{m}$ at I_a=5A

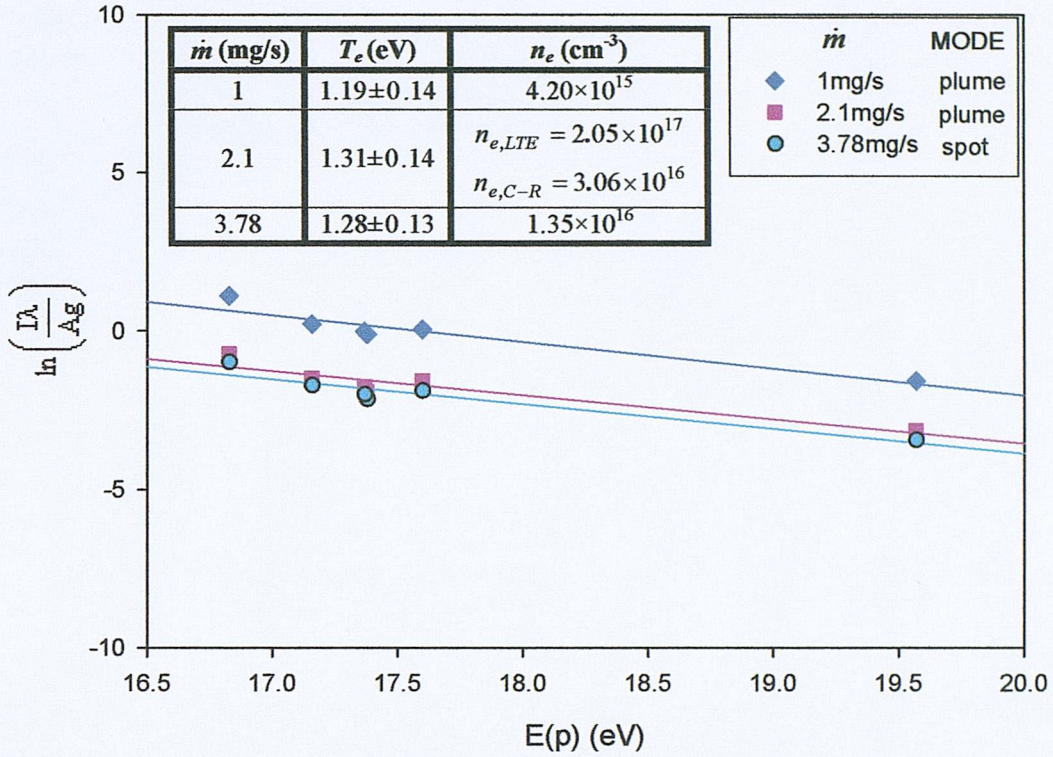

Figure 7.14: C-R Boltzmann plot of KrII lines from T6 cathode krypton discharges in both spot and plume modes at several values of $\dot{m}$, I_a=5A, correlation coefficient > 0.89

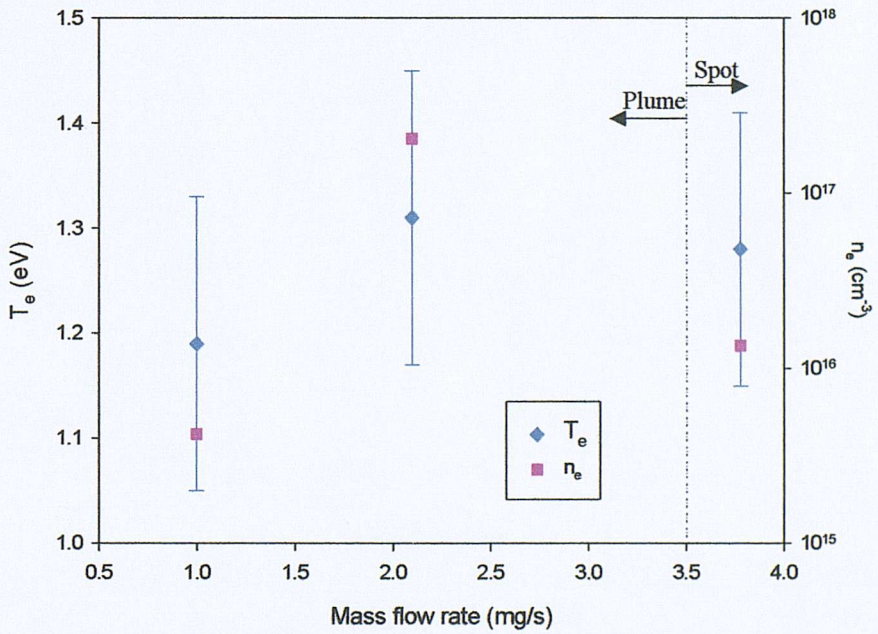

Figure 7.15: Electron temperature and density in the T6 HC operating on krypton as a function of $\dot{m}$ at I_a=5A

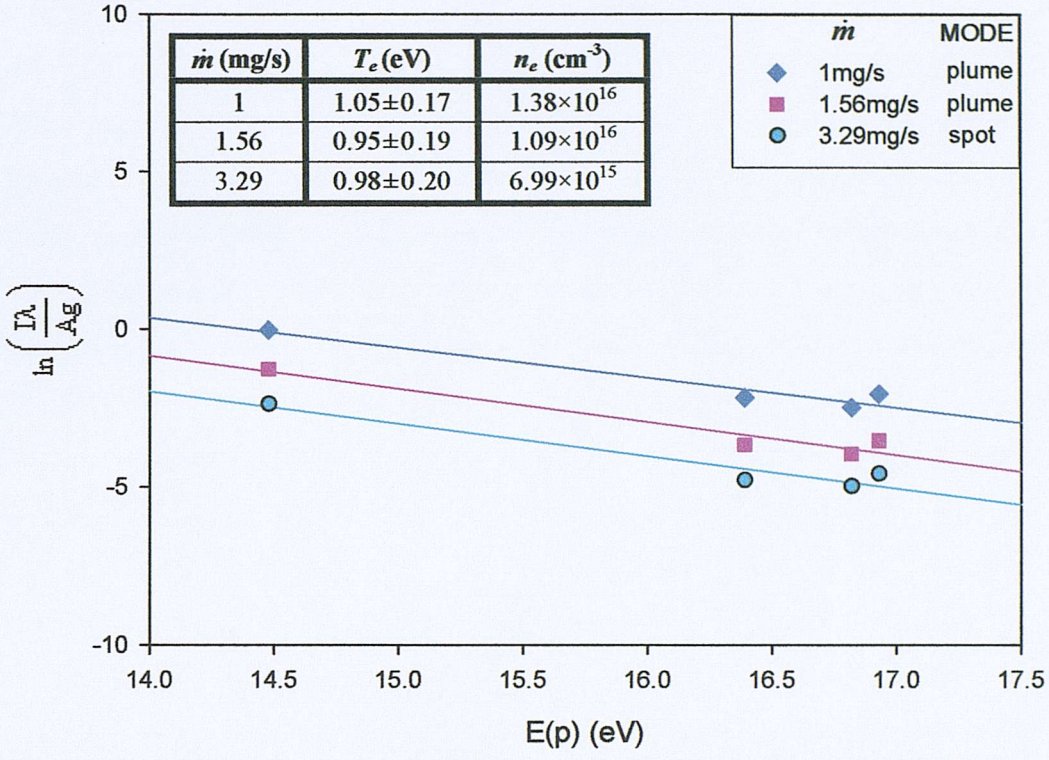

Figure 7.16: C-R Boltzmann plot of XeII lines from T6 cathode xenon discharges in both spot and plume modes at several values of ṁ, I_a=5A, correlation coefficient > 0.93

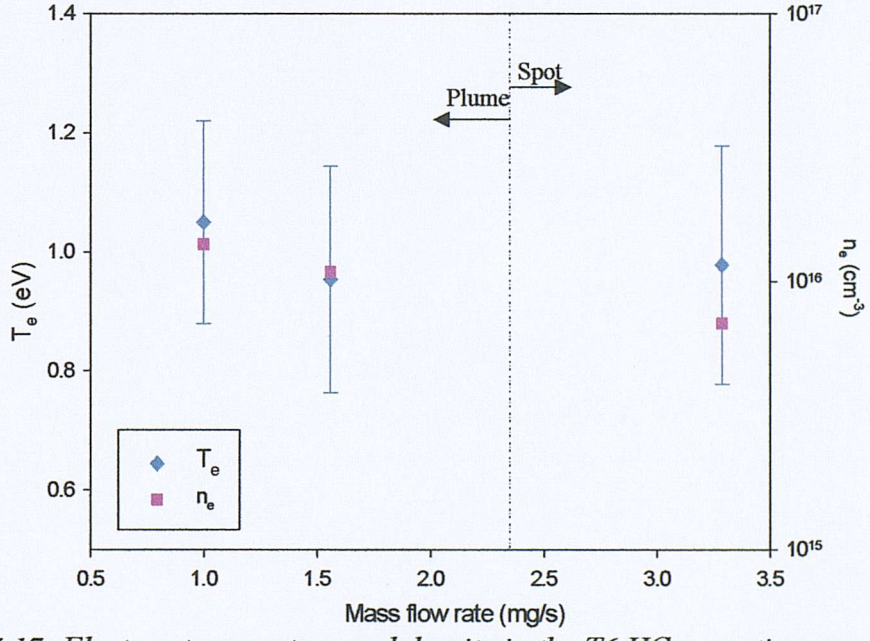

Figure 7.17: Electron temperature and density in the T6 HC operating on xenon as a function of ṁ at I_a=5A

Figures 7.12, 7.14 and 7.16 exhibit C-R Boltzmann plots: $ln(I_Z(p,q)\lambda_{pq}/[A(p,q)g_Z(p)])$ as a function of energy of the upper level $E_Z(p)$, for

argon, krypton and xenon first ionisation lines respectively. The emission lines were taken from optical emission spectra similar to those shown in figures 6.28 - 6.30, at several values of $\dot{m}$ and a constant discharge current of 5A. This enabled the estimation of plasma parameters in both the spot and plume modes. It was not possible to use all the identified emission lines in the wavelength range due to the lack of the necessary pertinent atomic data in the bibliography (most notably $A(p,q)$, the atomic transition probability). Thus, only those first ionisation emission lines provided with a complete set of atomic parameters in the literature were used (refer to table 6.1 - 6.3 for a complete listing of the available lines in the range 400-463nm). The intensity of the emission lines was corrected for the spectral transmission properties of the optics and the spectral response of the CCD. The corrected intensities were then used to construct the C-R Boltzmann plots. The resulting data are fitted to a straight line by the method of least squares linear regression. It was found that there was excellent correlation between the data and fit, with the correlation coefficient (R^2) greater than 0.92 for Ar, 0.89 for Kr and 0.93 for Xe. The electron temperature is calculated from the slope of the line, $S = -1/kT_e$. The calculated T_e for each value of $\dot{m}$ is included in the inset to the figures. The electron density was calculated using the LTE method represented by equation (7.12) and described in the preceding section. The n_e calculations were carried out using the experimentally measured ratio of the ArII 434.8064/ArI 420.0675nm lines in the case of argon, the KrII 435.5477/KrI 446.3689nm for krypton and the XeII 433.052/XeI 450.100nm ratio for xenon.

The variation in n_e and T_e with propellant flow rate is shown graphically in figures 7.13, 7.15 and 7.17 for argon, krypton and xenon propellants. The uncertainty in the T_e results, shown in the insets to the Boltzmann plots and graphically in the T_e plots, indicates the standard error in the linear regression fit, which is a function of both the goodness of fit and the number of data points used to construct the fit. Thus, the error is smallest for argon which possesses numerous emission lines which have been the subject of extensive study in the wavelength range, and the error is largest for xenon, which reflects rather the dearth in spectroscopic data as opposed to the goodness of the fit, which has been shown to be very good ($R^2 > 0.93$).

The results for n_e and T_e in argon and krypton show an interesting trend, increasing in the plume mode with $\dot{m}$ till a maximum value is reached then decreasing, as $\dot{m}$ is increased further, to a lower value in the spot mode. In the case of xenon, as will become later apparent, we have only captured the range of $\dot{m}$ in which T_e and n_e are decreasing functions of the propellant flow rate (the range of $\dot{m}$ was chosen prior to the discovery of this behaviour). The observed behaviour apparently contradicts previous studies [46, 115, 146], specifically, the Langmuir probe measurements in the HC interior plasma [146], in which the measured electron densities were an order of magnitude greater in the spot mode than in the plume mode. These trends can be understood in terms of visual observations of the discharge. In table 7.2 we recast the results according to the visual characteristics of the discharge. The first column shows and describes the visual appearance of the discharge in which the spectrum (from which the n_e and T_e results were calculated) was taken. The pictures shown were obtained in a xenon discharge in the T6. The same characteristics were observed in the other gases and are viewed here as illustrative of the visual appearance of the discharge. At low $\dot{m}$ a "luminous cloud" is observed which fills the inter-keeper-cathode space giving the appearance of an enlarged cathode spot. As $\dot{m}$ is increased, this cloud emerges from the keeper orifice and is now situated downstream of the keeper, making it clearly visible. When the spot mode is achieved, by further increasing $\dot{m}$, the cloud disappears abruptly and only the luminous cathode spot is observed. The origins, characteristics and effects of this cloud will be discussed in section (7.4.4) in terms of a proposed plume to spot transition theory. Suffice here to say that this cloud is a region of enhanced inelastic collisions (ionisation and excitation) due to the presence of a steep, electron accelerating gradient in the plasma potential just upstream of the cloud. With the optical fibre observing the hollow cathode from 135mm downstream of the tip (see figure 4.4), our plume results would represent the global values of n_e and T_e spatially integrated over the cloud as well as the HC plasma, leading to the higher than expected results. In the plume mode, local, spatially resolved measurements of n_e and T_e in the HC interior would indeed be expected to be lower than those measured here.

	Argon	Krypton	Xenon
 Plume mode: Luminous cloud upstream of keeper	$\dot{m}$ =1mg/s T_e=1.12±0.05eV n_e=3.10×10^{14}cm^{-3}	$\dot{m}$ =1mg/s T_e=1.19±0.14eV n_e=4.20×10^{15}cm^{-3}	Spectrum not available
 Plume mode: Luminous cloud downstream of keeper	$\dot{m}$ =1.5mg/s T_e=1.17±0.04eV n_e=8.85×10^{15}cm^{-3}	$\dot{m}$ =2.1mg/s T_e=1.19±0.14eV n_e=2.05×10^{17}cm^{-3}	$\dot{m}$ =1mg/s T_e=1.05±0.17eV n_e=1.38×10^{16}cm^{-3}
	$\dot{m}$ =1.8mg/s T_e=1.30±0.05eV n_e=8.51×10^{16}cm^{-3}		$\dot{m}$ =1.56mg/s T_e=0.954±0.19eV n_e=1.09×10^{16}cm^{-3}
	$\dot{m}$ =2.0mg/s T_e=1.38±0.05eV n_e=3.62×10^{17}cm^{-3}		
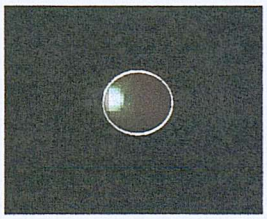 Spot mode: Luminous cloud disappeared	$\dot{m}$ =3.4mg/s T_e=1.32±0.05eV n_e=7.30×10^{15}cm^{-3}	$\dot{m}$ =3.78mg/s T_e=1.28±0.13eV n_e=1.35×10^{16}cm^{-3}	$\dot{m}$ =3.29mg/s T_e=0.978±0.20eV n_e=6.99×10^{15}cm^{-3}

Table 7.2: The plasma parameters (n_e, T_e) as a function $\dot{m}$ correlated to the visual appearance of the discharge

The results of T_e for xenon agree very well with those of Monterde (1.1±0.1eV) [115] and Malik (1.1eV) [101] on the UK-25 hollow cathode, which form the only measurements available to date on inert gas thruster cathodes. This effectively

validates the new method used in obtaining the T_e results. For the other gases, we observe that, in the spot mode, the electron temperature increases with the ionisation potential of the gas at approximately constant electron density (±50%). This comes about due to the factor $(T_e)^{3/2} exp(-E_{I\infty}/kT_e)$ in equation (7.12), which indicates, for a constant n_e and ignoring differences in atomic parameters, that as you increase the ionisation potential by changing the working gas, the electron temperature must increase to keep n_e constant. The exponential in the factor originates from the Saha equation used in deriving (7.12). What it describes is that, for a given electron distribution, the number of electrons capable of ionising collisions is a decreasing exponential function of a threshold energy (the ionisation potential of the gas). Thus, as the ionisation potential increases, less and less electrons are capable of ionising the gas atoms. In order to achieve the minimum electron density required for the spot mode, the discharge in the alternative gases needs to increase the number of electrons capable of ionisation, thus leading to the observed higher electron temperatures in krypton and argon.

Limitations of the analysis models

In deriving the ladder approximation to the C-R model of the HC plasma we refer to simple atomic systems, where the population rate equations are determined solely by the ground populations. In this analysis we ignore the excited levels by assuming that their relaxation times are orders of magnitude smaller and hence their transitions can be considered instantaneous with respect to the observation time. However, this is not strictly true for metastable levels, which are long lived and possess, albeit smaller, but comparable relaxation times to the ground population of the atom. Our model takes no account of these levels.

A possibly more important overlooked factor is the presence of impurities in the plasma (notably barium in our case). The presence of impurities, even in low concentration, can perturb overall plasma behaviour [17]. Barium has an ionisation potential lower than that of the inert gases, this leads to greater probability of ionisation even by electron collisions or by non-electron related ionising events (e.g.

Penning ionisation). The electron contribution from the impurity species not only modifies the electron density estimate, but also modifies the electron distribution function and thus our T_e estimate. However, a quantifying assessment of this effect is exceedingly difficult to realise because the impurity concentration is a complex function of several factors such as wall temperature, chemical reaction rates and cathode history.

7.3 Prediction of cathode operating parameters using a modified Siegfried-Wilbur model

In this section, the spectroscopically derived plasma parameters from the previous section are used to predict cathode operating parameters in a xenon discharge. The Siegfried-Wilbur model (section 3.3.1), with its idealised "Ion Production Region" (IPR) in which we assume uniform plasma properties, formed an ideal description of the HC for the measured global, spatially averaged, plasma parameters. Here only n_e and T_e values from the spot mode are employed as the plume mode results were distorted by the presence of a luminous cloud downstream of the cathode (see previous section for details).

Prior to the general application of the model, the cathode operating parameters are calculated at the specific experimental conditions in which the plasma parameters were derived, i.e. $\dot{m}$ = 3.29mg/s and I_a = 5A. In performing the calculations certain assumptions and modifications were made to the Siegfried-Wilbur model and are here summarised:

1) The Salhi-Turchi model of the HC showed that the emission length scales to one insert diameter [141] (refer to section 3.3.2). Hence we assume that L_e= 2mm, the internal diameter of the T6, thus forgoing the need for equations (3.70) and (3.71).
2) The electron density n_e is given by $n_e = \delta n_{e,LTE}$, where the LTE density is multiplied by a correction factor δ (estimated to be ≈ 0.1). This factor corrects for the roughly one order of magnitude overestimation of n_e by the LTE relation (7.12) (refer to section 7.2.1 for details).
3) Equation (3.67) for the energy balance in the IPR is modified to include energy input by Ohmic heating of the plasma. The plasma conductivity σ is given by the Spitzer relation [140], equations (3.77) and (3.78).
4) Essential to the application of the model is a reasonable estimation of $\dot{Q}_{th}$, the power loss from the emitting portion of the insert. We assume that the area of tantalum tube adjoining the emission zone is in perfect thermal contact and thus has the same temperature (T_s). The power loss is then calculated based on radiation from the cathode tip to ambient (T_o = 300K) and conduction down the length of tantalum tube to the cathode end flange, which is assumed to act as a

heat sink with a temperature of ≈ 773K. A temperature of 773K (500°C) was chosen based on thermocouple measurements carried out on the cathode end flange of an operating T6 cathode [44]. The power loss from the insert electron emitting area is thus given by:

$$\dot{Q}_{th} = \varepsilon \sigma_{SB} A_t \left(T_s^4 - 300^4\right) + k_c C_A \frac{\left(T_s - 773\right)}{\Delta x} \qquad (7.13)$$

where ε is the emissivity of the tantalum surface (0.21 [159]), σ_{SB} is the Stefan-Boltzmann constant, A_t is the exposed surface area of the cathode tip, k_c is the thermal conductivity of tantalum (57.5$Wm^{-1}K^{-1}$ [199]), C_A is the cross-sectional area of the tantalum tube and Δx is the distance from the emitting area of the insert to the cathode end flange. Note that the radiation power loss upstream is here neglected, as the radiation to the hot upstream surfaces is deemed negligible when compared to downstream surfaces at ambient temperature.

Table 7.3 gives the predicted cathode operating parameters from the modified Siegfried-Wilbur model at the discharge conditions in which the plasma parameters were measured.

Input Parameters			**HC operating parameters predicted by model**							
n_e (cm^{-3})	T_e (eV)	L_e (mm)	j_{ft} (Am^{-2})	j_i (Am^{-2})	I_i/I_D	V_p (V)	E_s (Vm^{-1})	ϕ_e (eV)	T_s (K)	ϕ_s (eV)
6.99×10^{14}	0.98	2	2.55×10^{5}	9.5×10^{4}	0.36	8.95	7.7×10^{6}	2.06	1482	2.17

Table 7.3: HC operating parameters predicted by a modified Siegfried-Wilbur model for a hollow cathode operating on xenon at $\dot{m}$ = 3.29mg/s and I_a = 5A

The contribution of the volume electron production processes in the IPR to the total discharge current is estimated at around 36%. This is only slightly higher than the experimentally measured values on mercury cathodes (28-31%) [145]. Furthermore, the predicted field-enhanced thermionic current density (j_{ft}) from the cathode surface of $2.55\times10^{5}Am^{-2}$ was well within the expected range of 2×10^{5} to $5\times10^{5}Am^{-2}$ gleaned from various experimental studies [46, 126] (section 2.2.2).

The model predicts a plasma potential of 8.95V at the given discharge conditions. This is in good agreement with Siegfried's averaged experimental value of 8.7V in the IPR. A reasonable estimate of the plasma potential just downstream of the orifice can be obtained from the keeper potential [44]. This was typically in the range 7.5-8.2V under the above discharge conditions, indicating that the estimate of the IPR plasma potential is indeed in the right range.

The dense plasma in a HC results in a very thin plasma sheath (~10^{-7}m), which leads to the establishment of very strong electric fields at the surface tending to extract electrons. For the given plasma conditions, the model predicts a value of 7.7×10^{6} V/m for the electric field. This produces an effective reduction of 0.11eV in the surface work function. Although this reduction appears small, its effect is substantial, as this reduction will nearly triple the thermionically emitted current of a surface operating at 1000°C.

The most significant of the model's predictions are those for the insert surface temperature (T_s) and surface work function (ϕ_s). For the discharge conditions, the model estimated an insert temperature of 1482K, which is in good agreement with recent tip temperature measurements in the T6 cathode [44]. The predicted surface work function (2.17eV), was remarkably close to the average work function of barium oxide on tungsten (2.2eV) [100].

In order to extend the model's predictions to the full range of sustainable discharge current, further assumptions in addition to the ones previously detailed, are necessary. Siegfried found that both T_e and V_p were relatively invariant with changes in $\dot{m}$ and I_D, and thus in his modelling they were assumed to be constants of the discharge. These assumptions are here adopted, and for V_p=8.95V, T_e=0.98eV, ϕ_s=2.17eV, L_e= 2mm and $\dot{m}$=3.29mg/s, figures 7.18 and 7.19 were produced for the dependence of n_e and T_s on discharge current.

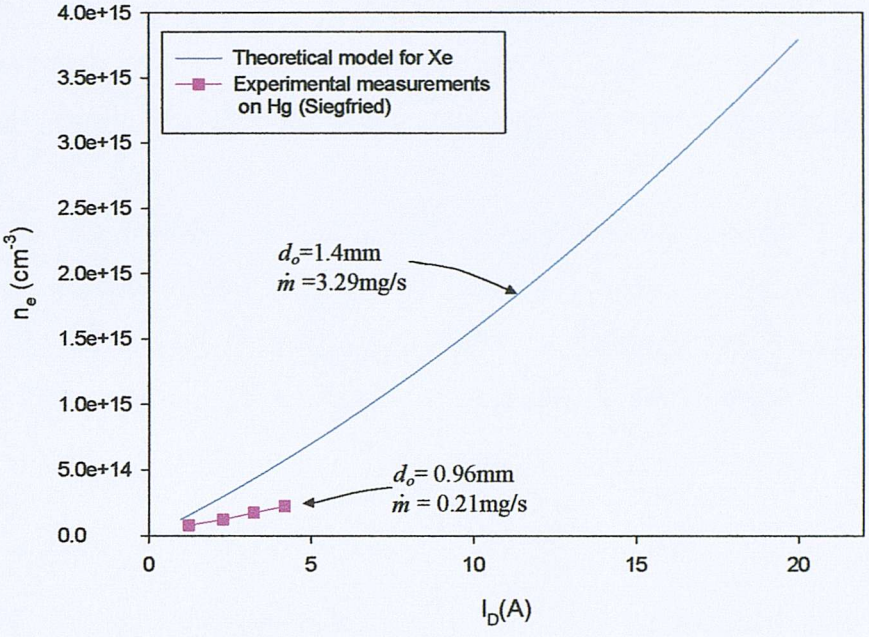

Figure 7.18: Effect of discharge current on plasma density, comparison between modelling results on Xe and experimental results from Siegfried [145] on Hg

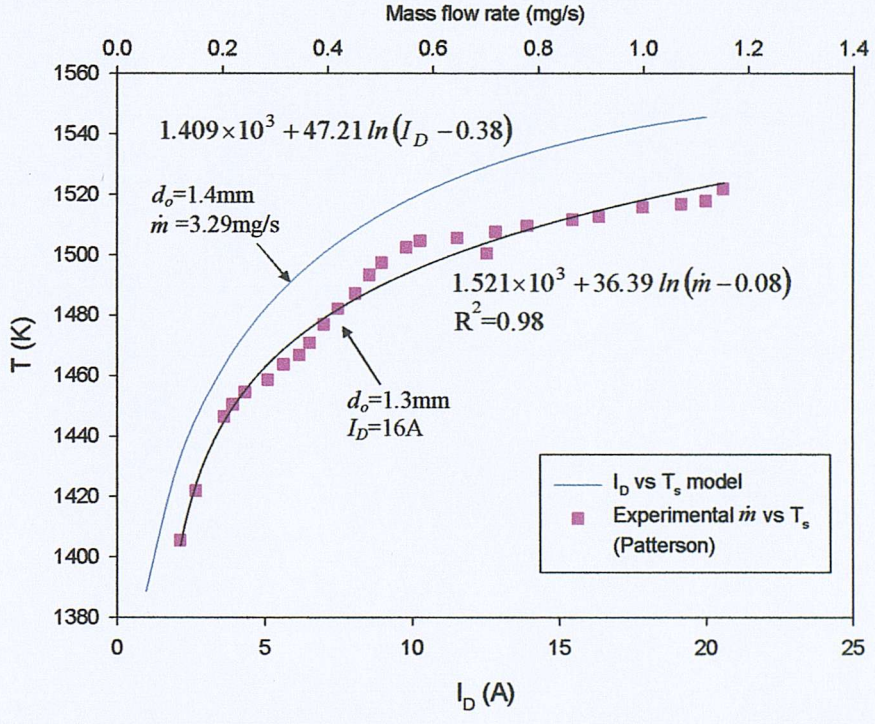

Figure 7.19: T_s as a function of discharge current, comparison between modelling and experimental results from a T6 cathode operating on Xe [44]

The plasma density predicted by the modified Siegfried-Wilbur model is plotted as a function of discharge current in figure 7.18. Siegfried's measurements in mercury cathodes [145] of plasma density just upstream of the tip are also included for

comparison. There is qualitative agreement between Siegfried's measurements and the model's predictions. The differences between them can be attributed to the different propellant, cathode geometry and the lower flow rate in the Hg experiments.

The model predicts that n_e is a quadratic function of discharge current. This is in good agreement with the results for the first ionisation emission line dependence on discharge current/power (figure 6.33), which is an indicator of the degree of ionisation, that showed a similar quadratic relationship to discharge power and current in the spot mode.

Figure 7.19 shows the predicted dependence of surface temperature on discharge current. For comparison, the figure also shows experimental measurements of tip temperature dependence on mass flow rate at I_D=16A for a similar T6 cathode operating on xenon [44]. The projected value of tip temperature from the experimental measurements at 3.29mg/s and I_D=16A only differs from the model value by 25°C (1.6%), which indicates excellent agreement between the model and experiment. From the figure it can also be observed that the temperature seems to have the same functional dependence on I_D and $\dot{m}$, indicating that $T_s \propto ln(I_D \times \dot{m})$.

The modified Siegfried-Wilbur model assumes that the electron emission process proceeds solely by the field-enhanced thermionic emission mechanism. The good agreement between model and experiment gives strong support to the view that the field-enhanced thermionic emission mechanism predominates in the HC under normal operating conditions.

7.4 Theory of plume to spot transition

This section begins with a review of the most significant and detailed investigations of discharge behaviour in both the plume and spot modes. It then moves on to present the observed visual, spectroscopic and electrical characteristics of the discharge in the present study using the various gases. This is followed by a review of the various theories put forward in the past in an attempt to explain the discharge modes and transition between them. Finally, a new theory of plume to spot transition is proposed, which is indeed demonstrated to fully describe and predict the observed phenomena and discharge behaviour in the current study and the extensive literature.

7.4.1 Review of previous discharge characterisation studies

7.4.1.1 Siegfried and Wilbur [146]

Siegfried and Wilbur carried out an experimental investigation on orificed mercury hollow cathodes using axially moveable Langmuir probes, which measured plasma properties both upstream and downstream of the orifice plate along the cathode centreline. Plasma properties were measured at 100 and 150mAequiv flow rates for a range of discharge currents which enabled observation of plasma property profiles in both the spot and plume modes. Some of the significant results (using finer Langmuir probes than those presented in chapter 2) are here reproduced in figures 7.20 - 7.23, with figures 7.20 and 7.21 representing plasma property measurements in the plume mode and figures 7.22 and 7.23 representing those in the spot mode.

Upstream of the orifice plate, the electron temperature ranged from 0.5 to 0.8eV. The plasma potential exhibited a monotonically increasing behaviour as the orifice plate is approached, with the plume mode curve exhibiting the steeper increase. The plasma potential just downstream of the orifice is estimated at 11-12V. The electron density upstream of the orifice plate has a steep density gradient in the direction of the orifice plate, with the curves for the plume and spot modes approximately parallel. The density in the spot mode is, however, an order of magnitude greater than that in the plume mode.

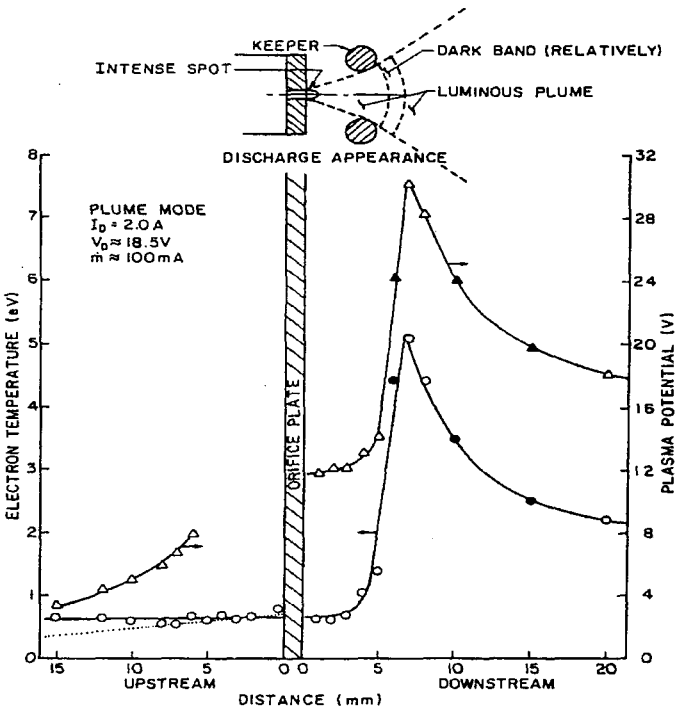

Figure 7.20: Electron temperature and plasma potential profiles in the plume mode [146]

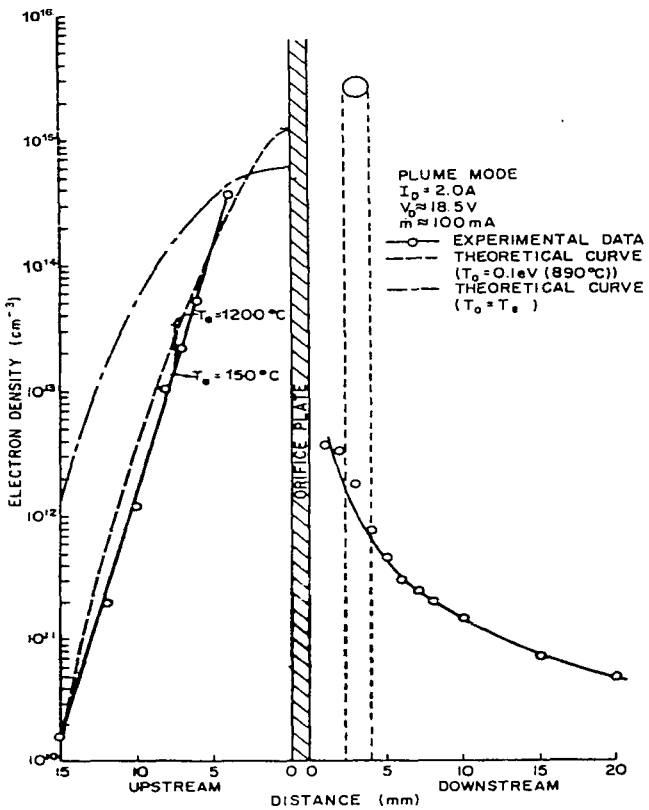

Figure 7.21: Electron density profiles in the plume mode [146]

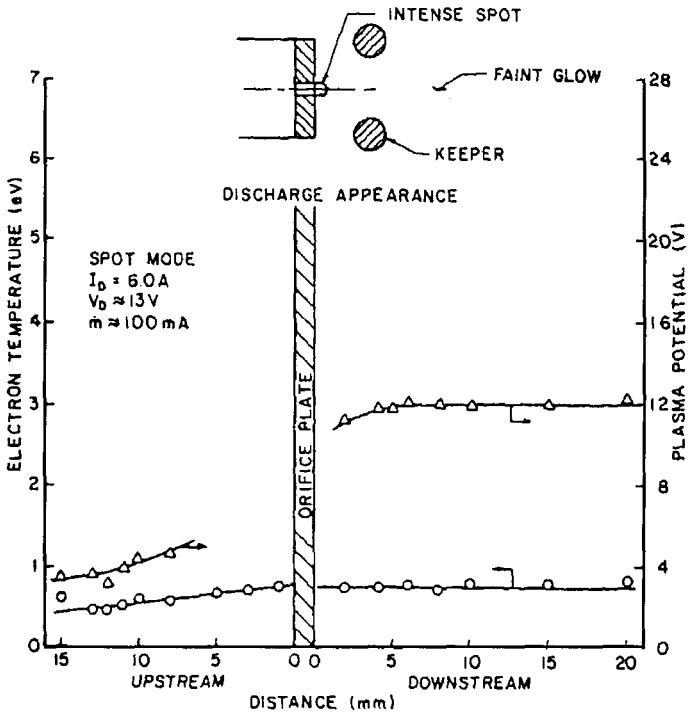

Figure 7.22: Electron temperature and plasma potential profiles in the spot mode [146]

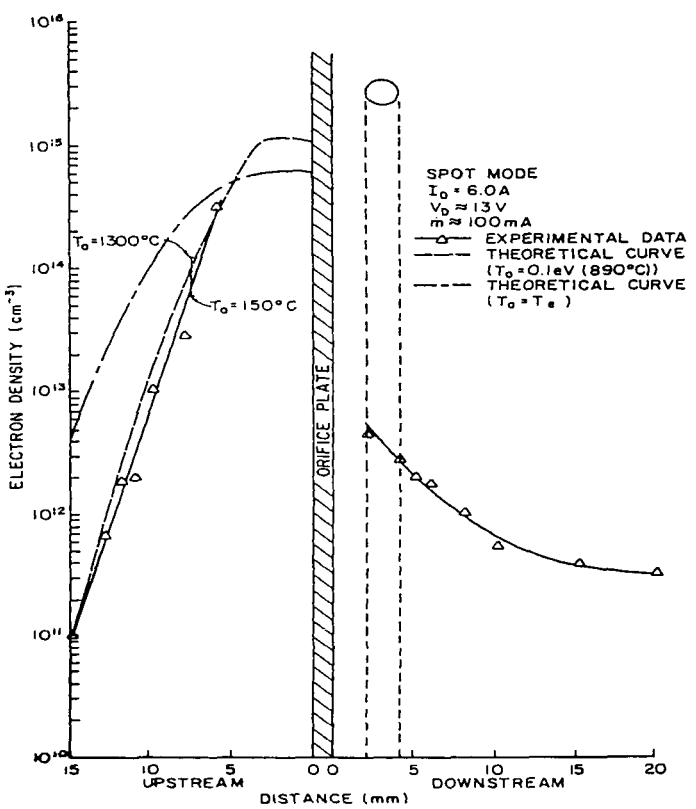

Figure 7.23: Electron density profiles in the spot mode [146]

The most significant difference in plasma properties between the two modes was observed downstream of the orifice, where a region of steep gradients in T_e and V_p is encountered in the plume mode 5-10mm downstream of the cathode tip. The region corresponds to what Siegfried and Wilbur describe as an electron "free-fall" region, where electrons are accelerated through a potential difference of about 20V over a short distance (few mm) without significant collisional interaction. The probe data is also supported by visual observation of the discharge, where a dark band followed by a region of much higher luminosity downstream is observed in the plume mode around the region corresponding to the measured plasma gradients, this is illustrated in figure 7.20. The banded structure and the gradients in plasma parameters were both absent in the spot mode, the luminous cathode spot was however observed in both modes. Near the peak of the V_p profile, monoenergetic primary electrons were detected with an energy of about 19eV, which correlates with the potential difference of 20V. These electrons passing through the potential difference in the dark band will have sufficient energy to cause the inelastic excitation reaction observed in the luminous region downstream. The primary electrons seem to thermalise to an electron temperature of ~2 eV as they diffuse away from the free-fall region.

The correlation between the free-fall region and the plume-to-spot transition was confirmed by the observation that the dark band was very close to the luminous cathode spot at low discharge current in the plume mode and moved downstream 5-10mm with increase in current. The change from plume to spot is characterised by the abrupt disappearance of the dark band.

Siegfried and Wilbur also carried out a spectroscopic investigation of the external discharge in which they observed several mercury atomic and singly ionised lines. The intensity of these lines increased with discharge current in the plume mode. When the discharge moved to the spot mode, many of these lines experienced either a significant reduction in intensity or disappeared altogether.

Another important piece of information pertinent to mode change was gained by using a moveable anode when the cathode was operating close to the transition point. Starting at the plume mode, a transition occurred spontaneously if the cathode-anode

separation was reduced. This was a reversible process, with the opposite change occurring when the cathode-anode separation was increased.

7.4.1.2 Fearn and Patterson

This modern study on the discharge characteristics of the T6 utilised xenon propellant. It represents one of the most comprehensive studies conducted on spot-to-plume transition to date, using a variety of instrumentation, and is published in a series of papers [40, 44, 45, 121, 122, 123, 124]. The importance of this body of work lies in the discovery of a fine structure to the plume mode.

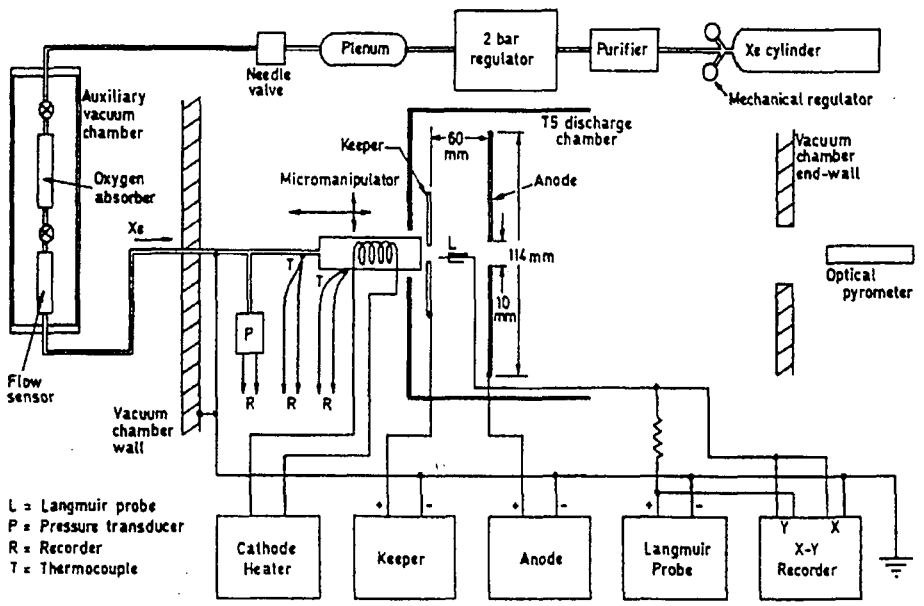

Figure 7.24: Illustration of the experimental apparatus used by Patterson and Fearn [40]

The experimental arrangement used in this study is illustrated in figure 7.24. The T6 hollow cathode was mounted on a micromanipulator to allow variation of the keeper-cathode separation (d_k). To simulate conditions in the coupling plasma of a T6 thruster, the total exit area from the discharge chamber was made equal to the baffle annulus area in the working thruster. A combination of optical pyrometry and thermocouples provided for multipoint temperature measurements along the cathode

body. A pressure transducer, mounted in the xenon feed pipe upstream of the HC, was used to estimate the pressure in the HC cavity.

The results of the xenon discharge characterisation revealed the presence of several, distinct discharge modes dictated by the anode current and mass flow rate. Figure 7.25 illustrates those regions, as a function of the two controlling parameters, for a cathode with an orifice diameter of 1.3mm, and using a conventional power supply for the anode. Patterson and Fearn also found that the boundaries of the various regions were extremely reproducible whether I_a or $\dot{m}$ was being changed.

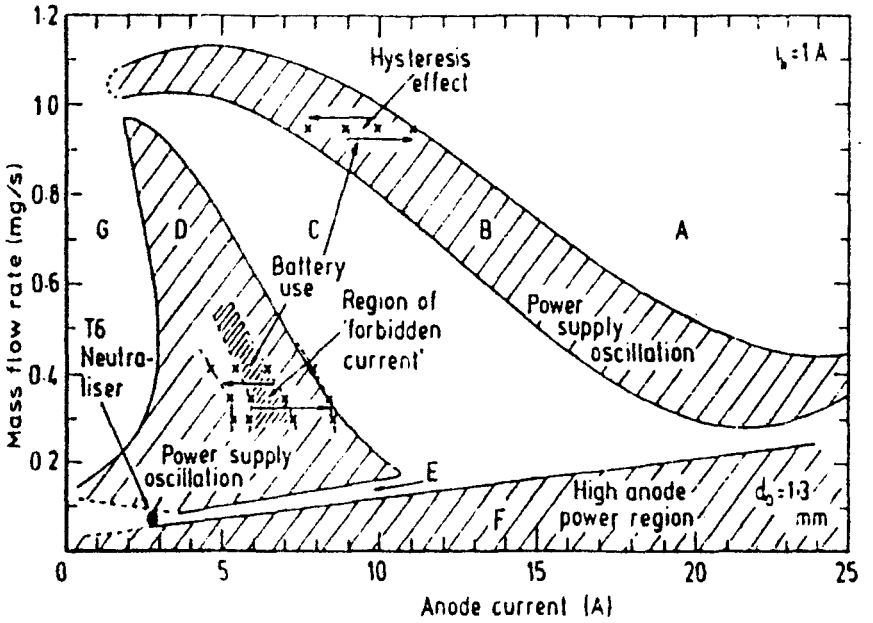

Figure 7.25: Discharge characteristics and discharge modes as a function of the main discharge parameters, for d_o=1.3mm, d_k=1.5mm and I_k=1A [45]

We now proceed to describe the various regions in the discharge:

Region A:- Occurs when the cathode is operated at high current and high flow. This region corresponds to operation in spot mode, in which the discharge is very stable and noise levels on the keeper and anode are almost negligible.

Region B:- This region is encountered by reducing either $\dot{m}$ or I_a. It is characterised by an increase in anode potential and oscillations in the keeper and anode voltages and discharge currents. The oscillations can have very large amplitudes, with the discharge visibly pulsing or flickering (refer to figure 7.26 for the anode and keeper

noise values plotted as a function of discharge current). Experiments in which the laboratory power supply was replaced by a battery, have shown that the region B as well as D were regions in which the discharge possessed a negative voltage-current characteristic.

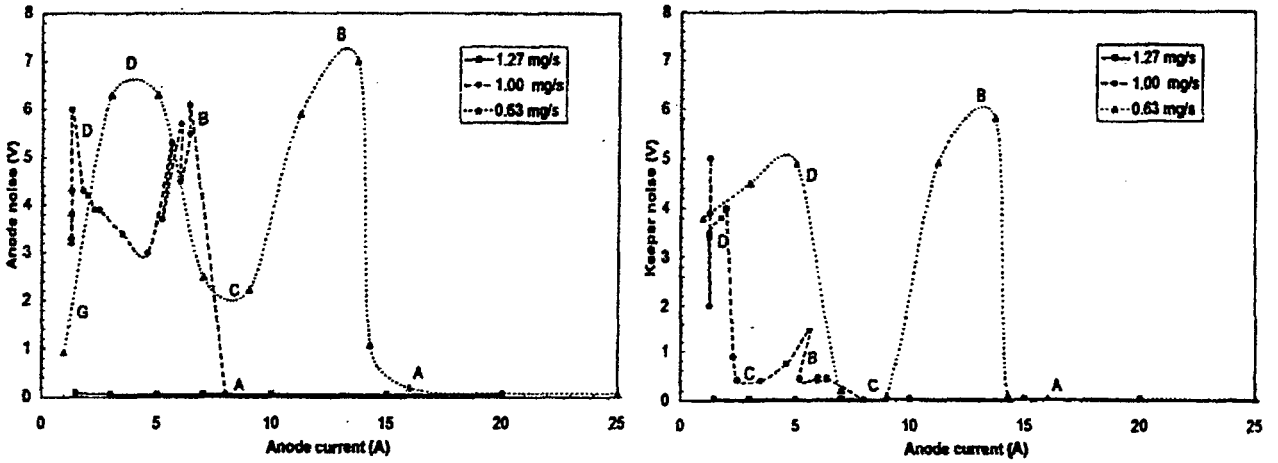

Figure 7.26: Anode and keeper noise as a function of I_a at several values of $\dot{m}$ [40]

Region C:- Further reduction in either $\dot{m}$ or I_a, moves the discharge to region C in which the oscillations are effectively eliminated. The noise levels on the keeper are much lower than those on the anode. This mode, although possessing higher noise levels than those in region A, presents a relatively stable, noise free regime in comparison to regions B and D. From visual observations, Patterson and Fearn also associated this mode to the "beam mode" observed in hollow cathode discharges [121], wherein the plasma forms a luminous, collimated beam extending from the cathode.

Region D:- Moving to region D, the discharge exhibits the same behaviour as that described for region B, with the discharge possessing a negative voltage-current characteristic, and elevated keeper and anode noise levels. Within region D there also exists a region of "forbidden current", indicated in figure 7.25, whose extent depends on the series resistance of the electric circuit.

Region E:- Region E is a narrow region separating regions D and F, and can be described as low-power, low-flow rate, but however, surprisingly, relatively quiet

discharge. Patterson and Fearn associated this region with the "neutraliser mode" found in earlier T5 studies [40].

Region F:- At very low $\dot{m}$ the discharge experiences very high noise levels, which were estimated at over 60V peak to peak. Patterson and Fearn reported that the keeper power supply, in spite of being current regulated, was forced to increase its current, while the anode power supply was incapable of sustaining the required current although it was operating below its maximum rated voltage. They further reported that most of the discharge power was deposited at the anode, resulting in severe heating and sputtering damage.

Operation in region F was also found to have an interesting influence on the cathode pressure. Figure 7.27 plots the cathode pressure as a function of $\dot{m}$ at I_a = 5A and 15A. The figure shows an anomalous increase in cathode pressure as $\dot{m}$ is reduced when region F is encountered.

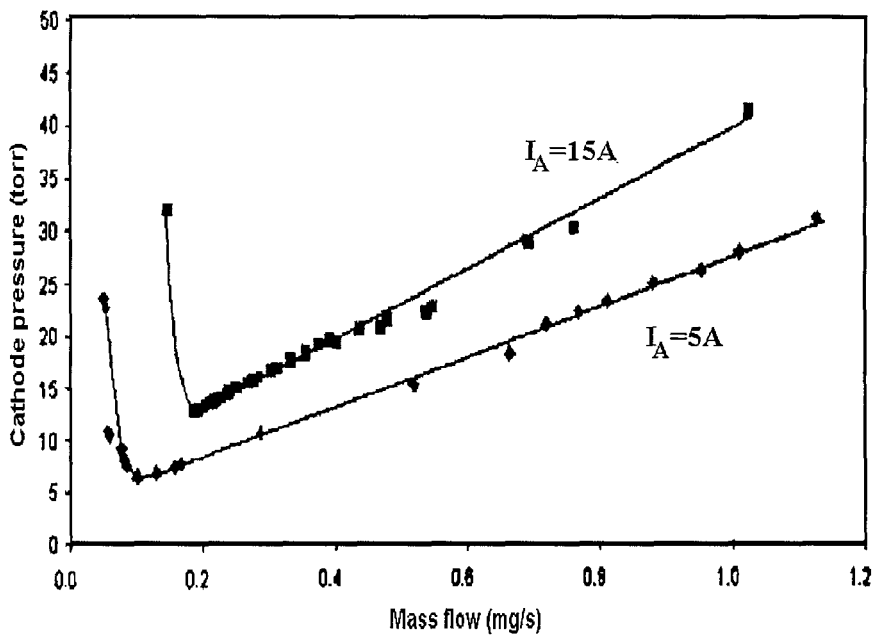

Figure 7.27: Cathode pressure as a function of $\dot{m}$ [121]

Region G:- At intermediate $\dot{m}$ and very low values of I_a, region G is encountered. This is described as a relatively quiet discharge, in which the discharge experiences low frequency oscillations (over a period of minutes) brought about by the cathode heating and cooling cycle.

Battery operation

In one of the most interesting features of their investigation, Patterson and Fearn showed that the oscillations encountered in the regions B and D were due to power supply interactions with the discharge. This was demonstrated conclusively by the replacement of the anode power supply with a battery-rheostat system which led to the complete removal of the violent oscillations in regions B and D, see figure 7.28.

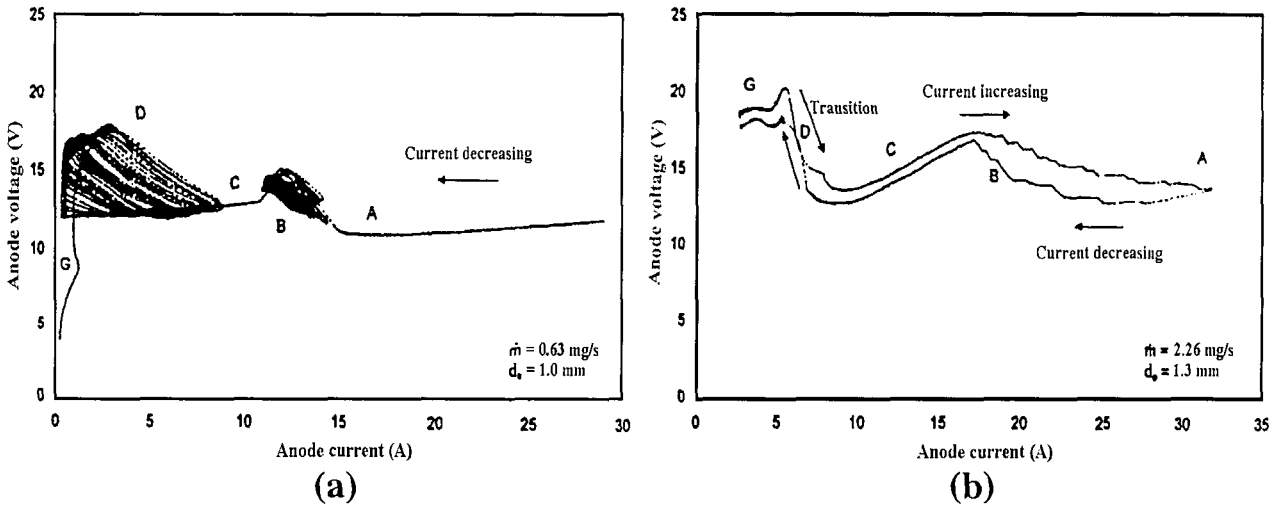

Figure 7.28: Anode voltage current characteristics using:
(a) *laboratory power supply* **(b)** *battery [40]*

The battery results exposed regions B and D to be regions of negative impedance. Patterson and Fearn concluded that the output ripple of the current-regulated supply triggers the oscillations by interacting with the discharge in the negative impedance regions.

Effect of cathode orifice diameter

It was expected that increasing cathode orifice size will have a reducing effect on cathode tip temperature, thereby prolonging cathode lifetime. Patterson and Fearn demonstrated this experimentally as shown in figure 7.29, which compares the effects of $\dot{m}$ and d_o on cathode temperature.

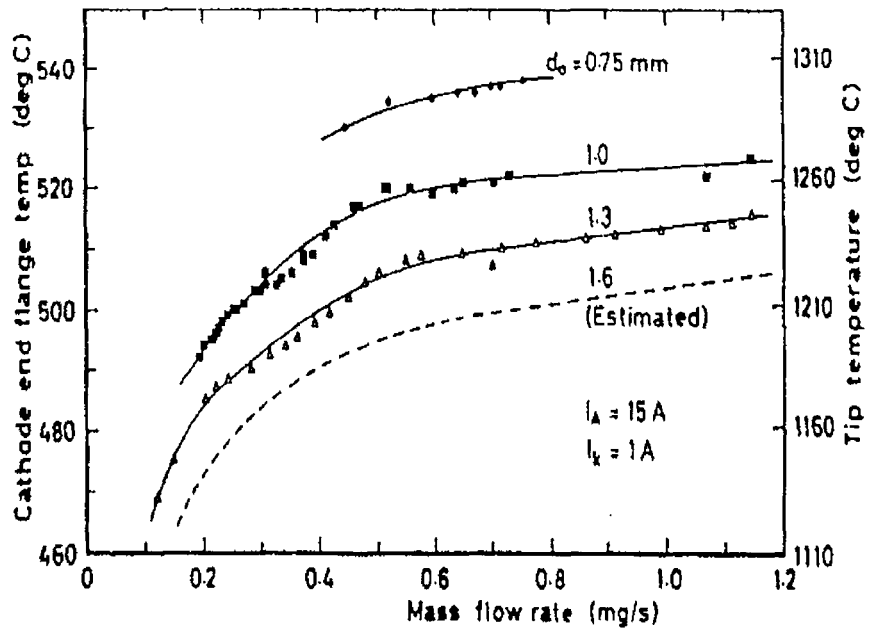

Figure 7.29: Cathode temperature as a function of $\dot{m}$ and d_o at I_a=15A [45]

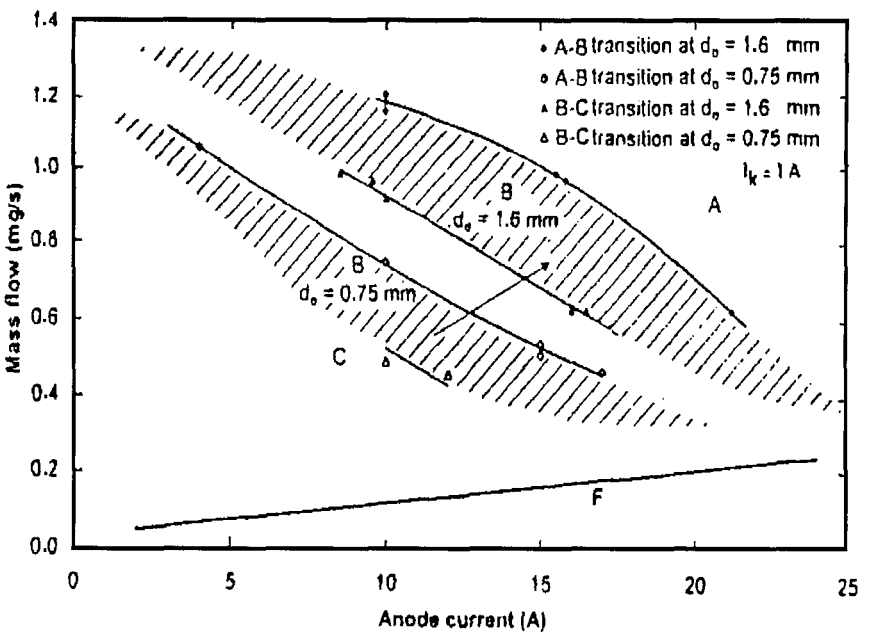

Figure 7.30: Influence of orifice diameter on the boundaries of the discharge regions [44]

It was also observed that the orifice diameter also has a significant influence on the position of the boundaries of the various discharge regions in terms of the controlling parameters $\dot{m}$ and I_a. With reference to figure 7.30, it can be observed that increasing d_o for a given value of I_a has moved the boundaries of the discharge regions to higher flow rates. Equivalently, a change in d_o leads to a similar effect on discharge current,

with higher discharge currents required, at constant $\dot{m}$, for a given transition when d_o is increased.

Effect of the keeper electrode

The keeper was found to have a significant influence on observed discharge behaviour. Figure 7.31 shows the boundaries of the various discharge regions as a function of d_k, the cathode-keeper separation. The plot shows that, although the effect on region D is small, the boundaries generally moved to higher discharge currents as d_k was increased.

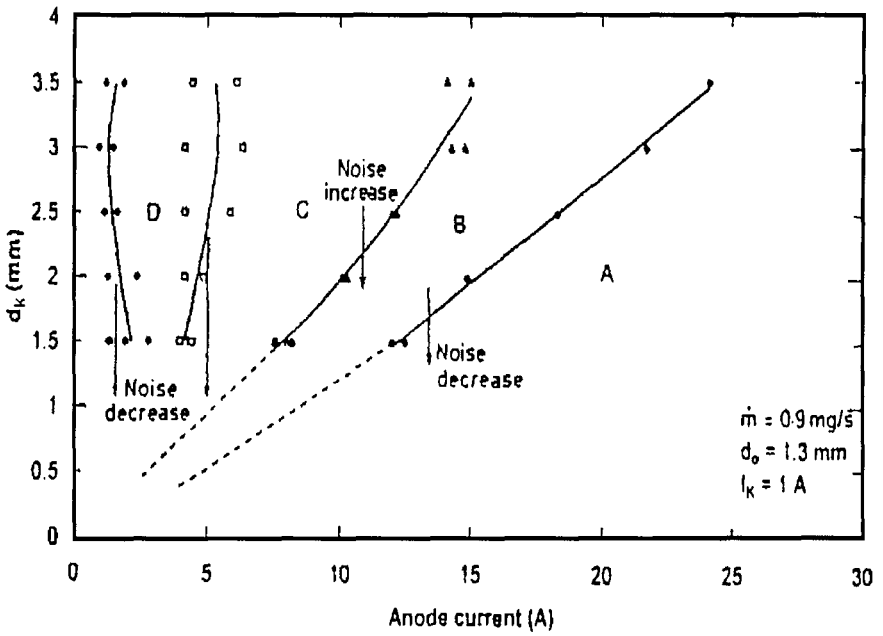

Figure 7.31: Effect of d_k on the boundaries of the discharge regions [44]

Moreover, it was also found that the keeper configuration also influenced discharge behaviour. The use of an enclosed-keeper design significantly altered the discharge behaviour in figure 7.25, reducing the area of the regions in which operation was undesirable (i.e. regions B and D), and thus indicating substantial benefits in employing this configuration.

7.4.2 Results of the discharge characterisation work in the present study

This section details some of the phenomena observed during the cathode characterisation, with particular emphasis on observations during the plume phase of the discharge. These observations include the voltage current characteristics, the spectral emission line intensity variation and the visual character of the discharge

Dependence on $\dot{m}$

Operating a cathode in the plume mode is generally coupled with the visual observation of a large luminous plume extending downstream of the cathode tip. It was discovered that within this plume there exists a region of increased luminosity at the very upstream edge of the plume. This region has the form of a "luminous (sometimes almost spherical) cloud" and is observed to be, at all times, on the cathode centreline. The characteristics of the discharge were found to be closely associated with the presence and motion of this luminous cloud.

Figure 7.32 illustrates for xenon, the anode and keeper voltage dependence on flow rate as $\dot{m}$ is increased, at 1 minute intervals, from 0.2 to 3.61mg/s at I_a = 5A and I_k = 1A. Shown also in the figure are photographs illustrating the visual appearance of the discharge with changing flow rate. These photographs are snapshots taken from a video recording of the discharge using a digital video camera, in which the exposure was intentionally lowered to prevent saturation of the CCD. This resulted in the complete removal of all but the most intense features of the discharge in the photographs, thus eliminating the plume and leaving only the luminous cloud and the cathode spot in the plume mode.

At low $\dot{m}$ the cloud is seen very close to the cathode tip and is observed to fill the inter-cathode-keeper space, hence giving the appearance of an enlarged cathode spot. With increasing $\dot{m}$, a point is reached when the cloud emerges from the keeper orifice and is clearly visible downstream of the keeper. This is usually marked by an abrupt,

substantial reduction in keeper noise. The cloud becomes more diffuse with increasing $\dot{m}$ and moves progressively further downstream, until the spot mode is established and the cloud abruptly disappears. If we proceed to decrease the flow rate after establishment of the spot mode the same phenomenon is observed in reverse.

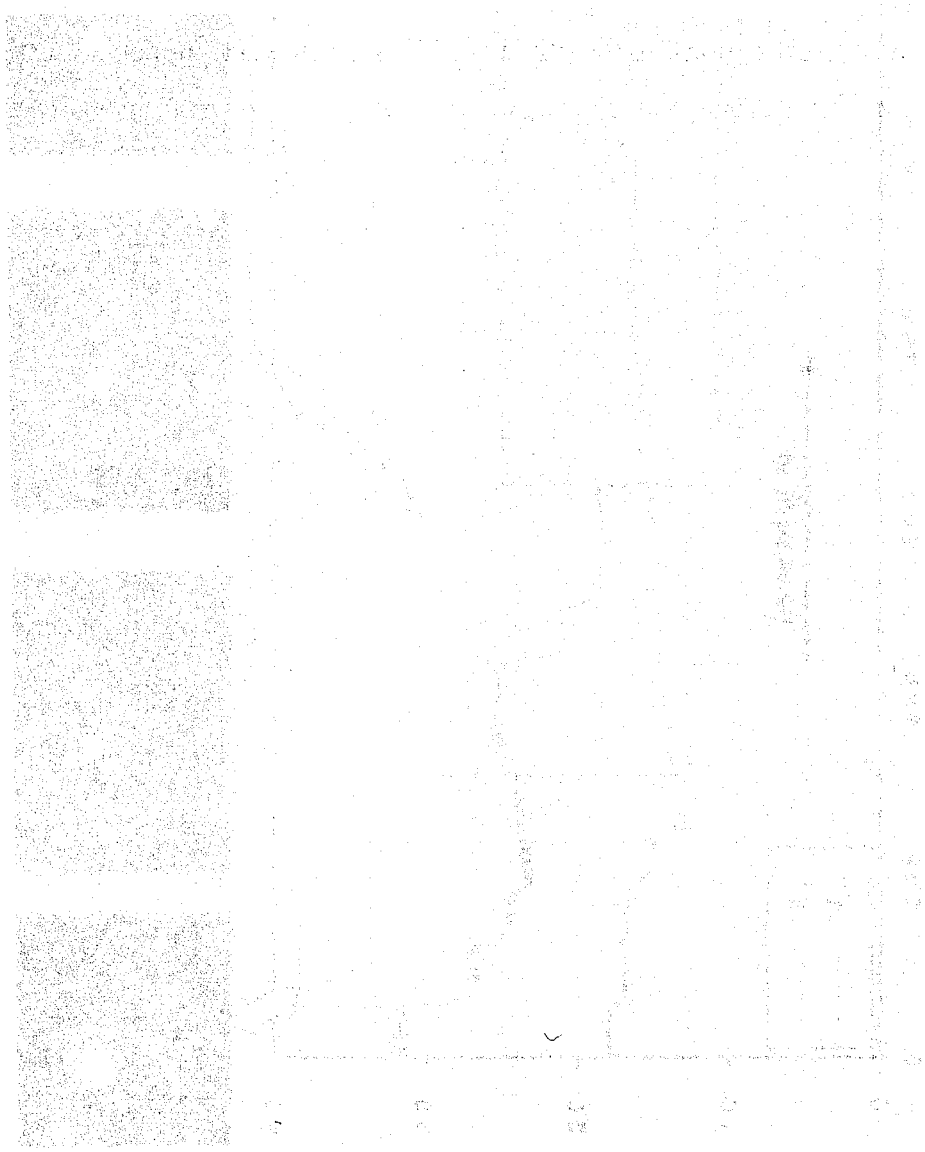

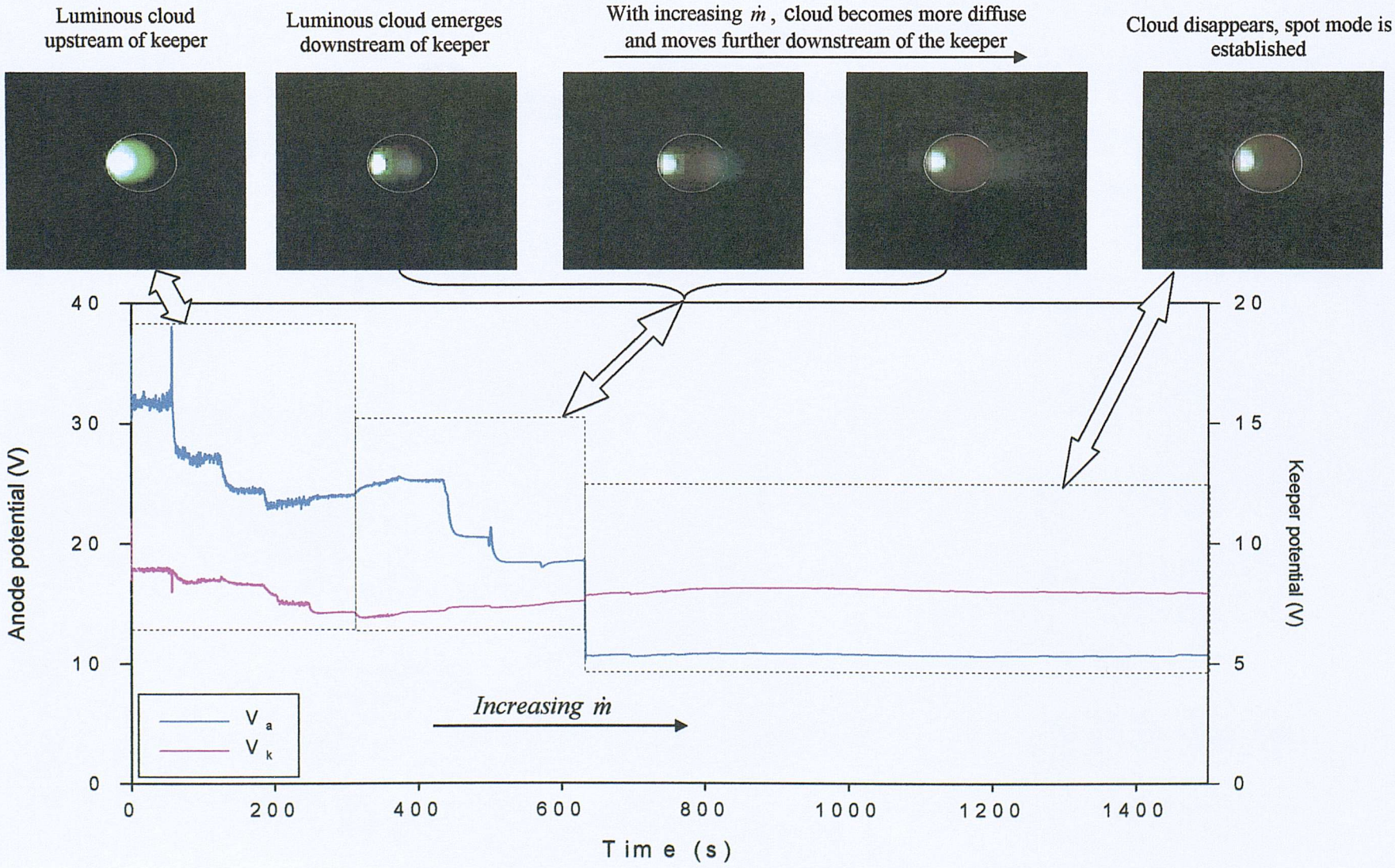

Figure 7.32: Effect of ṁ on the visual and electric characteristics of the discharge in both plume and spot modes for xenon at I_a=5A and I_k=1A

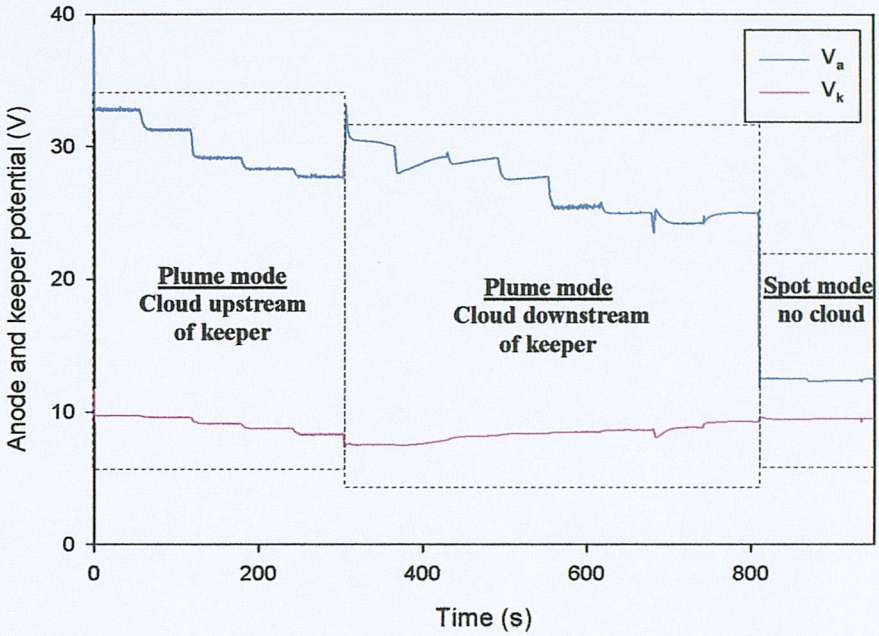

Figure 7.33: Visual observations and anode and keeper voltage dependence on $\dot{m}$ for an argon discharge at $I_a = 5A$ and $I_k = 1A$

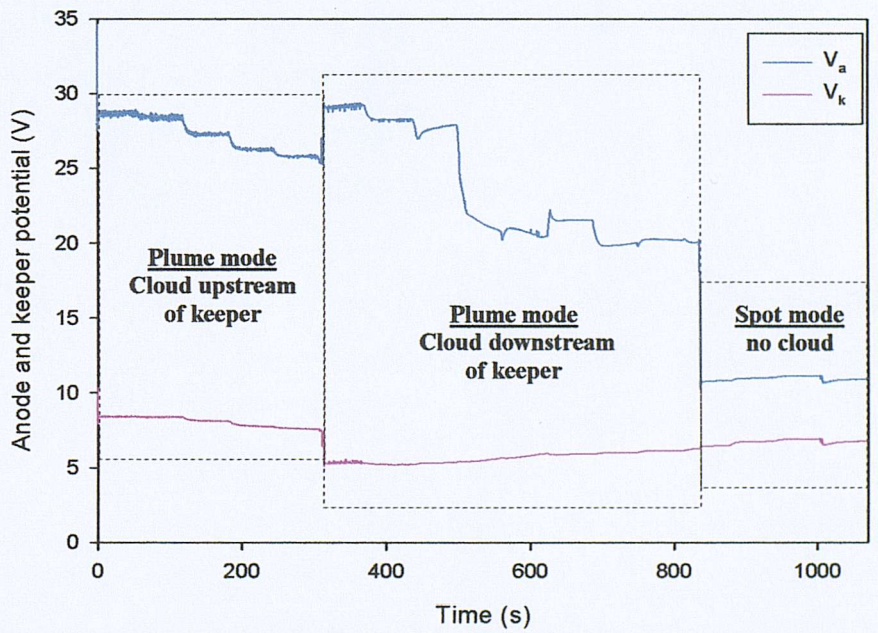

Figure 7.34: Visual observations and anode and keeper voltage dependence on $\dot{m}$ for a krypton discharge at $I_a = 5A$ and $I_k = 1A$

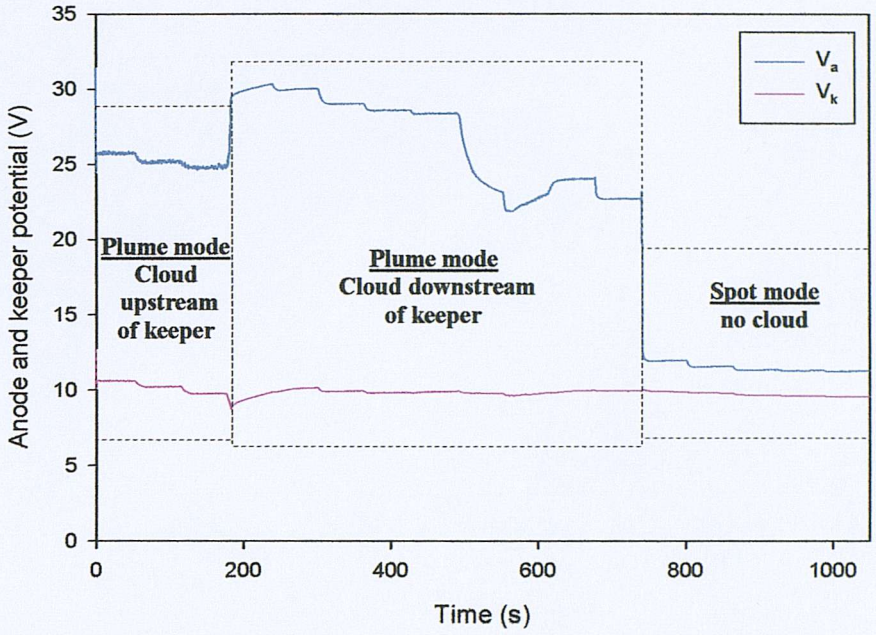

Figure 7.35: Visual observations and anode and keeper voltage dependence on $\dot{m}$ for a Kr/Xe mix discharge at I_a = 5A and I_k = 1A

It has also been revealed that the aforementioned process of cloud formation and migration in the plume mode manifests itself regardless of the propellant species in use. As indicated in figures 7.33 to 7.35, the cloud formation upstream of the keeper and its motion downstream with increasing flow rate until its abrupt disappearance in the spot mode was also observed in argon, krypton and Kr/Xe discharges. The only effect found for the change of propellant was in the range of $\dot{m}$ in which the cloud (and more generally, the plume mode) is observed, which was observed to increase with the first ionisation potential of the propellant.

Some interesting insight into the mechanism of mode change was also gained from the spectroscopic part of this investigation. Figure 7.36 compares the spectra obtained in an argon discharge at various values of $\dot{m}$ in the range 400 – 465nm. The emission line intensity in each spectrum was normalised with respect to the intensity of the ArII 434.8064nm singly ionised line. The values of flow rate represent the diverse observed conditions of the discharge: the spectrum at 1mg/s was obtained with the luminous cloud upstream of the keeper, the spectra at 1.5 and 2mg/s were taken with the cloud downstream of the keeper and the spectrum at 3.4mg/s was taken with the discharge in the spot mode, all at I_a = 5A and I_k = 1A.

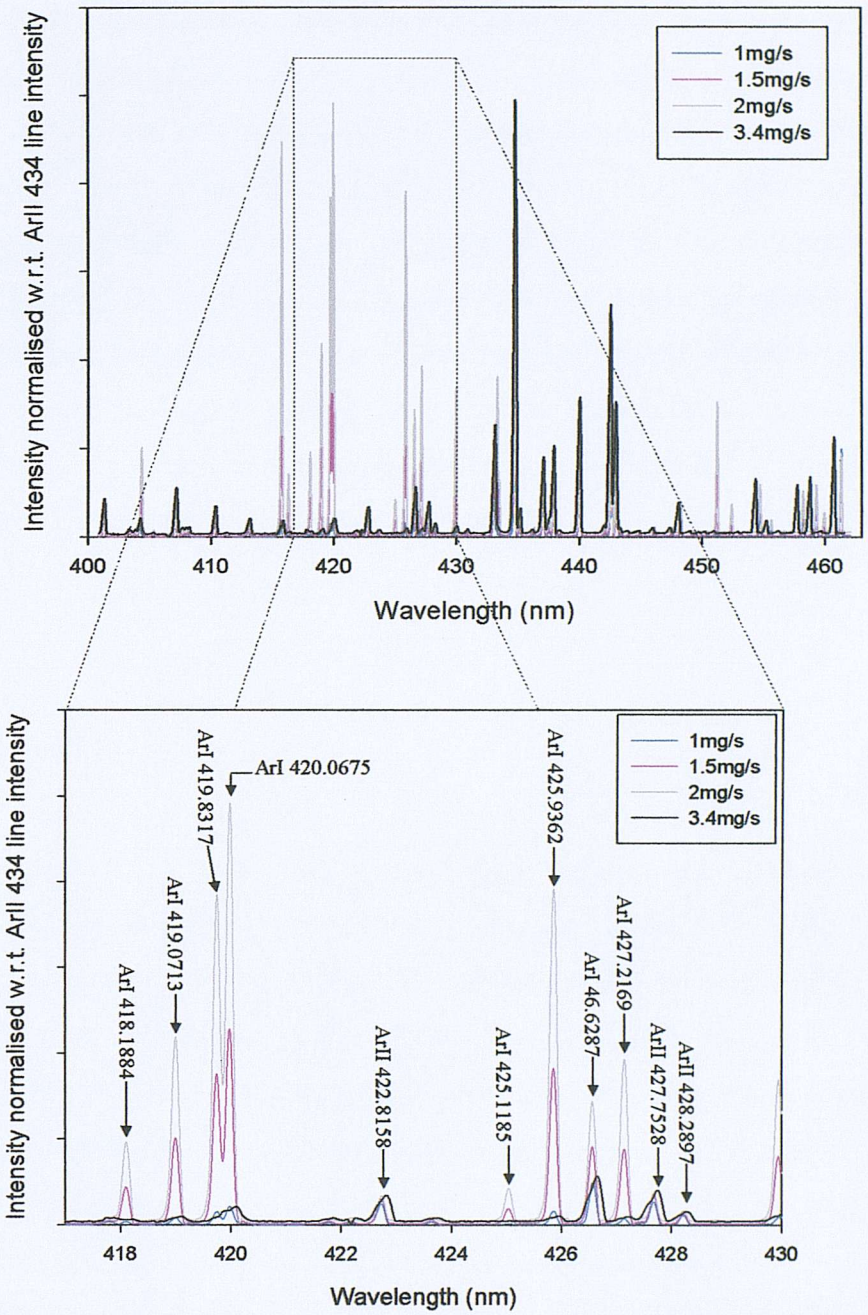

Figure 7.36: Comparison of the emission spectrum of argon discharge at 1mg (with luminous cloud upstream of keeper), 1.5mg/s, 2mg/s (both with luminous cloud downstream of keeper) and 3.4mg/s (spot mode), at I_a = 5A and I_k = 1A

The absolute intensity of the first ionisation lines was found to be highest when the cloud was inside the cathode-keeper space at 1mg/s, and decreased with increasing $\dot{m}$ being lowest at 3.4mg/s. The intensity of the ArII 434.8064nm line was 62 times higher at 1mg/s than at 3.4mg/s. When the intensity was normalised with respect to ArII 434.8064nm line, it was observed that there was a slight increase in the normalised first ionisation line intensity with flow rate. The increase was however not

appreciable. More significant was the behaviour of the neutral emission lines. It was revealed that with the presence of the cloud downstream of the keeper, the relative intensity of all the neutral emission lines increased substantially from their levels when the cloud was upstream of the keeper at lower $\dot{m}$. This enhancement was of such an extent that lines which were previously undetected were observed in the spectrum. When the flow rate was increased and the discharge was operating in the spot mode, the relative intensity of these lines was either significantly reduced or they disappeared altogether from the spectrum. All of the above points to an unknown auxiliary energy input mechanism operating, when the discharge is in the plume mode, causing the higher excitation and ionisation observed, which will be discussed in section 7.4.4.

Dependence on I_a

The experiments related to discharge dependence on I_a were hampered by the limitations imposed on the range of discharge current mentioned in chapter 5. The experiments, nevertheless, demonstrated the existence of the various operating modes reported by Patterson and Fearn [40] in all the gases, and that these modes are again closely related to the presence and behaviour of the luminous cloud. By increasing the discharge current in steps of 0.5A every minute from 0.5 or 1A to 5A at various mass flow rates and using the various inert gases, all of the operating modes described by Patterson and Fearn were observed with the exception of regions B and F. The spot mode results were discussed in chapter 6, and figures 7.37 – 7.40 show a selection of the discharge characterisation results in the plume mode for the various gases employed.

Figure 7.41 illustrates the visual observations associated with each of the operating modes identified in figures 7.37– 7.40.

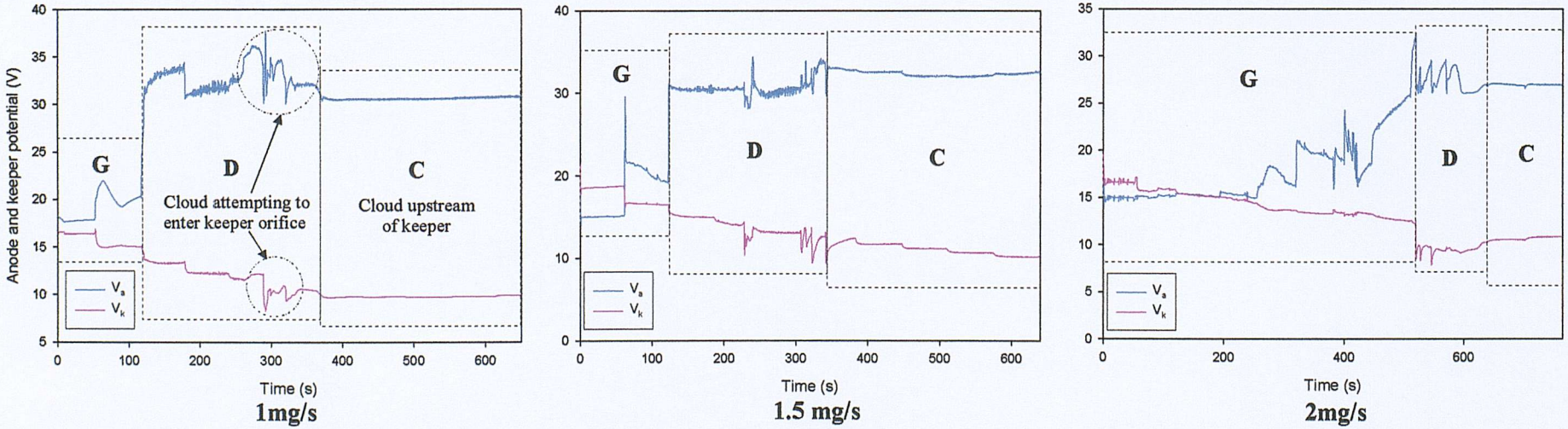

Figure 7.37: Anode and keeper voltage dependence on I_a for argon discharge, I_k = 1A

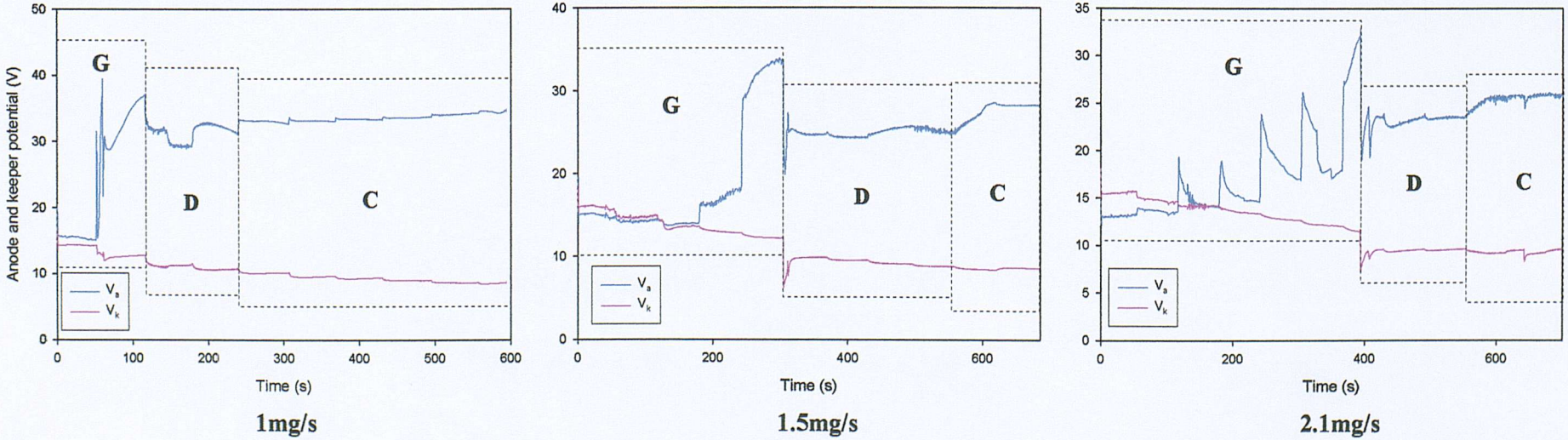

Figure 7.38: Anode and keeper voltage dependence on I_a for krypton discharge, I_k = 1A

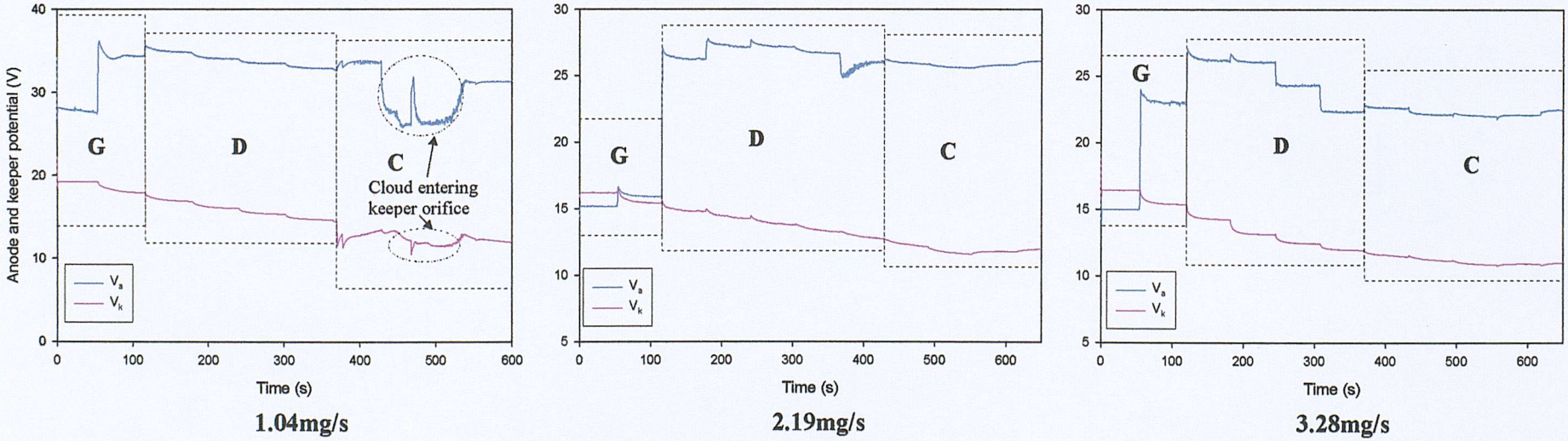

Figure 7.39: Anode and keeper voltage dependence on I_a for Kr/Xe mix discharge, I_k = 1A

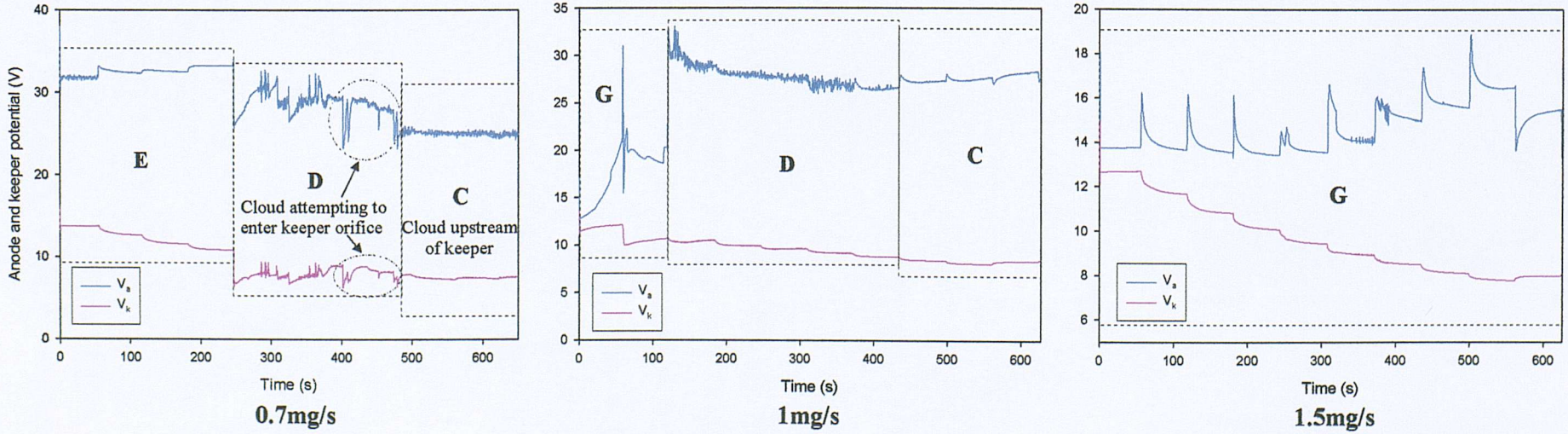

Figure 7.40: Anode and keeper voltage dependence on I_a for xenon discharge, I_k = 1A

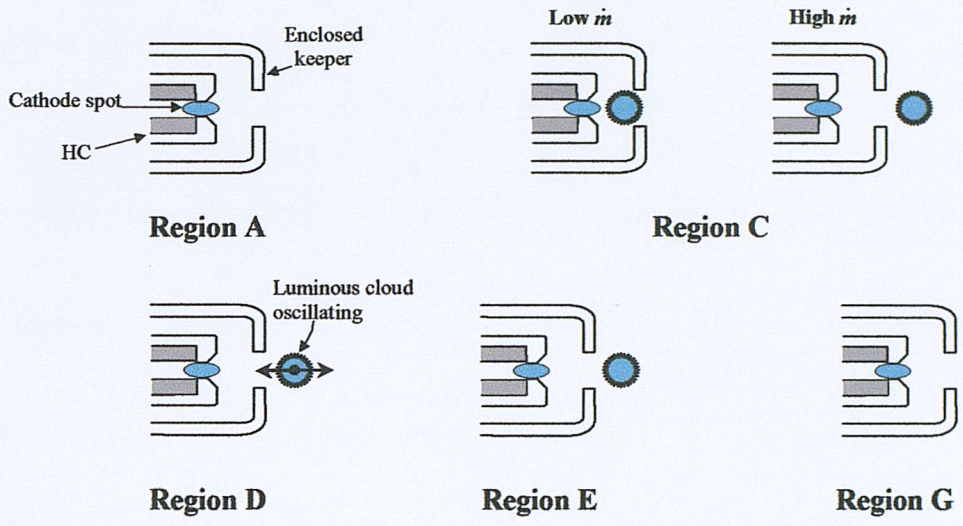

Figure 7.41: Visual characteristics of the discharge operating modes

The observed characteristics of the various operating modes were similar to those described by Patterson and Fearn [40]. When the luminous cloud existed, a general motion upstream was observed with increasing I_a over the range investigated. The characteristics of the operating modes are here summarised:

Region C: - Is a region in which the discharge was relatively quiet with no oscillations. A luminous cloud existed downstream of the cathode tip. At high $\dot{m}$ the luminous cloud was downstream of the keeper and the discharge was virtually noise-free. At lower $\dot{m}$, the cloud was upstream of the keeper and the noise appreciably increased. This is consistent with the observed dependence on $\dot{m}$ from above, and is also in agreement with Patterson and Fearn's observation that the discharge noise decreased with increasing flow rate (see figure 7.26).

Region D:- Elevated noise levels were experienced in this region and the discharge possessed a negative V_a - I_a characteristic. In this region replacing the operating gas affected the discharge behaviour. For krypton and Kr/Xe mix, and particularly in the case of the Kr/Xe mix, the noise levels were significantly reduced to almost region C values, despite the discharge still exhibiting the general negative V_a - I_a characteristic. Visually, the luminous cloud was observed to oscillate in this region in an upstream-downstream motion. At low $\dot{m}$, when the cloud was close to the downstream edge of the keeper, increasing the demanded anode current would cause the cloud to oscillate

violently, moving rapidly in and out of the keeper cavity. This resulted in the highest observed noise levels in both the keeper and anode traces. Moreover, in spite of being current controlled, the current drawn from the power supply was seen to fluctuate. Thus, the rapid movement of the cloud in and out of the keeper cavity was thought to correspond to the "forbidden current" region described by Patterson and Fearn [123].

Region E:- Is encountered at low flow rates and currents. It visually resembles region C, with the luminous cloud observed in the discharge. The noise levels in this region are significantly lower than those in region D.

Region G:- In this region the discharge experienced the low frequency oscillations described earlier, which are thought to be associated with the cathode's thermal inertia. Otherwise, the discharge seems to be relatively stable and, interestingly, has the same appearance as a discharge in the spot mode, with the only source of light emission being the cathode spot. The luminous cloud and the plume are both absent from the discharge.

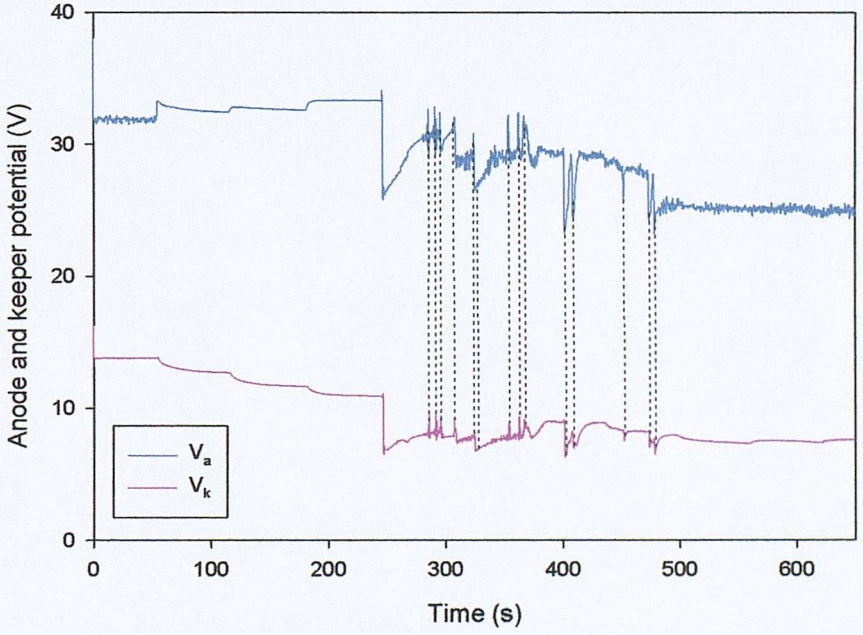

Figure 7.42: Correspondence between keeper noise and anode low frequency high amplitude noise when cloud is in keeper vicinity, xenon discharge $\dot{m}$ =0.7mg/s, I_k=1A

Two interesting observations can be made on the keeper behaviour. Firstly, ignoring the noise on the keeper trace, the keeper potential is always a decreasing function of the anode current. Secondly, as figure 7.42 illustrates more clearly, when the cloud is in the vicinity of the keeper orifice, the main features on the keeper trace correspond to the low frequency, high amplitude oscillations on the anode trace. This implies a coupling between the two power supplies in this region.

7.4.3 Existing theories for plume to spot transition

In this section we review the various theories in the literature proposed to explain the process of mode change.

Csiky **[28]** hypothesised that the discharge behaviour is related to the size and dimensions of the cathode sheath. Csiky carried out experiments on mercury hollow cathodes in diode configuration, in which both the spot and plume modes were observed. Based on Langmuir probe measurements downstream of the cathode, Csiky concluded that in the spot mode the high electron densities would result in a thin sheath over the cathode internal surfaces. Electrons emitted from the cathode surface would be effectively trapped in the cavity by reflections from the sheath. This would explain the higher electron densities, luminosity at the cathode orifice as well as the lack of luminosity elsewhere in the discharge in the spot mode. In the plume mode case, Csiky suggested that the lower electron densities would consequently lead to a much thicker sheath, which he proposed will be of larger dimensions than the orifice, and whose boundary exists downstream of the orifice. The emitted electrons thus are accelerated through the sheath without suffering any collisions, and only collide with neutrals downstream of the cathode, hence giving the plume mode its characteristic appearance.

This theory is, however, contradicted by two observations: First, contrary to the theory's predictions, the cathode spot is observed to persist in the plume mode in this work and others [146]. Second, later measurements in the hollow cathode plasma, by several methods, indicated plasma densities in the range 10^{18} m^{-3} – 10^{20} m^{-3} in both

the spot and plume modes. These plasma densities result in sheaths approximately 10^{-6} m – 10^{-7} m thick, orders of magnitude smaller than the orifice dimensions.

Fearn and Philip **[126]** found experimental evidence (based on unpublished work by Wells and Harrison [126]) to suggest that emission from the cathode surface occurs at constant current density. They further suggest that in the plume mode emission starts at the very downstream edge of the orifice. As the current demand increases, the emitting area progressively increases by further movement into the orifice. In the plume mode emission occurs exclusively from the cathode orifice. Plume to spot transition occurs when the discharge covers all of the available cathode orifice surface area. Further increase in current would result in the discharge stepping into the cathode body and emission is then demanded from the cathode internal walls. Results from experiments using various orifice sizes seem to confirm their hypothesis, and gave current densities between $2 - 5\times10^{5}$ Am^{-2}. This was further supported by further tests [46], in which experiments were carried out on a stepped orifice and an orifice with a smooth contour. The stepped orifice exhibited a double mode change, while the smoothly contoured orifice showed no abrupt mode transition, indicating a smooth discharge transfer from the orifice to the main cathode body.

Since the emission area is determined by the discharge current, it is unclear how this theory can explain the experimentally observed dependence of plume/spot mode transition on flow rate. Moreover, this theory cannot explain the transition dependence on geometrical factors such as the cathode-anode separation and the absence of the plume mode in the full thruster geometry.

Mandell and Katz **[102]** suggested that events at the keeper and not at the cathode are responsible for the different operating modes observed. They produced a model of the discharge, in which for simplicity, ionisation is considered to occur only in the orifice region. Based on the model predictions of the dependence of ion production on discharge current and flow rate, they propose that at high current and high $\dot{m}$, the ion production is sufficient for the keeper to collect current passively from the plasma and the discharge is in the spot mode. Whereas, at low flow rates and discharge currents an electron accelerating sheath is required at the keeper, and it is forced to actively collect current. The electrons accelerated by the sheath, in the keeper area and through

the keeper orifice are responsible for the production of the light emission in the plume mode.

However, we note that, based on this theory, the removal of the keeper electrode should eliminate the plume mode or at least radically alter the discharge behaviour. This, however, is contrary to experiments carried out in open diode configuration with no keeper electrode [45, 193], in which the plume mode was still present, and the general observed discharge characteristics were found to be unaltered by the removal of the keeper.

The theories and mechanisms described above can each explain part, but by no means all, of the extensive experimental observations. A unified theory of the plume to spot transition needs to account, not only for the dependence on the operating parameters, but also for the observed discharge behaviour including: the noise and oscillatory behaviour, the visual characteristics of the discharge, the spectroscopic measurements, the Langmuir probe results, the dependence on keeper configuration and current, the dependence on discharge geometry as well as the absence of the dual mode behaviour in a thruster geometry.

7.4.4 Proposed plume to spot transition theory

It is proposed here that the discharge modes and the associated experimental observations are attributable to the current collection mechanism at the *anode*. In what follows, we will demonstrate that this simple hypothesis can not only explain the overall discharge behaviour but it can also elucidate several hitherto inexplicable observations in hollow cathode discharges.

Langmuir and Mott-Smith [89], in a series of fundamental papers on gas discharges, described the impact of the local plasma current density on the mechanism of current collection at a collecting electrode. This is best illustrated by an example: Consider a disc shaped anode of unit cross sectional area in a cylindrical discharge tube of the

same diameter. Assume also that there is a uniform plasma current density at the anode location of $3Am^{-2}$, which implies that the anode "naturally" receives (with no sheath forming or bias relative to plasma potential) a current of 3A from the local plasma. If the external circuit demands only 1A from the anode, the anode will need to be negative with respect to the local plasma potential in order to repel $\frac{2}{3}$ of the electrons bound in its direction. Thus, due to the plasma current density, the anode will be surrounded by positive ions forming a positive space charge sheath and hence there will be a negative anode drop. If the anode area is reduced to $0.33m^2$ ($\frac{1}{3}$ of the tube cross section), there will be exactly enough electrons moving, out of their own volition, towards the anode to satisfy the 1A current requirement. So the negative potential drop disappears and the anode operates at the plasma potential. If however the anode area is reduced further to $0.1m^2$, the anode will only collect passively 0.3A of current, and the power supply will need to supply energy to the anode until 1A is drawn from the plasma. The anode will become positive with respect to the local plasma in order to actively collect the electron current.

An electrode which is slightly positive with respect to its surroundings will accumulate an excess of electrons in its vicinity, which leads to the formation of a negative electron sheath surrounding the anode. All of the rise in potential between the plasma and the anode will be concentrated within this sheath, with the negative electron space charge in the sheath being able to shield the local plasma from the positive charge of the collector, consequently, the field of the collector will not extend beyond the outer edge of the sheath. Thus, and this is crucial, the electron current collected by the anode is limited by the rate at which electrons reach the outer edge of the sheath, or as Langmuir stated [89] "the current increases with the voltage only in proportion to the surface of the outer edge of the sheath". Hence, when the diameter of the electrode is much larger than the thickness of the sheath (as is the case with the disc anode), the current to the anode cannot significantly increase with rising potential and the 1A current requirement cannot be satisfied even with the development of a positive anode fall. The anode potential rises until a suitable value is reached (usually a few volts above the ionising potential of the gas) for ionisation of the gas in the sheath by electrons accelerated in the anode fall to be appreciable, and the sheath ***breaks down***. Only a few ions are required to form for the anode sheath to break down, one ion for several hundred electrons, because of the relatively long residence

time of the ions resulting from their larger masses. It is important to note that three variables will enhance the ionisation process in the sheath: increasing the sheath thickness for a given neutral density (electron mean free path) will enhance the ionisation probability, increasing the neutral density at the sheath will decrease the mean free path and also increase the ionisation probability, and finally increasing the anode potential will increase the primary electron energy and consequently the collision cross section and hence the efficiency of the ionisation process. Thus the formation of a few ions in the sheath will neutralise the space charge of many more electrons and would decrease the overall space charge of the sheath, causing an increase in the sheath thickness which in turn further increases the ionisation in the sheath, and subsequently, the anode sheath suddenly breaks down. The breakdown of the sheath causes the formation of a highly defined luminous region close to the anode, which resembles a globular or semi-spherical region (also termed "fireball" by some authors) of much higher luminosity than the surroundings. This luminous region is a region of elevated ionisation and conductivity, while without in the ambient plasma, the conditions remain the same and the plasma is unperturbed. The outer edge of the luminous region is a double layer with an inner positive space charge and an outer negative space charge [90], and has been observed to extend to several centimetres from the anode [148]. The outer edge of the double layer is now essentially the collecting area for the electrons, forming what could be termed a "virtual anode". The thickness and thus the area of the virtual anode is determined by the ratio of the current required by the power supply and the available random "passive" electron current.

Returning to the example used above, the $0.1m^2$ anode in a plasma with $3Am^{-2}$ current density passively collects 0.3A of current. For it to collect the required 1A, its sheath breaks down forming a virtual anode with a $0.33m^2$ surface area, which allows its outer boundary to collect the desired current with no perturbation of the ambient plasma.

Based on the above discussion, we propose that in the diode hollow cathode tests, at low discharge currents and mass flow rates where the current density at the anode is expected to be low, the anode is forced to overcome the limitation on current collection imposed by its limited area by breaking down its sheath and forming a

virtual anode of larger surface area. The increased electron collection area and the increased plasma density near the electrode help to maintain the desired current. This constitutes the *plume mode* of operation. The *spot mode* occurs when the electron flux from the ambient plasma has sufficiently increased, due to increasing either I_a or $\dot{m}$, for the anode to forgo the need for an electron accelerating sheath, and it passively collects the required discharge current by being at or below the plasma potential. The details and mechanisms of the transition from plume to spot are more involved than the preceding description. We will here explain some of the more general observations of the hollow cathode discharge, deferring the more involved description to later sections.

The double layer forming the edge of the virtual anode in the plume mode can take a variety of forms, as illustrated in figure 7.43, depending on the location and number of the constituting parallel charge sheets. The shape, location, size and geometry of the double layer are determined mainly by the ion creation and loss rates and the electron and ion current densities. From the shape of the plasma potential profiles obtained by Siegfried [146] in the plume mode, figure 7.20, it can be inferred that the double layer at the edge of the virtual anode has the axial potential profile illustrated in figure 7.43 by the curve c (type (c) double layer). The reasons behind the formation of the type (c) double layer in the plume mode and the closely related visual characteristic of the discharge will be discussed next.

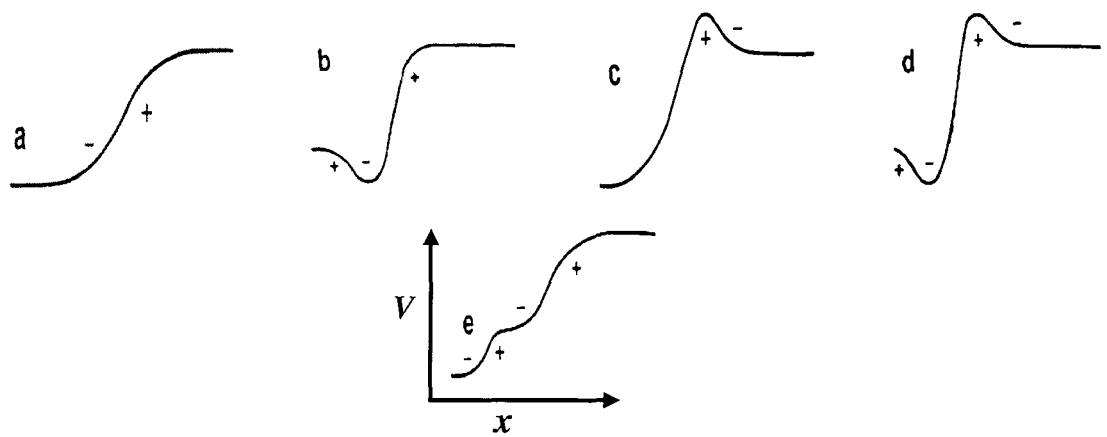

Figure 7.43: Illustration of a variety of double layer axial potential profiles corresponding to identical potential differences applied to the system boundaries. The structures are known as double layers due to the presence of at least two parallel charge sheets [61].

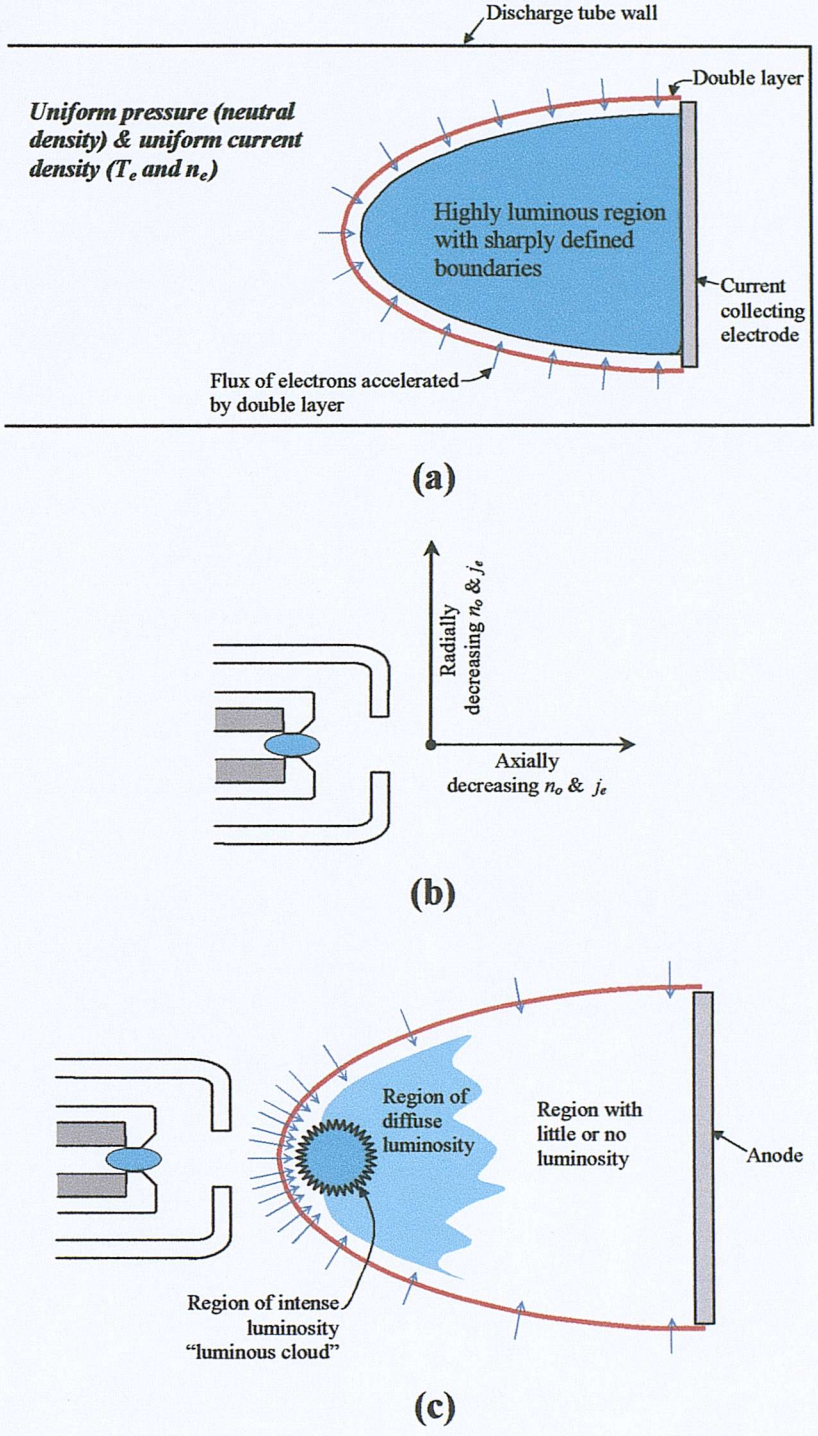

Figure 7.44: **(a)** *Visual characteristics of a virtual anode in a discharge with uniform plasma properties and pressure profile.* **(b)** *Expansion of operating gas and plasma downstream of a HC.* **(c)** *Illustration of the effect of the downstream expansion of plasma and propellant on the visual characteristic of a "virtual" anode in a HC discharge*

The visual characteristics of the protuberance from the anode, although not elucidated by Langmuir, can be easily seen to stem from the shape of the collector sheath. Due to

edge effects, the shape of the sheath on a circular disc collector is an oblate spheroid [89]. The experiments in which the virtual anode phenomena is observed usually had uniform, static gas pressure and the plasma properties (and hence the current density) were also approximately uniform in the collector vicinity [1, 89, 148]. As illustrated in figure 7.44(a), due to the uniform plasma properties, the rate of arrival of electrons at the double layer outer edge is the same over the entire double layer surface. These electrons are then accelerated by the double layer into a region of uniform neutral density and, for a sheath thickness of the order of an electron mean free path, the high energy electrons will cause uniform excitation and ionisation of the gas in the interior of the double layer. This results in the visual observation of a highly defined, extremely luminous semi-spherical region described in the literature and illustrated in figure 7.44(a). The boundaries of the luminous region are defined by the double layer, which due to the uniform ionisation in its interior, as seen in experiments [90, 148], will have the structure of a type (a) double layer, corresponding to two adjacent space charge regions, negative on the outer surface and positive on the inner surface.

The situation is however markedly different in a hollow cathode discharge. Due to the gasdynamic expansion of the gas from the cathode and keeper orifices into the discharge chamber, as indicated in figure 7.44(b), there is a very rapid decrease in neutral gas density in both the axial and radial directions, see also figures B.2 and B.5 in appendix B. The plasma extracted from the hollow cathode also undergoes a similar expansion as indicated by Langmuir probe results (see figure 7.21 and 7.23), thus the electron current density emitted from the hollow cathode also exhibits a rapid decrease in the axial and radial directions.

This has an immense impact on the visual characteristics of the discharge as illustrated in figure 7.44(c). The double layer forming the very upstream area of the sheath finds itself in a region in space with a relatively high electron current density which it accelerates. Due to the shape of the double layer in that region, the accelerated electrons are focused in a small area in space. As the neutral density is a decreasing function of the radial and axial distance from the cathode orifice, that small area just downstream of the double layer will have the highest neutral density, and hence the shortest ionising electron mean free path and consequently the highest ionisation efficiency of any region in the interior of the double layer. The ensuing

inelastic excitation and ionisation collisions result in a sharply defined region of extremely high luminosity, which correspond to the "luminous cloud" observed in this work and discussed earlier. The double layer surfaces just downstream of this area are influenced by two factors: First, the electron current density of the surrounding space is much reduced. This is not only due to the greater axial distance from the cathode. Due to the shape of the sheath, they are also collecting from a greater radial distance (refer to figure 7.44 (c)), further reducing the electron flux to the double layer. Second, although the path traversed by an electron in this region is longer, the neutral density has significantly decreased, due to the axial expansion, and the ionisation efficiency is reduced in this region. Both factors result in a region of diffuse luminosity existing just downstream of the highly luminous cloud, the physical extent of which is not well defined. The final structure in the virtual anode is the region further downstream adjoining to the anode electrode. The surface double layer of this region finds itself in a region of space with a very low electron current density. This, coupled with a further decrease in the neutral density in this region, results in very few excitation and ionisation collisions taking place, which results in this region having very little or no luminosity. Thus, the combination of the shape of the anode electron-accelerating sheath and the expansion of the neutral gas and plasma downstream of the HC, results in the characteristic visual appearance of the discharge in the plume mode (figure 7.44 (c)).

It can be seen that the above structure of the virtual anode explains the axial plasma potential profile found by Siegfried [146] in the plume mode (figure 7.20), what he termed the "electron free-fall region". Most of the ionisation necessary to maintain the area enhancing sheath takes place at the very upstream end of the virtual anode. The higher concentration of positive charge in this region raises its potential with respect to the surrounding space. Downstream of the luminous cloud, progressively less and less ionisation takes place and the plasma potential then gradually decreases with distance from the cathode. This is indeed the profile observed by Siegfried and corresponds to a type (c) double layer, i.e. the conditions in hollow cathode discharges have modified the structure of the double layer that forms the edge of the virtual anode from the type (a) found in discharges with uniform plasma and neutral gas properties to a type (c) double layer. Hence, the electron accelerating structure found

by Siegfried in the plume mode, which he termed an "electron free-fall region", is actually the double layer forming the edge of the virtual anode.

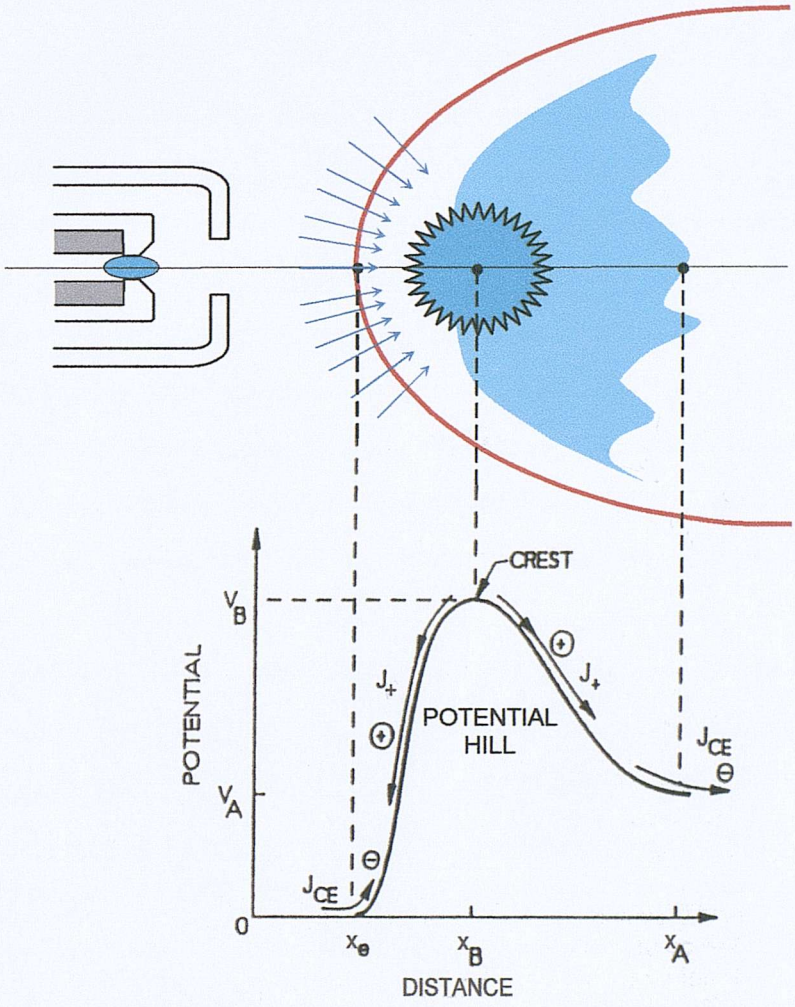

Figure 7.45: Axial potential profile of a "potential hill" detected by Williams and Wilbur [172] downstream of a HC in plasma contactor, shown to correspond to the visual structure of the type (c) double layer in the plume mode virtual anode

We also note that the type (c) double layer corresponds to the same structure found by Williams and Wilbur [172] downstream of a contactor HC at low current, which they refer to as a "potential hill". This potential hill is responsible for the formation of high energy ions detected in several experiments using different cathodes [121, 172, 171,194]. As mentioned above, when the cathode is operating in the plume mode, most of the ionisation necessary to maintain the area-enhancing sheath takes place at the very upstream end (the luminous cloud). The high ion production rate and the highly localised nature of this ion production region would cause its potential to rise with respect to the surrounding space, to values that can exceed the applied voltage.

The explanation based on the anode current collection mechanism in the plume mode indeed gives the underlying physical reason behind the formation of the potential hill, where the electron-accelerating upstream side of the double layer provides the energy input necessary to sustain the potential hill and ultimately the size and structure of the virtual anode. The ions produced in the crest of the ion production region are accelerated by the potential difference in all directions and constitute the high energy ion population observed. *The whole process of current collection in the plume mode is critically dependent on the rate of production and escape of these ions from the potential peak.* The above description is also consistent with Williams and Wilbur's [172] observation that the high energy ions seem to undergo an isotropic (spherically symmetric) expansion from their point of creation, which suggests that they originate from a highly localised region in space. The high energy ions cause the severe cathode tip erosion observed in the plume mode [132], and they are also responsible for the sputter erosion found on the face of the keeper facing away from the cathode.

It is interesting to note that although operation in the plume mode is usually undesirable, this unique ability of a type (c) double layer to produce high energy ions can probably be used in an interesting small (micro-) thruster concept. A hollow cathode mounted in diode configuration, where an anode of intentionally small surface area is used, is operated at low $\dot{m}$ in the plume mode. The type (c) double layer will result in an ion population with energies greater than those supplied by the power supply, which will cause an increase in thrust. Two main problems need to be overcome for this concept to work; the high electrode erosion rates and the expected high levels of noise in the plume mode discharge. The high erosion rates on the cathode and keeper can be reduced probably by using a low sputter-yield carbon keeper and the use of shielding on the cathode tip. The low frequency noise and oscillations in the discharge can be mitigated by using a battery supply for example.

The presence of this double layer also explains the higher than expected values of plasma parameter in the spectroscopic measurements when the discharge was operating in the plume mode (section 7.2.2). The double layer accelerates electrons from the ambient plasma, which leads to the breakdown of the sheath and the formation of a second plasma close to the anode. These primary electrons then thermalise to a temperature which is higher than they possessed prior to acceleration

by the double layer (see figure 7.20). With the optical fibre observing the hollow cathode from 135mm downstream of the tip, the plume results would represent the global values of n_e and T_e spatially integrated over the virtual anode region as well as the HC plasma, leading to the higher than expected results. Plume mode, spatially resolved, local measurements of the electron temperature and density in the HC interior plasma would indeed be expected to be lower than those measured here.

Let us recapitulate the general features of the theory: When the current density in the anode vicinity is insufficient to provide the desired current for the given anode's surface area, the plume mode occurs. The anode's electron-accelerating sheath breaks down, and the ions formed in the interior cause the expansion of the sheath leading to formation of a virtual anode with a larger surface area whose edge is a double layer. Both the increase in the electron collection area and the increased plasma density in the anode vicinity help to maintain the current balance at the anode surface. In hollow cathode discharges, due to a combination of propellant gas and plasma expansion downstream of the HC and the geometry of the anode sheath, most of the ionisation takes place at the very upstream edge of the virtual anode. This highly localised area, acting as the main ion production region, is fundamental in maintaining the size of the virtual anode and determining the shape of the double layer (also called "potential peak" or "electron free-fall region"). The structure of the virtual anode explains the visual observations in the plume mode and leads to several of the observed effects such as the formation of high energy ions, the higher sputter erosion rates on the upstream electrodes and the observed higher electron temperatures and densities in the plume mode.

The propellant flow rate and the discharge current drawn from the hollow cathode determine the electron density and the electron temperature in the cathode. Thus, assuming no extra ionisation occurs prior to reaching the double layer, the discharge current, $\dot{m}$ and the gas expansion determine the random current density ($j_e = n_e e\sqrt{(kT_e / 2\pi m_e)}$) in the ambient plasma at the double layer vicinity, and hence dictate the necessary surface area for the virtual anode to collect the desired current. The assumption that no ionisation takes place in the expansion region

downstream of the tip and upstream of the double layer is justified by the absence of any appreciable potential gradients (figures 7.20 and 7.22, see also reference [28]), thus the ionisation fraction in the external plasma upstream of the double layer can be expected to remain approximately the same as that in the HC interior [28]. The dynamic behaviour of the virtual anode with changes in current demand or the operating parameters upstream can explain the observed discharge characteristics and is discussed in detail in the subsequent sections.

7.4.4.1 Effect of propellant flow rate

With reference to the results of the discharge dependence on $\dot{m}$ at a constant anode current I_a= 5A and keeper current, figures 7.32 – 7.35 in section 7.4.2, at low $\dot{m}$ the current density inside the cathode, and by implication also at the anode location, is low. Moreover, the neutral gas density in the anode location will also be low, which means that higher voltages (i.e. primary electron energy) and a thicker sheath is required to maintain a given ion production rate. Due to both these factors, the current requirement of 5A in the plots would necessitate a very large current collection area; the virtual anode has to extend to the interior of the cathode-keeper space to collect the required current which leads to the enlarged appearance of the cathode spot, shown in figures 7.32, and the high anode voltages shown in figures 7.32 – 7.35. Siegfried's [146] measurements of the double layer indicate that it is of a sub-millimetre thickness, which allows penetration into the keeper orifice. As mentioned previously, the current collection requirement and the formation of the virtual anode are purely phenomena at the collecting electrode, and should not perturb the ambient plasma upstream of the double layer. However, as will be shown next, the proximity of the double layer to the cathode tip at low $\dot{m}$ influences the electron emission from the cathode and hence does have a perturbing effect on the surrounding plasma (as illustrated in figure 7.46), and resulted in the elevated low frequency noise levels observed on the anode and keeper traces in figures 7.32 – 7.35 when the luminous cloud was inside the cathode-keeper space.

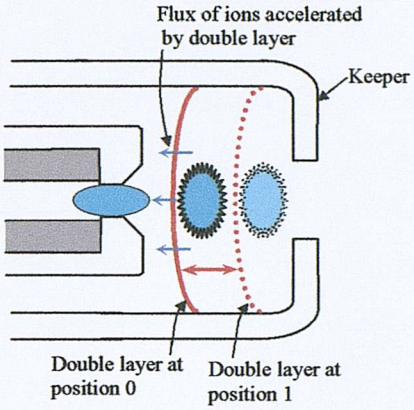

Figure 7.46: Ion current to HC with luminous cloud inside the cathode-keeper space.

The presence of the double layer in the cathode-keeper space will cause a low frequency noise on the anode trace due to the following effects: If the double layer is at position 0 (see figure 7.46), some of the ions produced at the potential peak will be accelerated upstream by the double layer, leading to increased electron emission from the cathode. The increased electron emission is a consequence of the increased secondary-emission by the high energy ion bombardment and the enhanced Schottky effect from the higher ion density in the cathode interior and in and around the cathode orifice. Hence, the presence of the double layer affects the plasma conditions upstream, and due to the resulting increased electron emission the anode finds itself collecting more current than the required 5A at position 0. The anode attempts to collect less current by reducing its potential, which leads to reduced ionisation downstream of the double layer and hence the virtual anode size decreases and the double layer is at position 1. This, however, leads to bombardment of the cathode by smaller ion flux of lower energy, which leads to a lower than expected cathode emission, the anode thus finds itself collecting less than the required 5A. The power supply thus orders more current to be collected by increasing V_a, the double layer expands we are back at position 0, and the process repeats itself. If sufficient time is not allowed for the cathode emission and the virtual anode to reach equilibrium this process leads to the generation of the low frequency noise observed on the anode trace.

The keeper, as will be shown in the next section, nearly always has enough electron current density at its surface for it to be collecting current passively, and an electron

retarding sheath is formed at its surface. However, with the cloud upstream of the keeper, the keeper power supply reacts to fluctuations in the plasma current density due to the motion of the anode double layer and the concomitant changes in the electron energies and plasma properties behind it, leading to the noise on the keeper trace. Only after movement of the cloud away from the keeper can the keeper experience relatively noise-free operation, with the emergence of the cloud from the keeper orifice usually occurring concurrently with a substantial, abrupt reduction in keeper noise.

As the propellant flow rate is increased, the neutral density in the cathode increases. Due to the increased electron-atom collision frequency, this leads to a rise in the plasma density in the cathode interior, which, assuming an approximately constant cathode sheath drop (from Siegfried's [145] empirical results, section 7.3), is described by equation (7.14) [53] for the volume ion production rate at the cathode (I_{pc}):

$$I_{pc} = \frac{dn_e}{dt} = n_{ep} n_o \sigma_i v_p \qquad (7.14)$$

where n_o is the neutral density, n_{ep} is the density of the primary electrons accelerated through the cathode fall, σ_i is the ionisation cross-section and v_p is the primary electron velocity. The resulting higher current density at the anode would necessitate a smaller virtual anode collection area for the desired current of 5A. Increasing the flow rate would also result in a higher neutral density downstream of the double layer, which leads to a lower voltage requirement for a given virtual anode ion production rate and hence a given sheath thickness. Taking both of the above factors into account, increasing $\dot{m}$, at a constant anode current requirement, consequently leads to a lower anode potential and a smaller virtual anode, which explains the negative gradient on the V_a-$\dot{m}$ curves in figures 7.32 – 7.35 and the downstream motion of the cloud. This situation continues until the cloud emerges from the keeper orifice.

With the luminous cloud emerging from the keeper orifice, a different scenario unfolds. The increase in $\dot{m}$ would result in a higher electron current density upstream of the double layer, as above, requiring a smaller virtual anode collection area for the 5A requirement and the cloud moves downstream out of the keeper cavity. Movement

outside of the keeper-cathode space would however result in a drastically reduced neutral density downstream of the double layer, which would necessitate an increase in the voltage across the double layer from its previous value, increasing the primary electron energy and hence the ionisation probability. The power supply current demand precludes increasing the sheath thickness, as any increase will result in the collection of more current than necessary. The ionisation process becomes highly inefficient due to the reduced neutral density downstream of the double layer. This manifests itself in several ways: i) Increasing V_a, as mentioned above, and exhibited in figures 7.32 – 7.35 for all gases, to enhance the ionisation probability. ii) Due to the consequent higher primary electron energy and the lower collision frequency with the less dense gas, the spectroscopically measured electron temperature (section 7.2.2) increases as the cloud moves outside the cathode, as illustrated in figures 7.13 & 7.15 and in table 7.2. iii) The inefficiency of the ionisation process exhibits itself most prominently in the spectra of the discharge in figure 7.36, with the relative intensity of the neutral lines (which is essentially a loss mechanism to the ionisation process) increasing radically with respect to the first ionisation lines when the cloud was downstream of the keeper. This even led to the observation of neutral lines which were undetectable when the cloud was upstream of the keeper or when the discharge was in the spot mode. Siegfried [146] and Monterde [115] reported the same observation with discharges operating in mercury and xenon respectively.

With the cloud now downstream of the keeper, increasing the propellant flow rate further leads to the continued increase in the current density upstream of the virtual anode. This is met at the anode by a decrease in the required virtual anode area for the collection of the 5A, thus decreasing the required ionisation rate and hence the required double layer potential. This results in V_a decreasing with $\dot{m}$ as shown in figures 7.32 – 7.35. The downstream motion of the double layer results in a longer electron mean free path (although the neutral density increases for a given position with $\dot{m}$, it decreases at a higher rate with downstream axial motion, compare figures B.2 and B.6 (Appendix B), with the net result being a lower neutral density downstream of the double layer with increasing $\dot{m}$). This, combined with lower electron energies due to a smaller double layer fall, would result in a more diffuse and less defined luminous cloud as illustrated in figure 7.47 and observed experimentally.

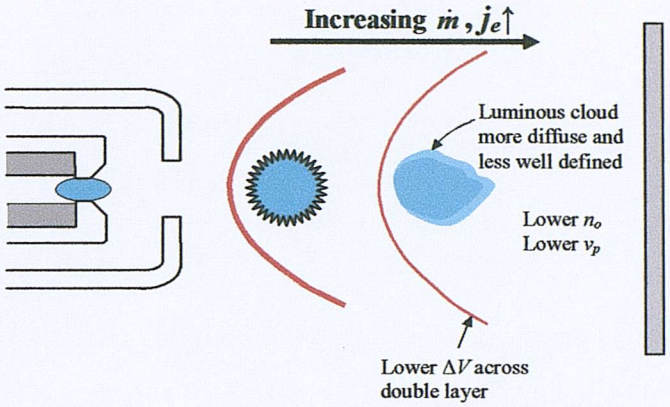

Figure 7.47: Effect of increasing $\dot{m}$ at constant I_a on the visual characteristics of the discharge

Accordingly, the luminous cloud moves further and further downstream and becoming more and more diffuse and less well defined, until finally the current density at the anode becomes sufficient for the sheath area required for current collection to be of the scale of the anode dimensions. No further area enhancement is therefore necessary, thus the virtual anode and associated double layer, downstream ionisation and luminosity all vanish. Consequently there is a sudden drop in V_a of the order of the ionisation potential of the gas, and the anode collects current passively in the spot mode, where by far most of the energy of the power supply is expended at the cathode.

Song et al. [148] formulated a relation for estimating the dependence of virtual anode size on the neutral number density. Assuming, for simplicity, a spherical virtual anode with uniform volume ionisation, stretching from the anode surface upstream towards the cathode a distance given by its diameter D. We can relate electron and ion fluxes into and out of the virtual anode by:

$$\varphi_e D \sigma_i(V_{dl}) n_o = \varphi_i \qquad (7.15)$$

where $\sigma_i(V_{dl})$ is the ionisation cross-section of primary electrons accelerated through a double layer with a potential fall V_{dl}. φ_e and φ_i, the electron and ion fluxes respectively, are linked by Song using Langmuir's relation for charge flow across a double layer:

$$\varphi_e = \left(\frac{m_i}{m_e}\right)^{1/2} \varphi_i \qquad (7.16)$$

Equation (7.15) basically states that the rate of ion production in the virtual anode must equal the rate of ion loss to the ambient plasma. The ion loss rate for the spherical surface is given by $4\pi(D/2)^2\varphi_i$. The ion production rate is approximately $4\pi(D/2)^2 D\sigma_i(V_{dl})n_o\varphi_e$, where $D\sigma_i(V_{dl})n_o$ is the ionisation probability for an electron, which is simply the ratio of the electron path length inside the virtual anode (D), to the ionisation collision mean free path for an electron accelerated through the potential difference V_{dl} ($1/[\sigma_i(V_{dl})n_o]$). Combining equations (7.15) and (7.16) gives:

$$D = \frac{1}{\sigma_i(V_{dl})n_o}\left(\frac{m_e}{m_i}\right)^{1/2} \qquad (7.17)$$

Equation (7.17) predicts a decreasing virtual anode diameter with increasing neutral density, in good qualitative agreement with the experimental results. Furthermore, using xenon as an example, for a flow rate of 1mg/s, the neutral density at the anode location was estimated to be approximately 3×10^{18}m^{-3} from extrapolation of computational modelling results (Appendix B) and from the measured vacuum chamber pressure. V_{dl} is estimated approximately at 20V from Siegfried's [146] Langmuir probe measurements (section 7.4.1.1), which gives a collision cross-section for xenon of $\sigma_i(V_{dl}) \approx 2.7\times10^{-20} m^2$ [63] and results in an approximate virtual anode diameter of 3cm. At 1mg/s the luminous cloud was observed to be just downstream of the keeper orifice (table 7.2), i.e. approximately 4cm upstream of the anode. The calculated diameter, in spite of the approximate nature of the figures and the simplifying nature of the equation, is of the order of the observed extent of the virtual anode.

7.4.4.2 Effect of discharge current

The random current received by an electrode of surface area A, immersed in a plasma at a given location in space with random current density j_e, is given by:

$$I = A j_e = A e n_e \sqrt{(kT_e / 2\pi m_e)} \qquad (7.18)$$

Generally, for arc discharges the electron temperature is a very weak function of arc current [89]. This was also shown to be true for HC discharges from Langmuir probe measurements inside the cathode (see section 7.3 and reference [145]). It was also observed that T_e is spatially invariant in the coupling plasma [117]. Moreover, j_e is a weak function of electron temperature, scaling with the square root of T_e. We can hence assume, to a first approximation, that the current collected by a collector of a given area, at a certain flow rate, is a function of n_e alone.

We define a variable $(n_e)_{A,p}$, which gives the 'required' electron density at the anode location for the anode to passively collect the current demanded by the power supply at the plasma potential. From equation 7.18, $(n_e)_{A,p}$ varies linearly with current demand, as illustrated in figure 7.48, with a slope given by $A e n_e \sqrt{(kT_e / 2\pi m_e)}$.

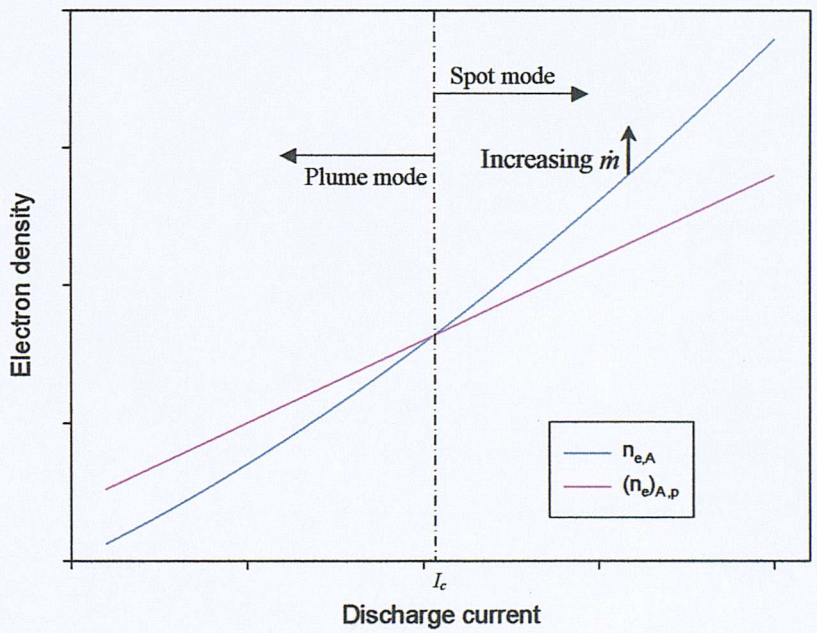

Figure 7.48: Functional dependence of the electron density at the anode location due to the expansion of the HC plasma ($n_{e,A}$), and ($(n_e)_{A,p}$) the required density at the anode location for passive current collection on I_a.

The electron density inside the HC was shown experimentally to increase with current drawn from the cathode. The modified Siegfried-Wilbur model predicted an approximately quadratic dependence for the cathode electron density on I_D (figure

7.18). We introduce another variable $n_{e,A}$, which gives the electron density at the anode location due to the expansion of the HC plasma, when no potential gradients, like the double layer, exist in the space between the anode and cathode. In other words $n_{e,A}$ gives the actual electron (and current) density at the anode produced by the cathode. $n_{e,A}$ will also have a quadratic dependence on I_D, as illustrated in figure 7.48, since it is the result of pure expansion of the HC plasma with no potential gradients and consequently no extra ionisation and the same ionisation fraction.

Figure 7.48 illustrates the functional dependence of $n_{e,A}$ and $(n_e)_{A,p}$ on I_D. At low values of I_D ($< I_c$), the electron density at the anode location will be less than that required for the collection of the current demanded by the power supply. The power supply increases the anode potential, breaking down the sheath and resulting in the formation of a virtual anode of sufficient surface area to collect the desired current. Under these conditions, the discharge is in the plume mode. As the discharge current is increased, the hollow cathode's electron production (represented by $n_{e,A}$) increases at a higher rate than the requirement at the anode for passive collection (represented by $(n_e)_{A,p}$). This continues until a critical value of current (I_c) is reached, where the current density at the anode can exactly satisfy the power supply requirement. The anode, no longer requiring a current collecting sheath, collects current passively at the plasma potential. The discharge has thus made the transition to the spot mode. Further increasing the discharge current causes the local current density to exceed demand. Consequently, the anode becomes negative with respect to the plasma potential to reject the excess current. For discharge currents greater than I_c, the rate of increase of current density at the anode with discharge current exceeds that for the demand. This forces the anode to become more and more negative with respect to the local plasma potential, and causes the negative V-I_a characteristic observed in the spot mode (figure 6.23).

The reader would note that there are no units on the graph in figure 7.48. This is intentionally done because a second important parameter, $\dot{m}$, fixes the position of the transition point where the two graphs intersect. As previously discussed in section 7.4.4.1, increasing $\dot{m}$ would result in a rise in the plasma density in the cathode interior, and consequently, at the anode location. This translates (as indicated in figure

7.48) to a shifting of the $n_{e,A}$ curve to higher electron densities, which causes the curves of the supply and demand to intersect at a lower value of discharge current. Thus over the same current range, increasing the value of $\dot{m}$ at which the discharge characterisation is carried out would cause the plume to spot transition to occur at progressively lower values of discharge current, with the opposite effect occurring if $\dot{m}$ is decreased. This is indeed the experimental observation, and is best illustrated by observing the boundary of the transition between regions B and A in the Fearn/Patterson [45] characterisation of the T6 (figures 7.25 and 7.51). It is intuitive to see that, at a high enough value of $\dot{m}$, a point is reached where the $n_{e,A}$ curve will always be higher than that for $(n_e)_{A,p}$, and the two curves will not intersect. This explains why, above a certain value of $\dot{m}$, the plume mode is never encountered and the discharge is always in spot mode. The opposite is also true, if $\dot{m}$ is decreased, a value is reached where the $n_{e,A}$ curve will always be lower than that for $(n_e)_{A,p}$ in the range of usable discharge currents, and they will again never intersect. For lower values of $\dot{m}$, the plume mode is always encountered under all discharge currents and no plume to spot transition is possible. These predictions are confirmed experimentally by virtually all investigations of the cathode discharge behaviour (refer for example to figures 7.25 and 7.51).

Plume mode characteristics

We now move on to describe the detailed behaviour of the discharge in the plume mode ($I_D < I_c$ in figure 7.48), using a similar analysis to the one used above.

It can be conceived, based on conditions at the anode that increasing the current demanded by the power supply would result in an increase in the current collection surface of the virtual anode and lead to an upstream motion of the double layer. This analysis, however, oversimplifies conditions in the HC discharge, as it implicitly assumes that plasma conditions upstream are independent of the discharge current. The discharge behaviour in the plume mode is primarily dictated by the virtual anode, the behaviour of which is determined by changes in ambient plasma conditions and changes in current demand.

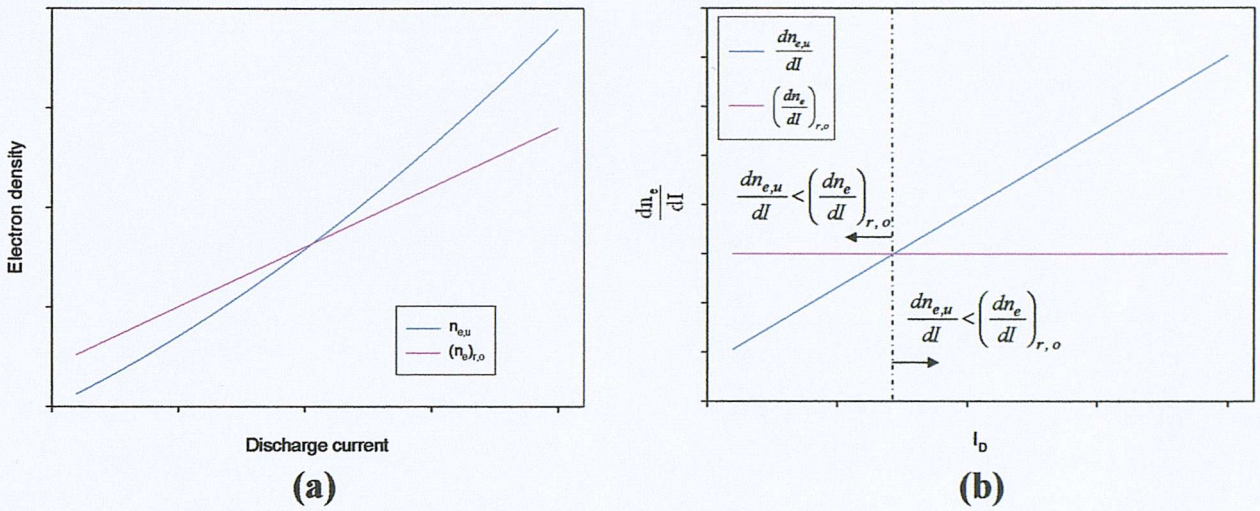

Figure 7.49: **(a)** *Functional dependence of the electron density upstream of double layer ($n_{e,u}$) on I_D from the modified Siegfried-Wilbur model, along with linear increase of $(n_e)_{r,o}$ the electron density required to keep virtual anode at same position O (figure 7.50) with I_D.* **(b)** *Comparison of rate of change of $(n_e)_{r,o}$ and $n_{e,u}$ with I_D*

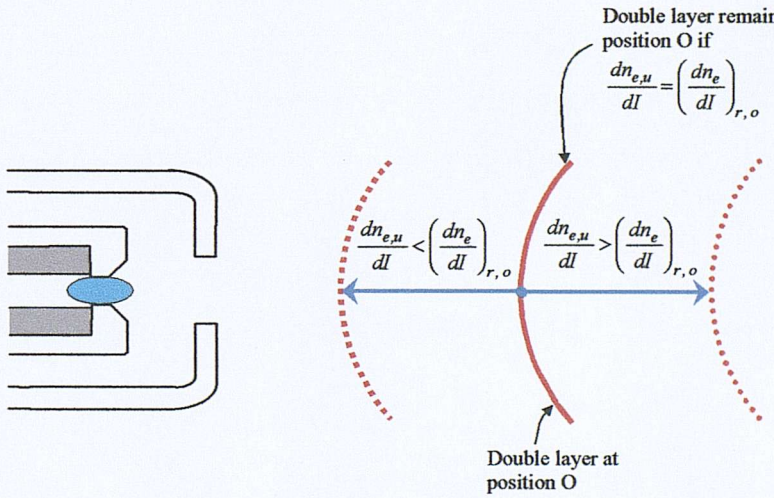

Figure 7.50: The three possible scenarios for dependence of the virtual anode size on discharge current: a) at low I_D, the rate of increase of upstream electron density with current demand is less than that required to maintain the virtual anode at position O and the virtual anode expands. b) both rates are equal and the virtual anode remains the same c) rate of electron production at cathode is greater than that required at O and virtual anode contracts

For a virtual anode located at an arbitrary position O, as illustrated in figure 7.50, if the current demand is increased by the power supply, it can only remain at position O if the electron density upstream of the double layer increases linearly with anode current. The condition of a stationary double layer is described by a variable $(n_e)_{r,o}$

which gives the required upstream electron density for the double layer to remain at a position O for a given current. From equation (7.18), $(n_e)_{r,o}$ varies linearly with current demand, illustrated in figure 7.49(a), and hence the rate of change of $(n_e)_{r,o}$ with discharge current $\left(\frac{dn_e}{dI}\right)_{r,o}$ is a constant given by $A_{dl}\, e\sqrt{(kT_e / 2\pi m_e)}$ (figure 7.49(b)), where A_{dl} is the surface area of the double layer at position O.

The electron density in the cathode, as predicted by the modified Siegfried-Wilbur model, will show an approximately quadratic dependence on the current drawn for the cathode. By implication, the electron density upstream of the virtual anode location ($n_{e,u}$), as illustrated in figure 7.49(a), will also demonstrate the same quadratic dependence on I_D. The rate of increase of $n_{e,u}$ with discharge current, $\frac{dn_{e,u}}{dI}$, thus varies linearly with discharge current, as shown in figure 7.49(b).

Let us start from a virtual anode at position O, of surface area $(A_{dl})_O$, with an electron density $n_{e,u}$ upstream of the double layer. The size and current collection of this virtual anode initially satisfy the demand of the power supply of a low current I. The situation that develops is as follows: For a double layer at position O at low I_a, increasing the discharge current would result in an increased electron density upstream of the double layer. However, the rate of increase will be less than that required to maintain the double layer at position O with the increased current demand $\left(\frac{dn_{e,u}}{dI} < \left(\frac{dn_e}{dI}\right)_{r,o}\right)$. The virtual anode finds itself collecting less current than required, it is then forced to increase its current collecting surface area, and expands to a new location upstream as illustrated in figure 7.50 and observed experimentally in this work. This situation continues with the virtual anode expanding with increased current demand until, as figure 7.49(b) illustrates, the rate of increase of $n_{e,u}$ with current demand exceeds that required to remain at a given position $\left(\frac{dn_{e,u}}{dI} > \left(\frac{dn_e}{dI}\right)_{r,o}\right)$, and the virtual anode has to contract to avoid collecting excessive current. From here on the virtual anode proceeds to shrink with increasing current demand until the electron density is sufficient to preclude an area enhancing sheath; the virtual anode disappears, leading to a discontinuous drop in potential due to the elimination of the need for sheath ionisation, and the anode collects current passively in the spot mode.

The latter case of the virtual anode moving downstream with increasing I_a was not observed in this work due to the limitations on discharge current. Siegfried [146], who was using an anode with a larger surface area, did however observe this predicted downstream motion preceding plume to spot transition.

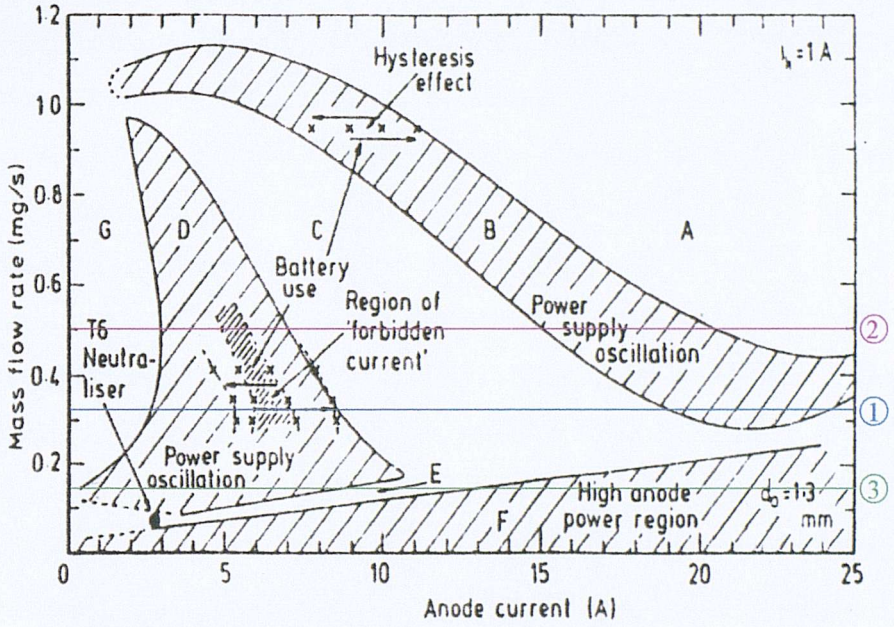

Figure 7.51: Reproduction of the discharge characteristics and discharge mode map of Patterson and Fearn [45], with lines of constant $\dot{m}$ inserted

We now proceed to describe the detailed operating characteristics of the discharge, to that end the detailed operating map of Patterson and Fearn [45] is reproduced here as figure 7.51 with lines of constant $\dot{m}$ drawn through them.

Starting with line (1) at a mass flow rate of 0.32mg/s:

$dn_{e,u}/dI < (dn_e/dI)_{r,o}$: At very low values of discharge current the current density at the anode plane is sufficient to supply the small current collection requirement, precluding the need for an area enhancing sheath. The discharge is then in region G, which explains both the visual observations (figure 7.41) and the quiescent nature of the discharge. This region was also observed by other investigators at very low discharge currents [51, 131]. As current demand increases, although the electron density at the anode increases, the required electron density ($(n_e)_{r,o}$) increases at a higher rate, thus the anode needs to increase the sheath potential in order to collect the required current. The situation continues until, the current collection limit is reached

for the physical size of the anode, the anode increases its potential until sheath breakdown ensues and a virtual anode of greater current collection surface area is formed.

The formation of the virtual anode moves the discharge to region D. The appearance of the virtual anode has several effects on the HC operation: i) It increases the ion current to the cathode, which reduces the electron current required at the anode at a given discharge current ($I_a=I_e+I_i$). ii) The increased ion current would result in an increase in the emitted electron current density at the cathode due to secondary emission and enhanced Schottky effect. The cathode would be thus emitting more electrons than the discharge requirement, which leads to the emission at the cathode becoming space-charge-limited; the extra electrons which are not accelerated by the field congregated near the cathode surface creating a space charge which suppresses further emission. When more current is permitted to flow, the plasma density at the cathode will increase due to the increased input power, the cathode sheath narrows due to the higher plasma density and the potential drop across the cathode *falls* [58] (note that although the voltage decreases with increasing current, the input power $V\times I$ increases). This situation continues until all the electrons from the cathode are drawn into the arc and the cathode makes the transition from space-charge-limited to emission limited operation, then the potential drop of the cathode rises with increasing current.

This has a profound effect on the characteristics of the discharge; ignoring the small potential gradient in the intermediate plasma column, the potential supplied by the anode power supply (V_a) is approximately the sum of the cathode fall (V_c) and the anode fall (V_{ad}), as shown by equation (7.19):

$$V_a \approx V_c + V_{ad} \tag{7.19}$$

The cathode potential, as mentioned above, will decrease with increasing discharge current. Remembering, however, that we are in the region where the rate of increase of electron density upstream of the double layer with discharge current is less than that required for the double layer to remain stationary ($dn_{e,u}/dI < (dn_e/dI)_{r,o}$), the virtual anode will need to expand with increasing current and hence the anode fall V_{ad}

increases. If the rate of decrease of V_c with discharge current exceeds the rate of increase of V_{ad}, the discharge experiences a negative voltage-current characteristic, as observed experimentally.

As observed and conclusively demonstrated by Patterson and Fearn [40], the interaction between the discharge and the power supply control loop in this region causes the observed low frequency oscillations. In a current controlled power supply, there always exists a current ripple in the power supply output, which Patterson and Fearn identified as the inducing factor for the oscillations. The output current cycles between values that are slightly higher or lower than a nominal set value. This process is due to the power supply voltage increasing slightly to achieve the nominal set value. The voltage, however, overshoots and too much current is allowed, so the voltage is then reduced again and the cycle continues.

For a discharge with a positive V_a-I_a characteristic in the $dn_{e,u}/dI < (dn_e/dI)_{r,o}$ region, a requirement for an increased current would require a concurrent increase in both V_c and V_{ad} as, although there is an increase in the electron production at the cathode, this needs to be augmented by an increase in the virtual anode size to provide the current. With the current ripple in the power supply, in a region with a negative V_a-I_a, the situation changes. To achieve an increase in current, the power supply voltage is raised and this results in the usual upstream expansion of the virtual anode. At the cathode, however, increasing V_c results in a *decrease* in the electron current density, thus the virtual anode finds itself collecting less current than required at its new position. The power supply reacts to this by further increasing its voltage and this situation continues until, as reference [122] describes, a point is reached when too much current is allowed to flow. The power supply's reaction now is to decrease the applied voltage. On re-entering the negative V_a-I_a, region, decreasing the applied voltage would result in the desired motion of the virtual anode downstream. Concurrently at the cathode, however, a reduction of the applied voltage would result in an increased electron production, causing the virtual anode to collect more current than required. This causes the power supply to reduce its potential further and further until the discharge exits the negative V_a-I_a region, wherein the power supply finds itself collecting too little current and the cycle repeats itself. This explains the low

frequency oscillations and the movement of the virtual anode explains the flickering and the upstream-downstream motion of the luminous cloud observed in region D. This situation persists until, with increasing current, all the available electron current is drawn from the cathode and the cathode makes the transition from space-charge-limited to emission-limited operation represented by region C. In this region the absence of the negative V_a-I_a characteristic causing the discharge-power supply interactions leads to the reduced noise levels in the anode trace. Increasing the current demand in this region would simply result in the observed upstream motion of the virtual anode, with no observed fluctuations in luminosity or position. Reference [121] suggested that a plasma focusing mechanism downstream of the cathode tip is necessary to explain the visual observation of the "beam mode", especially with a chamfered cathode orifice, in region C. It is interesting to observe that our proposed mechanism of current collection in the plume naturally provides such a mechanism. As illustrated in figures 7.44 and 7.45, the double layer shape introduces a lensing effect to the plasma electrons reaching its outer surface. These accelerated electrons then cause luminosity downstream of the double layer, which can, under the right conditions, resemble a beam emanating from the cathode.

$\underline{dn_{e,u}/dI > (dn_e/dI)_{r,o}}$: By increasing the current further the discharge eventually leaves region C and enters region B. The rate of electron current production has been increasing steadily with discharge current (see figure 7.49(b)). A point is reached, as has been earlier described, when the rate of increase of electron production at the cathode with discharge current exceeds that required to keep the virtual anode at a given position, and the virtual anode has to retreat downstream to avoid collecting excessive current. Hence, if more current is demanded, the cathode increases its sheath potential (V_c), at the same time the virtual anode has to decrease its size so V_{ad} *decreases*, and if the rate of decrease of V_{ad} with discharge current exceeds the rate of increase of V_c the discharge experiences another negative voltage-current characteristic. Due to its negative V_a-I_a characteristic region B will also experience the low frequency oscillations induced by the current ripple on the power supply output as described earlier for region D.

With increasing I_a the virtual anode size progressively decreases with increasing current density upstream until the required collection area is of the order of the

physical anode. This removes the need for sheath ionisation, so there is a discontinuous decrease in voltage and the anode then collects current passively from the plasma and the discharge is in the spot mode.

Increasing $\dot{m}$ to 0.5mg/s, line (2):

Due to the increased plasma density in the cathode with increasing $\dot{m}$, the available current density at the anode for a given current value would increase. This would lead to the expansion of the low current region where the anode can collect current passively (region G) to a higher current range. Increasing $\dot{m}$ also results in a thinner sheath across the cathode due to the greater plasma density. This reduced sheath size and drop would lead to a smaller space-charge-limitation effect at a given current, i.e. the discharge is expected to make the transition from space-charge-limited to emission limited operation at lower I_a. Resulting in the boundaries of region D narrowing with increasing $\dot{m}$ as observed in figure 7.51. As discussed earlier in figure 7.48, increasing $\dot{m}$ shifts the cathode production to higher densities and causes the $n_{e,A}$ and $(n_e)_{A,p}$ curves to intersect at a lower value of I_D. This leads to the shifting of the boundaries of region B to lower discharge currents with increasing $\dot{m}$, with transition to spot mode occurring at lower values of I_D as illustrated in figure 7.51.

Reducing $\dot{m}$ to 0.15mg/s represented by line (3):

As $\dot{m}$ is reduced, the electron current density at the anode decreases until an area enhancing sheath is required even at very low I_a. This results in the elimination of region G, and so region D now expands to occupy the lower I_a regions.

Further reduction of $\dot{m}$ leads to a lower plasma density in the cathode, this in turn decreases ion bombardment and the cathode runs cooler (see figure 7.29 from reference [45] for cathode temperature dependence on $\dot{m}$). Thus, at a low enough $\dot{m}$ there is not enough emission to produce space-charge limitation on the cathode, even with the virtual anode present, and the cathode is emission-limited even at low I_a. Thus region E, the neutraliser mode, is essentially the same as region C and hence has the same visual appearance (figure 7.41) and due to the lack of space-charge limitation is relatively quiet. Region E is essentially the low I_a and low $\dot{m}$ branch of region C and must connect to it, which is indeed what figure 7.51 shows.

Song et al. [148] demonstrated that below certain values of pressure, an electrode cannot settle into the double layer state of electron collection. The discharge is unable to "lock on" to this state permanently and observed surges in the electrode current. This is illustrated in figure 7.52, with figure (a) showing the spatially resolved Langmuir probe measurements of plasma potential in front of a collector during the formation stage of a type (a) double layer for current collection, and figure (b) showing its subsequent destruction.

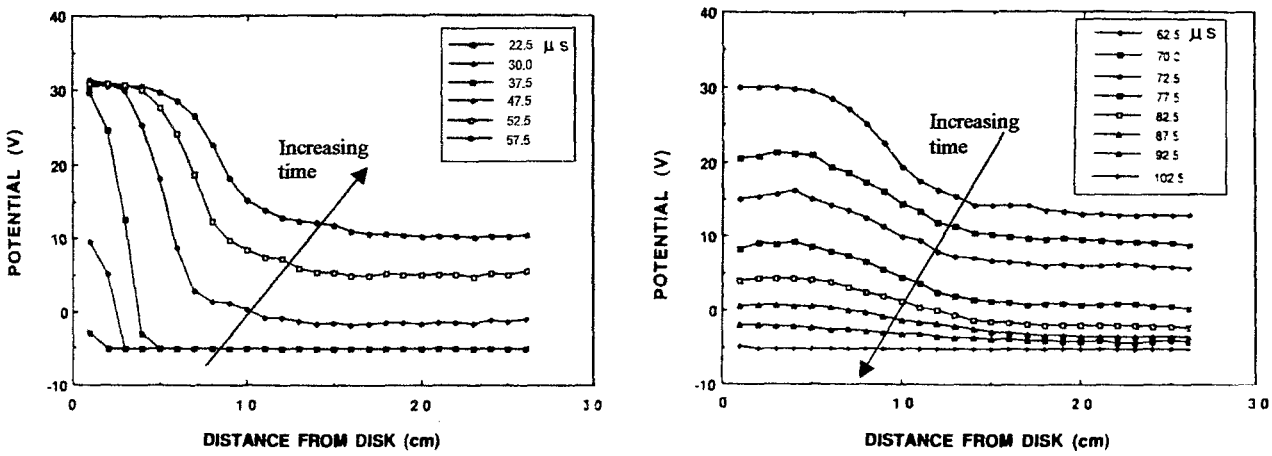

Figure 7.52: Time resolved plots of plasma potential in front of a current collecting disc at low pressure during **(a)** *formation of double layer and* **(b)** *destruction of double layer [148]*

The process of destruction of the double layer is related to the higher rate of ion loss from the potential peak of the double layer, due probably to the decreased ion-neutral collision rate at low pressure allowing a greater rate of ion escape than ion formation. The ions escaping upstream cause a potential rise in the ambient plasma, which lowers the potential difference across the double layer to less than the ionisation potential of the gas causing the double layer's subsequent collapse.

The above process is thought to occur in region F of a HC discharge. As $\dot{m}$ is very low in this region, the double layer is expected to be very close to the cathode, and to maintain it in such a position, the anode potential will need to be high to ensure sufficient ionisation downstream of the double layer in a relatively low density gas. Region F was shown [122] not to be able to maintain the discharge current even

though it was not operating at the maximum power supply voltage, which indeed fits the description given above for the destruction of the double layer structure due to the high ion escape rate in a low density gas. The formation and reformation cycle of the double layer will also account for the severe noise observed. As mentioned earlier in section 7.1.1., electrons such as these accelerated through high potentials have a low ionisation cross-section, and cannot dissipate much of their energy in ionisation, the extra energy is deposited at the anode, causing the significant anode heating observed by Fearn and Patterson [44]. The keeper, which usually collects current passively, receives a higher current than necessary from the double layer because of its proximity, and although it attempts to lower its potential to repel the electrons, it is unable to do so because of their high energy. Hence the keeper supply, in spite of being current regulated, will be forced to increase its current output. The ions escaping the double layer during its destruction phase form what could be termed "ion waves" streaming upstream towards the cathode. Because of the proximity of the double layer and their high energy, the streaming ions cause the anomalous cathode pressure increase observed in region F (figure 7.27).

Turning our attention to events at the keeper: The keeper voltage trace generally showed a decreasing trend with I_a (figures 7.37 – 7.40), which indicates that the keeper, due to its proximity to the cathode, always has sufficient current density at its vicinity to collect the required 1A current passively. When the anode current is increased, this causes an increase in the current density at the cathode and hence at the keeper location. The keeper then has to reduce its potential to repel the extra electrons and to collect only the 1A demanded, thus explaining the negative V_k - I_a trend. The oscillations on the keeper trace were found to correspond to those on the anode trace (figure 7.42), particularly in the regions with a negative voltage-current characteristic. In these, the keeper supply is simply reacting to the fluctuations in the keeper's plasma environment. For example, fluctuations in the flux and energy of ions bombarding the keeper surface originating from the virtual anode caused by rapid motion of the double layer. The most violent of these oscillations are observed when the double layer initially attempts to move upstream into the cathode-keeper space. This causes fluctuations in the current output of the current regulated supplies and is thought to correspond to the forbidden current region observed here and by Patterson and Fearn [123] with a battery supply. It is proposed that this is due to the presence of

the double layer in the immediate vicinity of the keeper, which disrupts the keeper current supply. The double layer can only exist upstream or downstream of the keeper location, with the forbidden current region being the condition corresponding to a double layer at the keeper location. This causes a coupling effect between the anode and keeper, with the keeper supply reacting by adjusting its potential to draw the 1A current required from it, and the desired anode current can not be drawn. This produces the observed violent fluctuations with a regulated power supply, or a jump in current with a battery supply.

Switching off the keeper would result in decreasing the current extracted from the cathode. This inevitably results in the reduction of the plasma density at the cathode and anode locations for a given anode current (see section 7.3 for dependence of electron density on discharge current). The expected outcome of switching off the keeper would hence be that the boundaries of the various regions shown in figure 7.51 would shift to higher currents, which is indeed the observed result [123].

7.4.4.3 Geometrical factors influencing discharge behaviour

Effect of electrode separation:

Siegfried [146], Philip [131], Csiky [28] and Rawlin [195] all reported that if the discharge was operating close to the transition point, plume to spot transition can take place spontaneously when the anode-cathode separation is reduced, with the opposite effect occurring if the process is reversed. This can be easily understood in terms of the expansion of the plasma from the cathode, where there exists a strong axial gradient in the plasma density. By physically moving the anode upstream, it is exposed to a region in space of a higher electron current density. If the discharge was operating close to the transition point, by moving the anode closer to the cathode, there comes a point when the available current density is sufficient to provide the desired current so that no area enhancing sheath arises, and the discharge makes a spontaneous transition to the spot mode.

Patterson and Fearn [123] reported, as illustrated by figure 7.31, that increasing the

cathode-keeper separation (d_k) resulted in shifting the boundaries of the discharge modes to higher currents. This was initially very puzzling, as the keeper separation was not expected to significantly influence conditions at the anode. It was then realised, however, that changes in d_k in the Patterson/Fearn experiments were effected by moving the cathode, which was mounted on a micro-manipulator (see figure 7.24). Thus, by decreasing d_k, they were effectively moving the cathode closer to the anode and hence causing mode change at lower I_a, with the opposite effect occurring when d_k was increased and the cathode was moved away from the anode. It has to be noted here that in these experiments the cathode was only moved a few millimetres (<4mm) with the anode being ~60mm from the cathode. However, if the discharge was operating close to the transition point, even small reductions in the cathode-anode spacing can lead to plume to spot transition due to the large axial gradient in plasma density. Therefore the experiments carried out by Patterson and Fearn on d_k are equivalent to those carried out earlier on the cathode-anode separation and have indeed yielded the same results, which have been shown here to be connected to the anode current collection mechanism.

Effect of cathode orifice diameter:

Enlarging the cathode orifice, at a given $\dot{m}$, causes a reduction of the neutral and plasma density inside the cathode. This decreases the ion bombardment heating of the surface and the cathode runs cooler, as shown in figure 7.29. Therefore, for a given current, increasing the orifice diameter reduces the electron current density at the anode, causing the boundaries of the discharge regions to move to higher currents. This effect was observed by Patterson & Fearn [40], Davies & Charlton [126] and Fearn, Singfield et al [51].

Effect of keeper configuration:

Using an enclosed keeper configuration would be expected to increase the neutral and plasma densities in the cathode-keeper space. With the enclosed keeper now acting as the effective orifice for expansion, the plasma density at the anode is expected to increase for the same flow rate and discharge current values. Thus, mode change is expected to occur at lower values of I_a, as demonstrated experimentally by Patterson and Fearn [123].

Effect of cathode orifice profile:

Similar phenomena to the ones described above for a current collecting electrode occur when an arc passes through a tube of variable diameter [26, 90]. If the tube profile undergoes a gradual decrease in cross-section in the direction of the anode, the random and drift (or arc) current densities will increase in unison, smoothly and in the same proportion, which leads to no discontinuities forming in the axial potential profile. If however a sudden decrease in tube cross-section, such as the one shown in figure 7.53 exists, and if, as reference [90] states, the product of the smaller cross-sectional area and the random current density in the larger section is less than the drift current in the small tube, then a potential difference must arise at the boundary of the two regions to enhance the ionisation in the smaller section and hence increasing the random current density in the small area tube. This potential difference is furnished by an electron accelerating double layer at the boundary, negative on the cathode facing side and positive on the anode facing side. Experimental investigations of discharge constrictions reported the formation of a clearly defined glow protruding from the smaller tube into the larger cross-section tube (see figure 7.53).

In one such investigation, Crawford and Freestone [26] formulated an expression for the potential difference between the two regions. With reference to figure 7.53, noting that the electron densities and temperatures in the smaller tube, region 2, will be higher than those in region one ($n_{e2} > n_{e1}$, $T_{e2} > T_{e1}$), and taking into account the drift current from region 1 (I_{s1}), the potential step (V_{dl}) at the double layer between the two regions can be found from:

$$V_{dl} = T_{e2} \ln\left(\frac{n_{e2}}{n_{e1}} \left(\frac{T_{e2}}{T_{e1}} \right)^{1/2} \frac{I_{s1}}{I_{s1} - I_D} \right) \qquad (7.20)$$

If the discharge current requirement is greater than the drift current at the entry of region 2 (i.e. $I_D > j_{s1}\left(\pi (d_2)^2\right)/4$), the current collection surface of the double layer is compelled to expand into the low density region.

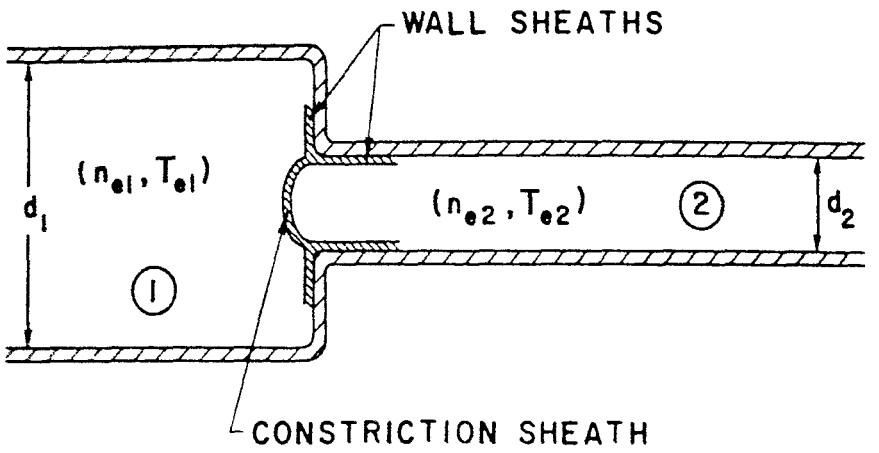

Figure 7.53: Illustration of double layer formed at boundaries of a discharge tube with variable cross-section [26]

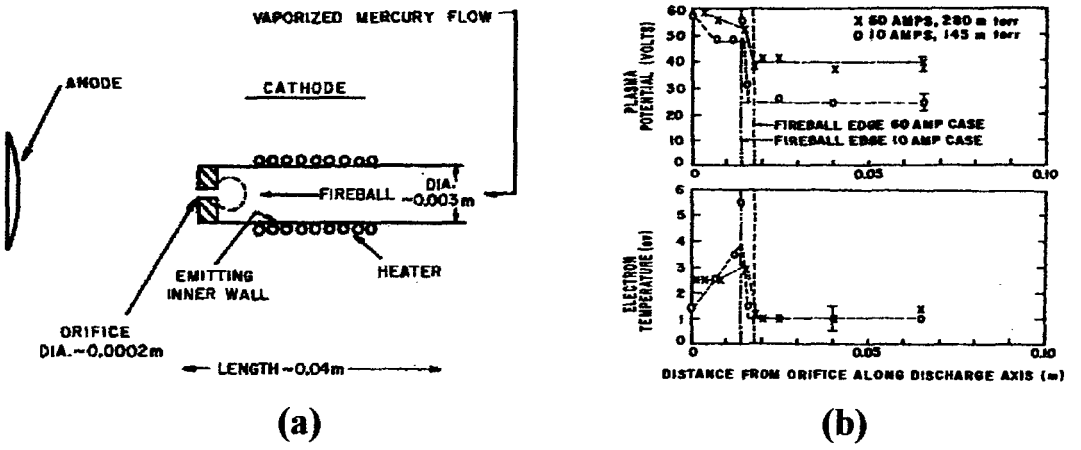

Figure 7.54: **(a)** *Schematic of HC with "fireball" indicated* **(b)** *Measured axial plasma potential and electron temperature profiles with "fireball" present [69]*

Jacobsen and Eubank [69], from measurements in similar devices, proposed the formation of a "fireball" upstream of the HC orifice as illustrated in figure 7.54(a). The results of their Langmuir probe measurements (figure 7.54(b)) indicated a step jump at the fireball edge and increase in T_e inside the fireball in comparison to the ambient plasma. Jacobsen and Eubank did not give any physical reason for the formation of the fireball, although they related the location of the fireball edge to the electron drift velocity exceeding the ion acoustic velocity. We can, however, conclude based on the preceding discussion, that what they observed was obviously a double layer formed due to the constriction in the discharge. Further corroboration comes from the observed effect of the fireball edge moving further upstream with increasing current (figure 7.55(b)), which is simply the double layer current collection surface expanding to collect the higher current, as described by Crawford and Freestone [26].

The formation of a double layer at the upstream edge of the orifice can provide explanation for several of the observed HC discharge characteristics. It can explain the visual observation of the exceedingly bright cathode spot, which is due to the electrons from the cathode interior gaining energy across the double layer. This is dissipated in inelastic collisions with neutrals in the orifice and heating of the secondary electrons resulting in the observed luminosity. When the ratio of the diameters of the two tube sections was large the discharge experienced more severe oscillations and increased plasma ball luminosity [26]. The absence of the sudden change in section and the associated double layer hence explains the benign operating characteristics of curved orifice hollow cathodes [46]. Qualifying the effect of changes of the orifice diameter to cathode internal diameter ratio on discharge noise is difficult, due to the concomitant impact of its variation on cathode internal pressure and the boundaries of the various discharge regions. There is, however, an impression that decreasing that ratio generally results in a reduction in the high frequency noise [196].

7.4.5 Full thruster configuration

We now examine the factors contributing to the suppression of the plume mode in the full thruster geometry:

a) Anode surface area: Gridded ion thrusters utilise cylindrical anodes, which are typically of much larger surface area than those employed in diode tests. For example, the cylindrical anode of the UK-25 thruster has a surface area over 11 times larger than the disc anode used in the present study. This increase in the physical collection surface allows for passive current collection even at the low values of current density expected at low $\dot{m}$ and I_a.

b) The baffle disc: The larger anode area is not in itself sufficient to suppress the plume mode operation because of the strong variation of plasma density with radial distance (figure B.5 in appendix B). Indeed, the first introduction of hollow cathodes resulted in comparatively poor and inefficient operation of the thrusters,

which previously utilised the more diffusely emitting thermionic emitters [33]. This was due to the peaked electron density radial profile and the uni-directional nature of the electron jet emanating from the cathode. The problem was eliminated by using a baffle disc positioned perpendicular to the downstream end of the inner pole piece. The baffle disc creates a more uniform discharge plasma and enhanced ionisation by the production of mono-energetic primary electrons. The potential difference between the coupling and discharge plasma regions determining the energy of these electrons results from the formation of a double layer at the baffle aperture region [112]. This process increases the current density at the anode and contributes to plume mode suppression

c) The magnetic field and main discharge flow: The axial, divergent magnetic field traps the primary electrons emanating from the coupling plasma in spiral paths along the field lines. The electrons travel back and forth along magnetic field lines due to reflection from the thruster sheath surfaces, increasing their path length and thus effectively increasing the probability of them achieving an ionising collision. The main discharge flow is introduced through the thruster backplate, with a typical ratio of cathode flow to main discharge flow of 3:7 in the UK-25 thruster. A primary electron spirals along the magnetic field lines until it participates in an ionising collision with a gas neutral. The thermalised primary and resulting secondary electron continue to spiral round the field lines and may take part in further ionising collisions until they diffuse across the field lines to the anode. The discharge chamber is the area where most of the ionisation takes place. The combination of magnetic field and main discharge flow hence causes ionisation in the anode *vicinity*, thus increasing the electron current density for a given discharge condition and also further inhibiting the plume mode in the thruster.

7.4.6 Implications of the theory

A theory has been proposed for the observed plume to spot transition in hollow cathode discharges. It relates the plume and spot modes and the transition between them to the current collection mechanism at the anode. This theory, applied self-

consistently, was shown to explain virtually all of the discharge behaviour observed in this work and others.

The major implication of this theory in the author's opinion is the recommendation made here for the abandonment of the diode configuration in its current form as a means of characterising hollow cathodes.

From the above theory, characterisation in diode configuration leads to several adverse effects:

- Diode tests result in a lack of reproducibility in comparing studies conducted by different investigators. To illustrate, Patterson and Fearn [45], using an identical cathode to the one used here, found for xenon that at a discharge current of 5A transition from plume to spot occurred at about 1.1mg/s (see figure 7.25). In the xenon part of this study, plume to spot transition was not possible at flow rates below 2.35mg/s, for the same anode and keeper currents. The required flow rate had more than doubled for, it has to be remembered, an identical cathode, both in diode configuration! This effect is due to their anode having nearly twice the surface area of ours, and the presence of the T5 discharge chamber, which increased the electron density at the anode in the Patterson/Fearn experiments. Thus any characterisation study, in diode configuration, is only valid under the strict geometrical arrangement in which it was conducted. This, however, is often overlooked, resulting in considerable confusion and irreproducibility even when using the same cathode, and makes comparison of different cathodes speculative.

- Any on-axis, spatially-averaged measurements of the HC plasma whether from upstream [101, 115] or downstream (the present study), will overestimate the plasma parameters during plume mode operation. Also, any spatially-resolved measurements, especially in the inter-keeper-anode space, will be affected by the presence of the virtual anode double layer creating a non-Maxwellian mono-energetic electron population. The character of these measurements will also depend on which region of the discharge they were obtained, for example, it is expected to be more difficult to conduct Langmuir probe measurements in regions B and D due to the elevated noise levels. Furthermore, the boundaries of these

regions are a function of the anode arrangement, which brings back the difficulty of comparing and reproducing such measurements in different arrangements without an exact knowledge of the discharge mode in which these measurements were taken and the relative position of the double layer.

- Conducting life-tests in diode configuration (except in the cases of neutraliser and Hall-thruster cathodes) will definitely not reflect conditions occurring in an operational thruster. Testing in the plume mode will result in severe sputter erosion and abnormal heating of the cathode, brought about by the formation and acceleration of high energy ions in the potential peak of the double layer.

- Any diode investigations of discharge noise will also suffer from the lack of fidelity to conditions in the thruster and from lack of reproducibility. The noise in the plume mode is partly due to the formation of the double layer and its interaction with the supplies.

- Finally and most fundamentally, the diode configuration was utilised as a simple, accessible means of characterising hollow cathodes. The plume mode of operation was, however, shown here to be a product of circumstances extraneous to the hollow cathode, with no bearing on its intrinsic behaviour. The complication of having to account for plume mode behaviour in any model or description of hollow cathodes has caused significant problems and confusion in the past. Thus, operating in diode configuration has in some ways hampered the complete understanding of the underlying physics of the hollow cathode.

Possible alternatives to the current disc anode, such as a low diameter to length ratio cylindrical anode, can be used if characterisation is required at low I_a or $\dot{m}$.

Another implication of the theory not related to mode change, is the possible beneficial consequences of using a smooth cathode orifice to thruster performance. This was demonstrated experimentally in a previous work [46], with this study giving the underlying physical reasoning behind this effect.

Chapter 8

CONCLUSIONS

The relatively limited body of work available makes the first objective of any study on HC physics the collection of as much empirical data as possible. A wide range of tests were thus conducted on a T6 HC using a variety of propellants, namely argon, krypton, xenon and a Kr/Xe mix in the naturally occurring ratio. The study utilised a variety of instrumentation and investigated both the discharge initiation and steady-state phases of operation. Consequently, some new insight has been gained into the underlying physics of HC operation. This chapter summarises the main conclusions drawn from the present work.

8.1 The HC breakdown characteristics

A systematic study of the breakdown characteristics of four propellants has been conducted. A study of such a scope has not been previously attempted, and is unique in the literature. The observed values of breakdown voltages were generally very low. Breakdown was assured for all the gases at potentials below 50V, even at 0.2mg/s flow rate and 929°C tip temperature. This was primarily due to the joint effect of the presence of low work function material and of the heating of the HC, leading to nearly an order of magnitude increase in Townsend's second coefficient. The breakdown voltages were found to scale with the first ionisation potential of the gas, being consistently lowest for xenon and highest for argon under a given set of cathode conditions.

The dependence of breakdown voltage on two of the key determining cathode operating parameters ($\dot{m}$ and T) was investigated. Breakdown behaviour with

propellant flow rate was found to show, as previously seen in the open keeper T6 with Xe [124], a severe departure from the classical Paschen behaviour for all the gases employed, exhibiting a double minimum instead of the expected one. This anomalous behaviour was shown here to be a manifestation of Penning ionisation taking place in the HC.

The Penning effect, which has not been previously associated with HC behaviour, occurs for gas mixtures satisfying the condition that the ionisation potential of the admixed gas is lower than the energy of the metastable levels of the main constituent gas. The metastable atoms then cause Penning ionisation of the admixed gas, which can result in orders of magnitude rise in the ionisation efficiency for a given imposed field. The process is highly efficient, as it effectively eliminates the electron energy loss to excitation, and the high probability of the event makes the effect of even minute concentrations of the admixture (as low as 10^{-4}%) appreciable. Barium, evaporating from the activated insert, was identified as the trace element in the gas, which does indeed satisfy the prime requisite for Penning ionisation to occur with its ionisation potential being lower than the energy of the metastables in all the inert gases. The barium evaporation rate from inserts of the same type as used in this work has been studied extensively [15, 27]. The evaporation rate is a strong function of the insert temperature, and is estimated to increase by several orders of magnitude when tip temperature is increased from 929°C to 1299°C. Barium was shown conclusively to exist in the HC discharge by the detection of BaII emission lines in the emission spectra and the discovery of traces of barium in the deposit found on the anode. The metastable concentration was estimated to be roughly comparable to the concentration of positive ions in the HC discharge. Consequently, the HC seems to have all the requirements for Penning ionisation to occur. The breakdown behaviour of the Penning mixture will thus exhibit two minima. The first, at low ($P \times d$), corresponds to that due to direct ionisation of the inert gas, while the second is formed by the enhanced electron production due to the Penning ionisation of the barium atoms by the metastables.

Broadly speaking, the results for tip temperature show that it has little influence on breakdown above 1100°C. When reduced below that value there is a dramatic increase

in breakdown potential. The breakdown behaviour for all the gases was found to be, contrary to previous experience with Hg [48], essentially completely reproducible over the entire range investigated. The spread in result was found to be a function of the cathode temperature, increasing when the temperature is lowered.

A comprehensive analysis of the breakdown statistics in HC's addressed the issue of reproducibility. The probability of a successful breakdown and the time to achieve it are functions of the rate of electron production, the gas pressure and the applied overvoltage. Increasing the HC temperature causes a higher thermionic electron production rate, hence increasing the probability of finding a significant number of initiatory electrons and reducing the probability of an interrupted avalanche for a given overvoltage. Increasing the HC temperature thus reduces the spread in results as observed experimentally. Raising the HC flow rate, at a given temperature, ensures a greater probability of a non-arrested avalanche by increasing the electron-neutral collision frequency, subsequently also leading to more reproducible results. 3-D computer simulations [25] have shown much greater levels of electric field penetration in the T6 when compared to the T4 cathodes used in the early Hg work. This was owing to the larger orifice diameter and the bevelled cathode tip. The higher field penetration and orifice size increased the probability of finding initiatory electrons at the right location for acceleration by the field and, subsequently, directly resulted in the more reproducible breakdown results in the newer cathode.

To complete the breakdown investigation, an unprecedented photomultiplier tube study of the breakdown plasma was also conducted. The PMT study exposed the temporal behaviour of the keeper voltage and the breakdown plasma emission, and their variation with changes in T and $\dot{m}$. It's most significant result is that the transitory period between the keeper voltage collapse and the establishment of a stand-by discharge can be divided into two parts: an initial phase characterised by a rapid and noisy drop in V_k, followed by a linear, quiescent increase (recovery) in V_k till voltage levels for a stand-by discharge are attained. Reaching a stand-by discharge takes a period of the order of 1ms, with the duration of the noisy period and the total time to stand-by discharge being inversely proportional to the gas flow rate and cathode tip temperature.

8.2 Characterisation of the steady-state HC discharge

The study of the HC discharge in steady state, although hampered by limitations on the discharge current drawn, covered a wide range of flow rates employing the three inert gases and the Kr/Xe mixture.

Both the plume and spot modes of operation were observed in the diode tests with all the various propellant discharges. The value of flow rate at which transition between the two modes occurs was found to be species dependent; increasing with the first ionisation potential of the gas. In the spot mode, the discharge had a negative voltage-current characteristic, indicating a fall in plasma impedance with discharge current. The keeper voltage generally showed a negative V_k - I_a characteristic regardless of discharge mode, and was largely insensitive to changes in flow rate. Notwithstanding the differences in the flow rates required to achieve it, the discharge voltages in the spot mode for the alternative gases were only a maximum of 2.3V higher than those for xenon.

The dependence of emission line intensity on discharge conditions was investigated for argon, krypton and xenon. In the spot mode, the first ionisation lines showed an instantaneous increase in intensity with discharge current. The increase in the first ionisation line intensity, which represents the degree of ionisation, was demonstrated to be a quadratic function of discharge power. On the other hand, the first ionisation line intensity decreases with increasing $\dot{m}$ for a discharge in the spot mode. This was ascribed to the decrease in electron mean free path and energy with increasing neutral density.

8.3 The HC discharge plasma parameter estimation, modelling and theory of operation in the plume and spot modes

As demonstrated by an earlier study on xenon [115], the HC internal plasma cannot be described by either the LTE or corona equilibrium models, and is best described by a Collisional-Radiative model. This was established here to be also the case with

discharges in krypton and argon. Full emission spectra were obtained for several flow rates at a fixed discharge current of 5A with argon, krypton and xenon. This enabled the estimation of plasma parameters in both the spot and plume modes. Several methods were considered to that end. The LTE Boltzmann plot method was shown to be applicable to plasmas in the C-R regime. The method was used, with great success, in estimating the electron temperature. Providing a good estimate of the plasma density was, however, more difficult. The simple C-R model used was found to be inadequate for the range of T_e and n_e of interest, estimating n_e to within six orders of magnitude. The electron density was eventually evaluated using an LTE model, which was assessed to overestimate the density by roughly an order of magnitude.

The electron temperature (integrated over the line of sight) in the spot mode was calculated to be 0.98±0.20eV for Xe, 1.28±0.13eV for Kr and 1.32±0.05eV for Ar, i.e. increasing with the first ionisation potential of the gas. The result for xenon compares well with previous measurements of around 1.1eV using a different cathode [101, 115]. The corresponding values for electron density were $6.99\times10^{15}cm^{-3}$, $1.35\times10^{16}cm^{-3}$ and $7.3\times10^{15}cm^{-3}$ for xenon, krypton and argon respectively. Estimates of the HC internal plasma parameters in the plume mode were found to be distorted by the presence of a double layer, causing the formation of a second plasma in the intervening space between the optical fibre and the HC tip.

The enormous benefits of possessing knowledge of the plasma conditions in the HC were also illustrated. Modifications were made to the Siegfried-Wilbur model and the spot mode plasma parameter estimates for xenon were inserted to predict the cathode operating conditions. The model's predictions of $2.55\times10^{5}A/m^{2}$ for the insert emission current density, a 36% contribution from volume ionisation to the total discharge current, a plasma potential of 8.95V and an insert surface work function of 2.17eV at the cathode operating condition of 5A and 3.29mg/s, were all in excellent agreement with experimental observations and estimates of these parameters found in the literature. The model's predictions were extended, via simple experimentally derived assumptions, to the full range of discharge currents. The resulting values for cathode operating temperature were in excellent agreement with empirical measurements on the T6 [44]. The success of this model, which assumes field-

enhanced thermionic emission as the sole mechanism for insert electron emission, gives strong support to the theory that this emission mechanism predominates in the HC under normal operating conditions.

Observations from the various experimental investigations were brought together leading to a new theory of HC operation in the plume and spot modes. The theory relates the plume and spot modes and transition between them to the current collection mechanism at the anode. The plume mode occurs when the anode physical area is insufficient for collecting the required current. The power supply current demand causes an increase in anode potential until the anode sheath breaks down, forming a virtual anode of greater surface area, whose edge now forms the current collecting area. Increasing the current density at the anode, by increasing $\dot{m}$ or I_a, ultimately removes the requirement for the enhanced current collection. The voltage then experiences a discontinuous drop, the anode is now collecting current passively and the discharge has completed transition to the spot mode.

This theory, applied self-consistently, was shown to explain virtually all of the observed discharge behaviour, in this work and elsewhere, including:

- The visual character of the discharge and its variation with cathode operating parameters
- The dependence of the mode transition on both $\dot{m}$ and I_a.
- The fine structure observed for the plume mode, including the noise and oscillatory regions in the discharge and the regions with a negative V-I_a characteristic.
- The formation of the high energy ions in the plume mode and the associated elevated electrode sputter erosion rates.
- The Langmuir probe profiles downstream of the cathode.
- The spectroscopic observations in the two modes.
- The dependence of the transition on keeper configuration and current.
- The discharge and transition dependence on geometrical factors such as electrode separation, cathode orifice diameter and profile.
- The suppression of the plume mode in the full thruster geometry.

8.4 Novelty and applicability of the work

A wide ranging study has been conducted, which is geared towards gaining a deeper physical insight into the poorly understood HC region of an ion thruster. Due to the range of applications for these devices, from primary electron source in a variety of thruster configurations to spacecraft space charge control, the results of this work have wide ranging applicability. Some of the areas where the results of the work hold significance to thruster design are here summarised.

Since alternative lighter propellants seem to be required to enable deep space missions, this study has aimed to characterise HC discharges operating on some of these gases. Although the discharge efficiency is expected to decrease, the diode tests with argon and krypton have demonstrated that operation with these gases is feasible with slight increases in the operating potentials. However, tests in full thruster geometry and with beam extraction are required if any direct comparison or performance assessment is to be made. The impact of the lighter propellants on thruster durability, through sputter erosion of thruster components, will also need to be qualified.

The Kr/Xe mix offers significant cost savings with minimal reduction in HC performance. Its use in a full thruster is however complicated by the difficulty of matching the ion optics to two atomic species. Nevertheless, this does not preclude its use in plasma contactors, in HC micro-thrusters and in ground test characterisation of hollow cathodes.

The breakdown study has certainly provided some insight into the processes taking place in this transient phase of HC operation. One important corollary is that judicious cathode tip design, coupled with reliable heater technology, can eliminate the need for the keeper high voltage supply. This would result in a reduction of thruster mass and complexity.

Acquiring measurements of the HC plasma temperature and density is of profound importance to the understanding of its basic physics. Using these results, a simple

phenomenological model was capable of good, useful predictions of cathode operating parameters, which can be used by designers for cathode scaling and lifetime optimisation.

The novel features of this work are summarised next:

Discharge initiation studies

- The systematic study of breakdown dependence on cathode parameters for four different gases is unique in the literature. Moreover no prior investigation exists for HC breakdown dependence on argon, krypton or a Kr/Xe mix.
- The PMT investigation of the temporal behaviour of HC breakdown is unprecedented.
- To explain the anomalous breakdown dependence on cathode flow rate, the Penning effect was invoked for the first time to explain HC behaviour. This also constituted the first observation in the literature of Penning ionisation of barium.

HC steady state investigations

- Characterisation of discharge behaviour of four different propellants is new to the T6 cathode, noting that no prior characterisation exercise was carried out on a Kr/Xe mix discharge.
- This work also included the first spectroscopic investigation of an ion thruster HC discharges in argon and krypton. It is also the first such measurements to be carried out in the T6 even for xenon.
- The development of a simple model for the HC discharge, largely based on the Siegfried-Wilbur model for mercury, which was implemented successfully.
- A considerable achievement of this work is the development of a qualitative theoretical explanation for the HC modes of operation, which was demonstrated to explain practically all the observations in the extensive literature.

The instrumented T6 HC and the sapphire optical fibre probes

This development work, which occupied the initial period of this PhD and is described in Appendix A, forms a significant feature of this work. The instrumented

HC/optical probe assembly gives unprecedented access to the HC cavity for spatially resolved plasma parameter evaluation in both the steady-state and during the transient breakdown phase. The sapphire optical fibre probes in particular constitutes a new type of non-intrusive diagnostic for in-situ evaluation of plasma properties in high temperature environment, which can thus be used in other research areas such as combustion research. This is now the subject of another study and is currently showing promising results.

8.5 Recommendations for future work

The present study has tackled a number of issues pertaining to the HC region of an ion thruster. The empirical data set produced is a notable addition to a field which has not received much attention, and where such measurements are sparse. Some of the issues have been investigated successfully. However, some questions still remain and new ones have been posed. Here, a few recommendations are presented for research projects that can help to further our understanding of this region. Some of these recommended studies are already being pursued.

- Carrying out experimental investigations using the instrumented T6/optical probe assembly to attain spatially-resolved plasma parameter profiles in both the steady-state and discharge initiation phases. This investigation should also include measurements of the insert temperature profile, which is critical to cathode life time, and its variation with discharge conditions.

- Development of a model of the HC breakdown, which can elucidate the mechanisms of formation and growth of the plasma. The model's predictions should then be verifiable by comparison with experimental observations.

- Thrust measurement of HC micro-thrusters, particularly during plume mode operation, where the virtual anode double layer is predicted here to lead to the production of high energy ions and probably higher thrust. This study should be

complemented by full Langmuir probe mapping of the inter-electrode space to determine the properties of the double layer and by measurements of the ion energy using a retarding ion probe.

- Full comparative assessment of the performance of alternative propellants, in full thruster configuration, including life testing of thrusters operating on these propellants.

- The development of a more rigorous Collisional-Radiative model of the HC plasma, taking into account the excited states, particularly the metastable levels of the atomic species, and producing population rate equations and detailed level kinetics. If possible, the model should also attempt to take into account the presence of impurity species and their effect on equilibrium. This model should result in better estimates of the plasma electron densities.

- Performing Optogalvanic Effect spectroscopy on the HC plasma, possibly using the instrumented cathode, to determine the role of metastable atoms in a HC discharge.

APPENDIX A

THE INSTRUMENTED T6 HOLLOW CATHODE

This appendix deals with the work that occupied the first two and a half years of this PhD. The work had several novel features and potential for giving new insight into the HC phenomena. Disappointingly, it was dogged by incessant delays on the part of the manufacturers. In spite of the completion of the design, manufacture and procurement phases of all but one of its components, this necessitated its abandonment at a late stage in favour of the work presented in the main body of this thesis. The work included here has become the subject of another PhD, and is currently demonstrating in practice the considerable promise it was envisaged to have at the outset.

The stated aim of the project was to achieve, through empirical study, a deeper understanding of the physical processes occurring in the HC. The starting point was the definition of an experimental project compatible with this aim, which included the selection of a subject cathode for study, the design of suitable diagnostic probes, the design of the experimental set-up and procurement of the experimental hardware required to conduct a study of the HC behaviour in both steady state and during discharge initiation.

From a review of the few studies conducted on the HC plasma (refer to chapter 2), it was clear from the outset that the nature of the method employed to diagnose the plasma had to be non-intrusive. This precluded Langmuir probing, which has been shown to induce significant plasma perturbation, and directed the study towards spectroscopic methods.

A.1 The modified T6 hollow cathode

Siegfried [146] has shown, through Langmuir probe measurements, that most of the ionisation takes place near or at the cathode orifice, and that appreciable gradients, especially in electron density, are observed with distance from the orifice. This spatial dependence of plasma parameters and the fact that the plasma only penetrates a short distance into the cathode (~2mm), has made the provision for spatial resolution in the plasma measurements highly desirable. However, the very limited physical size of the cavity makes such measurements very difficult, and the results of the earlier spectroscopic studies were only an average over the entire length of the cathode [101, 115]. This necessitated a cathode of modified design for this study, which is capable of providing spatially resolved optical access to its interior. Consequently, this also put a simultaneous requirement for minimising the size of these probes so as to decrease the impact of providing probe access on the operating characteristics of the HC. In this way, the characteristics of a cathode with probe access will not be substantially different from a cathode without.

Preliminary consideration of the required cathode design, and extensive consultations with DERA (now QinetiQ), has resulted in the decision that DERA, with their long experience in development of HC's for space applications, should undertake the manufacture of the HC in a collaborative effort with the University of Southampton. After discussions, it was decided that the cathode would be largely based on their highly successful T6 cathode. Figure A.1 illustrates the final design

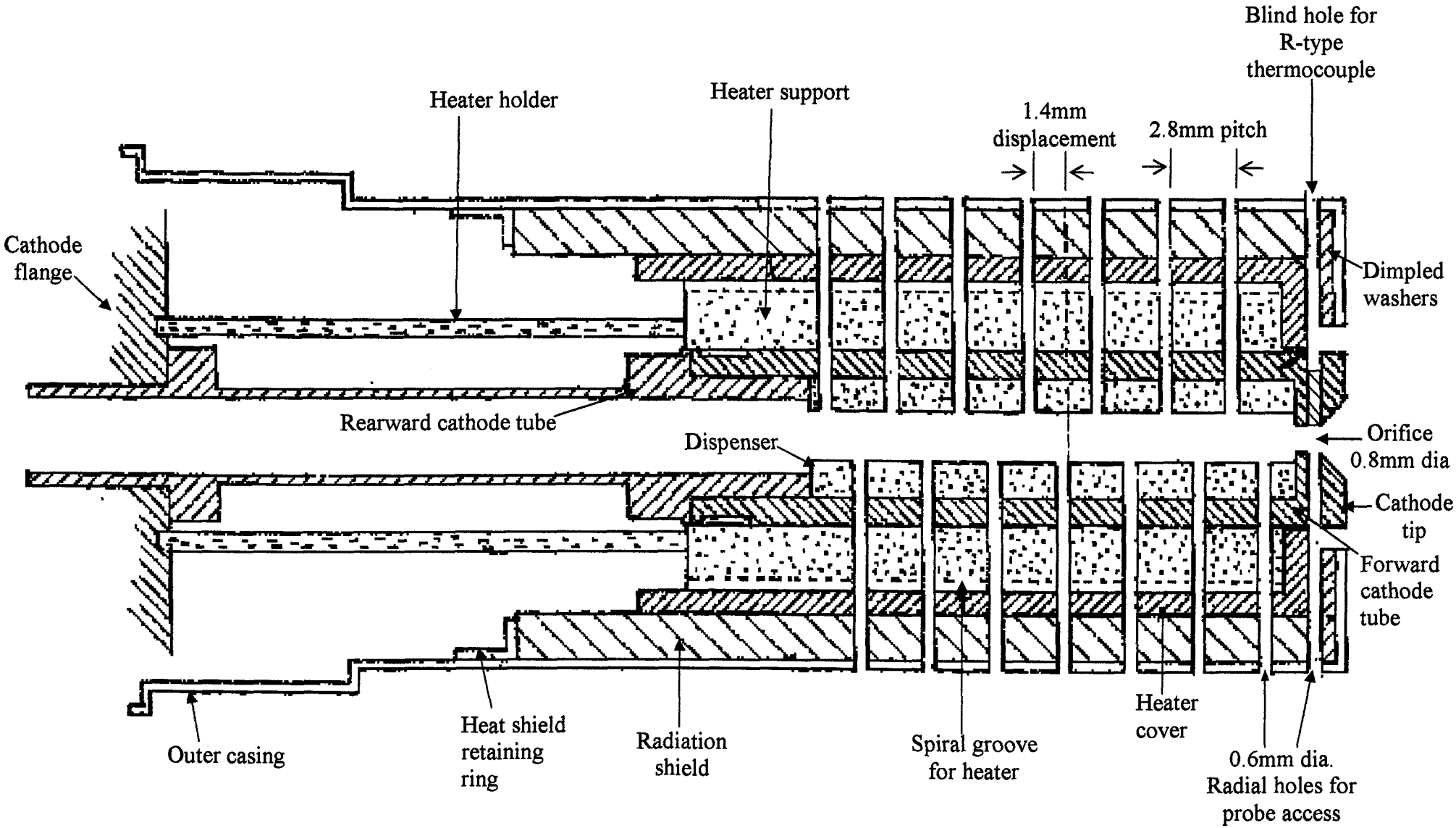

Figure A.1 Schematic of T6 hollow cathode for probe access [196]

The proposed cathode was essentially a standard T6 hollow cathode with few modifications. Only the major ones are mentioned here:

1. T6 cathodes usually have two heater wires, one primary and the other redundant. The requirements of this project necessitated the removal of the redundant heater winding to allow probe access.

2. Drilling of 0.6mm diameter radial holes from the opposite sides of a diameter through the cathode. They are spaced axially to coincide with the gaps left by the redundant heater, avoiding the primary heater winding. This dictates a pitch of 2.8mm and a stagger between opposing holes of 1.4mm. The configuration has the added benefit of maximising the spatial resolution available.

3. One of the two holes at the cathode tip will be a blind hole, to allow the attachment of an R-type thermocouple for tip temperature measurement.

Having a cathode based on a well tested design had several advantages: i) If the manufacturing was completed (with the only significant concern being drilling through the porous tungsten insert matrix) then it is highly probable that the instrumented cathode will operate successfully. ii) Assessing the impact of the probe access holes will be a relatively straightforward exercise, through simply comparing the instrumented cathode's operating characteristics with the readily available data on the T6.

The design of this cathode was finalised with DERA (QinetiQ) in October of 1999, with the agreement that DERA would undertake the manufacturing of this cathode.

A.2 Development of the sapphire fibre optic probe

An optical fibre waveguide system formed the ideal means to guide the light emission from the cathode interior plasma to a given detector. The high temperatures expected at the cathode insert and tip surfaces, however, precluded the use of the common

quartz or silica core fibres, which devitrify at around 1100°C. A more exotic and temperature resistant type of fibre had to be sought for.

After an exhaustive search, a company called Saphikon® was found which manufactures a novel type of optical fibre with a sapphire core. The optical fibre core has a maximum operating temperature of over 2000°C, which satisfies our high temperature requirement. However, there were several issues to be addressed. The fibres have not been used in vacuum before, and they were usually used for delivery of surgical lasers and have never been used as a sensor before, except for in-situ pyrometry in high temperature environment. Both these applications limited its use to the IR region. As a result, the manufacturer had no transmission data below 500nm, as shown in figure A1.2.

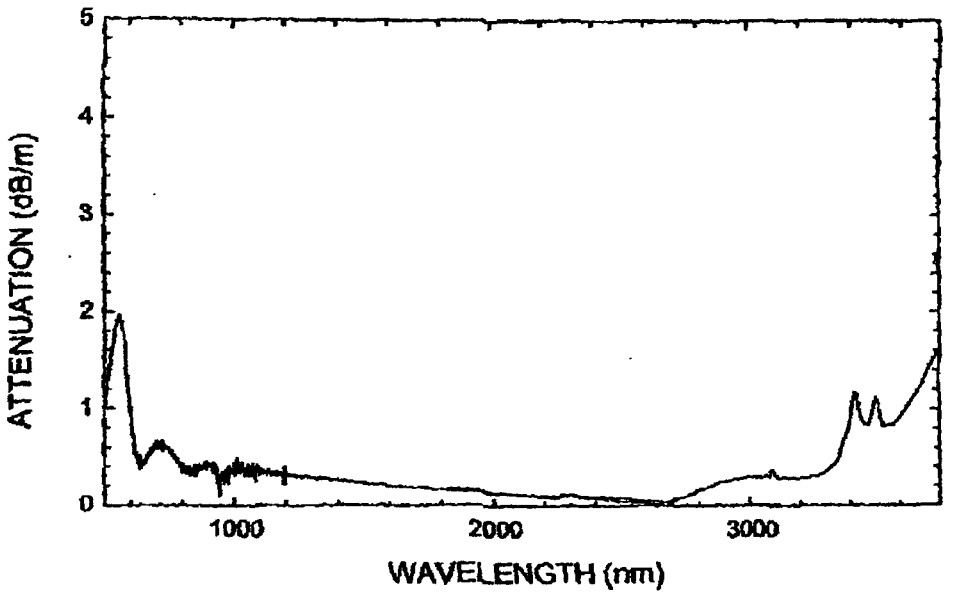

Figure A.2: Manufacturer's transmission plot for VIS-IR grade sapphire optical fibre

Sapphire, as a material, has good transmission properties from near UV to mid IR. Characterisation tests with samples of the sapphire fibre carried out here in the Astronautics Research Group using the Hg(Ar) calibration lamp (see section 5.3.5.1), indicated good transmission down to 300nm, which demonstrated possible use for spectroscopy in the VIS region.

It was important to minimise the size of the optical fibre probe to mitigate any impact its presence might have on the normal operation of the HC. Thus, it was decided to use a 0.15mm diameter VIS-IR grade sapphire fibre to make the probes. In order to prevent the sapphire fibre from blocking the working section of the hollow cathode and to protect the fibre from debris and damage, a metallic protective sheath was designed to surround the fibre core. The protective sheath consists basically of two welded metal tubes, which naturally divide it into two parts: the high-temperature region, and the low-temperature region. The high-temperature region is made of a tantalum tube with an outer diameter of 0.51mm and an internal diameter of 0.21mm and is 50mm long. The low-temperature section, to allow the probe to be bendable, is made of a stainless steel tube with an outer diameter of 1.1mm and an internal diameter of 0.685mm and is 500mm long (see figure A.3).

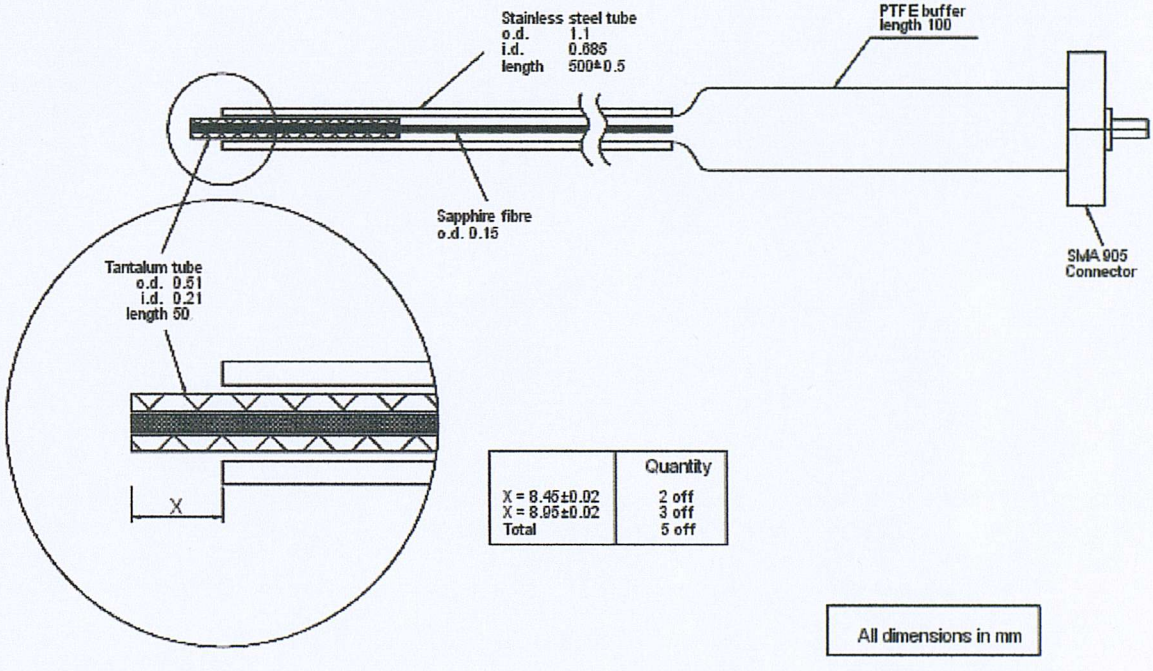

Figure A.3: Schematic of the sapphire fibre optic probe

The high temperature section penetrates into the hollow cathode body and operates at temperatures higher than the softening point of stainless steel. The stainless steel sheath outer diameter is larger than the hole for probe access in the cathode body (0.6mm) so that it acts as a locator for the probe and prevents it from contacting the internal plasma. Figure A.3 shows the complete sapphire fibre probe. Two different lengths were used for the high-temperature section since, as can be seen with

reference to figure A.1, the probes penetrating into the cathode orifice will need to be longer than those used for the insert region.

At the end of the stainless steel pipe a PTFE buffer coats the optical fibre core which is then surrounded by a PEEK jacket. These can withstand much lower temperatures (< 260°C). The PEEK jacket is epoxied to the stainless section using Torr Seal. The probe terminates in an SMA-905 connector, used to connect the probe to an FC-VFT-UV200 vacuum feedthrough, which in turn transmits the light to the exterior of the vacuum chamber. Care was taken to ensure that all the components of the sapphire probe were vacuum compatible. Figure A.4 is a photograph of the completed probe and table A.1 summarise the sapphire fibre's technical data.

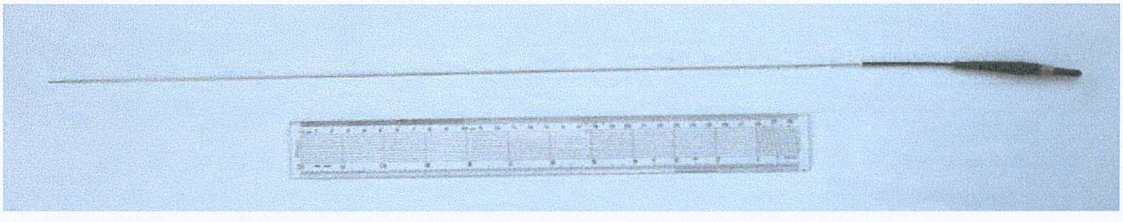

Figure A.4: Photograph of sapphire optical fibre probe

Core diameter	0.15mm
Usable transmission range	300 nm - mid IR
Minimum bend radius	20mm
Effective Numerical Aperture (NA)	0.12
Maximum operating temperature	2053°C

Table A.1: Technical specifications for the sapphire optical fibre

As with every new device, to arrive at the final design shown above, involved numerous tradeoffs and the manufacture of the probe was fraught with many technical difficulties, which required some innovative solutions to overcome them. In this limited space, the author does not wish to include an exhaustive list. However, the two most significant and noteworthy are here described:

- Following an exhaustive search, only one manufacturer was able to supply the tantalum high temperature tube, due to the small dimensions and tolerances required. However, the tube bore was not clean and was observed to have irregularities and burrs. Samples of the sapphire fibre could not be inserted through the tube, and some attempts resulted in breaking the fibre. Despite the manufacturer's best efforts, this problem could not be overcome. Contact with companies offering deburring services did not offer any solution due to either the metal type or the small tube size. An innovative solution was eventually found for cleaning the tubes which involved the following steps:

1. A 0.1mm diameter tungsten wire is dipped in lubricant and generous amounts of the lubricant is also applied to the Ta tube interior using a syringe. The W wire is then forced into and out of the Ta tube at least 20 times. Every two times the wire end is snipped and passed through metallographic grinding paper. This is done to avoid fraying the W wire end which would result in the wire getting stuck inside the tube. Lubricant is then reapplied and the procedure is repeated.
2. A weak emulsion, containing lubricant and a diamond abrasive putty is then made. The diamond putty contains small diamonds in a suspension and is usually used to polish metallic surfaces. The W wire is then dipped in the emulsion, which is also applied to the Ta tube interior using the syringe. The wire is again inserted into and out of the tube 20 times, interrupted by snipping and cleaning the W tip and reapplying the coating every two times.
3. The tube is then removed and put in an ultrasound bath to clean its interior from debris.
4. The wire is then dipped into the full strength diamond abrasive putty and inserted in and out of the Ta tube 20 times observing the above precautions. In the final stages of this step in the process, the amount of putty used is increased by applying it to the end of the Ta tube. At the end of the process the tube is put in an ultrasound bath.
5. Steps 1 through to 4 are then repeated using 0.15mm and 0.175mm diameter W wire. At the end the tube is removed and cleaned using methanol and in an ultrasound bath.

The above procedure, although time consuming (it took the author over 10days to clean all the Ta tubes), produced an extremely smooth bore and was finally tested by inserting samples of the sapphire fibre.

- Owing to the small dimensions of the tantalum and stainless steel tubes, laser welding was found to be the only means capable of welding the two tubes. This involves focusing a high-power laser at the intersection of the two metals which melts the metals and creates the bond without significant risk of deforming the tubes. Almost all the companies contacted felt that it cannot be done due to the two dissimilar metals (whether or not a metallurgical bond can be formed) and the gap between them. Only one felt confident in undertaking the task. However, they did not possess the necessary equipment to locate the two tubes to the high tolerances required. The high tolerances were required in the axial direction to prevent the high temperature section from protruding into the plasma and suffering excessive damage, which would result in a significant reduction in the fibre's transmission capability. It was also a requirement that the centrelines of the two tubes should coincide, so that the distance between them is ~87μm, thus making the laser weld feasible. A special jigging assembly was designed and manufactured here in the department to fulfil the above requirements and to facilitate the welding.

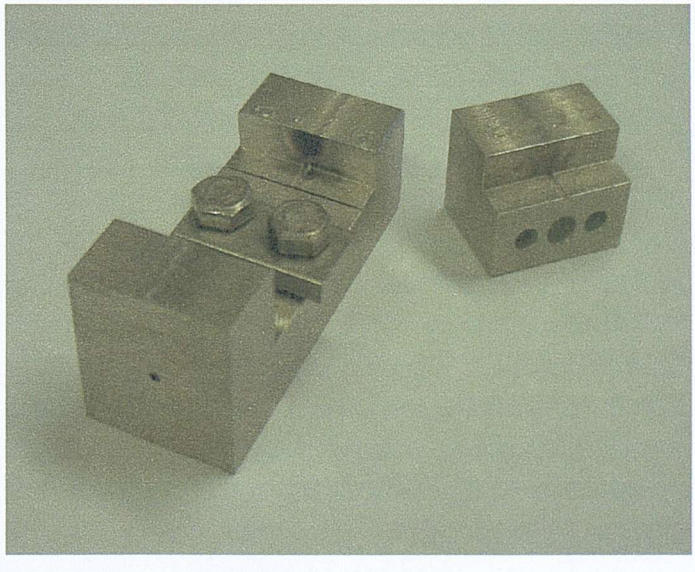

Figure A.5: Manufactured jigging assembly for laser welding of optical probe metal sheath.

A photograph of the completed assembly is shown in figure A.5. It consists of two parts, a clamp section and an end cap section. The clamp section is intended to hold the stainless steel part of the metal sheath. It is made by drilling through a block of mild steel. A hypodermic needle with an i.d. matching the o.d. of the stainless tube is then inserted and glued in place. A portion of the block is then slowly ground down to the centreline. The end cap section is made in a similar fashion. The block is, however, not drilled through: it is drilled to a depth greater than that required for the tantalum tube protrusion. The depth is then measured and the length of the block is ground to the required Ta tube length. Two interchangeable end caps were manufactured, for making different optical probe lengths for the insert and tip regions. The clamp section had provision for holding the tubes in place while the welding was taking place.

The two tubes were welded using four spot welds around the circumference. This was done to minimise thermal transmission to the stainless steel tube and the low melting point components down the length of the optical fibre probe. The laser weld was successful and the resulting metal sheaths were then sent to Saphikon® for integration into the completed sapphire fibre optic probes.

A.3 Experimental arrangements

The aim of the experiments and the design of the cathode/optical probe assembly was twofold: First, to achieve a spatially resolved measurement of plasma properties in the steady state using spectroscopic means. Second, to not only achieve a better understanding of the starting phenomena by studies of breakdown dependence on cathode parameters, but also to achieve a spatially, temporally as well as spectrally resolved picture of the formation of the breakdown plasma. In particular, understanding the mechanisms by which the plasma penetrates into the hollow cathode cavity under an opposing neutral flow.

Figure A.6 shows the experimental arrangement envisaged for the discharge initiation experiments in the modified T6 hollow cathode. Tip temperature is measured using an

R-type thermocouple inserted into a blind hole in the hollow cathode tip (see figure A.1). A PC equipped with an A/D converter is used to read the calibrated tip temperature. Three fibres are inserted into any of the sixteen available access holes depending on the region in the cathode under scrutiny. Two of the fibres are connected directly to a PMT with no spectral resolution, hence observing the broadband emission. To achieve spectral resolution, light from one optical fibre probe is coupled to a TJA MonoSpec18 monochromator with a PMT at the output slit. The signals from the PMTs are acquired, digitised and stored by a fast digitising oscilloscope.

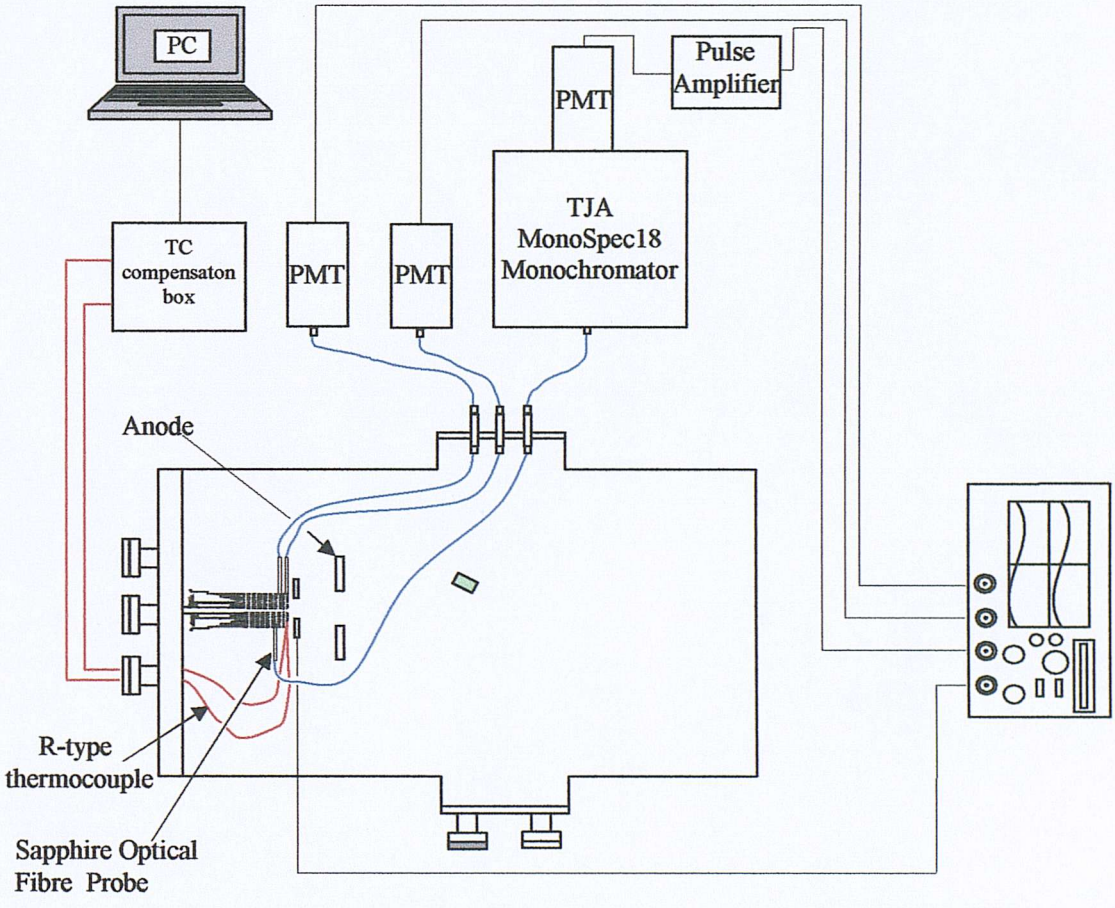

Figure A.6: Proposed experimental arrangement for spatially resolved discharge initiation experiments

At a specified mass flow rate and tip temperature, the keeper voltage is gradually increased until breakdown of the gas is achieved. Acquisition of the PMT signals is triggered by the first negative slope on the keeper voltage trace. The broadband PMT signals are used to establish the speed and extent of plasma establishment in the

hollow cathode cavity. The reproducibility of the discharge initiation in the T6 (see sections 2.2.5.2 and 6.2) allows an incremental picture of the process to be pieced together by repeating the experiment at the same tip temperature and mass flow rate. Thus by repeating the experiment under the same conditions, a single emission line can be tracked through the cathode interior (by coupling the monochromator to sapphire fibres at different locations) or different emission lines can be observed at the same location. A combination of the two creates a complete picture of the breakdown plasma, with spectral, spatial and temporal resolution.

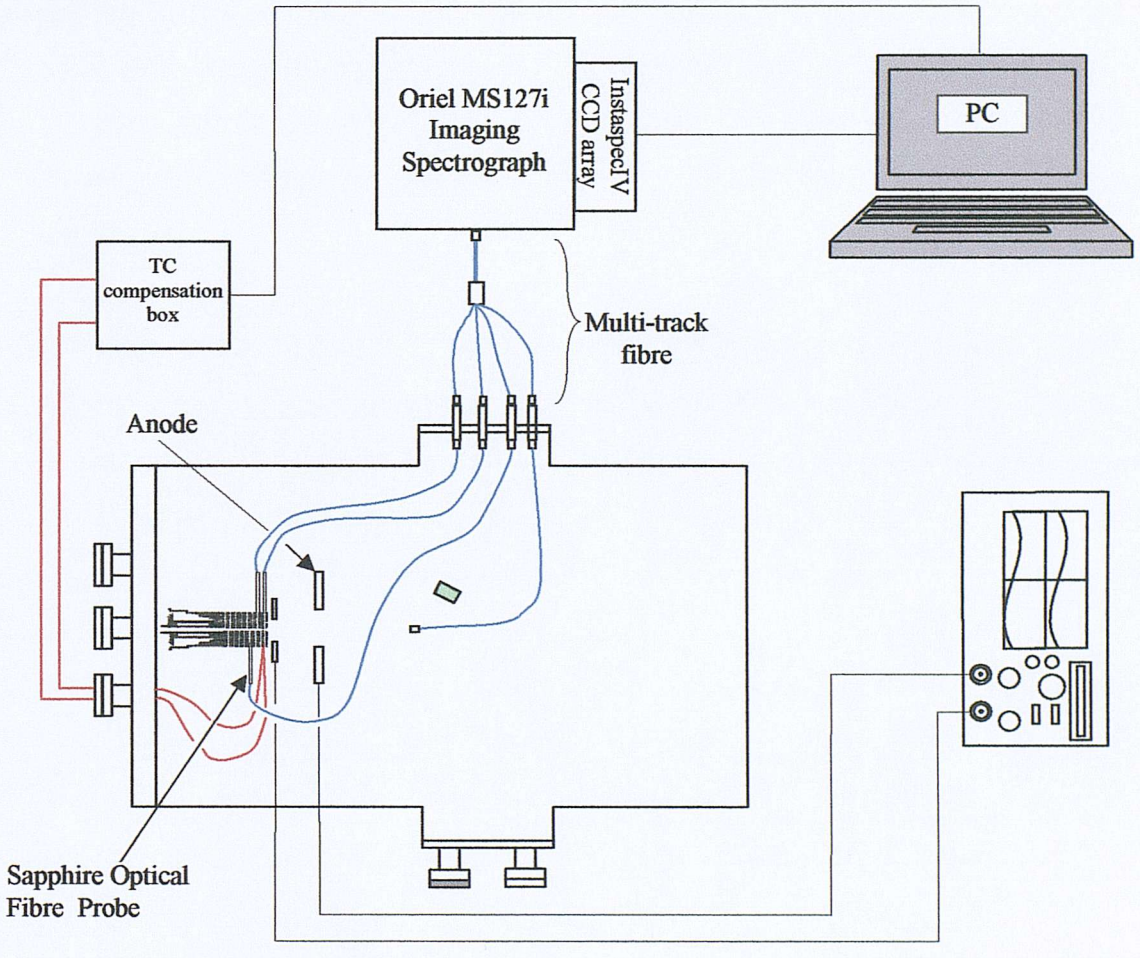

Figure A.7: Proposed experimental arrangement for spatially resolved spectroscopic measurements of the HC plasma in steady state.

Figure A.7 shows the experimental arrangement for spatially resolved steady state spectroscopy of the T6 hollow cathode internal plasma. The Oriel MS127i imaging spectrograph (section 4.4.1.1) is capable of multi-channel spectroscopy. The output from each cathode location is imaged separately on the CCD array's y-axis and the

results can be read off to produce a picture of the plasma properties at different locations in the hollow cathode. The keeper and discharge voltages are monitored and stored using a digitising scope, thus, monitoring the change in plasma properties with discharge conditions is also possible with this arrangement.

The two studies detailed above constituted the main goals of the development effort. However, the versatility and novelty of the instrumented T6/optical probe assembly provides the possibility of several, hitherto unfeasible, investigations. These include:

- *Monitoring the temperature distribution over the insert surface*:- The use of the CCD array during steady state enables the observation of the black body radiation in a given location from the opposite hot insert surface, which can then be used to determine its temperature, and also the temperature distribution along the cathode surface.

- *Investigations on cathode life-limiting factors*:- Monitoring barium emission lines enables direct spectroscopic observation of Ba emission sites and the impact of changes of cathode operating conditions on evaporation rate. This study would also be able to qualify the highly complex process of cathode ageing by monitoring the long term decrease in barium line intensity at the emission sites.

- *Investigating the role of metastable atoms in the HC discharge*:- As mentioned earlier, the sapphire fibres in the optical fibre probes were designed primarily for delivery of surgical lasers. This is due to their high melting point and high laser damage threshold (1200J/cm^2). This provides for a unique and interesting experimental investigation. As has been shown in this thesis, the metastable population plays a substantial role in determining the starting characteristics of the HC. Their role in steady state, whether in causing secondary emission from the insert surface or through secondary gas processes (i.e. Penning ionisation) is, however, unclear. The instrumented T6/optical probe assembly provides an opportunity to determine this by enabling a spatially resolved Optogalvanic Effect Spectroscopy (OGE) of the cathode plasma (refer to section 7.1.1.2). This involves shining a laser light, of frequencies that depopulate the metastable levels, via the

optical fibre probes, at a given location in the HC and monitoring the effect on the voltage-current characteristics of the discharge. Consequently, the study will not only determine the role of the metastable species but also, where in the HC will this effect be significant.

A.4 Conclusion

The design of the Instrumented T6 hollow cathode was finalised with DERA in October of 1999. Work was then directed towards designing and manufacturing the sapphire probes and the design, procurement and setting up of the experimental apparatus. These tasks were completed a few months later, which left the hollow cathode as the only component required to start the experimental side of this work. Regrettably, the instrumented cathode was a low priority at DERA. In spite of repeated attempts on our part to induce commencement of construction, they have failed to deliver the cathode to us. With two and a half years of the PhD already gone, the situation became intolerable, and this has lead to the abandonment of this project and to a redesign of the experimental apparatus in the spring of 2001 to conduct the experiments, which are the subject of the main body of this thesis.

Fortunately, the value and potential of this work was recognised by Dr. S.B.Gabriel, who instigated another PhD to continue the experimental part of this work. With the only task remaining being the delivery of the instrumented HC, negotiations with DERA (now QinetiQ) have finally resulted in the delivery of the HC in May of 2002.

The author is very happy to relate that initial cathode characterisation has shown good performance, with the access holes not seeming to have an adverse effect [200]. Tentative initial results with the optical fibre probes have led to the detection of the internal plasma in a HC argon discharge and the observation of several Ar lines. The results have also indicated a limited extent to the plasma penetration. Furthermore, some tentative estimates are now being made of the insert temperature.

With their demonstrated operation, the author believes that the results from the instrumented HC will indeed go a long way towards reaching a complete understanding of the physics of hollow cathodes, eventually making, it is hoped, the task of their design and scaling routine. The sapphire fibre optic probe forms a new type of non-intrusive diagnostic for in-situ evaluation of plasma properties in harsh, high-temperature environments. Its unique properties give it a wide scope of application that extends beyond HC's, and it is hoped that they maybe used in applications such as combustion research in the future.

The final figure in this appendix, figure A.8, shows the long-awaited modified T6 cathode.

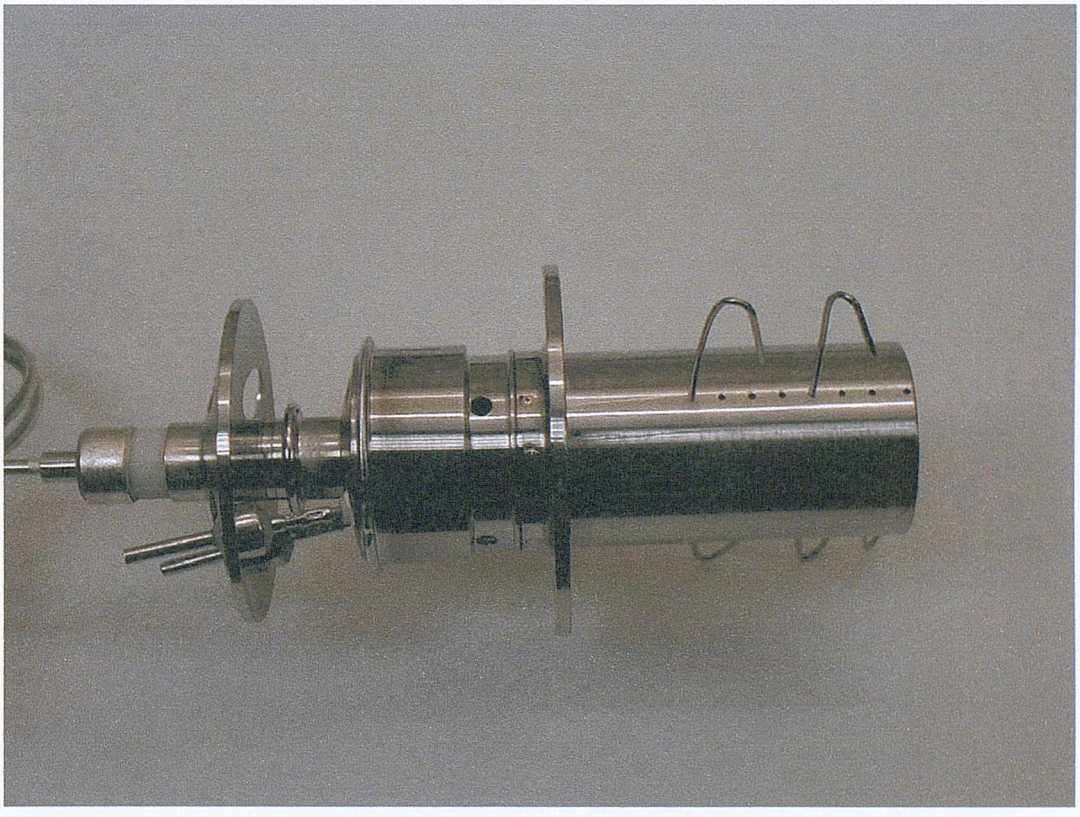

Figure A.8: Photograph of the completed modified T6 hollow cathode (Photo courtesy of QinetiQ)

Appendix B

COMPUTATIONAL MODELLING OF HC NEUTRAL FLOW

In parallel with the experimental program reported here, a complementary study was undertaken at the Astronautics Research Group of the University of Southampton to gain a better understanding of the plasma discharge in the HC via the alternative route of numerical simulation. This ongoing study by Crawford and Gabriel [25] aims to model both the neutral gas dynamics as well as concurrently modelling the plasma dynamic behaviour both inside and downstream of the HC cavity. With the goal of the study being that the code will ultimately form a design tool tailoring the geometry of the versatile HC to the variety of propulsive and space charge control applications. The neutral flow part of this study contributed some useful insight to the analysis presented in this thesis and deserves special acknowledgement.

The typically rarefied neutral flow through the cathode is modelled using a Direct Simulation Monte Carlo (DSMC) technique, which takes into account the energy input into the stream from a heated insert. Only the predictions of the DSMC model will be discussed here and the reader is directed to the above reference for a detailed description of the model. The results presented are for the reference geometry shown in figure B.1, which approximates the enclosed keeper experimental arrangement used in this work. For a 1mg/s xenon flow adjoining an insert at 1473K (1200°C), figures B.2 - B.4 illustrate respectively the centreline: neutral number density, gas pressure, and axial velocity profiles. Figure B.5 shows the radial density drop at an axial location 1mm downstream of the anode facing side of the keeper.

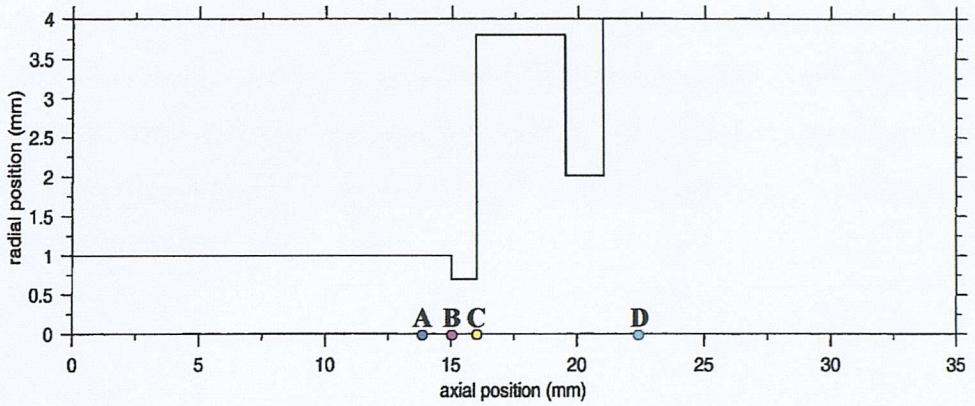

Figure B.1: Reference cathode geometry [25]

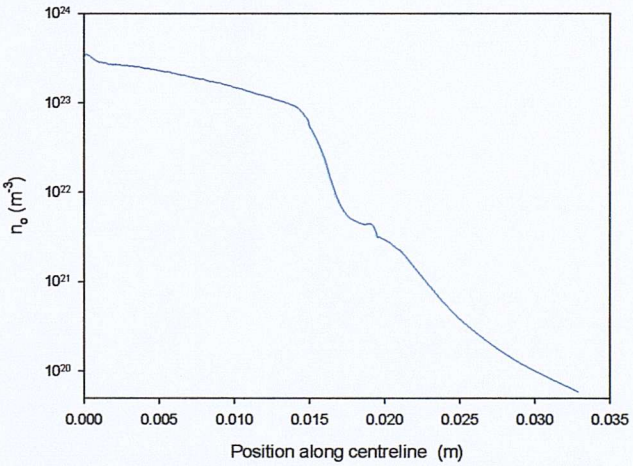

Figure B.2: Centreline axial neutral density profile, xenon 1mg/s, insert 1473K

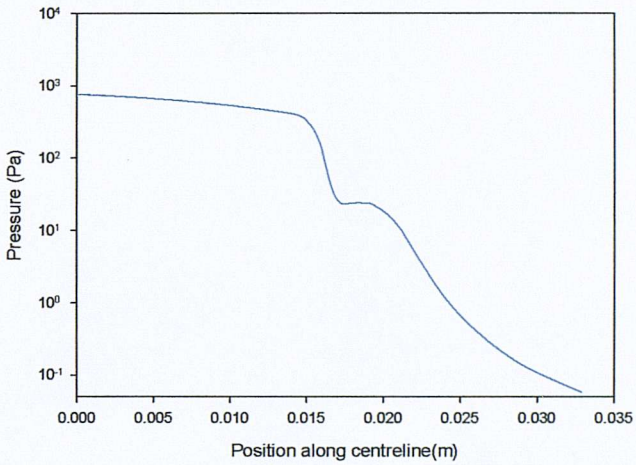

Figure B.3: Centreline axial pressure profile, xenon 1mg/s, insert 1473K

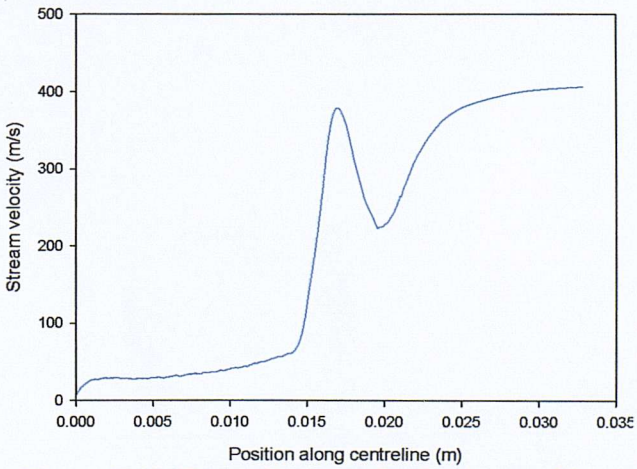

Figure B.4: Centreline axial velocity profile, xenon 1mg/s, insert 1473K

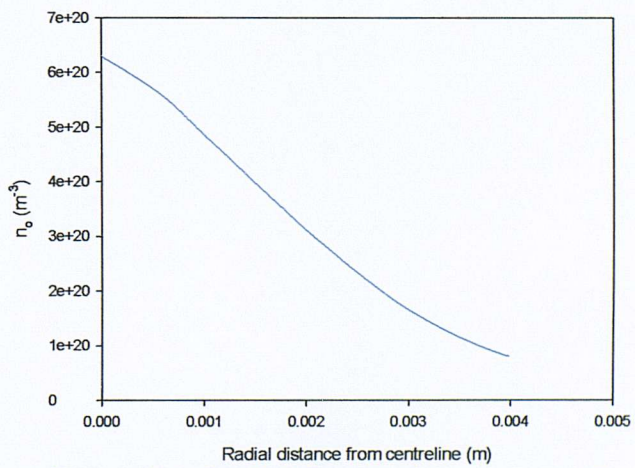

Figure B.5: Radial density drop at an axial location 1mm downstream of the anode facing side of the keeper

The neutral gas is accelerated by the expansion to velocities of several hundred m/s. Upstream of the orifice constriction, the neutral number density is in the 10^{23} m^{-3} range and the absolute pressure is of the order of 1000Pa. The kink observed downstream of the cathode orifice corresponds exactly to the position of the keeper, and is found to disappear in its absence. This is thought to be due to the energy input from the keeper to the cold expanding gas.

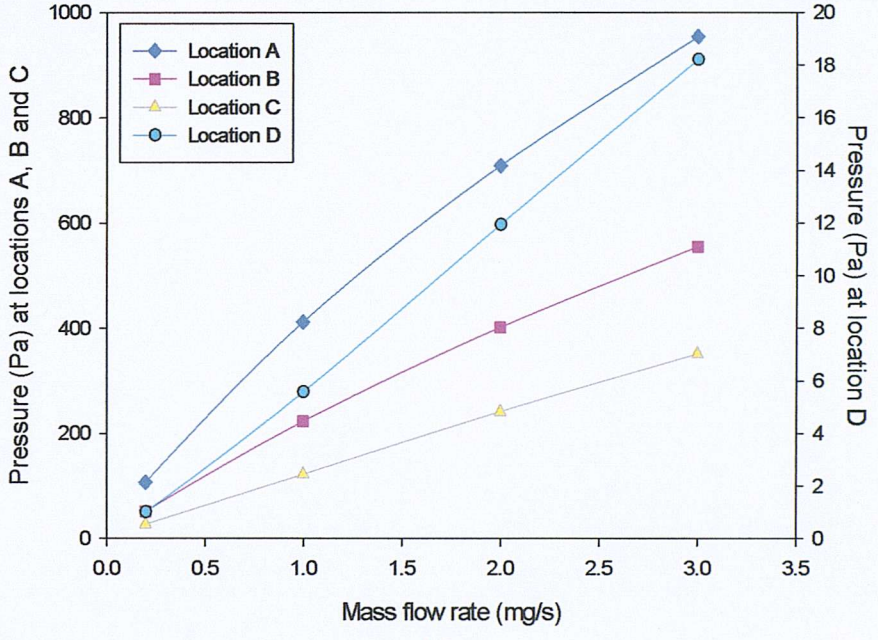

(a)

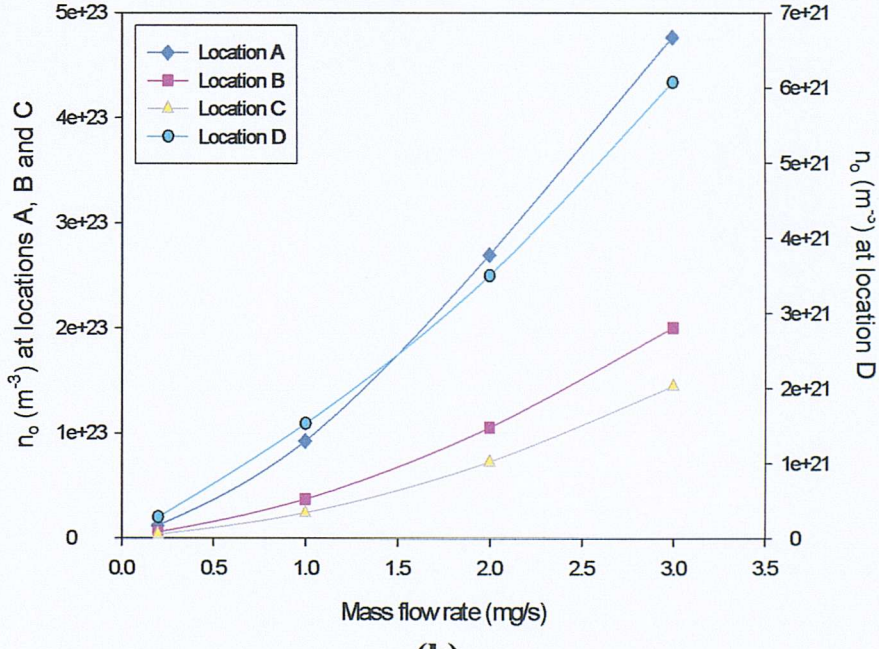

(b)

*Figure B.6: Pressure **(a)** and neutral density **(b)** as a function of mass flow rate at various locations (indicated in Figure B.1) on the cathode centreline.*

Figure B.6 illustrates the model's predictions for the variation of pressure and neutral density with $\dot{m}$ at various locations along the cathode centreline. It shows, as would be expected, that both quantities increase with increasing propellant flow rates.

Appendix C

Spectral line width and profiles

Ever since the work of Lorentz in 1905, it was recognised that the broadening and profile of a spectral line is a complex function of the environment of the radiating atom or ion. Hence it became a useful tool as a non-intrusive probe for the estimation of the plasma parameters.

The two dominant causes of line broadening are the Doppler effect and the Stark effect. Table C.1 lists the theoretical line half widths due to pure Doppler broadening or pure Stark broadening of two prominent hydrogen and helium lines at typical values of temperature and electron density. This is included to give an indication of which broadening mechanism is important at a certain combination of electron density and temperature and the amount of experimental spectral resolution required for precise measurements. It can be seen that Doppler broadening is independent of electron density and generally becomes more important at conditions of high temperature and low plasma density, while the reverse conditions cause Stark broadening to dominate.

		$T_e=10^4$ °K		$T_e=4\times10^4$ °K	
		$n_e=10^{14}cm^{-3}$	$n_e=10^{17}cm^{-3}$	$n_e=10^{14}cm^{-3}$	$n_e=10^{17}cm^{-3}$
H_β (4861Å)	$\Delta\lambda_{1/2}^{S}$	0.42	48	0.42	50
	$\Delta\lambda_{1/2}^{D}$	0.35	0.35	0.7	0.7
HeII (3203Å)	$\Delta\lambda_{1/2}^{S}$	0.27	24	0.29	32.5
	$\Delta\lambda_{1/2}^{D}$	0.16	0.16	0.32	0.32

Table C.1: Calculated Stark ($\Delta\lambda_{1/2}^{S}$) and Doppler ($\Delta\lambda_{1/2}^{D}$) half-widths (in Å) for two prominent lines at typical values of T_e and n_e [65].

In this appendix only a brief overview of the mechanisms responsible for line broadening is attempted. For detailed reviews of this extensive subject the reader is referred to the works of Griem [59, 201], Wiese [65] and Traving [94].

C.1 Natural broadening

The process leading to natural broadening of spectral lines is easily understood through classical considerations. According to Maxwell's equations, an accelerated charge looses energy by radiation. For an oscillator this energy loss can be envisaged as a frictional (damping) force acting on the oscillator with the damping constant [94]

$$\gamma_d = \frac{2e^2\omega_o^{\,2}}{3mc^3} \qquad \textit{Equation C.1}$$

where ω_o is the frequency at the line centre. Solving the equation of motion for the damped oscillator (for $\gamma_d << \omega_o$), then taking the Fourier transform of the corresponding decaying wave, leads to the so-called Lorentzian profile for the intensity of an emission line:

$$L(\omega) = \frac{1}{\pi}\frac{\omega_N}{\omega_N^{\,2} + (\omega - \omega_0)^2} \qquad \textit{Equation C.2}$$

where ω_N is the half width at half maximum (HWHM), which is half the width of the spectral line, in frequency units, at the point where the intensity reaches half its maximum value. The full width at half maximum (FWHM) of the line in wavelength units is independent of wavelength (λ), and is given by:

$$\Delta\lambda_N = \frac{2\pi c\gamma_d}{\omega_o^{\,2}} = \frac{4\pi e^2}{3mc^2} = 1.18\times10^{-5}\,nm \qquad \textit{Equation C. 3}$$

Thus, because of its small value, natural line broadening is always negligible in applications of plasma spectroscopy.

C.2 Doppler broadening

The motion of the radiating particles towards or away from an observer results in a Doppler shift in the observed wavelength of the emitted line. For a radiating particle having a velocity component u_s in the direction of observation, the wavelength appears shifted from the central wavelength λ_o by an amount:

$$\Delta\lambda = \pm\frac{u_s}{c}\lambda_o \qquad \textit{Equation C. 4}$$

Assuming that the velocities of the emitting particles are purely thermal, and hence described by a Maxwellian distribution, the fraction of particles moving in the line of sight with velocity components between u_s and u_s+du_s is given by:

$$\frac{dN}{N} = \frac{1}{\pi^{1/2}\,\Delta\lambda_D}\,exp\left[-\left(\frac{\lambda-\lambda_o}{\Delta\lambda_D}\right)^2\right]d(\Delta\lambda) \qquad \textit{Equation C.5}$$

With the Doppler width $\Delta\lambda_D$ defined as:

$$\Delta\lambda_D = (u/c)\lambda \qquad \textit{Equation C.6}$$

where $u = (2RT/\mu)^{1/2}$ is the most probable particle velocity, R is the gas constant and μ is the atomic weight.

In a plasma that is optically thin, the intensity I of an emission line is proportional to the concentration of radiating particles. Thus for a purely Doppler broadened line, the line profile, in the wavelength interval $\Delta\lambda = \lambda - \lambda_o$, has a Gaussian profile given by:

$$L(\Delta\lambda) = \frac{I_t}{\pi^{1/2}\,\Delta\lambda_D}\,exp\left[-\left(\frac{\Delta\lambda}{\Delta\lambda_D}\right)^2\right] \qquad \textit{Equation C.7}$$

Where I_t is the total line intensity. From equation C.7, we can see that, at the point where the line intensity reaches half its maximum value, the full width at half maximum is:

$$\Delta\lambda_{1/2} = 2(ln2)^{1/2}\Delta\lambda_D = 7.16\times10^{-7}\lambda(T/\mu)^{1/2} \qquad \textit{Equation C.8}$$

λ being in angstroms and T in ^{o}K units. Hence, Doppler broadening is most pronounced for lines from light atoms at high temperature.

C.3 Stark broadening

Stark broadening is a special case of the more general pressure broadening, which is the collective name for the phenomena of line broadening due to the interaction of the emitting species with the surrounding particles. Pressure broadening can be due to interaction of the emitters with either i) atoms of the same kind (resonance broadening), or ii) atoms or molecules of a different kind (Van der Walls broadening), or iii) charged particles, i.e., ions or electrons (Stark broadening). In plasmas with at least 1% ionisation, the neutral particle broadening mechanisms are negligible and the long range Coulomb perturbations, represented by Stark broadening, predominate [65].

The presentation of the highly complex theory of Stark broadening and its general validity criteria is far beyond the scope of this work. In order to calculate the Stark broadening of an emission line of a given element, the Stark parameters must be known for the experimental conditions. These are derived for the element through a process of complex theoretical calculation and experimental verification. The Stark broadening of the more intense hydrogen lines is well documented [65]. The relationship between the experimental FWHM and the electron density, for the hydrogen alpha and Balmer lines, can be given by:

$$\Delta\lambda_{1/2} = 2.5\times10^{-9}\alpha_{1/2}\, n_e^{3/2} \qquad \textit{Equation C.9}$$

Here $\alpha_{1/2}$ is the theoretical half width of the reduced Stark profile. The theoretical situation for heavier elements is less developed, particularly for those of interest in ion thrusters (namely Xe), where there is a lack of extensive reliable information on the theoretical Stark broadening of their lines. Investigators in such a position usually resort to introducing an impurity concentration of hydrogen into their plasmas, and

use the well known broadening parameters of the resulting hydrogen lines to infer their plasma properties. This approach was attempted by Monterde [115] and Malik[101] in their respective studies of the HC internal plasma, where the xenon plasma was seeded with a hydrogen impurity concentration of around 100ppm. Both, however, could not detect any of the hydrogen lines. This is due to the inherent limitations of this method: the amount of hydrogen doping has to be small since even low concentrations of impurity can perturb overall plasma behaviour [17]. As a consequence, the hydrogen emission was too weak to be useful in the HC discharge.

To conclude, spectral line broadening can be a useful tool in the non-intrusive measurements of plasma properties. However, its utility for the plasmas of interest in this work is tempered by the complexity of the theoretical treatment and the lack of extensive information on many of the heavier elements.

REFERENCES

[1] Anders, A & Anders, S. "Working Principles of the Hollow-Anode Plasma Source". *Plasma Sources, Science and Technology*, Vol.4, pgs. 571-575, 1995.

[2] Aston, G. "A Hollow Cathode and Ion Accelerator System for High Current Ion Sources". *9th Symp. on Eng. Problems of Fusion Research*, IEEE, Vol.2, pgs. 1498-1501, N.Y., 1981.

[3] Auday, G., Guillot, Ph., Galy, J. & Brunet, H. "Experimental Study of the Effective Secondary Emission Coefficient for Rare Gases and Copper Electrodes". *Journal of Applied Physics*, Vol.83, 11, pgs. 5917-5921, 1998.

[4] Bates, D.R., Kingston, A.E. & McWhirter, R.W.P. "Recombination Between Electrons and Atomic Ions I. Optically Thin Plasmas". *Proc. Royal Soc. A*, Vol.267, pgs. 297-312, 1962.

[5] Beattie, J.R. & Wilbur,P.J. "Cusped Magnetic Field Mercury Ion Thruster". *Journal of Spacecraft and Rockets*, Vol.14, No.12, pgs. 747-755, 1977.

[6] Bennet, G. , Brandhorst, H.W., Bankston, C.P., & Sovie R.J. "Electric Power System Development: A Companion Technology to Electric Propulsion". *33rd Joint Prop. Conf.*, AIAA 97-2784, Jul 1997.

[7] Biondi, M.A. "Diffusion, De-Excitation, and Ionisation Cross-Sections for Metastable Atoms. I". *Physical Review*, Vol.88, No.3, 1952.

[8] Biondi, M.A. "Ionisation of Argon Atoms by Helium or Neon Metastable Atoms". *Phys. Rev.*, Vol. 83, pgs. 653-654, 1951.

[9] Biondi, M.A. "Processes Involving Ions and Metastable Atoms in Mercury Afterglows". *Physical Review*, Vol.90, No.5, 1953.

[10] Boeuf, J-P. & Pitchford, L.C. "Pseudospark Discharges Via Computer Simulation". *IEEE Transactions on Plasma Science*, Vol.19,2, pgs.286-296,1991.

[11] Boffard, J.B. *et al.* "Measurement of the Electron-Impact Excitation Cross Section out of the Metastable Levels of Krypton". *54th Annual Gaseous Electronics Conference*, Penn. State Uni., Pennsylvania, 2001

[12] Bogaerts, A., Gijbels, R. & Vicek, J. "Collisional-Radiative Model for an Argon Glow Discharge". *Journal of Applied Physics*, Vol.84,1, pgs. 121-136, 1998.

[13] Bond, R.A. & Latham, P.M. "Extraction System Design and Modelling Using Computer Codes". *AIAA 23rd International Electric Propulsion Conference*, Abingdon, UK, IEPC-93-179, 1993.

[14] Brodie, I. & Jenkins, R.O. "The Evaporation of Barium from 'L' Cathodes". *Journal of Electronics*, pgs. 33-49, 1956.

[15] Brodie, I., Jenkins, R.O. & Trodden, W.G. "Evaporation of Barium from Cathodes Impregnated with Barium-Calcium-Aluminate". *Journal of Electronics & Control*, pgs. 149-161, 1959.

[16] Burt, E.G.C. "Space Science and Electrical Propulsion". *Proc. Roy. Soc. A.*, Vol. 308, pgs. 217-241, 1968.

[17] Bye, C. A., Scheeline, A. "Electron Density Profiles in Single Spark Discharges". *Jn. Quant. Spectrosc. Radiat. Transfer*, Vol.53, No.1, pgs.75-93, 1995.

[18] Byers, D.C. & Banks, B.A. "Survey of Electron-Bombardment Thruster Research". *IEEE Transactions on Plasma Science*, Vol.2, pgs. 1-9, 1973.

[19] Byers, D.C. & Staggs, J.F. "SERTII Flight-Type Thruster System Performance". *7th Electric Propulsion Conference*, Virginia, AIAA paper No. 69-235, 1969.

[20] Charlton, M.G., Davis, G.L. & Newson, D. "Investigations on Hollow Cathodes for Ion Thrusters". *Conf. on Elect. Prop. For Space Vehicles*, April, 1973.

[21] Choi, P. Aliaga, R. & Blottiere, B. "Experimental Studies of Ionisation Processes in the Breakdown Phase of a Transient Hollow Cathode Discharge". *Appl. Phys. Lett.*, Vol.63, 20, pgs. 2750-2752.

[22] Cobine, J.D. "Gaseous Conductors, Theory and Engineering Applications". *Dover Publications Inc.*, N.Y., 1958.

[23] Compton, K.T. & Langmuir, I. "Electrical Discharges in Gases Part I: Survey of Fundamental Processes". *Reviews of Modern Physics*, Vol. 2, No. 2, 1930.

[24] Cooper, J. "Plasma Spectroscopy". *Reports on Progress in Physics*, Vol.22, pgs. 35-130, 1966.

[25] Crawford, F.T.A. & Gabriel, S.B. "Modelling Small Hollow Cathode Discharges for Ion Microthrusters". AIAA paper 2002-2101, 2002.

[26] Crawford, F.W. & Freestone, I.L. "The Double Sheath at a Discharge Constriction". *6th Int. Conf. on Ionisation Phenomena in Gases*, Paris, 1963.

[27] Cronin, J.L. "Modern Dispenser Cathodes". *IEE PROC.*, Vol. 128, No.1, pgs. 19-32, 1981.

[28] Csiky, G. "Investigation of a Hollow Cathode Discharge Plasma". AIAA 69-258, 1969.

[29] Deininger, W.D., Aston, G. & Pless, L.C. "Hollow Cathode Plasma Source for Active Spacecraft Charge Control". *Rev. Sci. Instrum.*, Vol.58, No.6, 1987.

[30] Delcroix, J-L & Trindade, A.R. "Hollow Cathode Arcs". *Adv. In Electronics and Electron Physics*, Vol. 35, No.87, 1974.

[31] Den Hartog, D.J. & Holly, D.J. "A Simple, Low-Cost, Versatile Charge-Coupled Device Spectrometer for Plasma Spectroscopy". *Rev. Sci. Instrum.*, Vol. 68,1, pgs. 1036-1038, 1997.

[32] Druyvesteyn, M.J. & Penning, F.M. "The Mechanism of Electrical Discharges in Gases of Low Pressure". *Reviews of Modern Physics*, Vol.12, No.2, 1940.

[33] Edwards, C.H. "Discharge Characteristics and Instabilities in the UK-25 Ion Thruster Operating on Inert Gas Propellants". *PhD. Thesis, University of Southampton*, 1997.

[34] Eichorn, H., Schoenbach, K.H. & Tessnow, T. "Paschen's Law for a Hollow Cathode Discharge". *Appl. Phys. Lett.*, Vol. 63,18, pgs. 2481-2483, 1993.

[35] Eidmann, K. "Radiation Transport and Atomic Physics Modelling in High-Energy-Density Laser-Produced Plasmas". *Laser and Particle Beams*, Vol. 12,2, pgs. 223-244, 1994.

[36] Elwert, V.G., *Z. Naturforschg*, 9A, pgs. 637-653, 1954.

[37] Favre, M., Choi, P., Zambra,M., Moreno, J., Chuaqui, H., & Wyndham, E. "Hollow Cathode Ionization Processes in the Breakdown Phase of a Transient Hollow Cathode Discharge". *Symposium on Pulsed Power*, IEE, 1998.

[38] Favre, M., Moreno, J., Chuaqui, H., Wyndham, E., Zambra, M., Choi, P. & Dumitrescu-Zoita, C. "Pre-Breakdown Processes in the Hollow Cathode Region of a Transient Hollow Cathode Discharge". *Astrophysics and Space Science*, Vol. 256, pgs. 337-342, 1998.

[39] Favre, M., Zambra, M., Moreno, J., Chuaqui, H., Wyndham, E. & Choi, P. "Time Resolved Observations of Plasma Evolution in the Hollow Cathode Region of a

Transient Hollow Discharge". *11th International Conference on High Power Particle Beams*, 1996.

[40] Fearn D.G. & Patterson, S.W. "Characterisation of the High Current Hollow Cathode for the T6 Ion Thruster". *34th Joint Propulsion and Exhibit*, AIAA-98-3346, Cleveland, 1998.

[41] Fearn, D.G. "Spacecraft Ion Propulsion Development in the United Kingdom". *Proc. Instn. Mech. Engrs.*, Vol. 211, Part G, pgs. 103-112, 1996.

[42] Fearn, D.G. "The Possible Application of Ion Propulsion to Precursor Interstellar Missions". *36th Jnt. Prop. Conf.*, AIAA-2000-3415, Huntsville, Alabama, July 2000

[43] Fearn, D.G. "The UK-10 Ion Propulsion System- a Technology for Improving the Cost-Effectiveness of Communications Spacecraft". *22nd Int. Electric Prop. Conf.*, IEPC-91-009, 1991.

[44] Fearn, D.G. & Patterson S.W. "The Hollow Cathode- a Versatile Component of Electric Thrusters". *Proceedings of the 3rd conference on Spacecraft Propulsion*, 10-13 October, Cannes, 2000

[45] Fearn, D.G. & Patterson, S. W. "The Compatibility of Hollow Cathode Characteristics with a Variety of Ion Thruster Designs". *International Electric Propulsion Conference*, IEPC-99-133, 1999.

[46] Fearn, D.G. & Philip, C.M. "An Investigation of the Physical Processes in a Hollow Cathode Discharge". AIAA paper 72-416, 1972.

[47] Fearn, D.G. & Wallace, N.C. "Low Earth Orbit Application of Electric Propulsion". *Colloquium on Electric Propulsion for Spacecraft, IEE*, London, 1989.

[48] Fearn, D.G., Cox, A.S. & Moffitt, D.R. "An Investigation of the Initiation of Hollow Cathode Discharges". *Royal Aircraft Establishment Technical Report* 76054, April, 1976.

[49] Fearn, D.G., Martin, A.R. & Smith P. "Ion Propulsion Development in the UK". *29th Joint Propulsion Conference and Exhibit*, AIAA paper 93-2603, Monterey, June 1993.

[50] Fearn, D.G., Martin, A.R. & Smith, P. "Ion Propulsion Development in the UK". *Proc. Roy. Soc. A*, Vol. 308, pgs. 217-241, 1968.

[51] Fearn, D.G., Singfield, A.K., Wallace, N.C. "The Operation of Ion Thruster Hollow Cathodes Using Inert Gas Propellants". AIAA paper 90-2541, 1990.

[52] Forbes, G.F. "The Trajectory of a Powered Rocket in Space". *ARS Jn.*, 22:92, 1952.

[53] Forrester, A.T. "Large Ion Beams, Fundamentals of Generation and Propagation". *John Wiley & Sons*, 1988.

[54] Fortescue, P. & Stark, J. "Spacecraft Systems Engineering". *John Wiley & Sons* Ltd., 1997.

[55] Franklin, R.N. "Plasma Phenomena in Gas Discharges". *Clarendon Press-Oxford*, 1976.

[56] Friedly, V.J. & Wilbur, P.J. "High Current Hollow Cathode Phenomena". AIAA paper No. 90-2587,1990.

[57] Gair, S.A. & Harris, P.T. "A Review of the cathode Construction for the RAE 10/25mN Thruster". *Int. Electr. Prop. Conf.*, IEPC-88-078, 1988.

[58] Goldston, R.J. & Rutherford, P.H. "Introduction to Plasma Physics". *Institute of Physics Publishing*, 1995.

[59] Griem, H.R. "Principles of Plasma Spectroscopy". *Cambridge University Press*, 1997.

[60] Harbour, P.J., Wells, A.A., Harrison, M.F.A. & White, B.M. "Physical Processes Affecting the Design and Performance of Ion Thrusters with Particular Reference to the 10 cm, RAE/Culham T4 Thrustor". AIAA paper No.73-1112, *16th Electric Propulsion Conference*, 1973.

[61] Hershkowitz, N. "Review of Recent Laboratory Double Layer Experiments". *Space Science Reviews*, Vol.41, pgs. 351-391,1985.

[62] Hess, K.R. & Harrison, W.W. "The Role of Metastable Atoms in a Glow Discharge Ionisation Process". *Anal. Chem.*, Vol.60, pgs. 691-696, 1988.

[63] Higgins, M.J. *et al.* "Atomic and Molecular data for Fusion, Part 3, Recommended Cross Sections and Rates for Electron impact Ionisation of Atoms and Ions: Copper and Uranium". *Atomic Energy Authority*, 1989.

[64] Huba, J.D. "NRL Plasma Formulary". *Naval Research Laboratory*, 2000.

[65] Huddlestone, R.H. & Leonard, S.T. "Plasma Diagnostic Techniques". *Academic Press*, N.Y., 1965.

[66] Hutchinson, I.H., LaBombard, B. & Lipschultz, B. "Experimental Divertor Similarity Database Parameters". *MIT, Plasma Fusion Centre Research Report*, PFC/RR-95-12, 1995

[67] Hwang-Jin, H. "Physical Processes in Hollow Cathode Discharge Sources". *MSc. Thesis, Naval Postgraduate School*, 1989.

[68] Hyman Jr, J. & Dulgeroff, C.R. " Engineering Notes: Modularized Ion Thruster Development for Auxiliary Propulsion". *Journal of Spacecraft*, Vol. 15, pgs. 184-187.

[69] Jacobsen, R.A. & Eubank, H.P. "Evidence of Fireball Phenomena in Hollow Cathode of Electron Bombardment Ion Thrusters". *AIAA Journal*, Vol. 11, No. 3, pgs. 399-400, 1973.

[70] Jahn, R.G. "Physics of Electric Propulsion". *MacGraw-Hill Book Company*, N.Y., 1968.

[71] Joshi, N.K., Sahasrabudhe, S.N., Sreekumar, K.P. & Venkatramani, N. "Variation of Axial Temperature in Thermal Plasma Jets". *Meas. Sci. Technol.*, Vol.8, pgs. 1146-1150, 1997.

[72] Jung, E.C., Rho, S.P., Jongmin Lee, Jun-Hoi Lee & Hyuck Cho "Effect of penning Ionisation on the Optogalvanic Signal of Argon/Rare-Earth Metal Hollow Cathode Discharge". *Optics Communications*, Vol. 149, pgs. 283-288, 1998.

[73] Kameyama, I. & Wilbur, P.J. "Potential-Hill Model of High-Energy Ion Production near High-Current Hollow Cathodes". *21st International Symposium on Space Technology and Science*, Omiya, Japan, 1998.

[74] Katz, I., Mandell, M.J., Patterson, M. & Domonkos, M. "Sensitivity of Hollow Cathode Performance to Design and Operating Parameters". AIAA paper No. 99-2576, 1999.

[75] Kaufman, H.R. "An Ion Rocket with an Electron-Bombardment Ion Source". *Technical Note D-585, National Aeronautics and Space Administration*, pgs1-38, 1961.

[76] Kaufman, H.R. "Origin of the Electron-Bombardment Ion Thruster". *Jn. Spacecraft*, Vol.18, No.4, 1981.

[77] Kaufman, H.R. & Reader, P.D. "Experimental Performance of Ion Rockets Employing Electron-Bombardment Ion Sources". *Electric Propulsion Edition: Academic Press, Progress in Astronautics and Rocketry*, pgs. 3-20, 1961.

[78] Kaufman, H.R. & Reader, P.D. "Experimental Performance of Ion Rockets Employing Electron-Bombardment Ion Sources". *ARS Electrostatic propulsion Conference*, California, 1960.

[79] Kaufman, H.R. & Robinson, R.S. "Plasma Processes in Inert Gas Thrusters". *14th Int. Elec. Prop. Conf.*, 1979.

[80] Kaufman, H.R., Robinson, R.S. & Trock, D.C. "Inert Gas Thruster Technology". *Jn. Spacecraft and Rockets*, Vol.20, No.1, 1983.

[81] Kennedy, R.V. "Theory of the Arc Hollow Cathode". *J. Phys. D: Appl. Phys.*, Vol. 34, pgs. 787-793, 2001.

[82] Kerslake, W.R. & Byers, D.C. "SERT II Experimental Thrustor System". AIAA paper No. 67-700, *Electric Propulsion and Plasmadynamics Conference*, Colorado Springs, Colorado, September 11-13, 1967.

[83] Koester, J.K., Sajben, M. & Zukoski, E.E. "Analytical and Experimental Studies of Thermionically Emitting Electrodes in Contact with Dense, Seeded Plasmas". *Proc. 11th Symp. On Engineering Aspects of Magnetohydrodynamics*, pgs.54-60, 1970.

[84] Koschade, S.E. *et al.* "Development of a Flight Prototype of the RF-Ion Thruster RIT-10". Paper 72-471, AIAA, 1972.

[85] Kovaleski, S.D., Patterson, M.J., & Soulas, G.C.& Sarver-Verhey, T.R. "A Review of Testing of Hollow Cathodes for The International Space Station Plasma Contactor". *27th International Electric Propulsion Conference*, IEPC-01-276, Pasadena, CA, 15-19th October, 2001.

[86] Krishnan, M., Jahn, R.G., von Jaskowsky, W.F. & Clark, K.E. "Physical Processes in Hollow Cathodes". *AIAA Journal*, Vol.15, No.9, 1977.

[87] Kruithof, A.A. "Townsend's Ionisation Coefficients for Neon, Argon, Krypton and Xenon". *Physica VII*, No.6, 1940.

[88] Kruithof, A.A. & Penning, F.M. "Determination of the Townsend Ionisation Coefficient α for Mixtures of Neon and Argon". *Physica IV*, No.6, 1937.

[89] Langmuir, I & Mott-Smith, H. "Studies of Electric Discharges in Gases at Low Pressure". Parts 1-5, *General Electric Review*, Vol.27, pgs. 449-455, 538-548, 616-623, 762-771& 810-820, 1924.

[90] Langmuir, I. "The Interaction of Electron and Positive Ion Space Charges in Cathode Sheaths". *Physical Review*, Vol. 33, pgs.954-989, June 1929.

[91] Langmuir, I. & Compton, K.T. "Electrical Discharges in Gases Part II Fundamental Phenomena in Electrical Discharges". *Reviews of Modern Physics*, Vol.3, No.2, 1931.

[92] Latham, P.M., Martin, A.R. & Bond, A. "Design, Manufacture and Performance of the UK-25 Engineering Model Thruster". *21st International Electric Propulsion Conference*, AIAA - 90-2541, 1990.

[93] Lawden, D.F. "Note on a Paper by G.F. Forbes". *Journal of the British Interplanetary Society*, 9:230, 1950.

[94] Lochte-Holtgreven, W. "Plasma Diagnostics". *North-Holland Publishing Company*, Amsterdam, 1968.

[95] Lockwood, R.B., Anderson, L.W. "A Method for Measuring Cross-Sections for Electron-Impact Excitation out of Metastable Levels of Atoms". *Z. Phys. D - Atoms, Molecules and Clusters*, Vol.24, pgs. 155-160, 1992.

[96] Loeb, L.B. "Basic Processes of Gaseous Electronics". *University of California Press*, 1961.

[97] Loeb, L.B. "The Problem of the Mechanism of Static Spark Discharge". *Reviews of Modern Physics*, Vol. 8, pgs. 267-293, 1936.

[98] Longhurst, G.R. & Wilbur, P.J. "Multi-pole Mercury Ion Thruster". *13th International Electric Propulsion Conference*, IEPC-78-682, California, April 25-27, 1978.

[99] Malik, A.K. "The Effect of the VUV Irradiation on the Electron Emission and the Ion Wall Sheath in Hollow Cathodes". *DRA Working Paper* SP(92)-WP-22, 1992.

[100] Malik, A.K. & Fearn, D.G. "The Study of the Physics of Hollow Cathode Discharges". IEPC-93-026, 1993.

[101] Malik, A.K., Monterde, P. & Haines, M.G. "Spectroscopic Measurements on Xenon Plasma in a Hollow Cathode". *Journal of Applied Physics*, Vol. 33, pgs. 2037-2048, 2000.

[102] Mandell, M.J. & Katz, I. "Theory of Hollow Cathode Operation in Spot and Plume Modes". *Proceeding of the 30th Joint Propulsion Conference*, AIAA-94-3134, Indianapolis, IN., June 1994.

[103] Marotta, A. "Determination of Axial Thermal Plasma Temperatures Without Abel Inversion". *Journal of Applied Physics*, Vol.27, pgs. 268-272, 1994.

[104] Martin, A.R. "A comparison of Argon and Mercury Propelled Ion Engines". *Journal of the British Interplanetary Society*, Vol.25, pgs. 491-502, 1972.

[105] Martin, A.R. "Atomic Excitation Processes in the Discharges of Rare Gas Ion Engines". *J. Phys. B: Atom. Molec. Phys.*, Vol. 7, No.10, pgs. 1161-1166, 1974.

[106] Martin, A.R., Bond, A., Lavender, K.E., Harvey, M.S. & Latham, P.M. "A UK Large Diameter Ion Thruster for Primary Propulsion". *19th Int. Elec. Prop. Conf.*, AIAA-87-1031,Colorado Springs, 1987.

[107] Martin, A.R., Harvey, M.S. & Latham, P.M. "Performance Assessment of a UK Rare Gas Ion Thruster". *19th International Electric Propulsion Conference*, Colorado Springs, 1987.

[108] Mason, N.J. & Newell, W.R. "Total Cross Sections for Metastable Excitation in the Rare Gases". *Jn. Phys. B: At. Mol. Phys.*, Vol.20, pgs. 1357-1377, 1987.

[109] Meek, J.M. & Craggs, J.D. "Electrical Breakdown of Gases". First edition: *Oxford at the Clarendon Press*, 1953. Second Edition: *John Wiley & Sons*, 1978.

[110] Meijer, F.G. "Active and Passive Spectroscopy". *Transactions of Fusion Technology*, Vol.33, pgs. 321-327, 1998.

[111] Meijer, F.G. "Plasma Spectroscopy". *Transactions of Fusion Technology*, Vol.37, pgs. 352-359, 2000.

[112] Milligan, D.J. "The Baffle Aperture Region of an Ion Thruster". *PhD. Thesis, University of Southampton*, 2001.

[113] Milligan, D.J. & Gabriel, S.B. "Investigation of the Baffle Annulus Region of the UK25 Ion Thruster". *Proceedings of the 35th Joint Propulsion Conference*, Los Angeles, California, June 1999.

[114] Milligan, D.J. & Gabriel, S.B. "Plasma Properties around the Baffle Aperture Region of the UK25 Ion Thruster". *International Electric Propulsion Conference*, IEPC-99-157, 1999.

[115] Monterde, M.P. "Physics of the Hollow Cathode in a Kaufman-type Electrostatic Ion Thruster". *PhD. Thesis, Imperial College of Science Technology and Medicine*, 1996.

[116] Monterde, M.P., Dangor, A.E., Haines, M.G., Malik, A.K. & Fearn, D.G. "Spectroscopic Measurements of the Plasma within a Hollow Cathode". AIAA paper No. 95-2383, 1995.

[117] Monterde, M.P., Haines, M.G., Dangor, A.E., Malik, A.K. & Fearn, D.G. "Kaufman-type Xenon Ion Thruster Coupling Plasma: Langmuir Probe Measurements". *Jn. Phys. D: Appl. Phys.*, Vol.30, pgs. 842-855, 1997.

[118] Nagler, R.G. "Application of Spectroscopic Temperature Measuring Methods to Definition of a Plasma Arc Flame". *JPL Technical Report* no. 32-66, 1961.

[119] Newson, D., Charlton, M.G. & Davis,G.L. "Starting Behaviour of Hollow Cathodes Including Multiple Starts". *3rd European Electric Propulsion Conference*, Hinterzarten, Blackforest, Germany, 1974.

[120] Oberth, H. "Wege zur Raumshiffahrt". R. Oldenbourg, 1929.

[121] Patterson, S. W. & Fearn, D.G. "The Generation of High Energy Ions in Hollow Cathode Discharges". *International Electric Propulsion Conference* paper IEPC-99-125, 1999.

[122] Patterson, S. W., Khaliq Malik, A. & Fearn, D.G. "Noise and Oscillatory Disturbances in the T6 Ion Thruster Hollow Cathode". *Proceedings of the 35th Joint Propulsion Conference*, Los Angeles, California, June 1999.

[123] Patterson, S.W., Jack, T.M. & Fearn, D.G. "The Effect of the Keeper Electrode on Hollow Cathode Discharge Characteristics". *36th Joint Propulsion Conference and Exhibit*, 16-19 July, Huntsville, Alabama, 2000

[124] Patterson, S.W., Jugroot, M. & Fearn, D.G. "Discharge Initiation in the T6 Thruster Hollow Cathode". *36 Joint Propulsion Conference and Exhibi*t, AIAA-2000-3532, 16-19 July, Huntsville, Alabama, 2000.

[125] Penning, F.M. "Anomalous Variation of the Sparking Potential as a Function of Pod". *Proc. of the Roy. Ac. of Sci. Am.*, Vol.34, 1305, 1931.

[126] Philip, C.M. "A Study of Hollow Cathode Discharge Characteristics". AIAA paper 70-1087, 1970.

[127] Philip, C.M. & Fearn, D.G. "An Investigation of Physical Processes in a Hollow Cathode Discharge". *AIAA Journal*, Vol.11, No.2, pgs. 131-132, 1973.

[128] Philip, C.M. & Fearn, D.G. "Recent Hollow Cathode Investigations at the Royal Aircraft Establishment". *AIAA Journal*, Vol.12, No.10, pgs. 1319-1325, 1974.

[129] Philip, C.M. & Woods, M.O. "Some Investigations of Hollow Cathodes with Porous Dispensers". *3rd European Elect. Prop. Conf.*, DGLR, Germany, 1974.

[130] Philip,C.M. "A Study of Hollow Cathode Discharge Characteristics". *AIAA Journal*, Vol.9, No.11, 1971.

[131] Philip,C.M. "The Design and Operation of Hollow Cathode for Electron Bombardment Ion Thrusters". *RAE Technical Report No.*69213, 1969.

[132] Polk, J.E., Anderson, J.R., Brophy, J.R., Rawlin V.K., Patterson, M.J., Sovey, J. & Hamley, J. "An Overview of the Results from an 8200 Hour Wear Test of the NSTAR Ion Thruster". AIAA paper 99-2446, 1999.

[133] Prewett, P.D. & Allen, J.E. "The Double Sheath Associated with a Hot Cathode". *Proc. R. Soc. Lond.*, A.348, pgs. 435-446, 1976.

[134] Puech, V. & Mizzi, S. "Collision Cross Sections and Transport Parameters in Neon and Xenon". *Jn. Phys. D: Applied Phys.*, Vol.24, pgs. 1974-1985, 1991.

[135] Raether, H. "Electron Avalanches and Breakdown in Gases". *London Butterworths*, 1964.

[136] Rawlin, V.K. & Kerslake, W.R. "SERTII Durability of the Hollow Cathode and Future Applications of Hollow Cathodes". *J. Spacecraft*, Vol.7, No.1, pgs. 14-20, 1970.

[137] Romick, "Basic Design Principles Applicable to Reaction-Propelled Space Vehicles". *Fifth IAF Congress*, 1954.

[138] Rossetti, P., Paganucci, F. & Andrenucci, M. "A Hollow Cathode Model for Application to the Electric Propulsion". *Jnt. Prop. Conf.*, AIAA-2002-4239, 2002.

[139] Sakai, Y., Sawanda, S. & Tagashira, H. "Boltzmann Equation Analyses of Electron Swarm Parameters in Ar/Ne, Kr/Ne, Xe/Ne, Hg/Ar and Hg/Kr Mixtures and Derived Effective Excitation Cross Sections for Metastable States of Rare Atoms". *Jn. Phys. D: Appl. Phys.*, Vol.24, pgs. 283-289, 1991.

[140] Salhi, A. & Turchi, P.J. "A First-Principles Model for Orificed-Hollow Cathode Operation". AIAA-92-3742, 1992.

[141] Salhi, A. & Turchi, P.J. "Scaling Relations for Design and Operation of Orificed-Hollow Cathodes". *35th Jnt. Prop. Conf.*, AIAA-94-3133, IN., 1994.

[142] Schatz, M.F. "Heartless Ignition of Inert Gas Ion Thruster Hollow Cathodes". *NASA TM-87086 Technical Memorandum*, 1985.

[143] Shepherd, L.R. & Cleaver, A.V. "The Atomic Rocket". *Journal of the British Interplanetary Society*, vol.8, pg. 59, 1949.

[144] Shuker, R., Ben-Amar & Erez, G. "Optogalvanic Spectroscopy of Quasi-Resonant Penning Ionisation". *Jn. Appl. Phys.*, Vol.54, No.10, 1983.

[145] Siegfried, D.E. & Wilbur, P.J. "A Model for Mercury Orificed Hollow Cathodes: Theory and Experiment". *AIAA Journal*, Vol.22, No.10, 1984.

[146] Siegfried, D.E. & Wilbur, P.J. "An Investigation of Mercury Hollow Cathode Phenomena". *13th Int. Elect. Prop. Conf.*, IEPC-78-705, 1978.

[147] Siegfried, D.E. & Wilbur, P.J. "Phenomenological Model Describing Orificed, Hollow Cathode Operation". *AIAA Journal*, Vol.21, No.1, 1983.

[148] Song, B., D'Angelo, N. & Merino, R.L. "On Anode Spots, Double Layers and Plasma Contactors". *Journal of Physics*, Vol. 24, pgs. 1789-1795, 1991.

[149] Song, B., D'Angelo, N. & Merino, R.L. "Stability of a Spherical Double Layer Produced through ionisation". *Jn Phys. D: Appl. Phys.*, Vol. 25, pgs. 936-941, 1992.

[150] Sovey, J.S. "Characteristics of a 30-cm Diameter Argon Ion Source". AIAA paper No. 76-1017, 1976.

[151] Spitzer Jr., L. "Interplanetary Travel between Satellite Orbits". *J. Brit. Interplan. Soc.*, Vol.10, pg.249, 1952

[152] Stuhlinger, E. "Advanced Propulsion Systems for Space Ship Vehicles". *Proc. 9th Int. Astronautics Congress*, 1958.

[153] Stuhlinger, E. "Design and Performance Data of Space Ships with Ionic Propulsion Systems". *Proc. 8th Int. Astronautics Congress*, 1957.

[154] Stuhlinger, E. "Electrical Propulsion Systems for Space Ships with nuclear Power Source". *Second Annual Meeting American Astronautical Society,* 1955.

[155] Stuhlinger, E. "Possibilities of Electrical Space Ship Propulsion". *In Proc. 5th Int. Astronautics Congress*, 1954.

[156] Stuhlinger, E. & Seitz, R.N. "Electrostatic Propulsion Systems for Space Vehicles". *Advances in Space Science*, Vol. 2, pgs.263-345, 1960.

[157] "The Book of Photon Tools". *Oriel Instruments.*

[158] Tipler, P.A. "Physics for Scientists and Engineers". *W. H. Freeman and Company/Worth Publishers*, Fourth Edition, 1999.

[159] Touloukian, Y.S. & DeWitt, D.P. "Thermal Radiative Properties, Metallic Elements and Alloys". *Thermophysical Properties of Matter*, Vol.7, IFI/Plenum, N.Y., 1970.

[160] Vaulin, E.P., Kiryushkina, M.V., Obukhov, V.A. & Mai, S.F. & Riame Mai "Mathematical Modelling of Arc Hollow Cathodes". *32nd Jnt. Prop. Conf.*, AIAA-96-3184, 1996

[161] Vlcek, J."A Collisional-Radiative Model Applicable to Argon Discharges Over a Wide Range of Conditions. I: Formulation and Basic Data". *Journal of Applied Physics*, Vol.22, pgs. 623-631, 1989.

[162] von Engel, A. "Ionized Gases". *Oxford at the Clarendon Press*, 1965.

[163] von Engel,A. & Robson, A.E. ''The excitation theory of arcs with evaporating cathodes''. *Proceedings of the Royal Society*, A243, 1957.

[164] Wallace, N.C., Mundy, D.H., Fearn, D.G. & Edwards, C.E. "Evaluation of the Performance of the T6 Ion Thruster". *35th Jnt. Prop. Conf.*, AIAA-99-2442, June 1999

[165] Wang, J., Li, B., Gu, B., Zhang, J., Huang, X., Dong, J. & Li, H. "The Study on the Arc Plasma Temperature Measurement by Optical Emission Spectroscopy with Fibre Optical Transmission". *Spectroscopy Letters*, Vol.31,1, pgs.243-252, 1998.

[166] Watson, S.D. *et al.* "500 Hour Tests of the T5 Ion Thruster with Dual and Triple Grid Extraction Systems". *AIAA 23rd International Electric Propulsion Conference*, IEPC-93-170,1993.

[167] Waymouth, J.F. "Perturbation of a Plasma by a Probe". *The Physics of Fluids*, Vol.7, No.11, 1964.

[168] Wiese, W. and Saloman, E.B., National Institute of Standards Technology (NIST), *private communications*.

[169] Wiese, W.L., Brault, J.W., Danzmann, K., Helbig, V. & Kock, M. "Unified Set of Atomic Transition Probabilities for Neutral Argon". *Physics Review A*, Vol. 39,5, pgs. 2461-2471, 1989.

[170] Wilbur, P.J., Jahn, R.G. & Curran, F.C. "Space Electric Propulsion Plasmas". *IEEE Transactions on Plasma Science*, Vol. 19, No.6, pgs. 1167-1179, 1991.

[171] Williams, G.J. *et al.* "Laser Induced Fluorescence Characterisation of Ions emitted from Hollow Cathodes". AIAA paper 99-2862, 1999.

[172] Williams, J.D. & Wilbur, P.J. "Electron Emission from a Hollow Cathode-Based Plasma Contactor". *Journal of Spacecraft and Rockets*, Vol.29, No.6, 1992.

[173] Wilson, R. "The Spectroscopy on Non-Thermal Plasmas". *Journal of Quantitative Spectroscopy and Radiative Transfer*, Vol. 2, pgs. 477-490, 1962.

[174] Yalcin, S., Crosley, D.R., Smith, G.P. & Faris, G.W. "Influence of Ambient Conditions on the Laser Air Spark". *Applied Physics B*, Vol.68, pgs. 121-130, 1999.

[175] Yoshida, H., Kawauchi, H., Takama, S., Maeda, T., Higuchi, T. & Akai, K. "Performance Characteristics of a 35-cm Diameter Xenon Ion Thruster". *32nd Joint Propulsion Conference*, AIAA paper No. 96-2714, July 1-3, Lake Buena Vista, Florida, 1996.

[176] Zuccaro, D. "Mercury Vapor Hollow Cathode Component Studies". AIAA paper 73-1141, 1973.

[177] "CRC Handbook of Chemistry and Physics". 79th Edition, 1998-1999.

[178] Strigamov, A.R. & Sventitker, N.S. "Tables of spectral lines of neutral and ionised atoms". *IFI/Plenum*, 1968.

[179] National Institute of Standards and Technology (NIST) "Atomic Spectra Databases". http://physics.nist.gov/PhysRefData/ASD1/choice.html?nist_atomic_spectra.html

[180] Kelly, R.L. "Kelly Atomic Line Database". http://cfa-www.harvard.edu/amdata/ampdata/kelly/kelly.html

[181] Smith, P. L., Heise, C., Esmond, J. R. & Kurucz, R. L. "Atomic spectral line database". http://www.pmp.uni-hannover.de/cgi-bin/ssi/test/kurucz/sekur.html

[182] Wilson, A.D. *et al.* "Investigation into Nitrogen-Inert Gas Interactions in D.C. Diode Glow Discharges". *Surface & Coatings Technology*, pgs. 540-545, July 2001.

[183] Saccoccia, G. "Introduction of the European Activities in Electric Propulsion". IEPC-03-341, 2003.

[184] Sajben, M. "Boundary Conditions for Adsorbing-Emitting Electrodes in contact with a Seeded, Dense Plasmas". *AIAA Journal*, Vol. 8, pgs. 400- 406, 1970.

[185] Haas, J.M. *et al.* "Hall Thruster Discharge Chamber Plasma Characterisation using High Speed Axial Reciprocating Electrostatic Probes". *Jnt. Prop. Conf.*, AIAA-99-2426, 1999.

[186] Ferreira, C.M. & Delcroix, J.L. "Theory of the Hollow Cathode Arc". *Journal of Applied Physics*, Vol.49, No.4, pgs. 2380-2395, 1978.

[187] Crawford, F.T. & Gabriel, S.B. "Numerical Simulation of the Hollow Cathode Plasma using a PIC-DSMC Code". *Int. Elec. Prop. Conf.*, IEPC-2003-27, 2003.

[188] Martin, A.R. "Design and Operation of an Ion Engine using the Rare Gases". *Journal of the British Interplanetary Society*, Vol. 26, pgs. 742-753, 1973.

[189] Martin, A.R. "Physical Behaviour of the Rare Gases in an Electron Bombardment Ion Engine". *Proceedings of the Culham/IEE Conference on Electric Propulsion of Space Vehicles*, 1973.

[190] Byres, D.C. & Reader, P.D. "Operation of an Electron Bombardment Ion Source using various Gases". Technical Note D-6620, NASA, 1971.

[191] Kaufman, H.R. "Inert Gas Thrusters". NASA Contractor Report, NASA-CR-135226, 1977.

[192] The British Museum website: http://www.thebritishmuseum.ac.uk/science/techniques/sr-tech-xrf.html

[193] Gessini, P., University of Southampton, *private communications.*

[194] Korovkin, V.N. *et al.* "Research of Ion Thrusters in the USSR". AIAA paper 91-096, 1991.

[195] Rawlin, V.K. & Pawlik, E.V. "Mercury Plasma-Bridge Neutraliser". AIAA paper 67-670, 1967.

[196] Fearn, D.G., *private communications.*

[197] Stalder, K.R. & Vidmar, R.J. "Penning Ionisation of Cesium by Photoexcited Mercury, Radiation Transport Effects". *IEEE International Conference on Plasma Science*, 1997.

[198] Kono, A & Hattori, S. "Formation of Excited CuII Levels through Second-Kind Collisions in a Ne-Cu Discharge". *Physics Letters A*, Vol. 93A, pgs. 323-326, 1983.

[199] Goodfellow Catalogue, 1998/1999.

[200] Pottinger, S.J. & Gabriel, S.B. "Optical Probe Measurements on the Internal Plasma of a T6 Type Hollow Cathode". *28th International Electric Propulsion Conference*, IEPC-2003-219, 2003.

[201] Griem, H.R. "Spectral Line Broadening by Plasmas". *New York: Academic Press*, 1974.

[202] Crofton, M.W. "Preliminary Mass Spectrometry of a Xenon Hollow Cathode". *J. Propulsion*, Vol.16, No.1, pgs.157-159, 1999.

[203] Simpson, H.B. *et al.* "A Summary of the QinetiQ Hollow Cathode Development Programme in Support of European High Power Hall Effect and Gridded Thrusters". *28th International Electric Propulsion Conference*, IEPC-2003-210, 2003.

[204] Katz *et al.* "A Model of Hollow Cathode Plasma Chemistry". AIAA paper 2002-4241, 2002.

[205] Katz *et al.* "Model of Hollow Cathode Operation and Life Limiting Mechanism". AIAA paper 2003-0243, 2003.